14 July 2006 | $10

Science

AAAS

MX3005P™ System
Most Flexible

MX3000P® System
Most Affordable

Performance runs in the family.

Choose the personal QPCR system that's right for you.

Stratagene now offers two affordable, fully-featured quantitative PCR (QPCR) systems. The new five-color Mx3005P™ QPCR System includes expanded features to support a wider range of real-time QPCR applications, such as simultaneous five-target detection and alternative QPCR probe chemistries. The Mx3000P® QPCR System is still the most affordably priced four-color 96-well system available.

- **A four- or five-color instrument, with user-selected filters**
- **Advanced optical system design for true multiplexing capability, and wider application support**
- **MxPro™ QPCR Software with enhanced data analysis and export functionality**

Need More Information? Give Us A Call:

Stratagene US and Canada
Order: 800-424-5444 x3
Technical Service: 800-894-1304 x2

Stratagene Europe
Order: 00800-7000-7000
Technical Service: 00800-7400-7400

Stratagene Japan K.K.
Order: 3-5821-8077
Technical Service: 3-5821-8076

www.stratagene.com

STRATAGENE®

Show Them What You See In Your Research

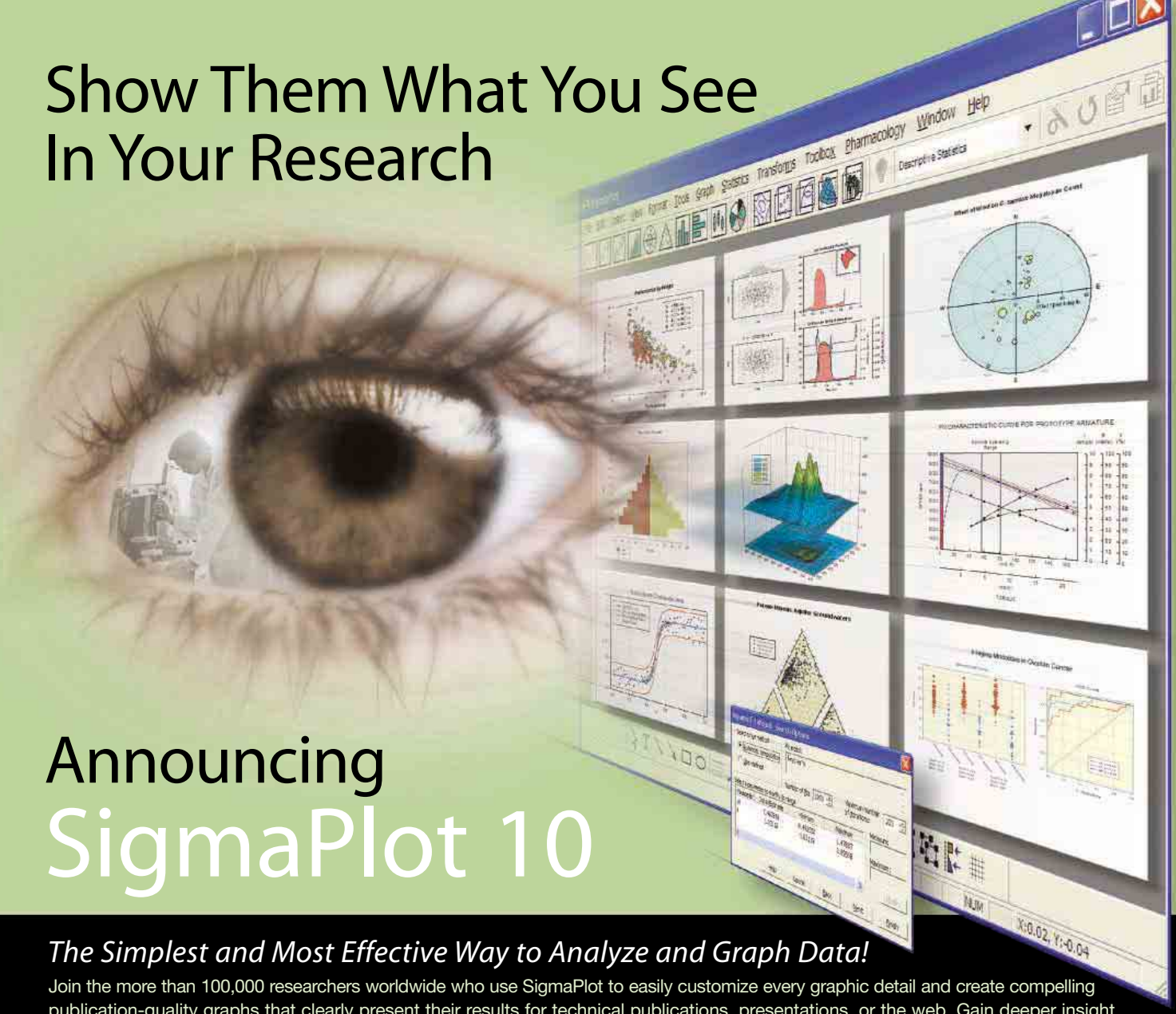

Announcing SigmaPlot 10

The Simplest and Most Effective Way to Analyze and Graph Data!

Join the more than 100,000 researchers worldwide who use SigmaPlot to easily customize every graphic detail and create compelling publication-quality graphs that clearly present their results for technical publications, presentations, or the web. Gain deeper insight into your data with easy-to-use data analysis tools — from sophisticated curve fitting to advanced mathematical calculations. Add SigmaStat and get 30 of the most frequently used statistical tests to analyze scientific research within SigmaPlot's statistics menu or take advantage of the optional Advisor Wizard that walks the non-statistician through the analysis of their data.

SigmaPlot allows you to:

> Create graphs easily and publish your work anywhere
> Import, analyze & manage data quickly and easily
> Choose over 80 different 2-D and 3-D graph types
> Customize every element of your graphs
> Instantly access SigmaPlot from Microsoft® Excel
> Streamline your work by automating repetitive tasks

SIGMAPLOT
Exact Graphs for Exact Science

Add SigmaStat to get easy-to-use, expert statistical analysis within SigmaPlot:

SigmaStat guides you through your analysis:

> Suggests the appropriate statistical test
> Checks assumptions in the data to avoid errors
> If your data violates any of those assumptions, the Advisor Wizard suggests another test
> Generates an intelligent report that explains your results in plain English – not statistical jargon
> Even handles messy data with missing values

Here are a few of the statistical tests SigmaStat performs:

> Regression (e.g., linear, multiple linear and nonlinear)
> Analysis-of-variance - ANOVA (e.g., independent, paired t-tests)
> Nonparametric statistics (e.g., Mann-Whitney, Wilcoxon)
> Rates and Proportions (e.g., Chi-square, contingency tables)
> Power and sample size (e.g., t-tests and proportions)
> Survival analysis (e.g., Kaplan-Meier, Gehan-Breslow)
> Regression diagnostics (e.g., multicollinearity, homoscedasticity)

FREE
INTERACTIVE DEMOS & 30-DAY TRIAL SOFTWARE AVAILABLE AT
WWW.SYSTAT.COM
OR CALL
1-800-797-7401

Systat Software, Inc.
phone: 800-797-7401
e-mail: info-usa@systat.com

Systat Software UK Limited
phone: +44-(0)208-538 0128
e-mail: uksales@systat.com

Systat Software GmbH
phone: +49.2104.9540
e-mail: eurosales@systat.com

Systat Software Asia Pacific Ltd.
phone: +91 - 80 - 4112 0000
e-mail: info-intl@systat.com

adsci

GE Healthcare

Faster protein purification? It's not rocket science.

HiTrap™ columns give you pure proteins with less effort. They come prepacked with the widest choice of media, ensuring results you can depend on in a broad range of applications, and the highest level of convenience.

But we're never content to stand still. We constantly strive for new innovations for tomorrow's research and drug development. And thanks to our technological achievements and global presence, we're able to help you turn your scientific ideas into reality – bringing science to life and helping transform healthcare.

We call it Life Science Re-imagined.

Discover how HiTrap columns can help power your protein purification.
Visit www.gehealthcare.com/life

imagination at work

GE05-06

Volume 313, Issue 5784

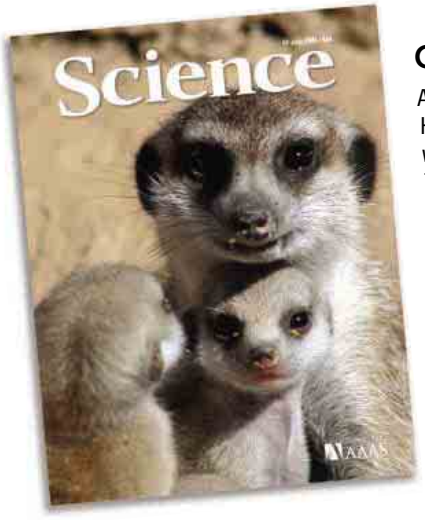

COVER

A meerkat helper huddles a young pup. Helpers teach pups by providing them with opportunities to handle live prey. Teaching may be widespread throughout the animal kingdom and not confined to humans, as has been assumed. See page 227.

Photo: Andrew Radford

DEPARTMENTS

EDITORIAL

NEWS OF THE WEEK

NEWS FOCUS

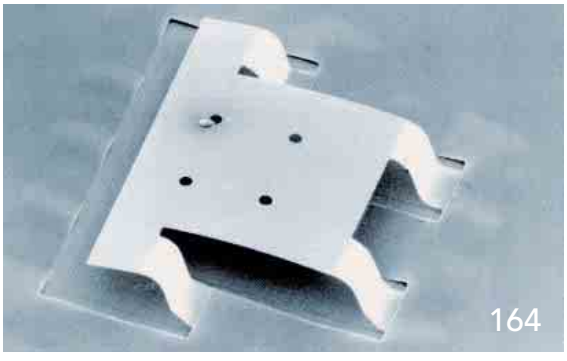

LETTERS

BOOKS *ET AL.*

POLICY FORUM

PERSPECTIVES

CONTENTS continued **>>**

LESS SAMPLE.

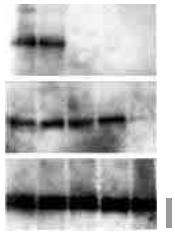

MORE STORY.

Sensitive and sensible, BioSource™ ELISA Kits deliver relevant data from as little as 50 µl. Or fewer than 10,000 cells if you're working with phosphoELISA™ Kits. We offer a wide range of ELISA and phosphoELISA™ Kits for measuring cytokines and phosphorylated proteins—with the exacting sensitivity and reproducibility you need. And faster incubation times. What are you waiting for? See how far your sample can go with BioSource™ ELISA Kits at **www.invitrogen.com/elisa**.

invitrogen™

SCIENCE EXPRESS

www.sciencexpress.org

ECOLOGY

Why Are There So Many Species of Herbivorous Insects in Tropical Rainforests?
V. Novotny et al.
The number of insect species in tropical and temperate forests is determined by the diversity of tree species.
10.1126/science.1129237

PLANETARY SCIENCE

Spitzer Spectral Observations of the Deep Impact Ejecta
C. M. Lisse et al.
The nucleus of comet Tempel 1 is made of minerals and organic compounds from throughout the proto–solar nebula.
10.1126/science.1124694

ATMOSPHERIC SCIENCE

Smoke and Pollution Aerosol Effect on Cloud Cover
Y. J. Kaufman and I. Koren
A higher concentration of aerosol particles increases cloudiness, but this effect is offset by the amount of sunlight absorbed by the clouds.
10.1126/science.1126232

PHYSICS

Violation of Kirchhoff's Laws for a Coherent *RC* Circuit
J. Gabelli et al.
Transport measurements on a fully coherent circuit highlight the difference between quantum and classical electronics.
10.1126/science.1126940

TECHNICAL COMMENT ABSTRACTS

BREVIA

RESEARCH ARTICLES

CONTENTS continued **>>**

TIME MACHINE

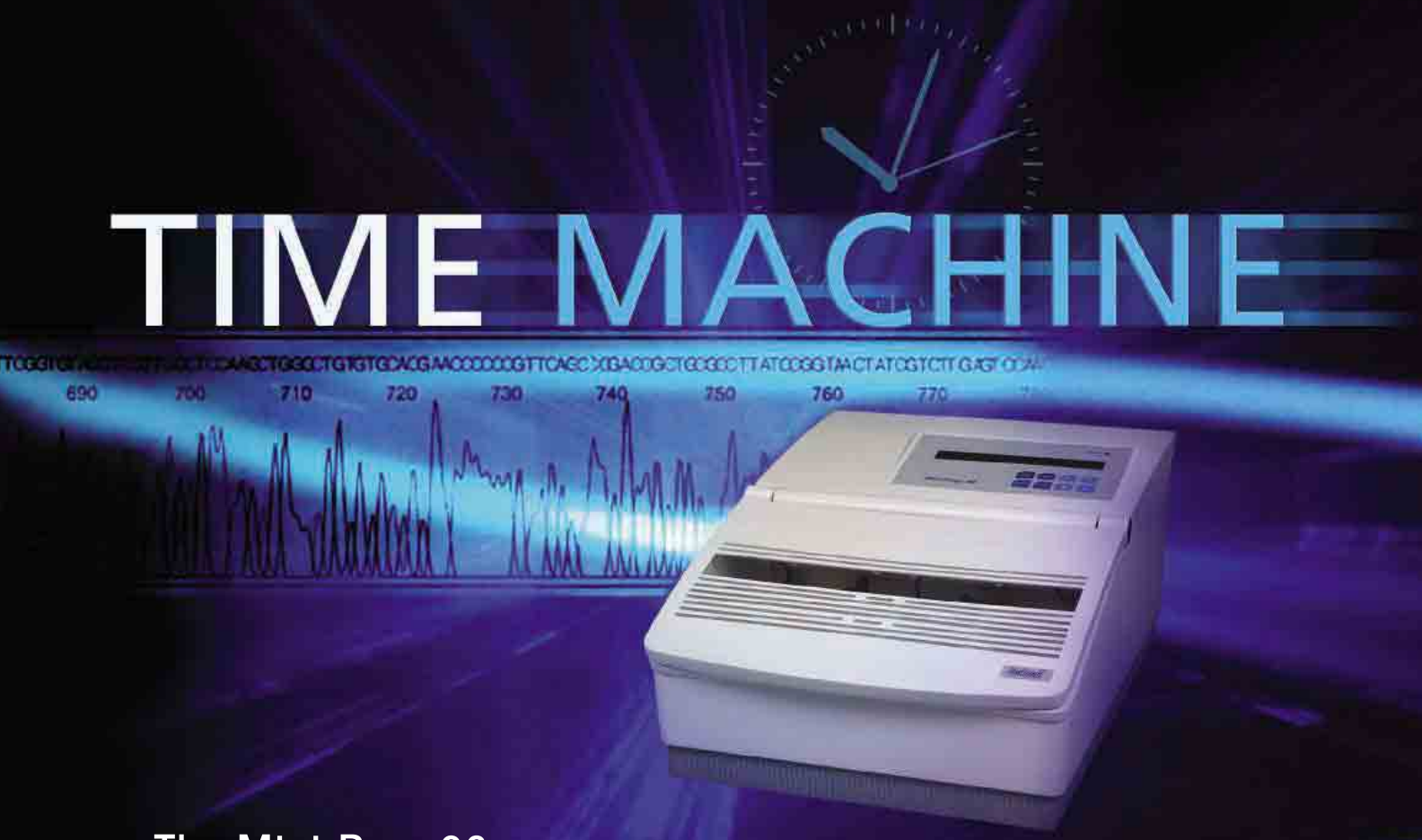

The Mini-Prep 96

A fully automatic, bench-top instrument that purifies plasmid and genomic DNA at the push of a button.

Call now or visit our website:
Your Time is Valuable.

MacConnell RESEARCH

800.466.7949 www.macconnell.com

Science

158 & 213

REPORTS

AAAS
ADVANCING SCIENCE, SERVING SOCIETY

SCIENCE (ISSN 0036-8075) is published weekly on Friday, except the last week in December, by the American Association for the Advancement of Science, 1200 New York Avenue, NW, Washington, DC 20005. Periodicals Mail postage (publication No. 484460) paid at Washington, DC, and additional mailing offices. The title SCIENCE is a registered trademark of the AAAS. Domestic individual membership and subscription (51 issues): $139 ($74 allocated to subscription). Domestic institutional subscription (51 issues): $650; Foreign postage extra: Mexico, Caribbean (surface mail) $55; other countries (air assist delivery) $85. First class, airmail, student, and emeritus rates on request. Canadian rates with GST available upon request, GST #1254 88122. Publications Mail Agreement Number 1069624. **Printed in the U.S.A.**

Change of address: Allow 4 weeks, giving old and new addresses and 8-digit account number. **Postmaster:** Send change of address to AAAS, P.O. Box 96178, Washington, DC 20090–6178. **Single-copy sales:** $10.00 current issue, $15.00 back issue prepaid includes surface postage; bulk rates on request. The identification code for *Science* is 0036-8075. *Science* is indexed in the *Reader's Guide to Periodical Literature* and in several specialized indexes.

CONTENTS continued **>>**

Subaru's sponsorship of the American Association for the Advancement of Science (AAAS) highlights our advanced design of symmetrical all-wheel drive technology to our target markets and underscores Subaru's commitment to further science, engineering and technology education both at the annual meeting and programs throughout the year. Subaru is proud to be the Premier Automotive Sponsor of the AAAS.

In a continuing effort to offer our partners unique and valuable benefits, we provide special offers for AAAS Members, the Subaru VIP Partners Program. AAAS Members can **save up to $3,000*** off the manufacturer's suggested retail price (depending on model and accessories) on the purchase or lease of a new Subaru from participating dealers. To qualify, you must be a AAAS member in good standing for at least six consecutive months prior to participation in this program. Please contact AAAS Member Services at 202.326.6417 or e-mail membership@aaas.org **BEFORE** visiting your local Subaru dealer. Access subaru.com to find a nearby dealer or learn more about Subaru vehicles.

Science
AAAS

Think. Feel. Drive.™

SUBARU

*From MSRP to dealer invoice. MSRP does not include tax, title, and registration fees. Limited time offer subject to change without notice. Terms and conditions apply. This offer replaces all other existing offers, cannot be redeemed for cash and is not applicable in Canada and Hawaii. † Based on Insurance Institute for Highway Safety 40 mph offset frontal crash test, 31 mph side impact test, and 20 mph rear impact test.

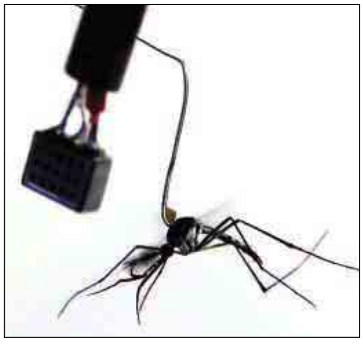

Mosquitoes coordinate their love buzz.

SCIENCE**NOW**

www.sciencenow.org DAILY NEWS COVERAGE

Global Warming's Wrath on Grapes
A hotter world may be bad for premium wine production.

The Buzz on Mosquito Mating
The frequency of a mosquito's hum helps a potential mate tell friend from beau.

Solving the Mystery of Desert Varnish
Dark, glassy substance that coats rocks may hold martian secrets.

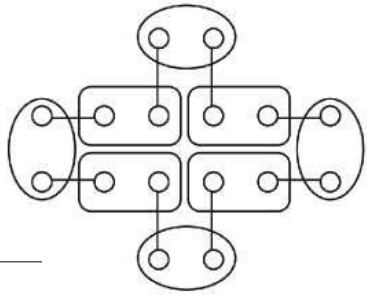

Modeling protein-protein interactions.

SCIENCE'S **STKE**

www.stke.org SIGNAL TRANSDUCTION KNOWLEDGE ENVIRONMENT

REVIEW: Rules for Modeling Signal-Transduction Systems
W. S. Hlavacek
Learn strategies for coping with the biochemical complexity of signaling systems that don't overwhelm the modeler or his computer.

EVENTS
New additions include meetings in Europe and Australia.

Sunny outlook for sustainable energy careers.

SCIENCE **CAREERS**

www.sciencecareers.org CAREER RESOURCES FOR SCIENTISTS

GLOBAL: Special Feature—Sustainable Energy Careers
A. Forde
Rising interest and investment in sustainable energy means career opportunities for scientists.

SPAIN: The Angst of Ramón y Cajal Researchers
E. Pain
A bridge to a permanent position lured many researchers to Spain, but some are struggling to find their place.

US: NIH and Resubmissions
GrantDoctor
An NIH pilot program aims to shorten the review cycle for new investigators.

CANADA: Hydrogen Energy
A. Fazekas
Hydrogen energy insiders across North America tell about training opportunities and career prospects.

US: Wind Energy
R. Arnette
A hurricane of activity in wind energy has opened up a number of career opportunities.

US: Financing Your Research in Alternative Energy
A. Kotok
Scientists interested in alternative energy can tap government funds and private capital for their research.

Separate individual or institutional subscriptions to these products may be required for full-text access.

EDITED BY STELLA HURTLEY AND PHIL SZUROMI

Enough Dust to Go Around

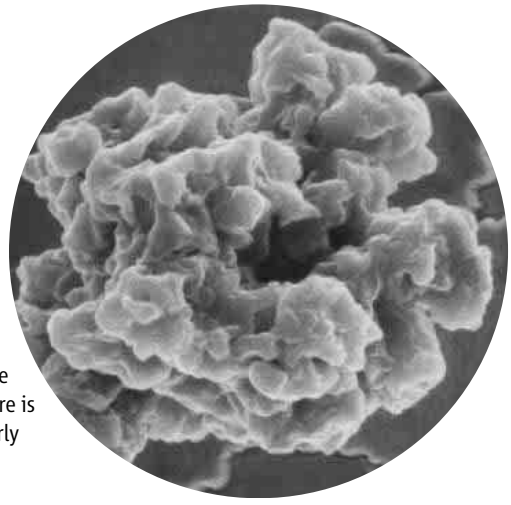

Supernova explosions are thought to have spread dust (mostly carbon and silicate grains) from the dying embers of stars throughout galaxies and beyond. Observations, however, have failed to find enough dust in supernovae to support this idea. **Sugerman *et al.*** (p. 196, published online 8 June; see the Perspective by **Dwek**) used the Spitzer Space Telescope to map the infrared glow from warm dust around the recent supernova SN 2003gd and found 10 times more dust than has been seen in any such object. The progenitor star that exploded as SN 2003gd was more massive than the Sun and similar to the massive and short-lived stars that would have been the first to explode in the early universe. The quantity of dust found here is sufficient for supernovae to have been the dominant dust factories in the early universe and later spreading heavy elements throughout the first galaxies.

The Ages of the Dinosaurs

Little has been known about the overall life histories of groups of dinosaurs, especially the fraction that survived into adulthood and old age. Using deposits near Alberta, Canada, that preserve remains of tyrannosaurs that died over a short period of time, and by making comparisons with other tyrannosaurs, **Erickson *et al.*** (p. 213; see the news story by **Stokstad**) constructed a survivorship life table. The results imply that juvenile survivorship was high but that only a small fraction reached extreme size and an old age of between 20 and 30 years.

Routes to Friction Control

As mechanical systems shrink in size, friction and wear must be treated differently than in macroscopic machines; there is less material to wear away before a device fails, and liquid lubricants tend to become viscous in confined spaces (see the Perspective by **Carpick**). **Socoliuc *et al.*** (p. 207) present a dynamic approach for reducing friction. They slide the sharp silicon tip of a friction force microscope over the surface of NaCl and KBr salt crystals while mechanical exciting the tip in the direction normal to the surface. When the frequency of oscillation matched a mechanical resonance of the tip in the normal direction (or half that value), the friction was sharply reduced; excitation of lateral resonances had no effect. The normal motion likely allows the tip to find regions of interaction where friction is still finite but stick-slip motion disappears. **Park *et al.*** (p. 186) found that charge accumulation or depletion modified the friction force between a silicon surface and a metal-coated probe tip of an atomic force microscope. When the sample was positively biased, the friction force increase for positively doped regions of the sample but stayed the same in negatively doped regions

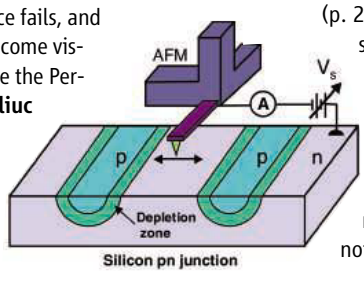

Examining Emulsions

Emulsions consist of two immiscible liquids that are mixed together, and often the droplets of one component are stabilized by the addition of a surfactant. For small-sized droplets, internal pressure stabilizes the droplets and interactions between droplets are not significant. At large sizes, deformation and hydrodynamic forces dominate, and these forces can be measured by a number of techniques. **Dagastine *et al.*** (p. 210) have developed a method to study droplets of intermediate size. Deformation, hydrodynamic drainage, and interaction forces all contribute to the overall behavior of droplet-droplet interactions, and thus current models of emulsion behavior may not be suitable.

One-Dimensional Wigner Crystal

Wigner crystallization is a natural correlated state for an electronic system whose Coulombic interaction is stronger than the kinetic energy of the electrons and has been seen in two- and three-dimensional systems. **Yamamoto *et al.*** (p. 204) performed Coulomb drag experiments in a one-dimensional realization with two closely spaced parallel nanowires, where the injection of current in one wire (the drive wire) drags electrons in the other wire. Usually, the direction of drag is in the direction of current flow, but in this case they observed negative Coulomb drag, where the drag current flows opposite to the driving current. They interpret this negative drag as the Wigner crystallization of the flowing electrons in the drag wire.

Nailing Down the Effects of Arginylation

Arginylation is a posttranslational modification critical for embryonic development, but the protein targets and molecular effects of arginylation are largely unknown. **Karakasova *et al.*** (p. 192, published online 22 June; see the Perspective by **Bulinski**) show the regulation of a single target protein by arginylation with effects on the molecular and cellular level. β-actin, an abundant, essential intracellular protein, is arginylated in vivo, and this modification regulates actin polymerization, cell motility, and lamella formation in motile cells.

A Study in Character Displacement

Long-term studies of wild populations of animals are key to the understanding of ecological and evolutionary processes. Previous work has already demonstrated the evolution of beak size in a population of Darwin's finches on a Galápagos island when food supply changes. Continua-

CREDITS (TOP TO BOTTOM): L. NITTLER/CARNEGIE INSTITUTION OF WASHINGTON; PARK *ET AL.*

tion of the study by **Grant and Grant** (p. 224; see the news story by **Pennisi**) has revealed an evolutionary shift caused by a competitor species that led to character displacement—a divergence in beak size between the two species. It is the strongest evolutionary change recorded in 33 years of study of this system. The demonstration of character displacement in nature strengthens theories of competitive interaction in speciation, adaptive radiation, and the assembly of ecological communities.

Destructive Influence

Certain bacterial pathogens inject their effector proteins into the target cell to wreak havoc. **Nomura *et al.*** (p. 220) now show what a *Pseudomonas* protein does once it is inside an *Arabidopsis* plant cell. The virulence protein, HopM1, targets a plant defense protein, AtMIN7, by escorting that protein to its destruction by the plant's own proteasome. AtMIN7 normally functions in the vesicle trafficking that builds up a cell-wall response to pathogen invasion.

This Is How We Catch Scorpions

Teaching is found in all human societies. Are there unambiguous examples of teaching in other species? **Thornton and McAuliffe** (p. 227; see the cover) describe observational and experimental field studies on the role of teaching in the development of prey capture in wild meerkats. Teachers modified their behavior in the presence of pups by gradually introducing them to live prey, monitoring their handling behavior, nudging prey, and retrieving and further modifying prey if necessary. Dangerous food items (such as scorpions) were more likely to be killed or disabled than other mobile prey. Helpers gained no direct benefits from their provisioning behavior and incurred costs through giving pups prey that was difficult to handle and that might escape.

A Getting-Inside Story

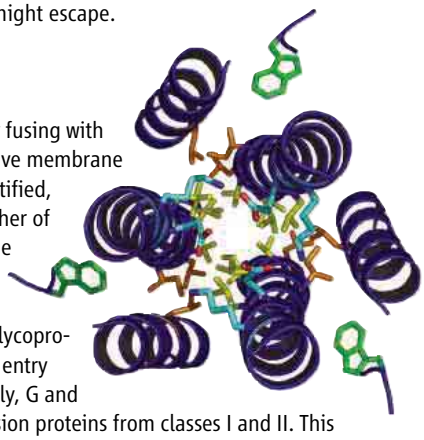

Enveloped viruses deliver their genome into the host by fusing with its membrane. Two classes of viral glycoproteins that drive membrane fusion through conformational changes have been identified, but a number of viral fusion proteins do not fall into either of these classes. **Roche *et al.*** (p. 187) have determined the crystal structure of the atypical membrane fusion glycoprotein (G) from vesicular stomatitis virus, and **Heldwein *et al.*** (p. 217) have determined the structure of glycoprotein B (gB), a conserved component of the complex cell entry machinery of herpes simplex virus (HSV-1). Unexpectedly, G and gB are homologous with both combining features of fusion proteins from classes I and II. This homology identifies gB as the viral fusogen in HSV-1 and has interesting implications in considering the evolution of viral fusion proteins (see the Perspective by **Steven and Spear**).

CREDIT: ROCHE *ET AL.*

New Role for Histone-Like Protein

Bacteria can incorporate exogenous DNA into their genomes (for example, antibiotic resistance genes and virulence factors), but this process must be control to prevent harmful effects. **Navarre *et al.*** (p. 236, published online 8 June) have evidence for a mechanism that regulates the influx of novel genes, but allows the evolution new function. Horizontally acquired DNA can often be recognized in bacteria by its bias in AT-GC content. Interestingly, a histone-like protein from Salmonella, H-NS (histone-like nucleoid structuring protein), has an enigmatic and nonspecific affinity for AT-rich regions, which then inhibits gene expression. It appears that this recognition of AT regions is a form of self-non-self discrimination.

Bacterial Gold Nuggets

Several studies have shown that microorganisms are involved in the cycling of gold in the environment, and microbial mechanisms for the formation of gold nuggets have been postulated. **Reith *et al.*** (p. 233; see the news story by **Kerr**) now find that active bacterial biofilms are associated with secondary gold grains obtained from Australian mines. They have assessed the community structure of these biofilms and identified key organisms associated with the gold grains as well as potential metabolisms for detoxification and precipitation of the precious metal.

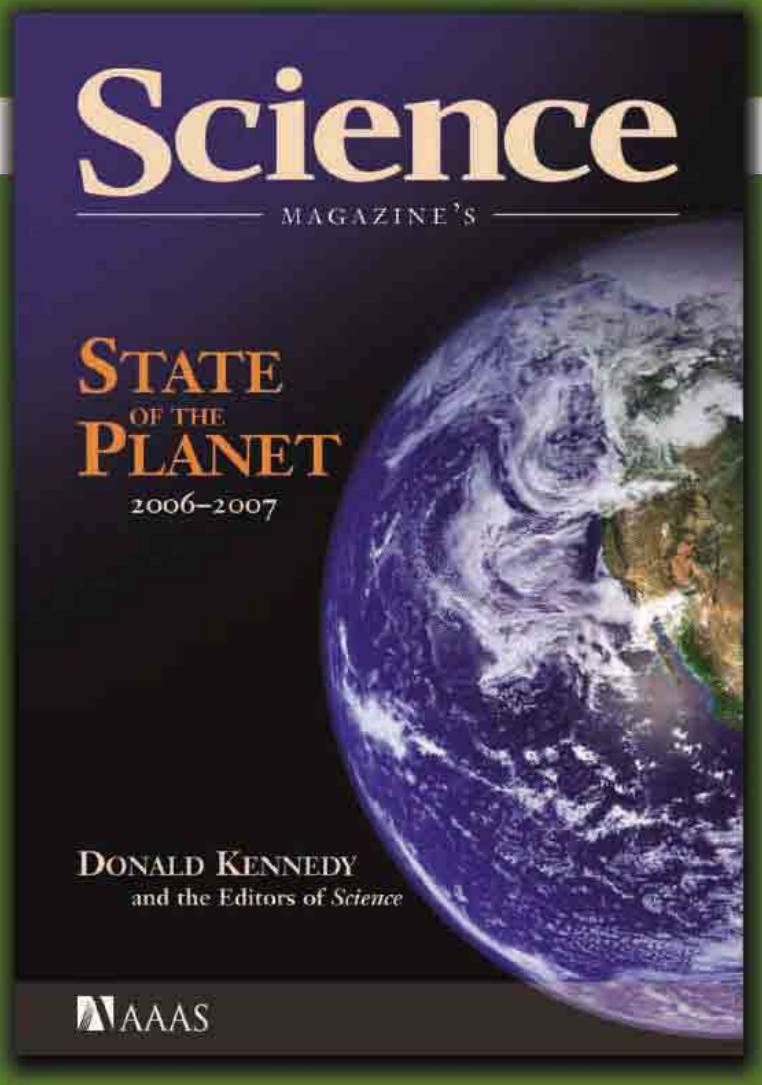

Science Magazine's
State of the Planet 2006-2007

Donald Kennedy, Editor-in-Chief, and the Editors of *Science*

The American Association for the Advancement of Science

The most authoritative voice in American science, *Science* magazine, brings you current knowledge on the most pressing environmental challenges, from population growth to climate change to biodiversity loss.

COMPREHENSIVE • CLEAR • ACCESSIBLE

ISLANDPRESS

Science
AAAS

islandpress.org

Dr. Angela Merkel is the Chancellor of Germany.

German Science Policy 2006

THE GERMAN GOVERNMENT RECOGNIZES THAT OUR FUTURE LIES IN A KNOWLEDGE-BASED SOCIETY founded on freedom and responsibility. This is what will enable Germany to rise to the challenges of today's world, be they national or global, or economic, social, or ecological in nature. That is why the promotion of science, research, and innovation is one of my top priorities.

"People love chopping wood," Albert Einstein once said. "In this activity one immediately sees results." Science policy, by contrast—like science itself—demands staying power. It requires cooperation between many different actors, the investment of considerable resources, and the courage to strike out in new directions. German science and research have a long and proud tradition that we must cultivate and build on. We want to offer German science and research conditions that rival the best in the world. Our benchmarks are excellence, internationality, and freedom. With our new 6-billion-Euro program to fund innovative beacon projects, we are investing more than ever before in top-flight science and research. The conceptual framework for this will be provided by a comprehensive high-tech strategy action plan. Our efforts to promote higher education and research institutions are geared to encouraging healthy competition. With our Excellence Initiative, Joint Initiative for Research and Innovation, and Pact for the Universities, we want to strengthen institutions and academics that are particularly outstanding and creative and also network successfully. By 2010, we aim to increase spending on R&D to 3% of gross domestic product. Science and research will be one of the priorities of Germany's European Union (EU) presidency.

We are working hard to make German higher education more international, because excellence today is defined in global terms. In a few years, we will have completed the switch to internationally compatible bachelor's and master's degree courses. We are keen for our higher education and research institutions to expand their international links and are also committed to strengthening cooperation in Europe. To build new experimental research facilities such as the x-ray free-electron laser in Hamburg, we have joined forces with partners from all over the world.

We also plan to give science and research a freer hand. The task of government is to create conditions in which they can flourish and to provide the right kind of stimulus. That means that our universities and research institutions must be given more independence. They need greater freedom to choose their students and staff, develop their own profiles, cooperate with industry, and spend their funds as they see fit.

We believe there should be intensified dialogue between policy-makers, scientists, and industry on all aspects of science and technology policy. This is particularly crucial in fields where new scientific advances may raise difficult ethical issues or where policy decisions on the right innovation strategy for the future are at stake. That is why I have established a Council for Innovation and Growth, which brings together prominent representatives of the scientific, business, and political communities. For the same reason, we strongly support, at the European level, the establishment of a European Research Council to advise and comment on research policy decisions of the EU.

Germany's future depends on first-class research, creative talent, and high-quality education and training that are geared toward international standards as well as a fair deal for everyone, irrespective of social or ethnic background, who is willing to contribute to our society. Dedicated people and pioneering spirits are our greatest assets. An important goal of the German government's science policy is to encourage the creative talent of everyone who lives, works, or conducts research in Germany and to ensure that their working conditions and quality of life are continually improved.

I profoundly believe (to quote Albert Einstein again) that "Concern for man himself and his fate must always form the chief interest for all technical endeavours . . . in order that the creations of our mind shall be a blessing and not a curse for mankind."

– Angela Merkel

10.1126/science.1131001

EDITED BY GILBERT CHIN AND JAKE YESTON

Grapes (*Vitis vinifera*, inset) grown along the Mokelumne River.

ECOLOGY/EVOLUTION

Subsidy from the Sea

Migratory species, by virtue of their movements, can be agents of nutrient transport between ecosystems. For example, stable isotope studies have shown that the carcasses of salmon can be a rich source of nutrients not only for the mountain streams in which they die but also for adjacent terrestrial habitats. Merz and Moyle have quantified the nutrient subsidy of Pacific salmon to Californian grape growers. They show that cultivated vines as well as native streamside vegetation bordering on salmon spawning grounds derive about 20% of their foliar nitrogen from marine sources via returning salmon. This is a classic example of what has become known as an ecosystem service—in this case, one of substantial economic and oenological value. — AMS

Ecol. Appl. **16**, 999 (2006).

CHEMISTRY

Tiny MOFs that Glow

The structural tunability of metal organic framework (MOF) solids, in which bridging organic ligands form a scaffold by coordinating to metal ions, has proven useful in bulk applications such as gas sorption. Pushing toward the opposite end of the size spectrum, Rieter *et al.* present a controlled approach to the synthesis of discrete nanometer-scale MOF assemblies. They combined trivalent gadolinium ions with a benzenedicarboxylate (BDC) salt in a microemulsion, created through surfactant addition to an isooctane/hexanol/water mixture. By modifying the water-to-surfactant ratio, the authors could tune the size of the resultant $Gd(BDC)_{1.5}(H_2O)_2$ rods from ~100 nm to ~1 μm in length, and ~40 to ~100 nm in diameter. The high gadolinium density in the rods is advantageous for contrast enhancement in magnetic resonance imaging; the rods evidenced remarkably high relaxivities ($>10^7$/s/mmol) during test runs using aqueous xanthan gum suspensions. Doping with alternative metals increased the versatility of potential imaging applications: addition of 5 mole % of either europium or terbium during the synthesis respectively induced red or green luminescence on ultraviolet irradiation of the rods in solution. — JSY

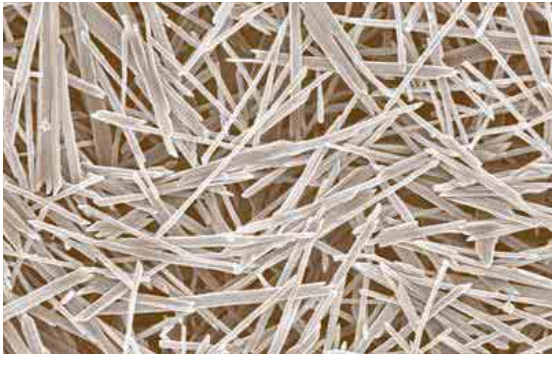

Magnified MOF nanorods.

J. Am. Chem. Soc. **128**, 10.1021/ja0627444 (2006).

PSYCHOLOGY

Close Encounters

The effect of contact between groups on prejudice has been a topic of research at least as far back as the middle of the 20th century. Since then, there have been a very large number of studies and many reviews of this literature. Pettigrew and Tropp have conducted a meta-analysis of what has become known as intergroup contact theory. They (and their dedicated research assistants) have combed through published papers and unpublished dissertations, using a methodological (rather than topical) basis for inclusion; the final data set covers 515 studies, containing over 700 independent samples representing a quarter million individuals spread over 38 countries. The summary finding is that intergroup contact reduces prejudice.

Their statistical analyses reveal that this cannot be ascribed to self-selection by the participants, or to a publication bias toward positive results, or to the rigor of the research (methodologically stronger studies yielded larger effect sizes). Roughly half of the studies focused on nonracial and nonethnic groups (as described by sexual orientation or physical or mental disability, for example), and the effect sizes seen within this subset were the same as that for the racial/ethnic targets that stimulated the historical development of intergroup contact theory. Furthermore, it appears that the effects on individual attitudes can generalize to other members of the outgroup and even to other outgroups.

How is this mediated? They find that Allport's four features (common goals, intergroup cooperation, equal status, and official sanction) contribute significantly to the reduction of prejudice but are not essential, and that the last of the four conditions may be the most important one. Greater contact may reduce feelings of uncertainty or discomfort that might otherwise coalesce into anxiety or perceived threat, which might in turn harden into prejudice. Yet these ameliorative shifts may not survive in the absence of normative or authoritarian support, and studies of why contact fails to curb prejudice are needed. — GJC

J. Pers. Soc. Psychol. **90**, 751 (2006).

CREDITS (TOP TO BOTTOM): J. E. MERZ.; RIETER *ET AL.*, *J. AM. CHEM. SOC.* **128**, 10.1021/JA0627444 (2006)

PHYSICS

Quark Plasma Reexamined

A fraction of a second after the Big Bang, the universe is thought to have consisted of a hot primordial soup of fundamental particles: a quark-gluon plasma. Researchers have sought to recreate this early matter by smashing heavy ions together. Because the quark soup lasts only for a short time and quarks cannot exist in free form, the formation of the plasma is diagnosed by what other kinds of particles emerge from the collision. Analysis of this collision process is predicated on important assumptions about the fluid dynamic properties of the quark plasma and the strength of interactions among the particles. One view has been that the data support the existence of a strongly coupled quark-gluon plasma.

Asakawa *et al.* propose an alternative picture to explain the fluid dynamics. Their analysis reaches back to theories from the 1960s that were developed to understand particle transport in turbulent magnetically confined plasmas. In this environment, excited oscillations of the plasma can scatter particles and strongly reduce the plasma viscosity, a phenomenon that came to be called anomalous transport. The authors find that a similar process, with quark-gluon forces replacing electromagnetic waves, could give rise to an anomalous viscosity in a weakly coupled plasma and thereby explain the fluid dynamic behavior revealed in recent experimental heavy-ion collision data. — DV

Phys. Rev. Lett. **96**, 252301 (2006).

CHEMISTRY

Warped Simulations

Aromatic molecules such as benzene and naphthalene are planar, but several electron-correlated ab initio computational methods (such as CISD, configuration interactions with single and double excitations), when used with certain commonly available basis sets, predict nonplanar structures and yield imaginary values for at least one vibrational frequency. Inherently one-electron methods such as Hartree-Fock predict the correct planar structures and real vibrational frequencies when the same basis sets are used.

Moran *et al.* analyzed the problem at the MP2 level (Møller-Plesset perturbation theory with two-electron correlations). After clearly ruling out numerical precision error, they found that basis sets lacking higher angular momentum functions (that is, too rich in s-, p-, and even d-orbital character) create artificially large correlation energies between σ and π electrons. This effect in turn leads to the distortions from planarity and imaginary vibrational frequencies. The authors also indicate the types of basis sets that minimize such errors. — PDS

J Am. Chem. Soc. **128**, 10.1021/ja0630285 (2006).

Science STKE AAAS

www.stke.org

<< Inhibiting the Restocking of the Store

Golli proteins, which are generated by alternative splicing from the gene that encodes myelin basic proteins (which are found only in the nervous system), are expressed not only in the nervous system but also in immune system tissues. Feng *et al.*, who previously showed that golli negatively regulates T cell activation, establish that this occurs via the inhibition of calcium influx. When stimulated with antibody directed against CD3 (anti-CD3) or with anti-CD3 plus anti-CD28, golli-deficient T cells proliferated more vigorously than did wild-type cells. Similarly, golli-deficient cells stimulated with anti-CD3 plus anti-CD20 produced more interleukin-2 (a T cell growth factor) than did wild-type cells. No differences between golli-deficient and wild-type T cells in extracellular receptor–activated kinase (ERK) or Jun N-terminal kinase (JNK) activation in response to anti-CD3 stimulation were apparent. On the other hand, the increase in intracellular calcium upon stimulation was enhanced. Calcium imaging in the presence or absence of extracellular calcium and thapsigargin suggested that golli inhibited calcium influx through store-operated calcium channels (these plasma membrane conduits open in response to a signal that calcium levels in internal compartments need replenishing). Moreover, patch-clamp analysis of golli-deficient cells revealed increased inward calcium current in response to store depletion. A portion of T cell golli protein was associated with the plasma membrane, and experiments in which cells were transfected with either wild-type golli protein or a myristoylation-deficient mutant indicated that membrane association was required for golli to inhibit calcium influx. Thus, the authors conclude that golli acts as a negative regulator of T cell activation by means of a mechanism completely distinct from that of other regulators of T cells. — EMA

Immunity **24**, 717 (2006).

www.sciencemag.org

Science

1200 New York Avenue, NW
Washington, DC 20005
Editorial: 202-326-6550, FAX 202-289-7562
News: 202-326-6500, FAX 202-371-9227

Bateman House, 82-88 Hills Road
Cambridge, UK CB2 1LQ
+44 (0) 1223 326500, FAX +44 (0) 1223 326501

Subscription Services For change of address, missing issues, new orders and renewals, and payment questions: 866-434-AAAS (2227) or 202-326-6417, FAX 202-842-1065. Mailing addresses: AAAS, P.O. Box 96178, Washington, DC 20090-6178 or AAAS Member Services, 1200 New York Avenue, NW, Washington, DC 20005

Institutional Site Licenses please call 202-326-6755 for any questions or information

Reprints: Author Inquiries 800-635-7181
Commercial Inquiries 803-359-4578
Corrections 202-326-6501

Permissions 202-326-7074, FAX 202-682-0816

Member Benefits Bookstore: AAAS/BarnesandNoble.com bookstore www.aaas.org/bn; Car purchase discount: Subaru VIP Program 202-326-6417; Credit Card: MBNA 800-847-7378; Car Rentals: Hertz 800-654-2200 CDP#343457, Dollar 800-800-4000 #AA1115; AAAS Travels: Betchart Expeditions 800-252-4910; Life Insurance: Seabury & Smith 800-424-9883; Other Benefits: AAAS Member Services 202-326-6417 or www.aaasmember.org.

science_editors@aaas.org	(for general editorial queries)
science_letters@aaas.org	(for queries about letters)
science_reviews@aaas.org	(for returning manuscript reviews)
science_bookrevs@aaas.org	(for book review queries)

Published by the American Association for the Advancement of Science (AAAS), *Science* serves its readers as a forum for the presentation and discussion of important issues related to the advancement of science, including the presentation of minority or conflicting points of view, rather than by publishing only material on which a consensus has been reached. Accordingly, all articles published in *Science*—including editorials, news and comment, and book reviews—are signed and reflect the individual views of the authors and not official points of view adopted by the AAAS or the institutions with which the authors are affiliated.

AAAS was founded in 1848 and incorporated in 1874. Its mission is to advance science and innovation throughout the world for the benefit of all people. The goals of the association are to: foster communication among scientists, engineers and the public; enhance international cooperation in science and its applications; promote the responsible conduct and use of science and technology; foster education in science and technology for everyone; enhance the science and technology workforce and infrastructure; increase public understanding and appreciation of science and technology; and strengthen support for the science and technology enterprise.

Information for Contributors

See pages 102 and 103 of the 6 January 2006 issue or access www.sciencemag.org/feature/contribinfo/home.shtml

EDITOR-IN-CHIEF **Donald Kennedy**
EXECUTIVE EDITOR **Monica M. Bradford**
DEPUTY EDITORS **R. Brooks Hanson, Katrina L. Kelner**
NEWS EDITOR **Colin Norman**

Editorial supervisory senior editors Barbara Jasny, Phillip D. Szuromi; **senior editor/perspectives** Lisa D. Chong; **senior editors** Gilbert J. Chin, Pamela J. Hines, Paula A. Kiberstis (Boston), Marc S. Lavine (Toronto), Beverly A. Purnell, L. Bryan Ray, Guy Riddihough (Manila), H. Jesse Smith, Valda Vinson, David Voss; **associate editors** Jake S. Yeston, Laura M. Zahn; **online editor** Stewart Wills; **associate online editor** Tara S. Marathe; **book review editor** Sherman J. Suter; **associate letters editor** Etta Kavanagh; **information specialist** Janet Kegg; **editorial manager** Cara Tate; **senior copy editors** Jeffrey E. Cook, Cynthia Howe, Harry Jach, Barbara P. Ordway, Jennifer Sills, Trista Wagoner; **copy editor** Peter Mooreside; **editorial coordinators** Carolyn Kyle, Beverly Shields; **publication assistants** Ramatoulaye Diop, Chris Filiatreau, Joi S. Granger, Jeffrey Hearn, Lisa Johnson, Scott Miller, Jerry Richardson, Brian White, Anita Wynn; **editorial assistants** Lauren Kmec, Patricia M. Moore, Michael Rodewald; **executive assistant** Sylvia S. Kihara; **administrative support** Maryrose Police

News senior correspondent Jean Marx; **deputy news editors** Robert Coontz, Jeffrey Mervis, Leslie Roberts, John Travis; **contributing editors** Elizabeth Culotta, Polly Shulman; **news writers** Yudhijit Bhattacharjee, Adrian Cho, Jennifer Couzin, David Grimm, Constance Holden, Jocelyn Kaiser, Richard A. Kerr, Eli Kintisch, Andrew Lawler (New England), Greg Miller, Elizabeth Pennisi, Robert F. Service (Pacific NW), Erik Stokstad; Diane Garcia, Briahna Gray (interns); **contributing correspondents** Barry A. Cipra, Jon Cohen (San Diego, CA), Daniel Ferber, Ann Gibbons, Robert Irion, Mitch Leslie (NetWatch), Charles C. Mann, Evelyn Strauss, Gary Taubes, Ingrid Wickelgren; **copy editors** Linda B. Felaco, Rachel Curran, Sean Richardson; **administrative support** Scherraine Mack, Fannie Groom **bureaus:** Berkeley, CA: 510-652-0302, FAX 510-652-1867, New England: 207-549-7755, San Diego, CA: 760-942-3252, FAX 760-942-4979, Pacific Northwest: 503-963-1940

Production director James Landry; **senior manager** Wendy K. Shank; **assistant manager** Rebecca Doshi; **senior specialists** Jay Covert, Chris Redwood; **specialist** Steve Forrester **Preflight director** David M. Tompkins; **manager** Marcus Spiegler; **specialist** Jessie Mudjitaba

Art director Joshua Moglia; **associate art director** Kelly Buckheit; **illustrators** Chris Bickel, Katharine Sutliff; **senior art associates** Holly Bishop, Laura Creveling, Preston Huey; **associate** Nayomi Kevitiyagala; **photo editor** Leslie Blizard

***Science* International**

Europe (science@science-int.co.uk) **editorial: international managing editor** Andrew M. Sugden; **senior editor/perspectives** Julia Fahrenkamp-Uppenbrink; **senior editors** Caroline Ash (Geneva: +41 (0) 222 346 3106), Stella M. Hurtley, Ian S. Osborne, Stephen J. Simpson, Peter Stern; **associate editor** Joanne Baker **editorial support** Alice Whaley; Deborah Dennison **administrative support** Janet Clements, Phil Marlow, Jill White; **news: international news editor** Eliot Marshall **deputy news editor** Daniel Clery; **correspondent** Gretchen Vogel (Berlin: +49 (0) 30 2809 3902, FAX +49 (0) 30 2809 8365); **contributing correspondents** Michael Balter (Paris), Martin Enserink (Amsterdam and Paris), John Bohannon (Berlin); **intern** Laura Blackburn

Asia Japan Office: Asca Corporation, Eiko Ishioka, Fusako Tamura, 1-8-13, Hirano-cho, Chuo-ku, Osaka-shi, Osaka, 541-0046 Japan; +81 (0) 6 6202 6272, FAX +81 (0) 6 6202 6271; asca@os.gulf.or.jp; **asia news editor** Richard Stone +66 2 662 5818 (rstone@aaas.org) **japan news bureau** Dennis Normile (contributing correspondent, +81 (0) 3 3391 0630, FAX 81 (0) 3 5936 3531; dnormile@gol.com); **china representative** Hao Xin, + 86 (0) 10 6307 4439 or 6307 3676, FAX +86 (0) 10 6307 4358; haoxin@earthlink.net; **south asia** Pallava Bagla (contributing correspondent +91 (0) 11 2271 2896; pbagla@vsnl.com) **Africa** Robert Koenig (contributing correspondent, rob.koenig@gmail.com)

EXECUTIVE PUBLISHER **Alan I. Leshner**
PUBLISHER **Beth Rosner**

Fulfillment & Membership Services (membership@aaas.org) **director** Marlene Zendell; **manager** Waylon Butler; **systems specialist** Andrew Vargo; **customer service supervisor** Pat Butler; **specialists** Laurie Baker, Tamara Alfson, Karena Smith, Vicki Linton; **circulation associate** Christopher Refice; **data entry supervisor** Cynthia Johnson

Business Operations and Administration director Deborah Rivera-Wienhold; **business manager** Randy Yi; **senior business analyst** Lisa Donovan; **business analyst** Jessica Tierney; **financial analyst** Michael LoBue, Farida Yeasmin; **rights and permissions: administrator** Emilie David; **associate** Elizabeth Sandler; **marketing: director** John Meyers; **marketing managers** Darryl Walter, Allison Pritchard; **marketing associates** Julianne Wielga, Mary Ellen Crowley, Catherine Featherston, Alison Chandler, Lauren Lamoureux; **international marketing manager** Wendy Sturley; **marketing/member services executive:** Linda Rusk; **japan sales** Jason Hannaford; **site license sales: director** Tom Ryan; **sales and customer service** Mehan Dossani, Kiki Forsythe, Catherine Holland, Wendy Wise; **electronic media: manager** Lizabeth Harman; **production associates** Amanda K. Skelton, Lisa Stanford, Nichele Johnston; **lead applications developer** Carl Saffell

Advertising director worldwide ad sales Bill Moran

Product (science_advertising@aaas.org); **midwest** Rick Bongiovanni: 330-405-7080, FAX 330-405-7081 • **west coast/w. canada** Teola Young: 650-964-2266 **east coast/e. canada** Christopher Breslin: 443-512-0330, FAX 443-512-0331 • **uk/europe/asia** Tracy Holmes: +44 (0) 1223-326-525, FAX +44 (0) 1223-325-532 **japan** Mashy Yoshikawa: +81 (0) 33235 5961, FAX +81 (0) 33235 5852 **traffic manager** Carol Maddox; **sales coordinator** Deiandra Simms

Classified (advertise@sciencecareers.org); **u.s.: sales director** Gabrielle Boguslawski: 718-491-1607, FAX 202-289-6742; **inside sales manager** Daryl Anderson: 202-326-6543; **west coast/midwest** Kristine von Zedlitz: 415-956-2531; **east coast** Jill Downing: 631-580-2445; **canada, meetings and announcements** Kathleen Clark: 510-271-8349; **sales coordinators** Erika Bryant; Rohan Edmonson, Allison Millar, Joyce Scott, Shirley Young; **international: sales manager** Tracy Holmes: +44 (0) 1223 326525, FAX +44 (0) 1223 326532; **sales** Christina Harrison, Svitlana Barnes; **sales assistant** Helen Moroney; **japan:** Jason Hannaford: +81 (0) 52 789 1860, FAX +81 (0) 52 789 1861; **production: manager** Jennifer Rankin; **assistant manager** Deborah Tompkins; **associates** Christine Hall; Amy Hardcastle; **publications assistants** Robert Buck; Mary Lagnaoui

IMAGES

To the Bone

Digital Morphology from the University of Texas, Austin, serves as a virtual anatomy lab for students and allows researchers to analyze hard-to-find specimens. The site uses an x-ray computed tomography scanner to peek inside more than 500 animals, plants, and fossils. For instance, you can call up the skull of the world's largest hummingbird (*Patagona gigas*; above), which tips the scales at 24 grams. Three-dimensional movies let you spin and flip the skull to study it from different angles. You can also view it slice by slice to highlight internal details, or compare the hummingbird's feeding adaptations to those of another nectar-slurping bird. The site provides background on each species, details on the specimens, and other information. >>
www.digimorph.org

RESOURCES

Immunologists of NIH, Unite!

Immunologists in the National Institutes of Health's (NIH's) intramural program are scattered among more than a dozen institutes. The new hub Immunology@NIH connects researchers in far-flung labs and helps outside scientists track down potential collaborators. The site holds a directory of some 150 NIH scientists who are probing the immune system. Visitors can also browse a listing of training opportunities or dig into a video archive that houses 4 years of immunology seminars by NIH staff members and other researchers. >> www.immunology.nih.gov

COMMUNITY SITE

Up on the Plateau

Tibet has lured researchers studying everything from traditional forms of conflict resolution to the effects of high elevation on child survival. Whether you're an anthropologist or a physiologist, you'll find plenty of information about the lofty region at the Web site of the Center for Research on Tibet at Case Western Reserve University in Cleveland, Ohio. Visitors can download papers and online books—written by researchers at the center and outside scholars—on marriage customs, social systems, and other topics. The average elevation on the Tibetan plateau exceeds 4000 meters, and the site houses more than a dozen publications on residents' adaptations. Tibetans can crank up blood flow to the brain faster than lowlanders can, for instance, and their lungs pump out more nitric oxide, which dilates vessels and appears to speed the absorption of oxygen. >>
www.cwru.edu/affil/tibet

HISTORY

Integrating Mathematics

When officials at Johns Hopkins University in Baltimore, Maryland, announced their math graduate fellowship in 1876, they were thrilled to offer admission to "C. Ladd"—not realizing that the "C" stood for "Christine." Thanks to the support of a powerful professor, Christine Ladd-Franklin (1847–1930) continued her studies at the school even though it was closed to women, and her later work on symbolic logic and visual optics was so well regarded that she merited an obituary in *Science* (21 March 1930, p. 307). Read more of Ladd-Franklin's story and those of other women mathematicians at this site from math professor Lawrence Riddle of Agnes Scott College in Decatur, Georgia. Brief biographies, some penned by students at the college, portray more than 190 numerically gifted women from as far back as the 6th century B.C.E. >>
www.agnesscott.edu/lriddle/women/women.htm

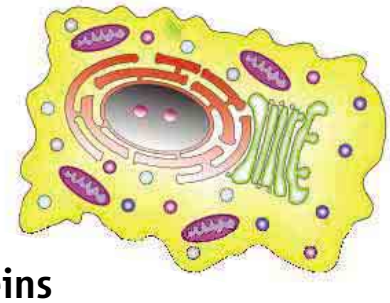

DATABASE

GPS for Proteins

Where a protein hangs out and how it interacts with the cell's membranes furnish clues to its function. At LOCATE, researchers can track down both types of information for a standard set of more than 33,000 mouse proteins. To pinpoint molecules, computational cell biologist Rohan Teasdale of the University of Queensland in St. Lucia, Australia, and colleagues drew on their own experiments and data from the literature. Click on a cell map to find out which proteins congregate in the nucleus, mitochondria, and other organelles. The site also classifies proteins according to their relationship to cell and organelle membranes, such as whether they pass through a membrane once or snake through several times. >>
locate.imb.uq.edu.au

Send site suggestions to >> netwatch@aaas.org
Archive: www.sciencemag.org/netwatch

CREDITS (TOP TO BOTTOM): DIGITAL MORPHOLOGY GROUP/UNIVERSITY OF TEXAS, AUSTIN; UNIVERSITY OF QUEENSLAND; CENTER FOR RESEARCH ON TIBET/CASE WESTERN RESERVE UNIVERSITY

Institutional Site License Available

Q What can *Science* STKE give me?

A The definitive resource on cellular regulation

STKE – Signal Transduction Knowledge Environment offers:

- A weekly electronic journal
- Information management tools
- A lab manual to help you organize your research
- An interactive database of signaling pathways

STKE gives you essential tools to power your understanding of cell signaling. It is also a vibrant virtual community, where researchers from around the world come together to exchange information and ideas. For more information go to www.stke.org

To sign up today, visit promo.aaas.org/stkeas

Sitewide access is available for institutions.
To find out more e-mail stkelicense@aaas.org

Science stke AAAS

Interspecies Cooperation

>> **An Asian toad plays St. Christopher, helping a mouse avoid monsoon waters in Lucknow, northern India. Monsoon rains in the region have been exceptionally heavy this year.**

MORE $ FOR CALIFORNIA STEM CELLS

The money keeps pouring into the Golden State. Last week, the University of California, Irvine (UCI), announced that William Gross, a California bond trader, and his wife Sue are donating $10 million for stem cell research. Two million dollars is earmarked for staffing and operation of the university's Stem Cell Research Center. The rest will go toward construction of a proposed new $80 million building for the center.

Gross, founder of the Newport Beach–based PIMCO, is emerging as a big figure in California philanthropy. UCI had been wooing the Grosses for a while, but it was reportedly a *60 Minutes* show run last February featuring UCI researcher Hans Keirstead, who does research using embryonic stem (ES) cells for spinal cord repair, that won them over. Keirstead, who works at the privately funded Reeve-Irvine Research Center, announced last month that he plans to generate as many as five new human ES cell lines for research.

Irvine is the third California university to receive a fat stem cell gift this year. UC San Francisco got $16 million from sound pioneer Ray Dolby this spring (*Science*, 26 May, p. 1135), and the University of Southern California in February announced a $25 million gift from the Broad Foundation.

REWIRING THE BRAIN

In June 2003, 39-year-old Arkansas resident Terry Wallis suddenly woke up and started talking after 19 years in a minimally conscious state.

Wallis's astonishing recovery, after a car accident that severely damaged his brain, attracted the attention of Nicholas Schiff, a neurologist at Weill Medical College of Cornell University. Schiff examined Wallis about 8 months after he began speaking, using a technique called diffusion tensor imaging. The imager, which provides information about the brain's white matter—the "wiring" supplied by axons—revealed unusually thick cables of axons linking the left and right sides at the back of the brain, areas some believe to be involved in consciousness. Other brain scans showed the cortical regions that they connected to be more active than normal, Schiff and colleagues report in the July issue of the *Journal of Clinical Investigation*.

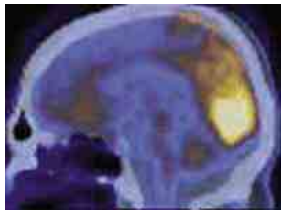

Reawakened brain.

A second examination 18 months later revealed new connections and unusually strong neural activity in Wallis's cerebellum, a region important for movement and coordination. These functions also improved substantially over that period, Schiff says. The findings suggest that while Wallis was unconscious, the brain regions that survived the accident forged new connections to compensate for those that were damaged, a process that continued after he regained consciousness.

Doctors don't know whether improvement will continue. But Steven Laureys, a neurologist at the Université de Liège in Belgium, says the case adds to other recent evidence that the adult brain may have more capacity to reorganize after injury than many researchers have assumed.

THE LOWDOWN ON LOW SOUNDS

No other musical instrument fascinates scientists quite like the violin. Now, physicist Alfred Hanssen of the University of Tromsø, Norway, has set out to determine how renowned soloist Mari Kimura is able to tickle tones far lower than a violin is designed to make.

When a violinist bows a string, it vibrates most energetically at a frequency determined by its mass, tension, and length. The musician can raise the frequency by holding the string to the fingerboard. The string also vibrates at multiples of this frequency. The mix of such "harmonics" gives the instrument its character. Kimura, by bowing a string in the right place at the right speed and pressure, has figured out how to produce and control tones with frequencies lower than the deepest pitch ordinarily attainable, which is G below middle C.

Other physicists have analyzed Kimura's technique, which she debuted in 1994. They found that, by feel, Kimura controls the frequency at which the bow hairs tug and release the string, accentuating the subharmonic frequencies and minimizing others. But previous theories cannot explain, for example, how she "slides" a note continuously down in pitch to an octave below low G, says Hanssen, who recently took detailed measurements of the sounds Kimura makes and the way her instrument vibrates. "There's a fundamental piece of physics missing, and we're on the track of it," he says. Kimura, who is also a composer, says she hopes a little more science can help her expand her art even further: "If scientists have a neat explanation for it, I may find something else I can do."

Kimura being tested at Tromsø.

CREDITS (TOP TO BOTTOM): PAWAN KUMAR/REUTERS; HENNING U. VOSS/WEILL CORNELL CITIGROUP BIOMEDICAL IMAGING CENTER; ALFRED HANSSEN/UNIVERSITY OF TROMSØ

Evolution in action 156

Gold bugs 159

CANCER RESEARCH

Fake Data, but Could the Idea Still Be Right?

European investigators last week confirmed that a pioneering oral cancer researcher in Norway had fabricated much of his work. The news left experts in his field with a pressing question: What should they believe now? Suppose his findings, which precisely identified people at high risk of the deadly disease, were accurate even though data were faked?

At least three groups—in the United Kingdom, the Netherlands, and Canada—are trying to determine whether oncologist Jon Sudbø of the University of Oslo's Norwegian Radium Hospital unwittingly hit on a way to identify those at high risk of oral cancer. A U.S. clinical trial, originally based on Sudbø's findings and since redesigned, could also offer some guidance.

Sudbø has acknowledged that he invented some data, and a five-person investigative panel led by Anders Ekbom of the Karolinska Institute in Stockholm last week issued a report saying the bulk of his work was invalid (*Science*, 7 July, p. 29). "A fairly gross fraud has been perpetrated here, but it's still worth following up," says Edward Odell, an oral pathologist at King's College London in the U.K. That's especially true, he says, because "the survival rate for oral carcinoma is very, very dependent on early diagnosis," making prevention especially critical.

Sudbø's work electrified the oral cancer community when it first appeared. In 2001 and 2004, he reported in *The New England Journal of Medicine* that individuals with mouth lesions that were aneuploid, containing an abnormal number of chromosomes, had an extraordinarily high risk of oral cancer, about 84%. He also claimed that this cohort was more likely to develop an aggressive form of the disease.

Sudbø's reports were highly plausible. Cancer specialists had previously found that many oral tumors are aneuploid, and they also knew that mouth lesions with less dramatic genetic abnormalities are more likely to turn cancerous. Aneuploidy "might be an invaluable marker" for identifying people at high risk of oral cancer, says Ruud Brakenhoff, a cancer geneticist at VU University Medical Center in Amsterdam, but "we do not know" this any more.

Brakenhoff and his colleagues quickly set about trying to replicate Sudbø's work. The Dutch group is studying tissue from mouth lesions collected from 150 to 200 people and assessing whether those with aneuploid lesions were more likely to develop cancer than the others.

Forecasting cancer. A panel headed by Anders Ekbom (*inset*) found that work on abnormalities predicting oral cancer (*above*) were faked, but the field wonders whether it can salvage the concept.

Odell's group, meanwhile, is examining tissue from about 150 people collected between 1990 and 1999 at his London hospital. "There is something in this," he says, although he believes that aneuploidy is a less effective predictor than Sudbø claimed. Still, says Odell, in his hands it's at least twice as good as one current predictive approach, which grades the severity of cellular abnormalities visible under a microscope, such as enlarged nuclei or the crowding of cells. Odell presented some of his findings last month at an oral pathology conference in Australia, and both he and Brakenhoff hope to submit their work for publication this fall.

"It's the start of stuff that needs to be done," says Richard Jordan, an oral pathologist at the University of California, San Francisco. Like others, he believes that the best way to prove or disprove the aneuploidy theory is with a trial that follows patients prospectively rather than relying on stored tissue. That's what Miriam Rosin of the British Columbia Cancer Agency in Vancouver, Canada, is pursuing, with 200 individuals with various types of lesions; Odell says he's also planning such a trial.

Meanwhile, a cancer prevention trial based on Sudbø's work has been overhauled in light of the misconduct. A multimillion-dollar trial funded in part by the U.S. National Cancer Institute (NCI) in Bethesda, Maryland, was poised to launch when the fraud came to light. The trial originally aimed to enroll individuals with aneuploid lesions and test the power of two drugs to prevent oral cancer.

Now, says Eva Szabo, chief of NCI's lung and upper aerodigestive cancer research group, the trial will enroll 150 people with another kind of mouth lesion called loss of heterozygosity. These lesions include deletion of parts of chromosomes. (Aneuploidy involves the loss of whole chromosomes.) Volunteers will receive either the cancer drug Tarceva or a placebo, and a subset with aneuploid lesions as well as loss of heterozygosity may provide clues about how aneuploidy's risks stack up, Szabo says. The trial will be led by Scott Lippman of the M. D. Anderson Cancer Center in Houston, Texas, a Sudbø collaborator who was cleared of any misconduct.

Oral cancer specialists originally wowed by Sudbø's research hope that the aneuploidy issue will be sorted out. "I think the question's going to be answered in the next 2 to 3 years," says Jay Boyle, a head and neck surgeon at Memorial Sloan-Kettering Cancer Center in New York City, who collaborated with Sudbø and visited him in Oslo. Like many others, Boyle recalls his excitement when he first heard of Sudbø's findings. They offered "the possibility … [of treating] the more worrisome lesions more aggressively," he says. Physicians like him still hope for some truth from the theory, although it may be less potent than the invented data suggested.

–JENNIFER COUZIN

CREDITS (LEFT TO RIGHT): SCIENCE PHOTO LIBRARY; CORNELIUS POPPE/SCANPIX/AP PHOTO

STEM CELLS

Team Claims Success With Cow-Mouse Nuclear Transfer

TORONTO, CANADA—The idea of creating an interspecies embryo makes some people squirm. But for scientists who hope to make genetically tailored embryonic stem (ES) cells, enlisting animal oocytes to reprogram human cells offers a possible alternative to using human oocytes, which are in short supply (see sidebar, below). And because such embryos would be unable to develop past the earliest stages, most researchers say there's nothing to be queasy about.

At a meeting* here last month, a South Korean team claimed a rare success with so-called interspecies somatic cell nuclear transfer (iSCNT). Chang-Kyu Lee of Seoul National University reported that he and his colleagues used bovine oocytes to reprogram mouse somatic cells and then derived a mouse stem cell line from the cloned embryo. Other researchers said the work is intriguing but remain skeptical until it is repeated.

Dozens of groups around the world have attempted iSCNT, and several live animals have been born after the DNA of an endangered species was transferred into an oocyte of a closely related domestic animal. But attempts to use oocytes of more distantly related species have largely failed. In 1998, the Worcester, Massachusetts–based biotech company Advanced Cell Technology (ACT) announced that it had used bovine oocytes to reprogram human somatic cells and develop a human ES cell line, but the company said it had discarded the cells without characterizing them (*Science*, 20 November 1998, p. 1390). And in 2003, Hui Zhen Sheng of Shanghai Second Medical University and her colleagues reported in the Chinese journal *Cell Research* that they had made ES cells by inserting human cells into rabbit oocytes. No other lab has successfully repeated either experiment.

As Lee described in Toronto, his team removed the DNA from cow eggs, injected a whole mouse somatic cell, and then used chemicals to kick-start embryonic development. The process was far from efficient, but Lee reported in a poster that his team managed to produce three blastocysts and a single ES cell line. The cells seemed to behave like normal mouse ES cells, forming various tissue types in the culture dish. When the team combined the cells with intact mouse embryos, they produced chimeric mice with two-colored fur. Lee says that since the poster was written, he and his colleagues have produced two more ES cell lines using the technique.

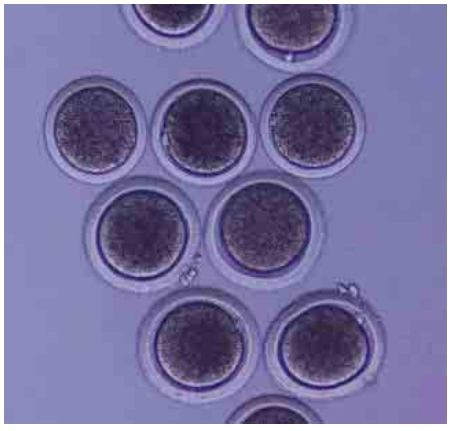

Alternative source. Bovine oocytes may be able to reprogram cells from other species.

Not everyone is convinced. Jose Cibelli of Michigan State University in East Lansing, formerly a member of the ACT team that attempted the cow-human nuclear transfer, says his lab at Michigan State spent 3 years ▶

CREDIT: CHANG-KYU LEE

* International Society for Stem Cell Research Annual Meeting, 29 June–1 July.

Ethical Oocytes: Available for a Price

TORONTO, CANADA—Obtaining human oocytes for embryonic stem (ES) cell experiments raises tricky ethical issues. Researchers want to be sure the donation is voluntary and that women are well-informed of the risks—two areas in which now-discredited stem cell researcher Woo Suk Hwang was faulted. At a recent meeting here, Ann Kiessling, director of the Bedford Stem Cell Research Foundation in Somerville, Massachusetts, described her group's successful efforts to recruit donors. Despite a rigorous screening process that eliminated more than 9 of 10 potential donors, the team had no shortage of oocytes. "We ran out of funds before we ran out of donors," she says. Nevertheless, her experience suggests that collecting hundreds of oocytes ethically and safely will be expensive and slow.

The group, which collected oocytes for its own experiments and also for the company Advanced Cell Technology in Worcester, Massachusetts, first placed an ad in *The Boston Globe* in September 2000 that read, "Research team seeks women aged 21 to 35 with at least one child to donate eggs for stem cell research; compensation for time, travel and child care expenses." The requirement that women already have one child does bar some potential donors, Kiessling says, but it greatly lowers certain risks. If a woman has had a successful pregnancy, she says, "you know she's fertile, you know how she manages the hormones, and you lower the chance that 10 years later she might have fertility problems" that might be traced back to the donation.

The *Globe* ad did not prompt a single response, Kiessling says, but ads in smaller regional papers were more successful. The team stopped running ads in 2003 because word of mouth had become the most effective source of donors. By the end of 2005, 391 women had inquired about the program; after a 12-step screening process, 28 started hormone injections, and 23 completed the process. Eight of those 23 donated twice; three donated three times. The donations yielded 274 oocytes, at an average cost of $3673 per egg. Factoring in the psychological and physical evaluations and the medical expenses, Kiessling says, the cost per woman of each completed donation cycle is $27,200.

Very little of that money went to the donors. Women were reimbursed between $560 and $4004, depending on how many steps they completed. Although fertility clinics routinely compensate women for egg donation, some ethicists are wary of any payments that might encourage women to donate for money. Kiessling says donor programs need to have rigorous safeguards to prevent possible exploitation of donors, "but not paying isn't the answer." More crucial, she says, is keeping the medical team separate from the research team and developing a rigorous screening program that ensures women are making well-informed decisions. Kathy Hudson of the Johns Hopkins University Genetics and Public Policy Center in Washington, D.C., agrees. Healthy volunteers are routinely paid for their participation in research projects, she says; "it seems just and fair that [oocyte donors] also be fairly compensated."

–GRETCHEN VOGEL

attempting iSCNT without success. "This could be a huge breakthrough, but it's going to be scrutinized heavily," he says.

One reason for the doubts is that many scientists expect that a chimera created through iSCNT would receive most of its mitochondria from the oocyte, which would be incompatible with the nuclear DNA of the cloned cell. Mitochondria, the cell's power factories, carry their own DNA and are inherited from the mother through the oocyte cytoplasm. But Lee reported that in his experiments the problem seemed to solve itself. The freshly derived ES cells contained mitochondria from both the cow oocyte and the mouse somatic cell. But as the cells grew in culture, the mouse mitochondria became more prevalent, and the bovine mitochondrial DNA seemed to disappear.

Lee says some species combinations may work better than others in iSCNT. His team had no luck trying to use mouse somatic cells and pig oocytes, he says, and bovine-human iSCNT is unlikely to work the same way as his bovine-mouse experiments. Until more studies are done, Cibelli says, Lee and other scientists with iSCNT claims "would have to do more than peer review" to convince their colleagues, perhaps allowing a separate lab to confirm the results.

–GRETCHEN VOGEL

EVOLUTION

Competition Drives Big Beaks Out of Business

When the new kid on the bus is bigger than you are, it might be time to give up your seat. That's what's happened to a small seed-eating bird in the Galápagos Islands. The medium ground finch used to have one island pretty much to itself—and free rein to eat whatever size seeds suited it most.

Then a competitor, the large ground finch, moved in. And when the going got tough—a drought decimated seed supplies—this intruder's presence led to a change in the diet of the medium ground finches, as almost only those eating small seeds survived, Peter and B. Rosemary Grant, a husband-and-wife team from Princeton University, report on page 224. In about a year, the resident finch population retooled: Their beaks shrank, becoming better equipped for this new diet.

This competitor-driven shift in beak size is an example of what evolutionary biologists call character displacement. Researchers have found apparent examples of displacement in natural settings and studied the process in laboratory experiments. But this is the first time they have seen it happen in real time in the wild, says Jonathan Losos, an animal ecologist at Harvard University: "This study will be an instant textbook classic."

Galápagos finches have fascinated biologists ever since Charles Darwin cataloged the great diversity of these birds' beaks. For the Grants, the finches have been their life's work. They have spent the past 33 years on one of the Galápagos' small volcanic islands, Daphne Major, recording the resident birds' births, deaths, eating habits, and so on, as well as weather and food-supply information.

At the beginning of the study, the medium ground finch (*Geospiza fortis*) shared the island only with the cactus finch, which uses its pointed beak to eat cactus fruit and pollen. Lacking competition from other finches, the blunt-beaked medium ground finch depended on smallish seeds, which were easier to eat. That is, until a severe drought in 1977 devastated the plants that produced small seeds. For the most part, only those birds with beaks big enough to break open large, hard-to-crack seeds survived; in just a few generations, there was a 4% increase in average beak size (*Science*, 26 April 2002, p. 707).

Beak push. For big seeds, the bill of the medium ground finch (*bottom*) was no match for that of the large ground finch (*top*).

In 1982, the large ground finch (*G. magnirostris*) settled on Daphne Major. At 30 grams, it was almost twice the size of the medium ground finch and easily cornered the market on a key food, *Tribulus cistoides* seeds.

At first, the newcomers didn't pose much of a problem because food was plentiful. But by 2003, their numbers had swelled to about 350, and a drought that year set the stage for stiff food competition. In 2004, there were about 150 large ground finches and about 235 medium ground finches, and the birds soon exhausted the supply of large seeds. The death toll was severe: About 152 medium ground finches died, as did 137 large ground finches. Among the medium ground finches, the ones that had the largest bills were the worst off; only about 13% of them survived.

Although the beaks of the island's large ground finch have not obviously changed since the drought, the medium ground finch seems to be returning to its smaller-beak days because of the selective pressure. Before the 2003 drought, medium ground finch males tended to have 11.2-millimeter-long bills, but by 2005, the bills averaged 10.6 millimeters, a 5% drop. The depth of the bill dropped from 9.4 millimeters to 8.6 millimeters on average, the Grants report.

The change occurred with surprising rapidity, says David Pfennig, an evolutionary biologist at the University of North Carolina (UNC), Chapel Hill: "I expected [character displacement] to take much longer." The Grants ruled out other possible causes of the change in beak size, such as the drought alone. After the 1977 drought, competition with another species was not a factor, and the beaks of the medium ground finches got bigger, not smaller. In this case, "you have the same drought, but selection is basically in the opposite direction," points out Joel Kingsolver, an evolutionary ecologist also at UNC Chapel Hill. "For a nonexperimental study, [the setup] doesn't get any better."

Evolutionary biologists consider the paper important because it demonstrates the interplay between population numbers and environmental factors: The shift in beak size occurred only when there were enough large ground finches and large seeds were scarce enough to cause a problem, says Pfennig. "This study," he adds, "will motivate researchers to go into the field and see if they can document other examples of character displacement in action."

–ELIZABETH PENNISI

CREDIT: B. R. GRANT *ET AL.*, *SCIENCE*

PLANETARY SCIENCE

Long-Term Mars Exploration Under Threat, Panel Warns

While astronomers fret about the fate of the Hubble Space Telescope and earth scientists fear that NASA's budget woes will sink their current projects, their colleagues who study Mars are busy operating or planning an ambitious flotilla of rovers, orbiters, and robotic science labs. But their relative good fortune may be short-lived, a National Research Council (NRC) panel warned last week.*

NASA currently spends $650 million a year on Mars exploration, and that figure was projected to double by 2010. But as a result of the demands of the space shuttle, President George W. Bush's human exploration initiative, and cost overruns among other science projects, Mars spending now is slated to remain flat through that period. The agency recently canceled a telecommunications orbiter, halted efforts to develop a Mars sample return, and proposed scaling back some smaller missions. "We're in pretty good shape in the near term," says Reta Beebe, an astronomer at New Mexico State University in Las Cruces who chaired the 15-member NRC panel. "But the future is pretty nebulous, and the entire Mars program is under threat."

Beebe's panel recommended that NASA resurrect the telecommunications orbiter and add a science component to study the martian upper atmosphere as well. The agency in recent months has quietly been considering a Mars Science and Telecommunications Orbiter (MSTO) to do just that. The spacecraft, which could be launched as early as 2013, would gather scientific data and then drop into an orbit where it would relay data from the martian surface to Earth. The NRC committee also suggested that NASA consider building a seismic network in 2016 to ensure that researchers don't neglect Mars's structure and evolution in their quest to find past or present life, and that it delay by 2 years the 2016 launch of the Astrobiology Field Laboratory to allow time to take into account data from earlier missions.

* Mars Architecture Assessment Committee (newton.nap.edu/catalog/11690.html#toc)

Calling Mars ... The NRC panel wants to resurrect the Mars Telecommunications Orbiter and give it additional capabilities.

CREDIT: JPL/NASA

The panel sidestepped the question of where funding for the orbiter would come from. But Beebe warned that sticking with a flat budget would mean that "we may not be able to sustain what we've developed" during the past decade. And she added that scientists are willing to be realistic. Although committee members are upset that the sample-return mission is no longer on the books, they also recognize that the fiscal constraints mean such a multibillion-dollar effort likely won't happen in the coming decade.

NASA's chief Mars exploration scientist, Michael Meyer, says the proposed cuts to future years forced the agency to push sample return and geophysical rovers into the unbudgeted future. But he's confident that building the MSTO is realistic and that international partnerships could make the other projects doable. But he warns that conducting both a 2016 mission and an astrobiology flight in 2018 might prove too costly.

Reaction from outside researchers was mixed. "We need to get our act together, but we are hamstrung by our budget," says Ray Arvidson, a planetary scientist at Washington University in St. Louis, Missouri. He praised the report as an important step in laying out a long-term plan. But Noel Hinners, a geochemist, former NASA manager, and now executive at Lockheed Martin Astronautics in Denver, Colorado, questions the need for a telecommunications orbiter. He adds that a sample return is still possible by 2016 or 2018 if NASA and Mars researchers made it a top priority.

–ANDREW LAWLER

Report Fuels Biomass Excitement

One-third of U.S. cars and trucks on the road in 2030 would be powered by biofuels under a Department of Energy (DOE) road map that spells out President George W. Bush's vision for breaking the country's addiction to oil, much of it foreign.

Released last week, the 200-page document sets interim and long-range goals for cellulosic ethanol research. According to the plan, researchers would aim within 5 years to allow refiners to make ethanol from cellulose derived from waste or plants such as switchgrass, poplars, or eucalyptus, assuming technological advances in the breakdown of cellulose and the fermentation of its sugars. That would be followed by entirely new energy crops with better ranges, and temperature and pest tolerances.

Justin Adams of British Petroleum, who participated in a 2005 workshop to develop the plan, calls the final result a "step forward." In the meantime, the president's request to spend $150 million next year on biomass research has been approved by the House and raised to $213 million by the Senate, which is still debating its version of DOE's 2007 budget.

–ELI KINTISCH

SOFIA Returns

NASA's Stratospheric Observatory for Infrared Astronomy (SOFIA) is officially off the chopping block. Space agency chief Michael Griffin told scientists at a Washington, D.C., meeting on 6 July that the project would go forward, despite cost overruns and delays in engineering an aircraft and its accompanying telescope. Those troubles led Griffin to not fund SOFIA in the agency's 2007 budget request released in February (*Science*, 23 June, p. 1729). But researchers in both the United States and Germany—a major partner on the project—objected strongly. Griffin also said that the Space Interferometry Mission, a complex effort to study extrasolar planets slated for the next decade, would be "refocused." NASA spokespeople said they were not sure what that means, but some scientists expect the comment to effectively mark the mission's death knell.

–ANDREW LAWLER

PALEONTOLOGY

Vigorous Youth for Tyrannosaurs

Childhood was the best time to be a tyrannosaur. So says the first study to chart the personal ups and downs of this famed group of predators. On page 213, a group led by Gregory Erickson of Florida State University in Tallahassee reports that juvenile tyrannosaurs enjoyed a survival rate unmatched by that of many modern vertebrates—humans excepted. Presumably, that was a perk of being the meanest kids on the block. But as soon as puberty hit, life got rough.

The findings come from survivorship curves, a type of demographic analysis that reveals what proportion of a birth cohort manages to escape dying each year. Researchers have plotted many such curves for modern animals but none for dinosaurs, because they lacked large samples and a way to determine how old the animals were at death.

The team looked at 22 individuals of a tyrannosaur called *Albertosaurus sarcophagus* from a Canadian site about 200 km northeast of Calgary. The skeletons probably washed up in riverbank deposits over weeks or months about 70 million years ago. To figure out the animals' ages at time of death, Erickson applied a relatively new technique (*Science*, 5 November 2004, p. 962), counting the annual growth lines preserved in the bones of their calves and feet. Because no hatchlings were found in the deposit, the team assumed that their mortality rate lay within the dismal range of 50% to 80% for modern vertebrates. A tender young tyrannosaur, they reasoned, would probably have been just as vulnerable as young birds or crocodiles to predation, starvation, or trampling.

Juveniles fared much better. Between the ages of 2 and 13, the average mortality rate dropped to 3.5%. Erickson thinks the young dinosaurs' size protected them: Even a 2-year-old was bigger than any other predator alive at the time. "I can't imagine too much tangling with a 2-meter-long tyrannosaur," Erickson says.

But hazards mounted once *Albertosaurus* entered its teens. The death rate for 14- to 23-year-olds climbed to an average of 22.9%. The team thinks fresh dangers may have arrived with sexual maturity. Females would have undergone the stress of laying eggs, and males might have competed for mates.

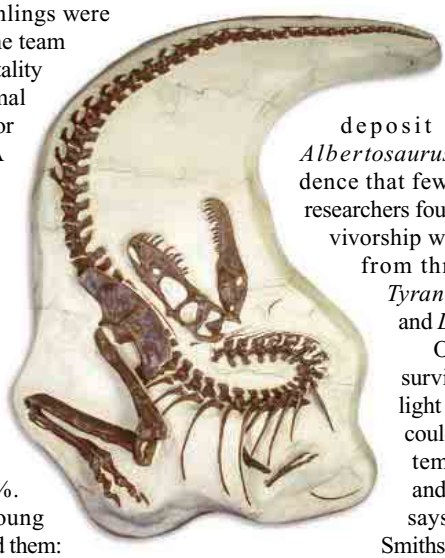

Unlucky exception. Juvenile tyrannosaurs, like this *Gorgosaurus*, are rare in the fossil record because they tended to escape death.

Old age was likely just as unpleasant. The deposit contained only one *Albertosaurus* as old as 28 years, evidence that few survived that long. The researchers found the same pattern of survivorship when they examined bones from three other tyrannosaurs: *Tyrannosaurus*, *Gorgosaurus*, and *Daspletosaurus*.

Other paleontologists say survivorship curves could shed light on dinosaur ecology. "You could build up a whole ecosystem of dinosaur populations and see how they interacted," says Matthew Carrano of the Smithsonian Institution's National Museum of Natural History in Washington, D.C. Adds Thomas Holtz of the University of Maryland, College Park, "There's a lot of potential here."

–ERIK STOKSTAD

PLANETARY SCIENCE

Peeling Back One More Layer of Asteroid Mystery

When NASA's NEAR Shoemaker mission reached the asteroid Eros 6 years ago, planetary scientists hoped it would settle a question that had vexed them for decades: Do ordinary chondrites, the most common meteorites that fall on Earth, come from big, roughly chondritelike bodies that make up most of the inner asteroid belt? Sadly, the orbiting craft's sensors left the question up in the air (*Science*, 14 December 2001, p. 2276). Now researchers say a closer look at the data shows that Eros could indeed be a source of chondrites—but skeptics say the case is still open.

"This is about as sure as things get when the rocks are not sitting on your lab table," says asteroid researcher Clark Chapman of the Southwest Research Institute in Boulder, Colorado. Other NEAR Shoemaker data, however, suggest there's more to Eros than ordinary chondrite.

The problem started with sulfur. Data from NEAR Shoemaker's spectrometers confirmed that Eros has the right mix of minerals and elements to be one big, ordinary chondrite, with one exception: Sulfur was less than half as abundant as it should be.

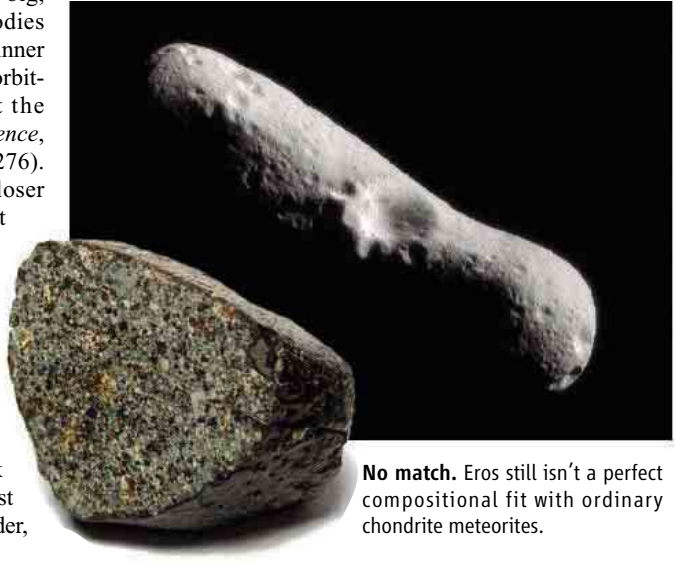

No match. Eros still isn't a perfect compositional fit with ordinary chondrite meteorites.

There were two possible scenarios. First, Eros is indeed an ordinary chondrite, but in its outermost few micrometers—the part sampled by x-ray spectrometry—more than half the sulfur has been vaporized by the solar wind or micrometeorites, so-called space weathering. The more dramatic possibility was that early in its history, Eros melted, and the molten rock carried much of its sulfur into its interior. In that case, rock from asteroids like Eros would now be very different from the asteroid's original composition—and thus could not have given rise to ordinary chondrites.

Cosmochemists Nicole Foley and Larry R. Nittler of the Carnegie Institution of Washington's Department of Terrestrial Magnetism, meteoriticist and team member Timothy McCoy of the National Museum of Natural History in Washington, D.C., and others decided to test the two scenarios. They looked at trace elements—minor components of ▶

CREDITS (TOP TO BOTTOM): ED GERKEN/BHIGR; EROS: JPL/NASA

the asteroid's recipe. The elements chromium, manganese, and nickel are all less volatile than sulfur and thus should be impervious to space weathering, Nittler says. But, like sulfur, they would be "strongly affected by any differentiation."

The group painstakingly analyzed readings from NEAR Shoemaker's x-ray spectrometer and compared them with compositions of ordinary chondrite meteorites. The results showed that the three trace elements are as abundant on Eros as in chondrites, the group reports in *Icarus* this month. "They've really made the case that space weathering was responsible for the depletion," says asteroid specialist Michael Gaffey of the University of North Dakota, Grand Forks.

Made it, but not quite closed it, Gaffey adds. It's still possible that Eros melted *slightly*—enough to wipe out the original mineral structure without changing Eros's elemental composition. In that case, Eros and its asteroid cousins would still be ruled out as sources of ordinary chondrites. And team member Lucy McFadden of the University of Maryland, College Park, and colleagues report discrepancies in data from NEAR Shoemaker's mineral-identifying, near-infrared spectrometer. "There's more there than just ordinary chondrite components," says McFadden, "but I don't know what it is."

"The only resolution is going to be getting a sample," McFadden says. "Our hope is that something fell into Hayabusa," the Japanese spacecraft that may or may not have collected a sample from the asteroid Itokawa (*Science*, 31 March, p. 1859) and may or may not make it back to Earth in 2010. **–RICHARD A. KERR**

MICROBIOLOGY

Bacteria Help Grow Gold Nuggets From Dirt

It's not just in fairy tales that buried treasure appears as if by magic. Australian researchers report on page 233 that they've found soil bacteria that pull dissolved gold from their surroundings and deposit it on grains of gold where they live. The study provides "sound and convincing evidence" that microorganisms can play a role in growing gold nuggets, says geomicrobiologist James Fredrickson of Pacific Northwest National Laboratory in Richland, Washington. Such bacteria may even have had a hand in producing some of the great gold ore deposits—but don't start strip-mining the backyard just yet.

Researchers had long suspected that bacteria help create the flecks and nuggets of "secondary" gold that prospectors pan from streams and miners dig from certain long-buried gold deposits. At microscopic scales, secondary gold can strikingly resemble mounds of bacteria, as if microbes had encased themselves in the metal. And in the lab, some bacteria defend themselves against toxic dissolved gold by turning it into the metallic form. But connecting the dots between field and laboratory evidence was "dicey at best," Fredrickson says.

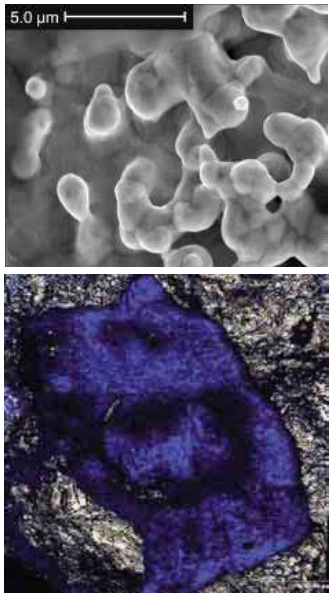

Bugs at work. Nuggets that up close look like gold-encrusted bacteria (*top*) are covered by biofilm (blue) of gold-depositing bacteria.

CREDITS: F. REITH *ET AL.*, *SCIENCE*

Geomicrobiologist Frank Reith of the Commonwealth Scientific and Industrial Research Organisation in Adelaide, Australia, and his colleagues set out to forge the link. At two Australian sites 3400 kilometers apart, they collected grains of secondary gold from soils that lie over rock whose gold leaches up into the soil. On the nearly pure gold grains, they found striking examples of "bacterioform" gold overlain by biofilms of bacteria and their exuded slime. Genetic analysis showed that the bacteria belonged to as many as 30 species, most of which could not be found in the surrounding soil. The most pervasive species was genetically nearly identical to the bacterium *Ralstonia metallidurans*, a microbe well-known for its ability to precipitate some heavy metals from solution in the lab. Reith and colleagues showed that *R. metallidurans* can also precipitate gold.

"I'm not claiming all the gold grains are formed by microorganisms," says Reith, but "there's certainly something going on. These organisms are active and creating gold." Fredrickson agrees that Reith and his colleagues have "made a strong case for microbiogenic gold mineralization" but cautions that the work can't prove that microbes grow gold nuggets. As a next step toward that goal, Fredrickson says, researchers must pin down exactly how they do it. **–RICHARD A. KERR**

To Toronto With Love

The Bush Administration has relaxed controversial attendance limits it had set for the world's largest AIDS meeting next month. In February, the State Department declared that the Department of Health and Human Services (HHS) could send no more than 50 staffers to the International AIDS Conference in Toronto, half from the National Institutes of Health (NIH) (*Science*, 24 February, p. 1086). The policy echoed a similar bar HHS set for the 2004 meeting, which shut out dozens of researchers and drew charges of political interference from lawmakers. After "negotiating" with HHS, says NIH spokesperson John Burklow, NIH will be allowed to send 43 staffers—a compromise between the original 25 and the 77 that NIH had planned to send.

–JOCELYN KAISER

Bullish on Brazilian Biotech

SÃO PAULO—A government advisory panel has called on the Brazilian government and industry to spend $3.2 billion on biotech over the next decade. Identifying Brazil's small private research base as a problem, the plan calls for investments that would lead to a 5-year doubling of the number of start-up companies as well as the creation of 20 Ph.D. programs.

President Luiz Inácio Lula da Silva, a strong agriculture advocate, is expected to send the plan to Congress, which would authorize the new spending. But given the environment ministry's record in blocking genetically modified crops from the market, biologist Marcelo Menossi of the University of Campinas in São Paulo says the regulatory framework also needs to change.

–MARCELO LEITE

Navy to Limit Sonar

The U.S. Navy has agreed to new limits on its use of sonar in military exercises. Responding to a suit filed by environmental groups, a federal judge on 3 July barred the Navy from using midfrequency active sonar during this week's multinational Rim of the Pacific exercises off Hawaii. Four days later, as part of an agreement lifting the restraining order, the Navy agreed to expand monitoring and avoid midrange sonar within 40 km of the new Northwestern Hawaiian Islands marine preserve. The judge noted "convincing scientific evidence … that the Navy's use of [midfrequency active] sonar can kill, injure, and disturb many marine species," but the agreement took no position on the issue of sonar's impact on whales. **–ELI KINTISCH**

Tomorrow's treatments today—that's the promise of a growing number of companies offering cell therapies untested in rigorous clinical trials. Some experts say the claims must be challenged

Selling the Stem Cell Dream

IF YOU SUFFER FROM AN INCURABLE neurological disease such as multiple sclerosis (MS), Parkinson's, amyotrophic lateral sclerosis (ALS), or Huntington's disease, a clinic in the Netherlands says it may be able to help you. In a procedure that takes just a few hours and costs $23,000, the Preventive Medicine Center (PMC) in Rotterdam will inject stem cells obtained from umbilical cord blood into your bloodstream and under your skin.

The clinic has treated more than 200 patients so far; the results are "often spectacular," according to its Web site. Although PMC sees mostly neurological patients, it offers stem cell treatments for a wide variety of other diseases as well, including arthritis, lupus, Crohn's disease, heart disease, hernia, insomnia, sexual dysfunction, depression, and loss of memory, hair, or appetite.

PMC is one of a growing and diverse group of companies and institutes around the globe offering patients stem cell therapies or related treatments that are viewed by mainstream researchers as unproven. Some clinics use umbilical cord blood, whereas others inject fetal cells or cells derived from patients' own bone marrow. Some carry out operations themselves, whereas others act as middlemen, providing cells and linking patients with doctors willing to inject them. Almost all have Web sites to advertise the promise of the new therapies, often with hopeful case reports. The sites help recruit patients with what regular medicine cannot provide: a hope of recovery.

Although these clinics have already treated thousands of patients, a dozen stem cell scientists and physicians familiar with one or more of the treatments told *Science* they oppose them, often vehemently. Not only is there little or no evidence for the procedures' efficacy, the experts say; in many cases, there's also no published animal work to suggest they might work in humans. Most clinics appear to have no interest in rigorously collecting data about benefits and risks, critics say, and some may harm patients' health. Some companies are "preying on desperate patients," says stem cell scientist Irving Weissman of Stanford University in Palo Alto, California. "It's a horrible disservice."

Most of the clinics have not revealed full details of their treatment protocols. A handful of researchers have attempted to get a foot in the door, however, hoping to glean information about risks and benefits of cell therapy by systematically studying patients before and after they embark on treatment. Patient organizations and research foundations are trying to find out more, too, although they say it can be impossible to get even basic facts about the treatments.

The result, Weissman fears, may be that stem cell research—already under criticism for its use of embryos and suffering from the Korean cloning scandal—could see its reputation tarnished further. "I'm beginning to get pretty angry about this," says stem cell researcher Christine Mummery of the Hubrecht Laboratory in Utrecht, the Netherlands. "I think as a scientific community we have to speak up," adds Stephen Minger, director of King's College's Stem Cell Laboratory in London.

Indeed, some scientists have asked regulatory authorities to intervene. After Dutch neurologists complained, for instance, the Dutch Health Inspectorate began looking into PMC and a second company in the Netherlands, Cells4Health.

A quest for a cure

John Franken of Landgraaf, the Netherlands, was a gymnastics champion before he broke his neck during a trampoline accident 18 years ago. Since then, Franken, 44, who has an administrative job at the Open University in Heerlen, has been unable to move without a wheelchair and unable to sit up for more than 6 hours a day. He

A wide net. Many providers of cell therapy recruit patients through their Web sites.

follows spinal cord research closely on the Internet, and he started a foundation to promote the search for a cure in 1995. He got very interested in Huang Hongyun, a doctor in Beijing who injects patients suffering from spinal cord injuries or neurological diseases with cells from aborted fetuses. But when Franken contacted Huang for an appointment, he learned that he'd be on the waiting list for years.

Then in May 2005, Franken read a message posted on a patient forum by Cornelis Kleinbloesem, director of Cells4Health, who said his company had helped a paraplegic patient get a treatment with her own bone marrow cells in a Turkish hospital. Four weeks later, she was able to walk again, as a Turkish magazine called *Tempo* had documented, Kleinbloesem wrote. A second patient had seen functional improvement as well; "these results are very promising," Kleinbloesem's message concluded.

After a series of medical tests, Franken was approved to undergo the same therapy. Friends and colleagues helped raise the $23,000 for medical fees and travel. In January, Franken flew to Baku, Azerbaijan; at a private clinic, neurosurgeon Elchin Jabrayilbayov made a 12-centimeter cut in his neck and upper back—the graphic pictures are on Franken's Web site—to inject the stem cells directly into the lesion.

When he returned home, Franken started describing his experiences on his Web site. "I know my body is working on something," he wrote after 3 weeks, "but I'm trying to be realistic." He was told it might take at least 6 weeks before the cells had any effect—and so he waited.

Franken's story is not unusual. Many patients hear about anecdotal evidence through the Internet, says John McCarty, a biologist hired last year by the ALS Treatment Development Foundation (ALSTDF) in Cambridge, Massachusetts, to investigate stem cell treatments and other new therapeutic options for ALS. Many spend upward of $20,000; some borrow to the limit or sell their homes, McCarty says.

What they get differs from clinic to clinic (see table, p. 162). Whereas PMC uses cells derived from cord blood, Cells4Health arranges for patients' own bone marrow cells to be transplanted directly at the site of the lesion to treat spinal cord injuries, vascular diseases, and damage from heart attacks and strokes. Huang, who works at the Beijing Xishan Institute for Neuroregeneration and Functional Recovery in Shijingshan District, says he uses so-called olfactory ensheathing glial (OEG) cells to treat neurological patients. In Kiev, Ukraine, a clinic called EmCell also uses various types of cells derived from fetuses to treat more than 50 different diseases, including many aging-related problems and HIV.

CREDIT: CHRIS KEULEN

Verifying the claims

Amid all the hype about stem cells, it's easy to forget that very few cell-based therapies have proven their mettle in rigorous clinical trials. For some leukemias, doctors can obliterate a patient's own bone marrow and transplant cells from a donor—a well-established stem cell therapy. In the past few years, several studies have also shown that bone marrow cells can help repair the heart after a myocardial infarction (*Science*, 9 April 2004, p. 192), and others have suggested benefit for patients with a damaged cornea. "That's it, in terms of stem cell therapy," says Minger.

For the moment, most stem cell scientists say they are working on basic questions: how to make stem cells morph into exactly the cell type needed to treat a condition and how to ensure that they survive after being injected, are not rejected by the host's immune system, and don't start multiplying unchecked.

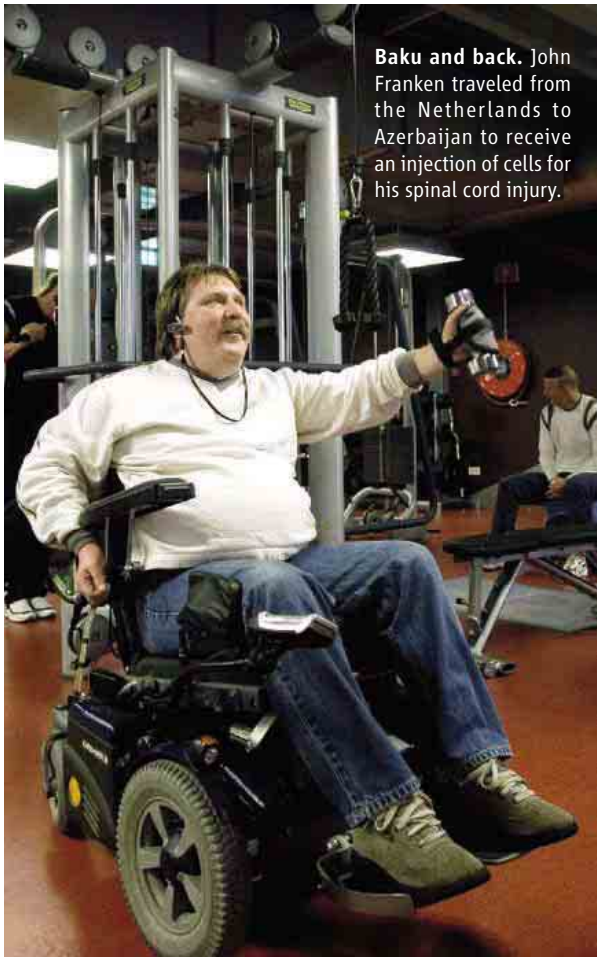

Baku and back. John Franken traveled from the Netherlands to Azerbaijan to receive an injection of cells for his spinal cord injury.

The cell clinics are forging ahead with treatments anyway. Take EmCell, which says it has experience in multiple diseases from treating more than 2000 patients in 13 years. ALSTDF decided to take a close look in 2004, after a story in a Wyoming newspaper reported that an ALS patient could walk again thanks to treatment by EmCell. According to a review on ALSTDF's Web site, the foundation's investigators talked to the doctor performing transplants and sent the company a detailed questionnaire. "EmCell didn't answer many of the questions, and in some areas refused to elaborate on important details such as their method for screening against the AIDS or hepatitis viruses," the ALSTDF report says.

But some of EmCell's procedures "clearly raise red flags," the report goes on. For instance, the company injects cells into patients' abdomens; most doctors think it's "implausible" that they would travel to the brain and work against ALS, the ALSTDF investigators say. The inventor of EmCell's therapy, according to the company's Web site, is its president, Alexandr Smikodub, who also heads the Cell Therapy Clinic at Ukraine's National Medical University. He has published seven PubMed-listed papers, six in Russian and one in Slovak, the last in 2001. In response to questions from *Science*, Smikodub sent a fax detailing his professional history and EmCell's procedures and giving examples of successfully treated patients. Although he has made presentations at many scientific meetings, Smikodub wrote, the international scientific community has largely ignored him. He did not respond to ALSTDF's allegations.

PMC Director Robert Trossel discussed his company's therapy but said details will be in a paper he plans to submit later this summer to *Nature*, *Science*, or *The Lancet*. "We're dying to let you know," Trossel says. (If accepted, the paper would be his first in a PubMed-listed journal.) PMC specializes in alternative treatments such as herbal medicine and ozone therapy. But recently, Trossel says, his team has learned how to make stem cells home in on the place where they are needed by coinjecting bits of messenger RNA and using each tissue's "specific electromagnetic frequency." (To avoid having the injected cells seek the wrong target, he also recommends that patients replace mercury-containing fillings first.)

The unconventional cell therapy that's received the most scientific scrutiny so far has been Huang's. With his staff of about 70, Huang has treated more than 1000 patients. His therapy is based on a line of research pioneered by neurobiologist Geoffrey Raisman at University College London, who discovered 20 years ago that OEG cells, which reside in the nasal

Selected Companies and Clinics Offering Stem Cell Therapies

Company	Location	Conditions	Patients treated	Cost ($)	Remarks
PATIENTS' OWN CELLS					
Cells4Health	Leuvenheim, the Netherlands	Myocardial infarction, vascular disease, spinal cord injury, stroke	NA	+25,000	Treatment takes place at clinics in Turkey and Azerbaijan
NeuraVita	Moscow, Russia	Neurological diseases and injuries	NA	~20,000	
FETAL CELLS					
EmCell	Kiev, Ukraine	More than 50, including neurological disorders, aging, impotence, diabetes, cancer, HIV	Almost 2000 in 13 years	+15,000	
Medra	Malibu, U.S.A.	More than 20, including neurological disorders, depression, autism, sickle cell anemia	More than 1000	NA	Procedures performed in Dominican Republic
Beijing Xishan Institute for Neuroregeneration and Functional Recovery	Beijing, China	Spinal cord injury, ALS, and other neurological conditions	More than 1000 since 2001	20,000	Thousands more on waiting list
Institute for Regenerative Medicine	St. John, Barbados	More than 40	More than 50 since 2004	25,000	Treatment based on research in the former Soviet Union
UMBILICAL CORD BLOOD CELLS					
Biomark	Atlanta, U.S.A.	ALS, Parkinson's, muscular dystrophy, and others	At least 23 in 2003	10,000 to 32,000	No longer operative; founders wanted by FBI
Advanced Cell Therapeutics	Zurich, Switzerland	More than 80	More than 600 in 4 years	25,000	Treatments performed at 12 collaborating clinics worldwide
Preventive Medicine Center	Rotterdam, the Netherlands	More than 50, including neurological, digestive, and psychological disorders and aging	More than 200 in 2 years	23,000	Also treats patients referred by Advanced Cell Therapeutics

SOURCE: COMPANY AND CLINIC WEB SITES, INFORMATION PACKAGES, INTERVIEWS, ALSTDF, BIOMARK CRIMINAL INDICTMENT. NA=INFORMATION NOT AVAILABLE.

mucosa, guide olfactory nerve fibers into the brain during development. After culturing, Raisman and others have found, these cells can help repair rats' damaged spinal cords. (Patients often refer to them as "stem cells" on the Internet, but Huang says they're not; Raisman says "you could call them adult stem cells.")

Raisman and colleagues are planning a small clinical trial in which they will treat patients who have a specific nerve injury that paralyzes the arm with their own OEG cells. But he points out that Huang's treatment is different: It uses fetal cells, which have not been proven effective in published animal studies and which could cause rejection problems because they are not matched to the patients' tissue type. Raisman sees little scientific basis for Huang's treatment, which "saddens" him.

Still, some scientists are intrigued by Huang's claims of success. In 2004, with Huang's consent, a group from the Miami Project to Cure Paralysis at the University of Miami in Florida sent two scientists, James Guest and Tie Qian, to Chaoyang Hospital in Beijing, where Huang then worked. The U.S. duo followed 12 patients from just before treatment until a few days after and took home a sample of therapeutic cells. In a report on the Miami Project Web site, the scientists say that they observed some "modest improvements" in the patients but also noted side effects, including meningitis. Earlier this year, Guest and Qian published an extensive report in *Spinal Cord* about one patient, an 18-year-old Japanese boy with spinal cord injury. They reported that he experienced "rapid partial recovery" after the procedure—even though a lab analysis cast doubt on the claim that the injected cells were OEG cells. The researchers suggested they might be another cell type and added that the injection may have contained other "neurotrophic" compounds.

Others became interested. Bruce Dobkin, a spinal cord–injury specialist at the University of California, Los Angeles, recalls how he and others quizzed Huang at a dinner party during a 2004 meeting in Vancouver, Canada. Several scientists offered to do a more extensive follow-up of his patients, Dobkin says. Huang appeared "delighted," and Dobkin, Guest, and Armin Curt of Balgrist University Hospital in Zürich, Switzerland, examined seven patients before they traveled to Huang's clinic and again up to 14 months after therapy.

Their paper in *Neurorehabilitation and Neural Repair* 2 months ago delivered a harsh verdict. Five patients came home with side effects, the U.S. group reported, including three with meningitis, and none showed improvement. What's more, the report says, Huang's team doesn't appear to follow up on patients, nor does it systematically collect data about the treatment's efficacy and risks. "It shocked even us," says Dobkin.

In an e-mail to *Science*, Huang called Dobkin's paper "rubbish" and a "vicious attack" that he would not discuss. The Miami team did not find OEG cells in his sample, he says, because they used the wrong staining techniques. And Huang accuses Guest of "misconduct" for publishing the paper in *Spinal Cord* without his permission and without consent from the Japanese patient. Huang has filed complaints with the University of Miami's Institutional Review Board and the Office of Research Integrity (ORI) at the U.S. Department of Health and Human Services. ORI says it has no jurisdiction, but a university panel is investigating the allegations.

Meanwhile, neuroscientist Wise Young of Rutgers University in Piscataway, New Jersey, where Huang worked from 1999 to 2000, has defended Huang. On CareCure, an Internet forum that Young administers, he wrote that Dobkin "evaluated seven patients out of several hundreds operated on by Dr. Huang … to make some far-reaching negative conclusions about the work."

Ideally, any unproven cell treatment that's tried on humans should be tested as part of a randomized, controlled clinical trial, most stem cell researchers say; patients should participate free of charge, be fully aware of the risks, and be carefully monitored. Few clinics or companies in the new cell-therapy market appear to have run trials on these lines.

But one of them has tried—only to be rebuffed. Cells4Health set up a clinical trial last year in collaboration with Massimo Mariani, a heart surgeon at Medisch Spectrum Twente, a regional hospital in the Netherlands. According to the protocol, approved by a hospital ethical panel, 10 myocardial infarction patients were to be injected with their own bone marrow cells. The trial was halted in March, however, after a second review by the Dutch Central Committee on Research Involving Human Subjects (CCMO), which criticized the poor trial design, the ill-defined role of Cells4Health, the risks to patients, and the poor information they received. Mariani, who strongly disagrees with the ver-

dict, says eight patients had already been treated before CCMO panned the study; he intends to publish the results.

In a regional hospital in Belgium, meanwhile, Cells4Health tried to set up a trial in stroke and spinal cord injury patients. Again, the trial design was poor, and there was "no scientific basis whatsoever," says Catherine Verfaillie, a stem cell researcher of Belgian origin at the University of Minnesota, Twin Cities, who was asked to review the study by the hospital. The trial was canceled. Cells4Health Director Kleinbloesem, citing recent "bad experiences" with the press, declined to be interviewed.

Regulatory patchwork

It's no coincidence, critics say, that most stem cell treatments take place in less-developed countries, where regulatory systems are weaker. But even in Western countries, cell-based treatments often fall into a regulatory gap.

Recently, U.S. Food and Drug Administration (FDA) agents investigated Biomark International, a company in Atlanta, Georgia, that provided stem cell therapies for ALS and other diseases. A 51-count indictment returned by a grand jury on 28 March charged that among other things, Biomark's founders, Laura Brown and Stephen van Rooyen, lured patients with "false, misleading, and inaccurate statements on the Biomark Web site and in other advertisements." A successful prosecution could put the duo in jail for many years. The pair is now wanted by federal authorities.

According to media reports, Van Rooyen returned to his native South Africa, and Brown is now involved in Advanced Cell Therapeutics (ACT), a company with a mailing address in Switzerland and a telephone number in London that the British MS Society says has treated well over 300 MS patients from the United Kingdom. (Its name resembles that of Advanced Cell Technology in Worcester, Massachusetts; the company was alerted to the existence of a second ACT only weeks ago, says Vice President of Research and Scientific Development Robert Lanza.)

According to a Web site maintained by Advanced Cell Therapeutics, its clinical procedures take place in 12 locations around the world, from Mexico and Argentina to Thailand and Pakistan. One of the clinics on the list is PMC in Rotterdam; ACT also provides PMC with its stem cells, says Trossel. Another one of ACT's collaborating clinics, in Cork, Ireland, is now under investigation by the Irish Medicines Board. (ACT offered to respond to questions sent by e-mail but didn't respond to e-mails or follow-up calls from *Science*.)

In response to media stories about stem cell companies, both the British and Belgian governments recently announced new rules to limit their activities. In the Netherlands, neurologist Rogier Hintzen of Erasmus Medical Center in Rotterdam prodded authorities last year to look at therapies offered by Cells4Health and PMC. A Dutch Health Inspectorate spokesperson says an investigation will be finished this summer. Pending the outcome, however, the agency issued an unusual letter to patients warning that there "is no scientific proof" for the treatments and that "skepticism and caution are in order." Elsewhere in Europe, stem cell treatments are governed by a patchwork of laws—or none at all. That could change; in order to facilitate Europe-wide market access for so-called advanced therapies, the European Commission recently proposed uniform new regulations, which include a new scientific panel at the European Medicines Agency in London to assess therapies. But its adoption could take years, and it's not clear it will cover work by clinics such as PMC.

And even if regulations are tightened up in Europe, it may be impossible to ban companies from flying patients to other countries for treatment, as Cells4Health does. The same is true in the United States: Medra, a company in Malibu, California, that says it has treated more than 1000 patients using fetus-derived stem cells, performs its procedures in the Dominican Republic.

Still waiting

Many stem cell companies quote recently published scientific studies on their Web sites. But at least one scientist has objected to being linked to what she considers a dubious company. Verfaillie says she was "horrified" when Biomark International cited her research on multipotent adult progenitor cells on its Web site. Her university alerted FDA multiple times, she says. Today, ACT uses the references to Verfaillie's work in its patient package.

Some say that scientists themselves may be partly to blame for the growing popularity of unproven therapies. The tremendous hype surrounding stem cells "has created very unrealistic expectations in patients," says neurologist Neil Scolding of the University of Bristol, U.K.—adding that researchers, politicians, and the media all bear some responsibility. "It's like the dot-com bubble," says Raisman. But others disagree. "The scientific community has been trying hard to educate the public," says Lanza; the field shouldn't be judged by "one or two bad apples," he adds.


NEWS REVIEW

Stem cell therapy is hailed as the holy grail of medicine. Scientists the world over have yet to unlock its secrets – but, still, demand is high. **Alasdair Palmer** talks to one woman who claims that it works for her

'I don't know the science behind my miracle cure – and I don't care'

Spreading hope. Personal stories have fueled interest in companies such as Advanced Cell Therapeutics, which is believed to have treated more than 300 British MS patients.

Still, scientists are finding that they have to throw cold water on the high hopes. At the request of the Association of British Neurologists, Scolding is currently drawing up guidelines for doctors confronted with MS patients inquiring about cell treatments. The sad message, he says: They just have to wait. There is no treatment yet.

John Franken is still waiting, too. Almost 6 months after his operation in Azerbaijan, he has noted some changes: One toe has become hypersensitive, for instance, and he can feel temperature changes in his left leg and knee. He hasn't regained control of his paralyzed muscles, however.

After his telephone interview, he asked *Science* in an e-mail not to write a negative story about Cells4Health. Scientists should give Kleinbloesem, "a courageous pioneer," a fair chance, says Franken, who says he may return to Baku: "I simply refuse to accept that I have to live like this the rest of my life."

–MARTIN ENSERINK

CREDIT: COURTESY OF *THE SUNDAY TELEGRAPH*, LONDON (29 JANUARY 2006)

Pretty as You Please, Curling Films Turn Themselves Into Nanodevices

Nanometer-thick films that roll themselves into tubes and fold up into elegant shapes promise a highly controllable way to make tiny gadgets

Sometimes the results of an experiment are so beautiful that researchers assume they must be useful, too. Just ask Detlev Grützmacher. Six years ago at a conference in St. Petersburg, Russia, Grützmacher, a physicist at the Paul Scherrer Institute in Villigen, Switzerland, spied images of the nanometer-sized tubes and helices a Russian colleague had fashioned from films of semiconductor, the stuff of microchips. The gracefully curling objects resembled modern sculpture.

"Immediately, I started fantasizing about what kind of things one could do with these," Grützmacher says. "Can I make a capacitor? Can I make an inductor? A sensor?" Now, he and a small but growing number of other researchers hope to turn the curlicues into a new form of nanotechnology.

For more than a decade, physicists and engineers have strived to make nanometer-sized gizmos. Some etch ever-smaller devices out of semiconductors, a "top-down" approach that seeks to raise three-dimensional (3D) structures from a succession of layers. Many are exploring a "bottom-up" approach that aims to assemble devices out of individual molecules, such as super-strong carbon nanotubes. To make a practical technology, however, researchers must coax the molecules to piece themselves together, and such self-assembly remains a distant goal.

But a handful of researchers think they can enjoy the best of both worlds. They are experimenting with films that roll themselves into delicate tubes or fold like minuscule cardboard boxes. The budding technology—known as strain architecture, rolled-up nanotech, or nano-origami—offers lithography's ability to put things exactly where they're needed. At the same time, the films curl themselves into novel 3D structures, adding an element of self-assembly.

"It's a whole new direction," says Max Lagally, a materials physicist at the University of Wisconsin, Madison. "Here you really have a way to make the same thing over and over with interesting properties that you can control."

Pablo Vaccaro, a physicist with the Advanced Telecommunications Research Institute International (ATR) in Kyoto, Japan, says the relatively simple and flexible technology will surely find applications. "I feel that we are just at the beginning of a big wave that will revitalize the field of semiconductors," he says.

That wave is still more of a ripple than a whitecap. Rolled-up nanotech probably won't wind its way into production lines for years.

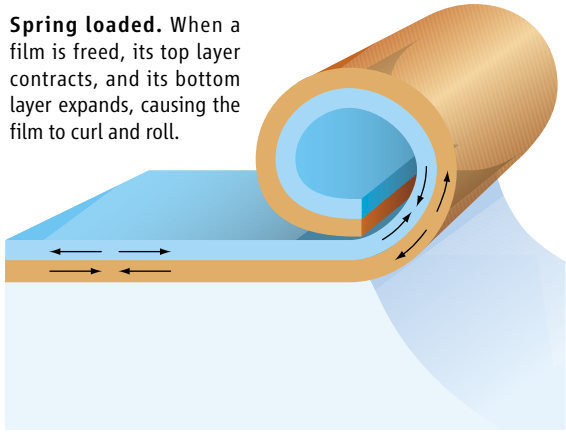

Spring loaded. When a film is freed, its top layer contracts, and its bottom layer expands, causing the film to curl and roll.

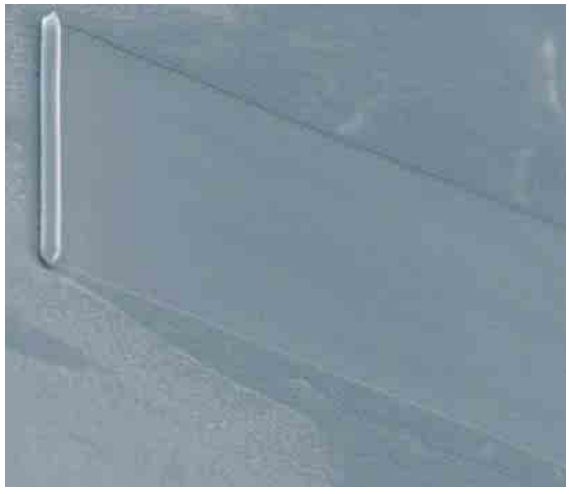

But proponents say the self-rolling tubes and helices may have more potential than competitors such as carbon nanotubes. Force sensors, tiny inkjet printers, and other experimental devices based on the wound-up technology may be around the corner.

Rolling out of Siberia

The technology was born by accident, in the laboratory of Victor Prinz, a physicist at the Russian Academy of Sciences Institute for Semiconductor Physics in Novosibirsk. In 1995, Prinz and colleagues were studying how electrons hop across a crack in a suspended film of semiconductor. They knew that a film consisting of two layers of different materials should bow, potentially allowing researchers to control the width of the crack. To their surprise, the "bilayer" curled into a tube.

That happens because the layers contain atoms of different sizes. For example, to form a film, researchers may lay down a layer of silicon mixed with germanium and top it with a layer of pure silicon, depositing the layers on a soluble "substrate." The atoms in the film arrange themselves in orderly arrays like oranges stacked neatly at a fruit stand. But because germanium atoms are bigger than silicon atoms, atoms in the silicon and germanium layer have to squeeze together and the atoms in the silicon layer have to stretch apart. So when researchers etch away the substrate, atoms in the upper layer snap back toward one another and those in the lower layer spring apart, causing the film to curl upward.

Theorists predicted that it would be impossible to etch away the substrate without damaging the film, or that films only a few layers of atoms thick would quickly oxidize, Prinz says. Yet, within a few years, he and his team had wound up tubes, coils, and helices with widths ranging from a few micrometers down to a few nanometers. "Never trust theorists in novel fields," Prinz says. "Trust only in your experiments."

As unlikely as it sounds, such films wind themselves into tight spirals resembling carpet rolls, with successive windings binding neatly to each other. Researchers can form more complex shapes such as helices by exploiting the fact that the films tend to curl perpendicular to certain rows of atoms, just as a carpet might roll most easily perpendicular to its warp. If researchers lay down a thin strip of film that's canted relative to the easy-rolling direction, it will curl into a helix instead of a tube.

The roll-up technique offers several advantages, proponents say. The approach begins with standard lithography to pattern films and etch away substrates, so it provides the exquisite control of that tried-and-true technology. The basic physics is so simple that the approach should work with a wide variety of materials. And because the technique works with semiconductors, it should be possible to roll up electronic circuits in the film or to integrate tiny tubes, coils, and other devices directly into microchips—at least that's the hope.

What's it good for?

For the moment, researchers are primarily studying the electrical, optical, and mechanical properties of the tubes and other shapes they've made. Two years ago, physicist Oliver Schmidt and colleagues at the Max Planck Institute for Solid State Research in Stuttgart, Germany,

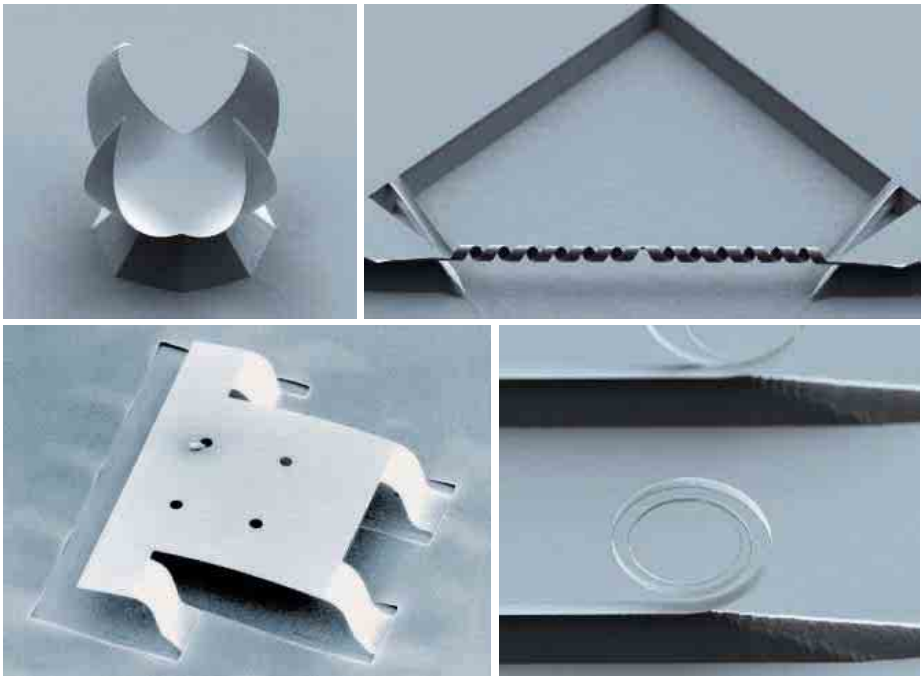

Les objets. Using the curling films and a little ingenuity, researchers can create a wide variety of potentially useful shapes, such as a grasping claw, a suspended spiral, and a delicate coil spring. The same basic physics can be used to make larger folding or pop-up structures, such as a microstage.

CREDITS (GROUP, TOP ROW AND BOTTOM RIGHT): L. ZHANG AND D. GRÜTZMACHER/PAUL SCHERRER INSTITUTE; (GROUP, BOTTOM LEFT) T. LEISCHMANN, K. KUBOTA, P. O. VACCARO, AND S. SARAVANAN; (BOTTOM) L. ZHANG *ET AL.*, *NANO LETT.* **6** (2006), ACS

showed that a rolled-up nanotube can convey liquid like a tiny pipe. Earlier this year, they reported in *Applied Physics Letters* that the tubes also guide light like optical fibers.

Schmidt and colleagues have recently rolled up films of a single material. They grow the film so thick that the atoms near the bottom squeeze together but those near the top feel no pinch. That's because faults develop in the stacking that allow the upper atoms to shift apart, Schmidt reported at a meeting of the American Physical Society in March. The advance could lead to a handier all-silicon technology. The tubes can also emit light, Schmidt says, a trait that could lead to rolled-up lasers on a chip, a potential boon for "optoelectronics."

Researchers have rolled up a variety of materials, including metals and insulators. The technique even works with polymers, physicist Manfred Stamm of the Leibniz Institute of Polymer Research Dresden in Germany and colleagues reported last year in *Advanced Materials*. They lay down a polymer that absorbs a solvent and swells, then top it with one that does not; the swelling curls the film. "Millions of different polymers exist with all sorts of functionalities," Stamm says, "and interfacing to biological systems may be easier because most biomaterials are polymers." Stamm hopes to use a polymer nanotube as the nozzle for a nano–inkjet printer that might spit out one macromolecule at a time.

Some researchers use curling films to connect larger plates and fold them into micrometer-sized devices in an approach known as nano- or micro-origami. ATR's Vaccaro and colleagues have used semiconductor films to make an array of pop-up mirrors and other structures without complex hinges or moving parts. Optics engineer George Barbastathis and colleagues at the Massachusetts Institute of Technology in Cambridge have made tiny fold-over capacitors, as they described in *Applied Physics Letters* in February, and the team's ultimate goal is to fold up accordionlike devices that manipulate light in novel ways. "We see this as an enabling technology," Barbastathis says. "We're trying to make it as manufacturing applicable as possible."

Experimental widgets based on the new technology are already starting to emerge. Physicists Tobias Kipp, Detlef Heitmann, and colleagues at the University of Hamburg in Germany have turned a semiconductor tube into an optical ring resonator, a device that resonates with light much as a whistle rings with sound. Described in *Physical Review Letters* in February, the resonator isn't yet as good as those made by other techniques. But the researchers think rolled-up resonators could someday play a part in quantum information technologies.

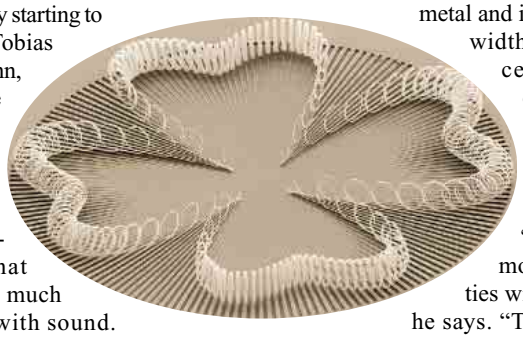

Employed like a probing finger, a drill-like helix should also make a good force sensor, says Bradley Nelson, a roboticist at the Swiss Federal Institute of Technology (ETH) in Zurich. Because the tubes bend much more easily than the probes used on atomic force microscopes, such a sensor should be extremely sensitive, says Nelson, who is collaborating with Grützmacher of the Paul Scherrer Institute. The team should have a working sensor within 6 months, Nelson says.

Perhaps most ambitiously, applied physicist Robert Blick and colleagues at the University of Wisconsin, Madison, hope to use free-floating silicon germanium tubes as chemical sensors that unwind when they encounter their target molecule. Researchers already do something similar with fluorescent quantum dots, whose light changes when the dots bind to their chemical target. The tubes "are a bit bigger, but they're a lot more flexible in that they can change their shape and you can incorporate electronics," Blick says. The project is in its early stages, but the researchers have shown that they can wind and unwind a tube by changing the salinity of the solution surrounding it.

Tube versus tube

Amid the parade of grand visions, some researchers say it's too early to tell whether the roll-your-own approach will pay off. "I don't see how one can claim it has any advantages versus bottom-up approaches, since neither has been demonstrated," says Charles Lieber, a chemist at Harvard University. Even the optimists acknowledge that technical hurdles lie ahead. For example, affixing electrical contacts to rolled-up devices can be tricky.

Researchers working with the curling films disagree on how they stack up against other forms of nanotechnology, in particular carbon nanotubes. The bizarre, elongated molecules of carbon possess electrical and mechanical properties that the larger semiconductor nanotubes cannot hope to match, says Wolfgang Hansen, a physicist at the University of Hamburg whose team has rolled up tubes containing layers of metal and insulator. "The bandwidth for applications is certainly larger" for carbon nanotubes, he says. ETH's Nelson, who works on both types of tube, sees it the opposite way. "There's just a lot more design possibilities with these little coils," he says. "There are a lot more materials and interesting geometries that you can produce."

All agree that finding a few killer applications would go a long way toward transforming vision into reality. Researchers can't yet say what those could be—perhaps something as simple as tiny inductive coils for electronics—but most are hopeful that they will come. The tale of this technology, they say, has only begun to unwind.

–ADRIAN CHO

A Strategy That Works: Hook 'Em While They're Young

A groundbreaking program is giving Chinese high schoolers a chance to try their hand in a university lab—and audition for roles in China's innovation drive

SHANGHAI—While his friends were babysitting or waiting tables, 18-year-old Jim Liu spent his summer vacation last year in Boston, developing software that allows children to construct LEGO Mindstorms robots able to do everything from play soccer to dispense candy. Liu, a native of Shanghai, was one of 88 teenagers from across the world selected for the Research Science Institute (RSI), an all-expenses-paid summer program at the Massachusetts Institute of Technology (MIT). Now back home, Liu is hoping some of the excitement he felt will rub off on fellow teens in China. He's a counselor with the inaugural RSI-China, which began last week here at Fudan University and will run through 15 August.

Showtime. Jim Liu (*above, center*) demonstrates his summer project to fellow students at MIT. He hopes his enthusiasm will infect compatriots at Fudan University (*right*).

The program is trailblazing in other ways: It's the first time a Chinese university has partnered with a U.S. organization to sponsor a high-school program. Run by the Center for Excellence in Education (CEE), a nonprofit organization based in McLean, Virginia, and Fudan University, RSI-China aims to build on the success of its flagship MIT program to train innovative young Chinese minds. "High-school students bring a new perspective [to the lab], and a new discovery is even possible," says Lu Fang, physics dean at Fudan and co-director of RSI-China.

For 6 weeks, 35 of the brightest high-school juniors in Shanghai will experience a reprieve from cramming for university entrance exams to work in Fudan labs. They will also attend classes and lectures on hot research areas. Half the Shanghai staff are graduates of the MIT program. RSI-China culminates with students presenting findings in talks and undergraduate-level term papers. This format has worked well for RSI-MIT, which has had an impressive track record over its 23-year lifetime for hooking students on science: Some 80% of alumni have gone on to graduate school in the sciences.

Following the success of similar programs in Boston, Bulgaria, Israel, and Singapore, CEE sought a foothold in China and got a warm welcome from the government. A philanthropist steered CEE to Fudan, where university administrators were eager to host RSI-China. They see it as a way to hold on to some of Shanghai's top students, many of whom end up in Beijing at Qinghua University or Beijing University. To bankroll the program's first year, organizers signed up local backers: Shanghai Educational Press Group and Shanghai Wall Street Advisors.

RSI-China applicants faced stiff competition. More than 30 schools across Shanghai nominated their top 10 students, although the program could accommodate only 10% of this elite pool. CEE staff interviewed each student to find those with a passion for science outside the classroom, Lu says.

Fudan professors say they welcome the opportunity to work with talented high schoolers. "It's a very good idea. They can already start doing interesting stuff," says Rudolf Fleischer, a computer scientist at Fudan who has volunteered to mentor one student on a project employing computational geometry to improve optical character recognition. "My goal is to show them what happens at university, because if you start early, you get better students," Fleischer says. For many Chinese professors, he adds, mentoring is a new skill: "Traditional Chinese education is based on memorizing. Mentoring is not a concept that many Chinese professors understand well."

RSI-China is a small step toward addressing a widespread shortcoming of Chinese schools: Few offer hands-on science instruction, let alone lab facilities. "This is a very different concept for educating students in China," says CEE President Joann DiGennaro. The main aim in Chinese schools is to hone test-taking skills, says Liu. After RSI, he says, "creativity will be activated. Now, all that high-school students seem to think about is the entrance exam, and that's not good." After spending the 2004–'05 academic year as an exchange student at T. C. Williams High School in Alexandria, Virginia, Qian Yingzhi, a member of RSI-China's inaugural class, says she appreciates the rare invitation to work in a Chinese lab. "I want to expand my horizons," she says.

The projects are "real research that we undertake every day," says Yang Zhong, executive dean of life sciences at Fudan. He is hosting a student who will fish flavonoid genes out of Tibetan plants as part of a project to detect adaptation through molecular evolution. Other projects include working on solar energy cells, examining the nonlinear behavior of yeast cells zapped with electrical currents, and screening for microbes that break down pollutants.

The grand challenge of RSI-China is to facilitate the exchange of ideas with the international community, says Lu. "China is an emerging world power in academics," adds DiGennaro. She hopes the program will be able to improve international relations between China and the United States while teaching students to think on their own. Lu agrees that this is a worthwhile aim. "We don't want the professor to teach the student but rather the student to teach himself," he says.

Lu has lofty aspirations for RSI-China. If all goes well this summer, he hopes that next year the program can recruit students from across the country. For Liu, the taste of real research last summer impelled him to pursue a science career in the United States; as a first step on that journey, he is enrolling at MIT this fall. He hopes the experience will be equally motivating for RSI-China's freshman class. At least it will be a refreshing break from having to memorize their science textbooks.

–JERRY GUO

Jerry Guo is a freelance writer in New Haven, Connecticut.

CREDITS: JIM LIU; (INSET) CAIO CAMARGO

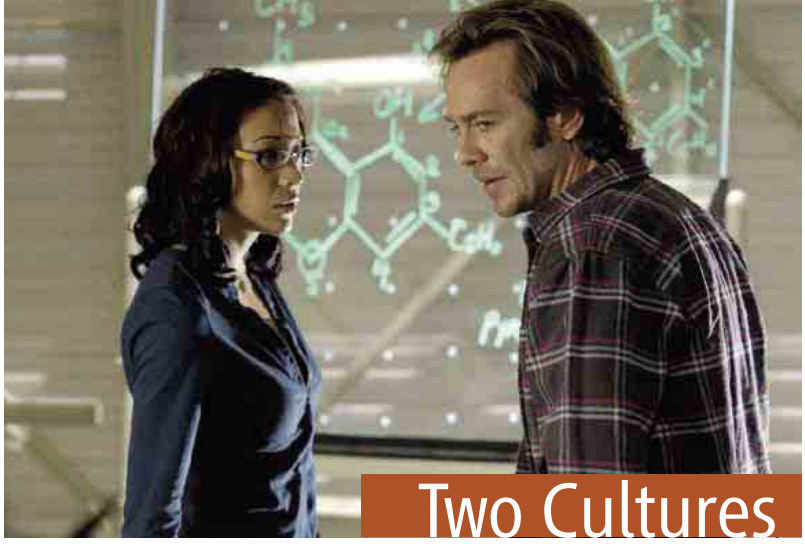

Two Cultures

SCIENCE FICTIONALIZED. When Canadian writer and filmmaker Christina Jennings found herself asking questions such as whether to vaccinate her child or eat genetically modified food, she had an insight about the broad impact of science on everyday lives: "I realized it wasn't just me, that these were water-cooler conversations."

The thought led Jennings (below) to create *ReGenesis*, a science-based television drama whose second season ended last month. Broadcast in 80 countries including Canada, the show's hourlong episodes have probed the ethical challenges presented by cloning, engineered viruses, and other scientific advances. One tells the story of a dying boy who suspects he is a clone of his overbearing genius father. In another episode, researchers discover a "gay gene" and struggle with the fallout. "The scientists are in the same dilemma with what to do about the results as the average person on the street," says Aled Edwards, the show's scientific consultant and a proteomics researcher at the University of Toronto.

Jennings starts shooting the show's third season later this summer. "Someone asked me if we're going to run out of stories," she says. "I said, 'You're kidding.' There are hundreds of science stories out there."

POLITICS

AXED. India's foremost medical research institution, the All India Institute of Medical Sciences (AIIMS) in New Delhi, is in turmoil after its director was fired last week. Cardiac surgeon Panangipalli Venugopal, 64 (left), was dismissed by the institute's governing body for allegedly violating the code of conduct for civil servants. In response to a suit by Venugopal, the Delhi high court on 7 July temporarily suspended the dismissal until the next hearing of the case in mid-August.

Trouble between the director and the government began this spring after the government rolled out a controversial plan to increase the quota of government jobs and university positions for people from disadvantaged social groups (*Science*, 2 June, p. 1291). Protests erupted, and officials claimed Venugopal had gone against the government line by allowing protesters to stage demonstrations on AIIMS grounds. Last month, Venugopal criticized India's health minister, Anbumani Ramadoss (right), for meddling with the institute's autonomy. On 5 July, AIIMS's governors accused Venugopal of "indiscipline" and fired him in the "public interest."

The dismissal "hurts terribly," Venugopal told *The Indian Express*. He has spent 47 years at AIIMS and performed more than 50,000 open-heart surgeries. Sanjiv Malik, president of the Indian Medical Association, has condemned the firing as "an attempt to bulldoze the autonomy of [India's] medical institutions." It has certainly roiled AIIMS: As *Science* went to press, most medical staff were on strike, crippling patient care.

CREDITS (TOP TO BOTTOM): STEVE WILKIE; VENETIA BURNEY PHAIR; STEVE WILKIE; MANISH SWARUP/AP PHOTO

Honors >>

A NAME TO REMEMBER. Astronomers have a special place in their hearts for Venetia (Burney) Phair, an 87-year-old retired schoolteacher in Epsom, U.K. She has an asteroid named after her, and she received a personal invitation from NASA to attend the launch of the New Horizons spacecraft in January. And last month, one of the instruments on that spacecraft was named in her honor.

The reason for these honors is that in 1930, at age 11, Venetia Burney came up with the name Pluto for the newly discovered ninth planet. On 14 March that year, she was at breakfast when her grandfather Falconer Madan read to her about the discovery from *The Times* of London newspaper. "For some reason I, after a short pause, said, 'Why not call it Pluto?' " Phair told NASA public affairs in an interview earlier this year, explaining that she had been a keen reader of Greek and Roman myths. Madan, the retired librarian of Oxford University's Bodleian Library, passed the idea to Oxford astronomer Herbert Hall Turner, who cabled it to the Lowell Observatory in Arizona, where the discovery had been made. The rest is history.

New Horizons, the first spacecraft to travel to Pluto, set off on 19 January carrying a dust-counting instrument designed, built, and operated by students. Last month, it was named the Venetia Burney Student Dust Counter. By the time the instrument reaches Pluto in 2015, its namesake will be the venerable age of 96.

IN BRIEF

BACK TO TEACHING. A year and a half after his controversial remarks on the scientific talents of women, Lawrence Summers has stepped down from Harvard's presidency. Last month, the 51-year-old economist was appointed a professor at the university's Kennedy School of Government and the Harvard Business School. He will begin teaching and research in the fall of 2007, after a year's sabbatical.

Got a tip for this page? E-mail people@aaas.org

NEW

Announcing New *Science* Online Seminars. Now showing on a computer near you.

Now you can have your very own personal presentation of the latest breakthrough papers in *Science*, presented by the authors, with our new *Science* Online Seminars.

Powered by Biocompare, *Science* Online Seminars give you a web-based audio and visual presentation of an author discussing and showing the application of the research and/or methods and protocol. Best of all, you can access these Seminars whenever you want.

Sound like a good idea? Then why not go and try it now. Go to:
www.sciencemag.org/onlineseminars

Science
AAAS

LETTERS

edited by Etta Kavanagh

Difficulties for Foreign Scientists in Coming to the United States

THE RECENT EDITORIAL "THE HIGH COST OF COMING TO AMERICA" BY A. TEICH and W. D. White (5 May, p. 657) calls attention to the humiliating and unjustifiable treatment of distinguished scientists such as Goverdhan Mehta in the Visas Mantis program.

> "It is in the [U.S.] national interest **to find a more favorable balance between regulations** that aim to exclude terrorists and the need to rally the best of the international scientific community to meet pressing challenges."
>
> —D'Elia ***et al.***

The Visas Mantis program is just the tip of a larger iceberg involving not only the U.S. Department of State, but also the U.S. Citizenship and Immigration Services (USCIS) of the Department of Homeland Security. In January 2006, Secretaries Rice (State) and Chertoff (Homeland Security) announced an initiative ("Secure Borders and Open Doors in the Information Age") to correct and improve U.S. performance in balancing security and openness. But hearings before the House Committee on Government Reform in April 2006 showed how bad this balance is, largely because of cumbersome administrative processes in the hands of too few, inadequately trained consular staff (*1*). High-profile incidents such as that suffered by Mehta are too often repeated with less distinguished but vitally needed foreign scientists and technologists. The reforms proposed by Rice and Chertoff need to be put in place with a greater sense of urgency than is apparent.

The collateral costs of these failing visa and immigration policies are substantive. Universities have had to increase the resources allocated for international student services and are now burdened with extensive, unfunded reporting requirements such as the Student and Exchange Visitor Information System (SEVIS). The United States risks losing its market share in an "industry" (higher education) in which it has been a world leader and accrues substantial opportunity costs as it fails to attract and retain the needed international scientific talent that it used to take for granted.

It is in the national interest to find a more favorable balance between regulations that aim to exclude terrorists and the need to rally the best of the international scientific community to meet pressing challenges.

CHRISTOPHER F. D'ELIA,[1]* GAYLEN BRADLEY,[2]† ROLAND SCHMITT[3]‡

[1]University of South Florida, St. Petersburg, FL 33701, USA. [2]Penn State University, Hershey, PA 17033, USA. [3]American Institute of Physics, Post Office Box 240, Rexford, NY 12148, USA.

*Past Chair, Council of Scientific Society Presidents (CSSP)
†Liaison Past Presidents to CSSP
‡Chair Emeritus, CSSP

Reference

1. Testimony of Jess T. Ford of the U.S. General Accouting Office before the House Committee on Government Reform, 4 April 2006 (available at http://reform.house.gov/UploadedFiles/GAO%20-%20Ford%20Visa%20Testimony.pdf).

Bridging the Divide or Deepening It?

IN "BRIDGING THE DIVIDE IN THE HOLY LAND" (News Focus, 21 Apr., p. 352), J. Bohannon discusses his view of how Israeli and Palestinian scientists are working together within the frame of the Israeli-Palestinian Scientific Organization (IPSO). The article ends on an optimistic note, with the Palestinian scientist Mukhles Sowwan stating that "science is a universal language, like music. It can make people understand each other."

In a section of the article subtitled "Where collaboration is a dirty word," mention is made of "one Israeli professor," who "railed" against the IPSO program. The unnamed professor is the signatory of this letter. I am also cited as stating that the program is "dangerous" and "playing into the hands of terrorists." This information has no factual basis. It is correct that I expressed my opposition to the launching of IPSO under the present circumstances in a letter to Menahem Yaari, Deputy Chairperson of the Executive Council of IPSO and one of the founders of the organization. The reason for my opposition was the partisan character of the organization, which drew support, on the Israeli side, exclusively from persons of a political orientation unabashedly critical of the policies of recent Israeli governments toward the Palestinians. At the very least, I would have expected Yaari to encourage Bohannon to read my letter and Bohannon to contact me in person and enable me to present my arguments directly to him and not by proxy.

As for the text, cited statements, and pictorial material figuring in the article, many of these are not "facts" but markedly biased political declarations, representing exclusively the Palestinian view and, again, that of one extreme pole of political opinion in Israel, referred to above.

The aerial picture of the "security barrier" and the associated text (box on p. 354) do not explain that the barrier was an option forced on Israel by the grim reality of the killing and maiming of innocents by Palestinian terrorists. A juxtaposed picture of the horror on the streets of Tel Aviv or Jerusalem after one of the bomb attacks (not "bomb plots") would, perhaps, have been appropriate. The building of the barrier has the support of the overwhelming majority of the Israeli electorate, and the highly respected Israeli Supreme Court of Justice is dealing with every complaint concerning the barrier, whether submitted by Palestinians or Israelis. The claims (unproven) that the barrier is depriving Palestinians of water and blocking animal migration

must be weighed against its (proven) life-saving effects.

On page 356, readers are shown Viveca Hazboun in front of her clinic, which is said to have been destroyed by Israeli artillery fire. Assuming that the facts are correct, don't the readers of *Science* deserve to be fairly informed about the background to the shelling? There is a war in the Holy Land and civilians, as innocent as Hazboun, were victims of Palestinian sniper fire. Thus, any description of the unfortunate results of warfare should be presented in the context of the events having led to these results.

I think that Sowwan got cause and effect in the wrong order: "People must understand each other first; then they can do science and play music together."

EDGAR PICK

Professor, Director, the Julius Friedrich Cohnheim–Minerva Center for Phagocyte Research; Head, the Ela Kodesz Institute of Host Defense against Infectious Diseases; Incumbent, Roberts-Guthman Chair in Immunopharmacology, Sackler School of Medicine, Tel Aviv University, Tel Aviv 69978, Israel.

Scientific Activity Should Have No Borders

BOHANNON'S WELL-RESEARCHED AND BALanced article "Bridging the divide in the Holy Land" (News Focus, 21 Apr., p. 352) might be criticized by some as "political activism," but it is an excellent example of scientific activism. He takes on a host of controversial issues: terrorism, the human right to move freely, environmental degradation, and barriers to scientific collaboration. In these days of debates on borders that impede the free movement of people—the U.S.-Mexican border, the European Union–African maritime borders, and the Israeli-Palestinian separation wall—Bohannon reminds us that science is an international activity that knows and should know no border.

Scientists understand the importance of the free flow of ideas, knowledge, and professionals. When scientific collaboration is seen as enemy collaborationism, science is losing against confrontational politics. While the battle against terrorism is of great importance, walls and barriers are against the essence of science.

FRANCISCO LEON

Bristol-Myers Squibb, Princeton, NJ 08540, USA.

Reexamining Fusion Power

FOR THE REASONS GIVEN IN W. E. PARKINS'S Policy Forum "Fusion power: will it ever come?" (10 Mar., p. 1380), interest from the utility companies in hot fusion is nonexistent and will probably remain so for the foreseeable future. No utility company would even consider either of the two hot fusion concepts—the tokamak or inertial. The reasons are fundamental and cannot be remedied by any known materials or design.

We have reviewed the National Research Council Burning Plasma Science Assessment Committee papers of 2002 and 2003 (*1*) to see whether the rough plant design estimates presented by Parkins remain valid. In recent years, the fusion community has been very innovative in condensing the proposed burning plasma experiment, but seems to have given little consideration to the practical engineering and economics of the unique heat conversion and maintenance systems of a full-scale demonstration plant, which are the core of Parkins's criticisms. The size caused by the unique heat transfer limitations of the concepts calls for a huge lump capital investment beyond the risk level of any utility system. Most of the output energy is in the form of 14-Mev neutrons, which means that the bulk of available energy is in the blanket material and structure. Such bombardment will eventually cause intolerable neutron damage in any blanket and structural material, and induce radioactivity in almost every part of the internal structure. Thus, long-life maintenance becomes essential but impractical, especially with the huge blanket required. Even in the present commercial fission plants, "hot" maintenance creates a heavy manpower burden with the limited exposure personnel are permitted. The concepts require vacuum-tight containment, but vacuum maintenance in large structures requires constant pumping and leak repair.

The electric utilities' first priorities are the economic and operating problems they must solve in commercial fission plants. Any concept that multiplies these difficulties gets a cold reception. The lack of operating utility interest in today's hot fusion concepts is a reality that is not likely to change in the foreseeable future.

CHAUNCEY STARR,[1] ROBERT L. HIRSCH,[2] HERMAN DIECKAMP,[3] LEONARD J. KOCH[4]

[1]President Emeritus, Electric Power Research Institute, 3420 Hillview Avenue, Palo Alto, CA 94304, USA. [2]Vice President, Electric Power Research Institute, retired, 122 Princess Street, Alexandria, VA 22314, USA. [3]President, General Public Utilities, retired, 29 Crystal Road, Mountain Lakes, NJ 07046, USA. [4]Vice President, Illinois Power Co., retired, 1 East Desert Sky Road #16, Tucson, AZ 85737–7689, USA.

Reference

1. Included in the Department of Energy Budget Requests for Fusion Energy Sciences, 2003 and 2004 (www.ofes.fusion.doe.gov/FusionDocs.html).

ALTHOUGH ONE MAY CRITICIZE THE LATE W. E. Parkins for using dated information in his Policy Forum "Fusion power: will it ever come?" (10 Mar., p. 1380), the general spirit of his comments still rings true. The tokamak confinement concept became the front-runner in 1968 after the Soviets found high electron temperatures in one of their experiments. The result was that all of the fusion eggs were thrown into the tokamak basket and the search for more attractive concepts declined worldwide. U.S. fusion funding levels, now about 1.5 IWDs ["Iraq War Days," a unit of currency equal to the amount the United States spends in Iraq in one day (about $190 million)], does not permit exploration of innovations at the level required. If this were increased to, say, 4 to 5 IWDs, then I believe we would be able to find fusion concepts that are tolerably compact and have attractive (e.g., axisymmetric) geometry, acceptable recirculating power, decently high fusion power density, magnetic fields that are realizable at large scale, and a cost-effective means for blanket change-out and refurbishing. Perhaps if we could get the military-industrial complex and their lobbyist colleagues behind us, such funding would be forthcoming.

ROBERT BOURQUE

Los Alamos National Laboratory, Los Alamos, NM 87545, USA. E-mail: bourque@lanl.gov

IT IS NOT CLEAR WHY *SCIENCE* HAS CHOSEN TO publish a reiteration of arguments against the development of fusion power ("Fusion power: will it ever come?", W. E. Parkins, Policy Forum, 10 Mar., p. 1380) that were already shown to be wrong when the author first published them in 1997 (*1*). There have been no new developments since then that have made the arguments that were wrong then valid now or that have removed the need for a sustainable energy option. What is new since 1997 is a thorough European study of the prospective fusion power plants, addressing safety and environmental impact, economics, and development needs (*2*). The points raised by Parkins are fully answered in this study.

Internal components of the fusion reactor will indeed have to be periodically replaced by remote maintenance, while the vacuum vessel and the magnets are designed for the lifetime of the reactor. Maintaining vacuum integrity in a large toroidal system—flagged as an insurmountable problem by Parkins—is in fact already demonstrated in many large fusion devices. The projected cost of fusion electricity is comparable to other sustainable energy technologies.

On 24 May, China, India, South Korea, Japan, the Russian Federation, the United

Letters to the Editor

Letters (~300 words) discuss material published in *Science* in the previous 6 months or issues of general interest. They can be submitted through the Web (www.submit2science.org) or by regular mail (1200 New York Ave., NW, Washington, DC 20005, USA). Letters are not acknowledged upon receipt, nor are authors generally consulted before publication. Whether published in full or in part, letters are subject to editing for clarity and space.

States, and the EU signed the agreement to build the international fusion experiment ITER, which will demonstrate 10-fold power multiplication in a fusion reactor, at the 500-MW power level. Parallel to ITER, a technology and materials program is being mounted, so that soon after ITER is built, physics and technology can be combined into a demonstration reactor. As European and U.S. studies have shown, fusion could deliver electricity to the grid in 30 to 35 years.

NIEK LOPES CARDOZO,[1] ALEX BRADSHAW,[2] PAUL VANDENPLAS[3]

[1]FOM Institute for Plasma Physics Rijnhuizen, Association Euratom-FOM, Post Office Box 1207, 3430 BE Nieuwegein, the Netherlands. [2]Max-Planck-Institut fur Plasmaphysik, Boltzmannstrasse 2, D-85748 Garching, Germany. [3]Association Euratom–Belgium State Fusion, Avenue de la Renaissance, 30, Kunstherlevinglaan, B-1000 Brussels, Belgium.

References

1. W. E. Parkins *et al.*, *Phys. Today* **1997**, 15 (Mar. 1997).
2. D. Maisonnier *et al.*, A Conceptual Study of Commercial Fusion Power Plants, Final Report of the Power Plant Conceptual Study, 13 April 2005 (available at www.efda.org/ppcs.pdf).

Auxin Signaling in Plant Defense

IN THEIR REPORT "A PLANT MIRNA CONTRIBUTES to antibacterial resistance by repressing auxin signaling" (21 Apr., p. 436), L. Navarro *et al.* demonstrate a link between auxin signaling in plants and resistance to bacterial pathogens. As part of a plant-induced immune response, bacterial pathogen-associated molecular pattern (PAMP) recognition down-regulates auxin signaling in *Arabidopsis* by targeting auxin receptor transcripts. These results indicate that decreasing plant auxin signaling can increase resistance to bacterial pathogens; Navarro *et al.* also showed that exogenous application of auxin enhances susceptibility to the bacterial pathogen.

We note that auxins, as exemplified by indole-3-acetic acid (IAA), can also have a direct effect on pathogen survival and its resistance to plant defense. Some microorganisms, independent of their ability to produce IAA, use auxin as a signaling molecule. For example, IAA can act as a signaling molecule in microorganisms such as *Azospirillum brasilense* (*1*, *2*), *Escherichia coli* (*3*), *Agrobacterium* (*4*), and even yeast (*5*). It can induce the expression of genes related to survival under stress conditions in *E. coli* (*3*). Furthermore, a knockout *A. brasilense* mutant with decreased IAA production is strongly impaired in stationary phase survival (*6*). Consistently, *E. coli* cells treated with IAA survive substantially longer than untreated cells (*3*).

These findings shed new light on IAA and its role as a signaling molecule.

ROSELINE REMANS, STIJN SPAEPEN, JOS VANDERLEYDEN*

Centre of Microbial and Plant Genetics, Katholieke Universiteit Leuven, Kasteelpark Arenberg 20, B-3001 Heverlee, Belgium.

*To whom correspondence should be addressed. E-mail: Jozef.Vanderleyden@biw.kuleuven.be

References

1. M. Lambrecht, A. Vande Broek, F. Dosselaere, J. Vanderleyden, *Mol. Microbiol.* **32**, 889 (1999).
2. A. Vande Broek *et al.*, *Mol. Plant Microbe Interact.* **18**, 311 (2005).
3. C. Bianco *et al.*, *Arch. Microbiol.* **185**, 373 (2006).
4. P. Liu, E. W. Nester, *Proc. Natl. Acad. Sci. U.S.A.* **103**, 4658 (2006).
5. R. Prusty, P. Grisafi, G. R. Fink, *Proc. Natl. Acad. Sci. U.S.A.* **101**, 4153 (2004).
6. O. Ona, Ph.D. thesis, K. U. Leuven, Heverlee, Belgium (2005).

Women Science Faculty at MIT

A QUOTE FROM ME IN AN ARTICLE BY A. LAWLER ("Progress on hiring women science faculty members stalls at MIT," News of the Week, 21 Apr., p. 347) may have left an incorrect impression about tenure rates for female versus male faculty in the School of Science at the Massachusetts Institute of Technology (MIT). Over many years, women faculty in the school have received tenure at the same rate as men. The reason that the number of women faculty in science at MIT did not increase from 2001 to 2005, following a rapid increase from 1997 to 2000, was due to normal attrition rates combined with a difference in the rate of hiring. In the 3-year period between 1997 and 2000, women were hired at a rate of nearly four per year among the six departments in the School of Science; in contrast, in the 5 years from 2001 to 2005, women were hired at a rate of about two per year.

A further correction to the article is in the number of women joining the MIT faculty in the two 5-year periods before and after 2000: 15 joined between 1996 and 2000, and 11 joined between 2001 and 2005, not 13 and 12, as stated in the article.

ROBERT J. SILBEY

Dean of the School of Science, Massachusetts Institute of Technology, Cambridge, MA 02139, USA.

Clarifying Cancer Mortality Rates

YOUR ISSUE ON THE STATE OF CANCER RESEARCH (Special Section: Cancer treatment gets personal, 26 May) uses an incomplete reading of cancer trend statistics to support a misleading conclusion on the progress made in cancer mortality. In H. Varmus's Perspective "The new era in cancer research" (p. 1162) and in the Introduction (p. 1157), it is noted that cancer mortality rates today are very close to where

they were 50 years ago.

In fact, death rates from cancer have changed dramatically over the past 50 years. Age-standardized death rates (deaths per 100,000 population) from cancer increased from 195.4 in 1950 to 215.1 in 1991, primarily because of increases in smoking-related cancers, particularly lung cancer. In the early 1990s, reductions in smoking as well as advances in treatment and early detection led to a drop of about 1% per year in the overall mortality rate, which brought the rate back to 190.1 by 2003. That same year, the number of actual cancer deaths dropped for the first time since mortality record-keeping was instituted in 1930, as the decreasing mortality rate overtook population factors that have obscured the progress made.

CAROLYN D. RUNOWICZ

President, American Cancer Society, Inc., 1599 Clifton Road, NE, Atlanta, GA 30329, USA.

TECHNICAL COMMENT ABSTRACTS

COMMENT ON "Ongoing Adaptive Evolution of *ASPM*, a Brain Size Determinant in *Homo sapiens*" and "*Microcephalin*, a Gene Regulating Brain Size, Continues to Evolve Adaptively in Humans"

Mathias Currat, Laurent Excoffier, Wayne Maddison, Sarah P. Otto, Nicolas Ray, Michael C. Whitlock, Sam Yeaman

Mekel-Bobrov *et al*. and Evans *et al*. (Reports, 9 Sept. 2005, p. 1720 and p. 1717, respectively) examined sequence data from modern humans within two gene regions associated with brain development, *ASPM* and *microcephalin*, and concluded that selection of these genes must be ongoing. We show that models of human history that include both population growth and spatial structure can generate the observed patterns without selection.

Full text at www.sciencemag.org/cgi/content/full/313/5784/172a

RESPONSE TO COMMENT ON "Ongoing Adaptive Evolution of *ASPM*, a Brain Size Determinant in *Homo sapiens*" and "*Microcephalin*, a Gene Regulating Brain Size, Continues to Evolve Adaptively in Humans"

Nitzan Mekel-Bobrov, Patrick D. Evans, Sandra L. Gilbert, Eric J. Vallender, Richard R. Hudson, Bruce T. Lahn

Currat *et al.* present computer simulations to argue that the haplotype structure found at the *microcephalin* and *ASPM* genes can be better explained by demographic history rather than by selection. The demographic models they adopt, however, strongly contradict a decade of empirical research on human demographic history and do not account for the critical features of the data on which our argument for selection was based.

Full text at www.sciencemag.org/cgi/content/full/313/5784/172b

ANTHROPOLOGY

From Foraging to Planting

Deborah M. Pearsall

Behavioral Ecology and the Transition to Agriculture

Douglas J. Kennett and Bruce Winterhalder, Eds.

University of California Press, Berkeley, 2006. 408 pp. $60, £38.95. ISBN 0-520-24647-0.

Plant and animal domestication and the transition to agriculture are topics of intense interest in archaeology. The early Holocene transformation of human societies around the globe from foraging to agriculture constitutes the most important development for our species since the emergence of modern humans. The transition spurred population growth, affected (often negatively) the health of individuals, and led to changes in how people related to each other and to their world.

Three seminal works (*1*–*3*) from the long history of research on agricultural origins have shaped my perception that agriculture is an outgrowth of normal plant-people relationships—i.e., is fundamentally ethnobiological—and that our understanding of this transformation requires systematic recovery of the remains of the plants and animals used by humans.

Behavioral Ecology and the Transition to Agriculture is poised to become a similar work for scholars who are part of an emerging consensus that plant domestication and agriculture are outgrowths of foraging behavior. As Robert Bettinger notes, "This volume marks a turning point in the development of human behavioral ecology…, whose past efforts have spoken to a research agenda largely crafted in the biological sciences by individuals interested in nonhuman species." The volume's chapters reflect a maturing of human behavioral ecology; their approach to the landmark transformation of agricultural origins illustrates the increasing sophistication in modeling.

At the core of human behavioral ecology, as Douglas Kennett and Bruce Winterhalder note, is optimization: "As a result of natural and cultural evolutionary processes, behavior will tend toward constrained optimization." Foraging efficiency enhances fitness by providing adequate food and freeing the forager to undertake nonsubsistence activities that may enhance fitness, such as acquiring prestige. A central feature of diet breadth, the most commonly used model, is that individuals make rational decisions about whether to take an encountered animal or plant (from a set of ranked resources) based on the costs and benefits of doing so (measured in the "currency" of food energy) within the constraints of a goal, such as maximizing energy return or minimizing risk. Changes in costs or benefits—e.g., environmental change that alters resource abundances—cause changes in diet breadth, such as widening to include lower ranked resources. In Renee Barlow's formulation, "The model predicts that foragers will farm when the expected marginal energetic return for a particular farming activity (kcal/hr) is greater than the immediate return rate for foraging (kcal/hr)…." Applying human behavioral ecology requires that the archaeological record, which captures the actions of groups and rarely individuals, is adequate to model such a process.

Human behavioral ecology models differ from coevolutionary approaches, which do not rely on decision-making as outlined above. From a coevolutionary perspective, foraging is characterized by mutualism (*2*). Through foraging, humans contribute to plant propagation—some seeds survive digestion and form new populations; root tips left in the ground multiply. Plants that respond in these ways increase in abundance and therefore are increasingly foraged. Over time, the cycle of planting (inadvertent or deliberate) and harvesting leads to morphological changes that mark domestication (*3*).

What coevolution contributes to the "how" of agricultural origins is the notion that people's routine interactions with plants and animals have the potential to change those species. What we know from ethnobiological studies of contemporary foragers is that humans are active manipulators of environments, not passive responders. Management practices that increase stands of desirable wild resources, such as controlled burning and replanting, demonstrate that foragers control a suite of skills that could lead to agriculture. Human behavioral ecology provides a framework for understanding which resources would be targeted for management.

One theme running through the volume is that human behavioral ecology approaches are useful regardless of whether specific models can be tested. Kristen Gremillion puts it well: "The goal of this exercise is neither to test the predictions of central place foraging theory against the archaeological record, nor to assess the validity of the models themselves. The theoretical model is used to provide a framework for analysis and to identify variables relevant to decision making…." Nonetheless, Gremillion demonstrates the usefulness of central place foraging theory (that foragers or farmers will select residential base locations that maximize net foraging or farming return) through a simulation that predicts return rates of different cultivation strategies and generates testable hypotheses. Ideal free distribution modeling (that individuals will select habitats that maximize net foraging or farming return), such as that presented by Kennett, Atholl Anderson, and Winterhalder for the dispersal of people across the Pacific, also generates testable hypotheses on site locations, pace of colonization, and habitat change. Central place foraging and ideal free distribution are powerful approaches in part because they generate predictions that can be tested with archaeological site distribution and paleoenvironmental data.

Artifacts from a flexible culture. Although they cultivated maize, the people who produced Fremont assemblages (Utah, CE 600 to 1300) continued to rely on hunting and foraging.

CREDIT: PHOTO BY K. RENEE BARLOW; ARTIFACTS COURTESY OF THE UTAH MUSEUM OF NATURAL HISTORY

Diet-breadth models are more challenging to evaluate. Ideally, testing would rely on temporal sequences of quantitative data on utilized plant and animal species. Problems include the differential preservation of different species and tissues and the difficulties of both species-level identifications and determination of which recovered species were foods.

Using ubiquity (the percentage of observations in which a species is found) as a proxy for energy returns and richness (the number of species recovered) may facilitate evaluation of models, as in the study of early agriculture in Arizona by Michael Diehl and Jennifer Waters. Furthermore, using ubiquity and richness allows a single ranking of both plants and animals based on disparate data, such as seeds preserved by charring and tubers preserved as

The reviewer is at the Department of Anthropology, 107 Swallow Hall, University of Missouri, Columbia, MO 65211, USA. E-mail: pearsalld@missouri.edu

starch or phytolith residues on tools. These proxy indicators are not divorced from sample size effects, however, and do not help the analyst interpret absence: Is this lack of use of a resource? Or extreme preservation bias? Such issues are important in evaluating temporal sequences of data.

Behavioral Ecology and the Transition to Agriculture illustrates the power and the limitations of human behavioral ecology as well as how it contributes to our understanding of that landmark transformation. Realizing the full potential of foraging theory modeling will, however, require more than good archaeology. One theme shared by many chapters is the difficulty of arriving at realistic estimates of costs and benefits of available resources. New ethnographic data, plant distribution studies, and paleoenvironmental data are needed to feed the models. Agricultural origins research is fundamentally interdisciplinary and, as such, among the most challenging topics we face.

References

1. C. O. Sauer, *Agricultural Origins and Dispersals* (American Geographical Society, New York, 1952).
2. D. Rindos, *The Origins of Agriculture: An Evolutionary Perspective* (Academic Press, Orlando, FL, 1984).
3. J. R. Harlan, *Crops and Man* (American Society of Agronomy and Crop Science Society of America, Madison, WI, ed. 2, 1992).

10.1126/science.1130120

HUMAN EVOLUTION

Silverbacks and Their Satellites

Rebecca L. Cann

Nicholas Wade's latest book, *Before the Dawn*, extends many of the subjects he has previously written about (social evolution, gender roles, race, language, intelligence, migration, and genetic identity) for the *New York Times* to a full-length discussion of human evolution. Many American geneticists consider Wade to be the most important general science writer covering their field. The breadth of his writing allows him to include lice, sperm competition, microcephaly, proto-IndoEuropean, lactose intolerance, and cannibalism in a single chapter. As a graduate student, I was amazed by the number of books popularizing human paleontology that ignored human genetics, and I often wished that there were science writers energized to follow the new insights from geneticists as closely and rapidly as others reported interpretations of fragmentary fossils. Well, be careful what you wish for. The book also reveals some unpleasant truths about science writing that currently passes for objective and informed. Only smugness that one's sources must be correct because they represent a scientific elite group having new and exclusive truths about human evolution makes it possible to write, in 2006, sentences such as, "The Australian and New Guinean branch [of our phylogenetic tree] soon settled into a time warp of perpetual stagnation."

Wade's marketing of his non–politically correct views of human history as hard science with a genetic basis in modern molecular biology leads him to emphasize the role of warfare as the most critically important feature shaping human dispersal, mate choice, and competition—ideas that channel Richard Alexander's papers on conflicts between polygynous and monogamous societies. Napoleon Chagnon's Yanomamo work is also revisited, but without the alternative background previously exposed by Patrick Tierney's "Darkness in Eldorado" episode (*1*). Instead, Wade fleshes out Alexander's, William Hamilton's, Richard Wrangham's, and Robert Trivers's theses within a modern frame as the simple extension of chimpanzee social behaviors, because modern molecular genetics has now given us a comparative genome-wide basis for documenting recent shared, common ancestry. It is clear that Wade has chosen to focus on one species of chimpanzee (the common, rather than the bonobo) to supply data supporting claims of innate human male aggression, without considering the ecological box all African ape species find themselves driven into by expanding human encroachment. Instead, he dwells on the supposed stability of ape society and their conservatism in the face of ecological change, compared to innovative humans. His statements about conservatism of ape behavior jumped from the page as I viewed a PBS film about an orangutan sanctuary in Borneo, captivated by footage of a young female named Princess who knuckle-walks down a narrow dock, unmoors a canoe, loads her infant, lifts the paddle, and heads downstream to feed (*2*).

From Wade's perspective, archaeologist Richard Klein's claims that early modern humans were anatomically advanced but not behaviorally tempered (*3*) are completely in agreement with molecular genetics. Wade allows that others—notably Sally McBrearty, Alison Brooks, and Christopher Henshilwood (*4*, *5*)—see a different record, but he clearly champions Klein. Language genes are the reason, and the FoxP2 story is again recounted, without all the uncertainties and comparative carnivore information that make many inferences suspect. At the beginning of the book, Wade states that modern humans were confined to North Africa 50 thousand years ago (ka), a place and time at odds with the deep divergence of maternal genetic lineages within the Andamanese he notes elsewhere. The Toba volcanic eruption on Sumatra (73 ka), which would have destroyed previous evidence of an earlier African dispersal in this region, is consistent with the genetic data but gets no mention.

The author's consideration of competitive interactions between modern humans and archaic species is particularly problematic. According to Wade, modern humans carried out a continual campaign of active genetic cleansing against Neandertals that lasted at least 30,000 years. Considering that any human isolate bottled up with nonhuman primates on a separate, tropical continent for 500,000 years is likely to have brought some nasty pathogens when it arrived in habitats harboring appropriate insect vectors, some alternative explanations for the disappearance of Neandertals and *Homo floresiensis* are in order.

Before the Dawn
Recovering the Lost History of Our Ancestors
by Nicholas Wade
Penguin, New York, 2006. 319 pp. $24.95. ISBN 1-59420-079-3.

Informed readers will find many other questionable interpretations. For example, instead of postulating agriculture as a condition to sedentism and the rise of the city state, Wade believes that affinity to place arose before a technology gave added value to place. New alleles for philopatry did not kick highborn European second sons out of kingships and into armies or the clergy; the stimulus was birth order. And, rather than characterize the inheritance of certain behavioral or disease traits as Mendelian versus complex, the appropriate distinction is simple Mendelian versus quantitative.

How many of our individual accomplishments are really due to hard work, dedication, and motivation, rather than the genetic lottery we may or may not have won? Many geneticists who probe such questions are uneasy, and journalists who know they are should understand the consequences of oversimplified answers. *Before the Dawn* will do little to cheer such scientists up. Accepted uncritically, it could even help shift the emphasis in popular culture and politics from individual values to group means and their stereotypes.

References

1. C. C. Mann, *Science* **291**, 416 (2001).
2. "From Orphan to King," an episode in PBS's *Nature* series.
3. R. G. Klein, *The Human Career* (Univ. Chicago Press, Chicago, ed. 2, 1999).
4. S. McBrearty, A. S. Brooks, *J. Hum. Evol.* **39**, 453 (2000).
5. C. Henshilwood, F. d'Errico, M. Vanhaeren, K. van Niekirk, Z. Jacobs, *Science* **304**, 404 (2004).

10.1126/science.1130539

The reviewer is at the Department of Cell and Molecular Biology, University of Hawaii at Manoa, 1960 East-West Road, Honolulu, HI 96822, USA. E-mail: rcann@hawaii.edu

PUBLIC HEALTH

Diabetes and Disease Surveillance

Where should the line be drawn between good public health practice and government intrusion?

Amy L. Fairchild

If New York City comes to serve as a model, public health surveillance in the United States will take on a radical new form, entailing a reconfiguration of the relation between public health and medicine. Recent events raise questions about the relations between privacy and public health and the obligations and limits of the state in clinical disease management.

In July 2005, New York City Health Commissioner Thomas Frieden described diabetes as "the only major health problem in this country that's getting worse and getting worse quickly" (*1*). To make an impact on the epidemic, the New York City health department put forward a bold proposal for electronic laboratory-based reporting of hemoglobin A1C tests for all city residents (*2*). Commissioner Frieden explained that it was essential for health officials to gain a view of the problem that would facilitate improvements in care and public savings. But more than conventional surveillance was involved. According to the health department, 31% of diabetic patients in commercial managed care and 42% in Medicaid Managed Care in New York State have an A1C of greater than 9%, indicative of poor control. Yet only 10% of people with diabetes are aware of their A1C levels (*3*). The health department thus proposed to use its authority to contact both doctors and patients when A1C levels suggested the need to review the clinical picture or to modify the course of treatment. Although it acknowledged that the proposed surveillance and intervention measure represented an unprecedented step, the department underscored its legal mandate to prevent and control chronic, as well as communicable, disease, citing cancer, dementia, and congenital malformations registries as providing established precedents for diabetes surveillance (*3*).

Never has a government initiated ongoing, systematic diabetes surveillance for an entire population (*4*), although there have been voluntary efforts based on the use of surveys or administrative data, like billing records, to assess prevalence levels. In Israel, for example, a state-funded health service network serving more than a million members uses an internal diabetes registry and computer monitoring system to track patient health status and care (*5*). Sweden's voluntary National Diabetes Registry draws data from participating primary health care and hospital outpatient clinics that have gained the informed consent of eligible patients (*6*). Efforts are being made to construct diabetes registries across Canada and Europe (*7*, *8*). Registries have been pilot tested in the United States (*9*).

CREDIT: JOE SUTLIFF

The author is at the Center for the History and Ethics of Public Health, Mailman School of Public Health, Columbia University, New York, NY 10502, USA. E-mail: alf4@columbia.edu

Although the New York surveillance effort will cover the entire city, the disease management intervention will be piloted first in the South Bronx, a poor, largely African-American and Hispanic-American community with particularly high rates of diabetes. Thus, the measure is also groundbreaking in that public health is responding to what it has taken to be a moral duty to meet the needs of and, indeed, empower populations that have been inadequately served by the existing health care system.

The Surveillance Initiative and Debate

As the city health department began to develop its surveillance scheme, officials consulted with organizations such as the Centers for Disease Control and Prevention, the American Diabetes Association (ADA), major New York City hospitals, clinicians, and patients with diabetes. Remarkably, the county, state, and national medical associations were not consulted. Privacy advocates were also not included in the early discussion.

In response to patient concerns about stigma and discrimination, Frieden argued that the privacy protections for the registry would be "stronger even than [those that] are in place for communicable disease reporting." Confidentiality provisions, the department asserted, would explicitly prohibit data sharing "to make it more difficult for persons with diabetes to obtain or renew a driver's license, health insurance, life insurance, etc." (*3*). Indeed, health officials assured the public that data would not be released to other parties other than the patient's physician.

The leadership of the ADA was quite receptive to surveillance, some viewing it as crucial for patients on the margins of the health care system—those who had no ongoing relationship with health practitioners. The organization, however, ultimately yielded to concerns of their membership and resolved that it could support A1C surveillance only if patients gave their informed consent.

Citizen objections to the surveillance proposal voiced at a public hearing in August 2005 were based on privacy and autonomy concerns. A medical privacy attorney, who explained that she also managed a chronic health condition, commented, "To me diabetes is a very private matter that would become a public matter." One diabetic expressed his "desire as a private citizen to keep my personal medical information private between my physician and myself and nobody else" (*3*).

The proposed incursion on privacy was unacceptable to such opponents because diabetes posed no communicable risk. One patient who testified against the proposal stressed "that as a diabetic I am not a threat to the City's public health, nor do I wish to be treated as one" (*3*). This was echoed by the American Clinical Laboratory Association, which objected that the measure placed burdens on laboratories in the absence of a clear public health "danger" (*10*). One attorney representing health care groups concerned with medical privacy asked, "What gives New York City the right to take my private information from me without my consent and usurp it as their own? Do I pose a bioterrorist threat? No. Is there some type of infectious disease threat? No. Is

there an imminent threat that I will harm someone else? No." (*3*).

Absent the possibility of harm to others, the proposed system was characterized as an unwarranted intrusion into the domain of medicine. As did other ideologically libertarian organizations, the Association of American Physicians and Surgeons objected to lab-based A1C reporting as a "blatant invasion of patient privacy that will cause many patients to avoid testing and treatment." It saw the plan as "replacing individualized medical care with population-based medicine for patients having one of our nation's most significant chronic diseases" (*11*).

Diabetes registration could, argued opponents, only open the door to greater intrusions and drive people away from health care. One patient flatly rejected what he called a "Big Brother approach to diabetes management" (*3*). He shared the concerns of another citizen who asked, "Are you going to demand what I can and can't eat?" (*12*). Only informed consent could mitigate such fears.

Against the claims of the individual were counterpoised those of the common good. That diabetes control, in particular, had been identified as a priority area for quality improvement both in the United States and internationally was reflected in the roster of physicians who advocated for laboratory-based A1C reporting at the public hearing. A mantra of the testimony from the quality improvement community was "what you don't measure you can't improve." Informed consent requirements, supporters agreed, would result in a "grossly inaccurate undercount" of cases and undo the effort (*3*).

Remarkably, none of the other privacy advocates and organizations that had been so engaged in debates about surveillance during the past two decades of heightened concerns spawned by the AIDS epidemic, the federal Privacy Rule, and bioterrorism appeared at the public hearing or made any comment on diabetes surveillance. More surprising was the degree to which physicians—who have been the most ardent opponents of public health reporting efforts for more than a century, particularly when they have involved any kind of interference with patients or their treatment—failed to object. The Medical Society of the State of New York, while noting the new regime, offered no comment on it (*13*). The New York County Medical Society, like the American Medical Association, was unaware of the measure even after it received the imprimatur of law.

The lack of physician involvement may be explained by the routine experience of third-party oversight with the rise of managed care. Whether they bristle at the requirements or not, doctors now view as unremarkable the need to seek prior approval for or review of their clinical decisions. Outside of the private sector, Medicaid and Medicare and other publicly funded health-care initiatives have given birth to governmental agencies that have treated the kind of surveillance involved in quality assurance and improvement as central to the fulfillment of a fiduciary responsibility to taxpayers.

Despite the absence of broad-based opposition, the little that initially arose caused the health department to modify its initial proposal. Although universal laboratory-based A1C would remain mandatory, patients would be given the right to opt out of clinical supervision and intervention on the part of the health department.

> "Never has a government initiated **ongoing, systematic diabetes surveillance** for an entire population."
>
> —Amy Fairchild

Privacy, Social Justice, and the Future

The opening debate over diabetes surveillance and intervention was limited—the health department received fewer than 50 oral and written comments—and appeared to have been brought to a conclusion when the New York City Board of Health unanimously approved the surveillance measure in December 2005. Yet as the pilot clinical intervention program is implemented in the Bronx with the intent of eventually rolling it out to the city as a whole, many issues revolving around how patient privacy and autonomy might limit the uses of surveillance data remain to be resolved. They have been thrown into bold relief by an emergent, fractious debate over proposals to extend the new surveillance paradigm to HIV, where Commissioner Frieden has argued that, by monitoring patient viral loads and drug resistance, the city can ensure that patients receive appropriate treatment (*14*). Some members of the New York City Council, as part of its deliberations over the health department's budget for fiscal year 2007, pressed for the health department to adopt an informed consent model (*15*). The American Civil Liberties Union is currently strategizing about how to weigh in on both the developments in diabetes and HIV surveillance. The time is thus right for an explicit discussion of the relations between public health surveillance, the claims of privacy, and the duty of public health to protect the interests of the most vulnerable.

Public health policy-makers must consider whether diabetes surveillance can really achieve all that it promises. But as important, and ultimately more vexing, are the underlying philosophical and political issues: We must distinguish paternalism in its most pejorative sense of overriding the judgment of individuals about their own health care from the commitment to providing for the most vulnerable in society who do not enjoy the benefit of a consistent, reliable relationship to a single provider or group of practitioners. Viewed from one vantage point, paternalism amounts to an unwarranted denial of privacy and choice; viewed from another, it holds the prospect of enhancing access to appropriate care, representing a commitment to social justice (*16*).

What distinguishes hard paternalism from its softer counterpart is the role of coercion. Despite the bristling rhetoric of those who would oppose diabetes surveillance—and, indeed, of city officials like Mayor Michael Bloomberg who have called for "the forceful application of law … as the principal instrument of our public health policy"—no one would be forced to undergo treatment or lifestyle change. If city officials hold true to their commitment to moving forward with such measures only when "democratically debated and approved," surveillance can promote empowerment (*17*).

References and Notes

1. N. R. Kleinfield, *New York Times*, 9 and 10 January 2006; (www.nytimes.com).
2. B. Brewin, *Gov. Health IT*, 13 July 2005 (http://govhealthit.com/article90741-09-12-05-Print).
3. Public Hearing on Intention to Amend Article 13 of the New York City Health Code, 16 August 2005.
4. R. Stein, *Washington Post*, 11 January 2006, p. A3; (www.washingtonpost.com).
5. M. Spero, A. Kenet, B. Porter, *Eff. Clin. Pract.* **1**,90 (1998).
6. S. Gudbjornsdottir *et al.*, *Diabetes Care* **26**, 1270 (2003).
7. K. Piwernetz, *Int. Clin. Psychopharmacol.* **16** (suppl. 3), S5 (2001).
8. Registration in the Belgian Diabetes Registry; (www.bdronline.be).
9. C. D. MacLean *et al.*, *Clin. Trials* **1**, 534 (2004).
10. Letter from P. M. Kazon, Alston & Bird, LLP, on behalf of the American Clinical Laboratory Association, 16 August 2005; available from (*18*).
11. A. Schlafly, General Council, Association of American Physicians and Surgeons, Inc., letter to New York City Department of Health and Mental Hygiene, 17 August 2005; available from (*18*).
12. Written communication in the Department of Public Health and Hygiene's collection of public responses, available from (*18*).
13. Medical Society of the State of New York, MSSNY e-news, *Wkly. Update New York State Physicians* **5**, 28 (4 August 2005); (www.mssny.org), accessed 15 January 2005.
14. T. R. Frieden, New York City Department of Health and Mental Hygiene, letter to community members, 6 March 2006; available from (*18*).
15. "Mayor's FY '06 Preliminary Management Report" and Agency Oversight Hearings, available from (www.nyccouncil.info/).
16. A. L. Fairchild, R. Bayer, J. Colgrove, D. Wolfe, *Searching Eyes: Privacy, the State, and Disease Surveillance* (Univ. of California Press, Berkeley, CA, in press).
17. D. Cardwell, *New York Times,* 15 June 2006, p. B3.
18. The Diabetes Prevention and Control Program, New York City Department of Health and Mental Hygiene, 2 Lafayette Street, 20th Floor, CN 46, New York, NY 10007, USA.

19. I thank R. Bayer, G. Carrino, and the two anonymous reviewers for their insightful comments and A. Alkon for her research assistance.

10.1126/science.1127610

BIOCHEMISTRY

Viral Glycoproteins and an Evolutionary Conundrum

Glycoproteins from two entirely different viruses share the same novel structure, raising intriguing questions about the evolutionary origins of these and other viruses.

Alasdair C. Steven and Patricia G. Spear

Many animal viruses are surrounded by an envelope—a membrane that consists of a lipid bilayer derived from some host cell compartment, studded with spikes of virally encoded glycoproteins. These proteins are the targets of neutralizing antibodies and are thus of great interest as potential vaccines. From a viral perspective, glycoproteins recognize which cells a given virus may infect by binding to surface receptors and effect cell entry after initial contact has been made. Two reports in this issue on page 217 and 187 (*1*, *2*) broaden the current perspective of glycoprotein structure and the roles of these molecules in virus infection.

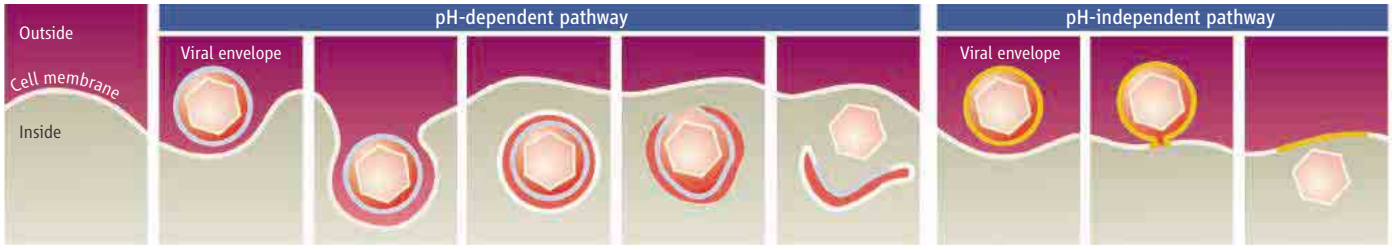

Two pathways whereby enveloped viruses enter cells.

Viruses use at least two pathways to enter host cells (see the first figure). In pH-dependent cell entry (also called receptor-mediated endocytosis), the virus is engulfed in a host cell membrane. After this vesicle has pinched off in the cytoplasm, its interior acidifies; the resulting drop in pH triggers fusion of the vesicle membrane with the viral envelope, releasing the viral genome together with associated proteins into the cytoplasm. In pH-independent or direct entry, the viral envelope fuses directly with the plasma membrane of the infected cell. In either case, fusion is orchestrated by the viral glycoprotein and powered by a radical change in the conformation of this protein.

Viral glycoproteins have three parts: the external ectodomain, which interacts with the host; a transmembrane segment, typically a single α helix; and the internal part, the endodomain. All known glycoproteins that are capable of membrane fusion are trimers for at least part of the infection cycle.

The first ectodomain structure to be determined was that of hemagglutinin (HA) of influenza virus (*3*), which was solved in its prefusion state in 1981. Since then, crystal structures have been determined for several other ectodomains or fragments thereof. The prevailing paradigm is that they fall into two classes (*4*). Class I molecules share the principal features of HA: They are trimers, the ectodomain is at the amino terminus, and they have a triple coiled-coil stem that is reinforced in the postfusion state, giving a distinctive six-helix bundle. Class II molecules, found in flaviviruses and alphaviruses, are initially dimers in icosahedrally ordered lattices, switching to trimers as they swivel outward in a pH-induced transition. Both class I and class II have hydrophobic "fusion" peptides in conserved positions that are initially sequestered and become exposed in this transition.

The two newly determined ectodomain structures (see the second figure) (*1*, *2*) enforce a revision of this picture. A priori there was reason to suspect that glycoprotein B of herpes simplex virus (HSV) and G protein of vesicular stomatitis virus (VSV) might not fit neatly into either class, but there was no reason to anticipate that they would be so similar.

In most respects, the two viruses are poles apart. HSV is a double-stranded DNA virus with a large genome that codes for some 80 genes. The virus particle has a protein shell (capsid) packed with DNA, surrounded by a set of proteins called the tegument, and an envelope derived from an internal compartment of its cell of origin. The envelope contains twelve different glycoproteins, four of which are essential for cell entry (*5*); glycoprotein B contributes only about 5% of the roughly 800 spikes per virion. In contrast, VSV has a single-stranded RNA genome that encodes only five genes. In its bullet-shaped virion (see the second figure, bottom right), the RNA is coated with N protein and coiled into a solenoid. VSV buds through the plasma membrane of its host cell and, in infection, enters through a pH-dependent pathway. Its envelope contains ~400 trimers of a single glycoprotein (called G protein).

The similarity of the structures of HSV glycoprotein B and VSV G protein (see the second figure) leaves little doubt that they have a common evolutionary origin, although no amino acid sequence similarity remains. Both contain at least one "pleckstrin homology" (PH) domain [a large family of cellular proteins implicated in lipid binding and signaling functions (*6*)]. The folds of corresponding domains and the connectivity of the polypeptide chain are essentially the same in both proteins. Both proteins have three-stranded coiled coils at the trimer axis (reminiscent of class I) and a long three-stranded β sheet with a structure similar to that of a class II motif but with different strand topology. Overall, however, they so little resemble the canonical class I and class II molecules as to suggest that they form a third class.

Fascinating as these structures are, there are some loose ends. For example, it remains unclear which functional states have been captured. Heldwein *et al.* tentatively interpret the glycoprotein B structure as a post-fusion state. However, no fusion peptide has previously been identified on glycoprotein B, and the region that corresponds structurally to the fusion peptide of G protein appears suboptimal for membrane insertion without local conformational changes. Roche *et al.* propose that their G protein is in the postfusion state, although the crystals solved were grown at pH 7 and the prefusion state usually predominates at this pH (*7*). Arguments in favor of this assignment are a prominent six-helix bundle and a molecular length some 50% greater than that estimated for the prefusion state.

How are viral genomes compiled, and how do they evolve? These questions are brought to the fore by the unexpected relationship of HSV and VSV, which are so similar in their glycoproteins and so different in almost everything else.

A. C. Steven is at the Laboratory of Structural Biology, National Institute of Arthritis and Musculoskeletal and Skin Diseases, 50 South Drive, Bethesda, MD 20892, USA. E-mail: stevena@mail.nih.gov P. G. Spear is at the Feinberg School of Medicine, Northwestern University, Chicago, IL 60611, USA. E-mail: p-spear@northwestern.edu

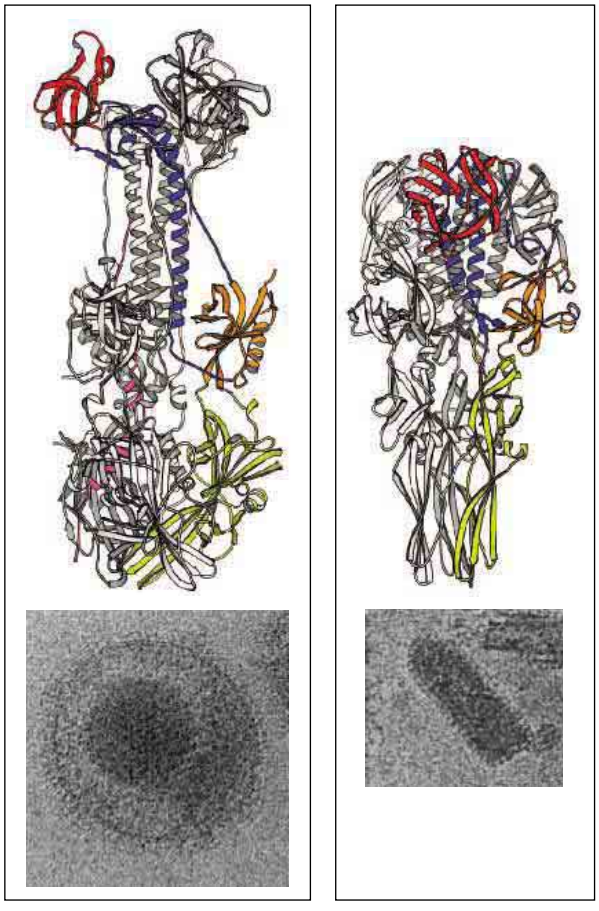

Similarities and differences. (**Top**) Ribbon diagrams of the ectodomain trimers of glycoprotein B of HSV (left) and G protein of VSV (right). On a single subunit, corresponding domains are coded in yellow, orange, blue, and red; the extra domain V on glycoprotein B is pink. In both cases, the other two subunits are white and pale gray. (**Bottom**) Cryoelectron micrographs of HSV (left) and VSV virions (right) in their prefusion state at neutral pH. Note the fringes of glycoproteins at the peripheries. HSV has a diameter of 220 nm; the two viruses are shown at the same magnification.

Maybe two stages are involved in the evolution of viruses: first the primordial establishment of a basic self-replicating gene system, and then elaboration and diversification, partly in response to host evolution, via three mechanisms—cumulative point mutations, gene duplication, and gene capture. All three are implicated in herpesvirus evolution (*8*).

Another equally improbable ancestral relationship of herpesviruses has gradually emerged, linking them to the tailed bacteriophages via their capsid proteins and assembly mechanisms (*9, 10*). For example, the prototypic capsid protein is exemplified in phage HK97 (*11*), whose fold has been retained by HSV while adding a long C-terminal extension (*12*). As these two viruses diverged from their presumptive common ancestor, they acquired specialized cell entry systems in the form of tails (phage) or envelopes (herpesviruses), with glycoprotein B being acquired by HSV at some point. One may further speculate that VSV started as a simple filamentous nucleocapsid that became enveloped, acquiring G protein from the same source as glycoprotein B.

As sometimes happens with major advances, the present observations raise or accentuate as many questions as they answer. In addition to their pertinence to the diversity of membrane fusion mechanisms, the structures of glycoprotein B and G protein presented by Heldwein *et al.* and Roche *et al.* bring some puzzling issues concerning the earliest stages of virus evolution into sharp focus.

References

1. E. E. Heldwein *et al.*, *Science* **313**, 217 (2006).
2. S. Roche, S. Bressanelli, F. A. Rey, Y. Gaudin, *Science* **313**, 187 (2006).
3. J. J. Skehel, D. C. Wiley, *Annu. Rev. Biochem.* **69**, 531 (2000).
4. S. C. Harrison, *Adv. Virus Res.* **64**, 231 (2005).
5. P. G. Spear, *Cell. Microbiol.* **6**, 401 (2004).
6. J. P. DiNitto, T. C. Cronin, D. G. Lambright, *Sci. STKE* **2003**, re16 (2003).
7. S. Roche, Y. Gaudin, *Virology* **297**, 128 (2002).
8. D. J. McGeoch, F. J. Rixon, A. J. Davison, *Virus Res.* **117**, 90 (2006).
9. A. C. Steven, P. G. Spear, in *Structural Biology of Viruses*, W. Chiu, R. M. Burnett, R. L. Garcea, Eds. (Oxford Univ. Press, New York, 1997), pp. 312–351.
10. A. C. Steven, J. B. Heymann, N. Cheng, B. L. Trus, J. F. Conway, *Curr. Opin. Struct. Biol.* **15**, 227 (2005).
11. W. R. Wikoff *et al.*, *Science* **289**, 2129 (2000).
12. M. L. Baker, W. Jiang, F. J. Rixon, W. Chiu, *J. Virol.* **79**, 14967 (2005).

10.1126/science.1129761

ASTRONOMY

The Supernova Origin of Interstellar Dust

Interstellar dust grains are prevalent in the universe, but their origin is unclear. Massive stellar explosions may be the most important source of such dust grains.

Eli Dwek

Interstellar dust grains are prevalent in almost any astrophysical environment, and manifest their existence in many different ways. Yet, the origin and production rate of these grains are still uncertain. On page 196 of this issue, Sugerman and co-workers (*1*) take a hard look at the production of dust in massive supernovae, potentially the most important source of interstellar dust.

Interstellar dust, consisting of small submicrometer-sized grains of predominantly silicate and carbonaceous composition, can be found in the interplanetary medium in our solar system; the gaseous nebulae around stars that have finished the normal hydrogen-burning part of their lives; and the general interstellar medium in normal galaxies like our own, in extremely luminous galaxies undergoing intense star formation or harboring a massive black hole, as well as in very young galaxies at correspondingly large distances from the Milky Way. Even though interstellar dust constitutes less than 1% of the mass of the interstellar medium, it plays a crucial role in regulating its thermal energy balance, in catalyzing chemical reactions in molecular clouds, and in providing the basic building blocks for the formation of planetesimals in protoplanetary disks around main-sequence stars. In our Galaxy, the presence of dust grains is primarily inferred from their interaction with electromagnetic radiation, which gives rise to absorption, scattering, and polarization of Galactic starlight; infrared, submillimeter, and microwave emission, including the broad solid-state emission and absorption features; and the production of scattering halos around x-ray sources. In addition, the existence of dust is also inferred from the depletion of various refractory elements from the gas phase of the interstellar medium. Finally, interstellar dust grains have actually been found in meteorites, with peculiar isotopic

The author is at the Observational Cosmology Laboratory, NASA Goddard Space Flight Center, Greenbelt, MD 20771, USA. E-mail: eli.dwek@nasa.gov

compositions that, like cosmic fingerprints, enable scientists to trace their origins back to the dust factories that produced them.

Following their production, interstellar dust grains are injected into the diffuse interstellar medium where they are subjected to a host of changes. Expanding supernova blast waves sweep up the grains, subjecting them to various destructive processes, including thermal sputtering, vaporizing grain-grain collisions, and collisions that shatter large grains into smaller fragments. As the shocked gas cools, the surviving grains may find themselves inside the relative protective environment of the denser molecular clouds, where chemical reactions, accretion from the gas, and coagulating collisions reconstitute the grains, permeating and coating them with complex refractory organic compounds and more volatile ices. This period of reconstitution is abruptly halted with the formation of massive stars that rip the molecular cloud apart, dispersing its contents into the more hostile environment of the diffuse interstellar medium, where they are again subjected to the destructive forces of interstellar shock waves.

The complex life of interstellar dust grains can be cast in a quantitative chemical evolution model that follows the formative and destructive processes that alter the abundance and composition of the dust (*2*, *3*). The models show that supernova blast waves are very efficient in destroying dust, and that the lifetime of dust is about 600 million years, whereas the rate at which the dust is replenished is longer, about 3 billion years. According to these theoretical calculations, interstellar dust should not exist at all.

The discrepancy stems from our incomplete understanding of the efficiency of the various physical processes that form, destroy, or reconstitute the grains in the interstellar medium. The main interstellar dust factories are Asymptotic Giant Branch (AGB) stars, which produce dust in quiescent mass outflows, and core-collapse supernovae, which return their nucleosynthetic products explosively back to the interstellar medium. In their research article, Sugerman and co-workers address the formation rate of dust in supernovae. If all the refractory elements hurled into space in the explosions condense efficiently in the cooling ejecta, then supernovae are the most important source of interstellar dust. A single supernova can then produce about 1 $M_\odot$ dust (*4*), balancing the amount of dust its shock wave destroys in the interstellar medium ($M_\odot$ is the solar mass).

The potential of supernovae as efficient interstellar dust factories was first raised as far back as the 1960s (*5*, *6*), but gained new interest when Clayton (*7*) suggested that supernova-condensed dust grains were the carriers of various extinct radioactivities in the solar system [see also the recent review by Clayton and Nittler (*8*)]. As grains condense in the cooling supernova ejecta, they preserve the distinct isotopic composition of the elements that precipitated from the gas. The figure shows scanning electron micrographs of presolar grains with highly unusual isotopic composition that pinpoints their origin to the carbon-rich layers of a core-collapse supernova (*8*). The question of how much dust supernovae can produce, and whether their dust production rate can balance the amount of grain destruction in the interstellar medium, remains, however, unanswered by these discoveries.

More recently, the discovery of more than 10^8 $M_\odot$ of dust in young, high-redshift galaxies, when the universe was a mere 800 million years old, offered the first tantalizing evidence that supernovae must be efficient producers of interstellar dust. At this age, most of the AGB progenitor stars have not yet evolved off the main sequence and enriched the interstellar medium with their dust products. The dust observed in high-redshift galaxies must therefore have been produced by supernovae, which return their nucleosynthetic products back to the interstellar medium relatively promptly after their formation. Theoretical estimates show that an average supernova must produce about 0.3 to 1 $M_\odot$ of dust in order to account for the mass of dust seen in these young galaxies, when the effect of grain destruction is taken into account. But how can observers turn these suggestive observations into concrete evidence for the efficient production of dust in supernovae? What is the total amount of dust produced in a single supernova event?

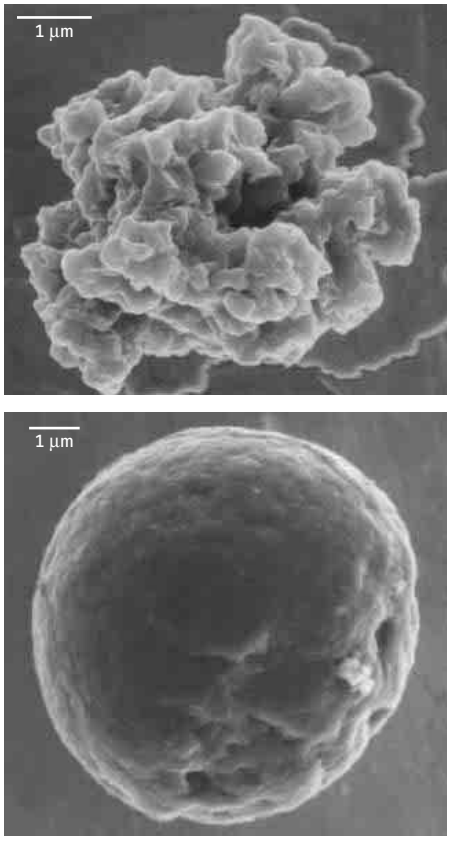

Supernova signatures. Scanning electron micrographs of grains from supernova ejecta. (**Top**) Silicon carbide and (**bottom**) graphite found in meteorites.

CREDIT: SILICON CARBIDE, L. NITTLER/CARNEGIE INSTITUTION OF WASHINGTON; GRAPHITE, S. AMARI/WASHINGTON UNIVERSITY, ST. LOUIS

The production of dust in supernovae leaves several distinct observable signatures that can be used to estimate the total amount of dust that condensed in their ejecta. The kinetic energy of the ejecta is imparted by the explosion, but its radiative output is powered by the radioactive decay of the explosively synthesized ^{56}Ni via the chain ^{56}Ni (with half-life $\tau_{1/2}$ = 5.9 days) → ^{56}Co ($\tau_{1/2}$ = 77.3 days) → ^{56}Fe. The γ-rays emitted in the process are degraded by repeated absorption and emission processes in the ejecta to x-ray and ultimately ultraviolet and optical photons. The dust that forms about a year after the explosion, when the ejecta temperature has dropped to temperatures below (1 to 2) × 10^3 K, absorbs the ambient ultraviolet-optical radiation, reradiating this energy at infrared wavelengths. This process produces two observable effects: (i) the sudden appearance of a mid-infrared thermal emission component and (ii) a concurrent decrease in the ultraviolet-optical light curve of the supernova. The interpretation of these effects is, however, not without ambiguity: The sudden appearance of a thermal infrared emission component could be produced by the delayed arrival (echo) of the infrared emission from any circumstellar dust shell that was heated by the initial ultraviolet-optical outburst of the supernova, and the decrease in the ultraviolet-optical light curve could be caused by the increased transparency of the ejecta to the γ-rays and x-rays. The formation of dust can independently be inferred from the sudden disappearance of refractory elements in the supernova ejecta. Such an effect was observed in SN 1987A, when ~530 days after the explosion, the flux in the [Si I] 1.65-μm line suddenly faded compared to the flux in the neighboring continuum (*9*). However, the interpretation that the depletion of silicon is the result of dust formation is not unique, because a drop in the temperature of the ejecta would have the same observational effect. Finally, the most unambiguous signature of the presence of dust in supernovae is the appearance of an asymmetry in the emission-line profile of elements in the ejecta. The sudden appearance of dust will preferentially obscure the emission from the receding part of the ejecta, reducing the red wings of the profile, and give rise to an asymmetric blue-shifted emission line. These signatures have been observed in SN 1987A, providing conclusive evidence for the formation of dust about 530 days after the explosion. Analysis of the infrared emission was used to derive a total mass of about 10^{-3} $M_\odot$, substantially less than the yield required to account for the amount of dust seen in high-redshift galaxies, or in the general interstellar medium of our Galaxy.

The mass of dust derived from the infrared emission is only a lower limit on the amount of dust that may be present in the supernova

ejecta. In general, such ejecta are clumpy, and a large fraction of the dust may be in these clumps and be too cold to give rise to mid-infrared emission. Motivated to search for the "missing" dust, and aware of the possible pitfalls in the interpretation of supernovae spectra, Sugerman and co-workers searched for several of the dust-formation signatures in the optical to mid-infrared spectrum of the Type II SN 2003gd in the galaxy NGC 628. SN 2003gd is the first supernova with a confirmed red-giant progenitor. This star's mass was between 6 and 12 $M_{\odot}$. Models predict that a star of that mass would eject 0.3 $M_{\odot}$ of refractory elements in a supernova explosion. Collecting data from several epochs, they showed that the optical and mid-infrared spectrum of this supernova showed several telltale signs of dust formation: the appearance of a mid-infrared excess, an increase in the optical extinction, and a blueshifting of the Hα emission line. The manifestation of the three signatures provides very compelling evidence that dust has formed in this supernova about 500 to 680 days after the outburst. They also allow for a comprehensive analysis of the data in order to infer the dust mass. Using a radiative transfer code to simultaneously account for the optical extinction and infrared emission, Sugerman *et al*. conclude that the supernova formed about 0.04 $M_{\odot}$ of dust, about 13% of the mass of dust that could have formed if all refractory elements in the ejecta condensed into dust grains.

The yield of SN 2003gd is the largest found in supernova ejecta thus far, and therefore represents an important milestone in the quest for the origin of interstellar dust. However, the yield still falls short of making supernovae the dominant dust factories required to balance the amount of grain destruction in the interstellar medium, or to account for the mass of dust observed in high-redshift galaxies. If future observations find this to be a typical yield, then scientists will have to take a harder look at other processes that determine the evolution of dust, such as the rate of their destruction in the general interstellar medium, and the accretion rate in molecular clouds.

References and Notes

1. B. E. K. Sugerman *et al*., *Science* **313**, 196 (2006); published online 8 June 2006 (10.1126/science.1128131).
2. E. Dwek, *Astrophys. J.* **501**, 643 (1998).
3. A. P. Jones, in *Astrophysics of Dust, Astron. Soc. Pac. Conf. Series* 309, A. N. Witt, G. C. Clayton, B. T. Draine, Eds. (Astronomical Society of the Pacific, San Francisco, CA, 2004), p. 347.
4. T. Kosaza, H. Hasegawa, K. Nomoto, *Astrophys. J.* **344**, 325 (1989).
5. F. Cernuschi, F. R. Marsicano, I. Kimel, *Ann. Astrophys.* **28**, 860 (1965).
6. F. Hoyle, N. C. Wickramasinghe, *Nature*, **226**, 62 (1970).
7. D. D. Clayton, *Astrophys. J.* **199**, 765 (1975).
8. D. D. Clayton, L. R. Nittler, *Annu. Rev. Astron. Astrophys.* **42**, 39 (2004).
9. L. B. Lucy, I. J. Danziger, C. Gouiffes, P. Bouchet, in *Supernovae. The Tenth Santa Cruz Workshop in Astronomy and Astrophysics*, S. E. Woosley, Ed. (Springer-Verlag, New York, 1991), p. 82.

10. The author acknowledges support from NASA LTSA03.

10.1126/science.1130423

CELL BIOLOGY

Actin Discrimination

Addition of arginine to a type of actin restricts this cytoskeletal protein to the front end of cells where it helps cells to move.

J. Chloë Bulinski

Actin is one of the most abundant proteins in eukaryotic cells. Among its functions, it is one of the main constituents of the cell's dynamic cytoskeletal infrastructure. It is also highly conserved. From birds to humans, each of the six actin isoforms shares 100% amino acid sequence identity across species, with individual gene products showing tissue-specific, rather than species-specific, sequence differences (*1*). Within all species, there is an unprecedented sequence conservation between the β and γ isoforms of actin—they differ in only 4 out of their 373 amino acid residues. It has been widely assumed that these isoforms perform distinct functions in the cytoplasm, as evolutionary conservation of protein sequences has been taken to imply functional importance (*2*). However, data supporting this quite reasonable assumption have been slow in coming. On page 192 of this issue, Karakozova *et al*. (*3*) put to rest the long-standing puzzle of the simultaneous expression of these nearly identical actin isoforms in nonmuscle cells. Chemical modification of β-actin allows cells to discriminate this isoform and restrict its assembly into higher order actin networks that assist in cell motility.

Although the β and γ isoforms of actin are both expressed in varying amounts in the same tissues throughout an organism (*4*), the subcellular localization of the messenger RNAs (mRNAs) that encode them—and therefore, their sites of synthesis—are markedly different. β-actin mRNA is concentrated near the very front, or leading edge, of a moving fibroblast cell (see the figure) (*5*). In contrast, γ-actin mRNA is localized throughout the central region of the cell. This finding suggested that newly synthesized β-actin could perhaps find specific binding partners in the broad, actin-filled extensions at the leading edge that enable cells to move (lamellipodia). β-actin could also preferentially interact there with myosin, actin's force-generating protein partner. In many cases, though, cell size made these notions unsatisfying: Why would

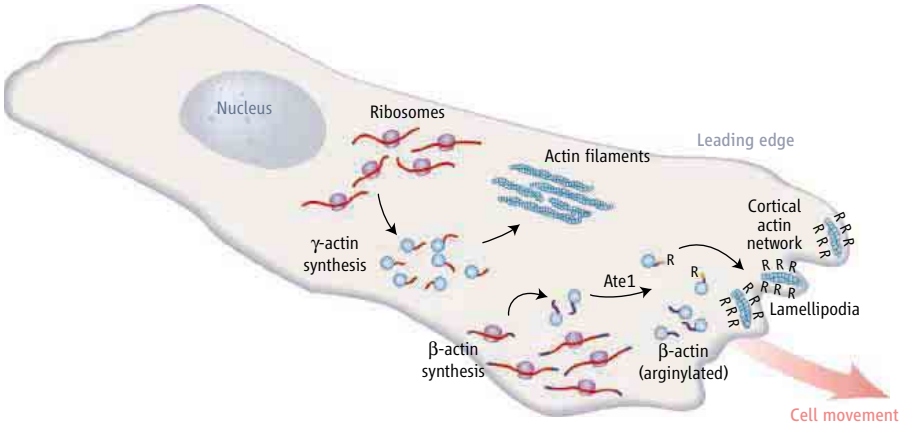

Arginylated actin. β-actin is synthesized at the leading edge of motile fibroblast cells. Some of it is modified with arginine (R). The presence of this bulky moiety on the surface of β-actin filaments restricts its assembly into individual filaments in lamellipodia. In contrast, γ-actin is synthesized in the central region of the cell, is not arginylated, and forms large filament bundles that cannot gain entry to lamellipodia. This segregated synthesis and organization of the two actin isoforms facilitates cell movement.

The author is in the Department of Biological Sciences and the Department of Pathology and Cell Biology, Columbia University, 1212 Amsterdam Avenue, New York, NY 10027–2450, USA. E-mail: jcb4@columbia.edu

these two isoforms not mix, through diffusion, during their residence time in the cytoplasm? After all, their sites of synthesis are, on average, only 1 to 10 μm away from one another, and their turnover time is several days. Besides, even with disparate localizations of β- and γ-actin mRNA synthesis, the conundrum remained: Could the slight differences in their sequences imbue them with differences in function?

The fact that antibodies were generated that specifically recognize the amino-terminal differences between β- and γ-actin (*4*) raised the possibility that cellular proteins could also exhibit isoform-specific recognition. A few glimmers of suggestive evidence were tantalizing. These two isoforms of actin can form biochemically distinct complexes with the actin-binding protein profilin (*6*). The actin-binding protein betaCap73 discriminates between nonmuscle β-actin and muscle α-actin, which are more divergent in amino acid sequence than β- and γ-actin (*7*). However, no binding proteins specific for β- or γ-actin emerged.

That is, until now. Karakozova *et al*. demonstrate recognition of β-actin, but not γ-actin, by the enzyme Ate1 (Arg–tRNA protein transferase 1). Ate1 catalyzes the addition of an arginine residue to the amino terminus of target proteins (*8*), a modification thought to mark proteins for prompt ubiquitination and proteasome-mediated degradation. As a result, the two actin isoforms are not only chemically different, but the authors further demonstrate that the two isoforms take on wholly different organizations of the filamentous actin (f-actin) in which they are enriched. Arginylated β-actin forms single f-actin filaments, whereas γ-actin forms dense parallel bundles of filaments. The authors also reveal that each isoform's filament organization provides a possible mechanism for maintaining the two actins as separate pools. The leading edge can accommodate a fibrous meshwork of actin filaments, such as that generated by individual filaments of β-actin. More interior to the cell, thick filament bundles of γ-actin prevail, as they are too large to invade the leading edge. Strikingly, at least one of the elusive isoform-specific actin-binding proteins turns out to be actin itself. Actin filaments containing arginylated β-actin appear to repel one another instead of forming bundles.

The mystery of the two isoforms was solved, as is often the case, by investigators seemingly unconcerned by the arcane and long-standing question of actin's molecular evolution. Karakozova *et al*. were sleuthing a mystery of their own: Investigating the N-end rule of protein modification, which relates the half-life of a protein to the identity of its amino-terminal residue (*9*), led the authors to engineer mice lacking Ate1. The Ate1-deficient mice died during embryogenesis as a result of cardiovascular defects, suggesting that the enzyme plays a vital role in turnover of its substrate proteins.

Surprisingly, although β-actin was identified as a major substrate of Ate1, its isoform-specific arginylation seems to have nothing to do with shortening its half-life. Instead, arginylation of β-actin at its amino terminus—a domain that projects from β-actin filaments (*10*)—restricts the organization of β-actin filaments, and apparently prolongs the restricted subcellular localization of the β-actin isoform to the lamellipodial region where it was synthesized. The authors demonstrate that preventing arginylation of β-actin in fibroblasts causes inappropriate bundling of β-actin filaments within the cortical actin network (the cytoskeleton that lies just beneath the plasma membrane) at the leading edge, thus contributing to the defects in cell motility.

It is clear from the work of Karakozova *et al*. that posttranslational arginylation of a single protein target can induce global changes on the cellular level. Ate1 is evolutionarily conserved, and there are undoubtedly other substrates whose modification similarly results in altered properties that affect their cellular functions (or their degradation). Does this modification affect the cardiac muscle α-actin isoform, given that the similarity of its amino terminus to β-actin (*2*) makes it a possible substrate for Ate1? Is the modification reversible? The answer to one conundrum has, not surprisingly, given rise to many more questions.

References

1. J. Vandekerckhove, K. Weber, *J. Mol. Biol.* **126**, 783 (1978).
2. J. Das, S. T. Miller, D. L. Stern, *Mol. Biol. Evol.* **21**, 1572 (2004).
3. M. Karakozova *et al*., *Science* **313**, 192 (2006); published online 22 June 2006 (10.1126/science.1129344).
4. C. A. Otey, M. H. Kalnoski, J. C. Bulinski, *J. Cell Biochem.* **34**, 113 (1987).
5. J. B. Lawrence, R. H. Singer, *Cell* **45**, 407 (1986).
6. M. Segura, U. Lindberg, *J. Biol. Chem.* **259**, 3949 (1984).
7. C. B. Shuster, A. Y. Lin, R. Nayak, I. M. Herman, *Cell Motil. Cytoskelet.* **35**, 175 (1996).
8. Y. T. Kwon *et al.*, *Science* **297**, 96 (2002).
9. A. Varshavsky, *Nat. Cell Biol.* **5**, 373 (2003).
10. K. C. Holmes, D. Popp, W. Gebhard, W. Kabsch, *Nature* **347**, 44 (1990).

10.1126/science.1130813

APPLIED PHYSICS

Tunneling Across a Ferroelectric

Evgeny Y. Tsymbal and Hermann Kohlstedt

Spontaneously polarized materials through which electrons pass by tunneling may be used in novel electronic devices and may reveal new basic physics at the nanometer scale.

The phenomenon of electron tunneling has been known since the advent of quantum mechanics, but it continues to enrich our understanding of many fields of physics, as well as offering a route toward useful devices. A tunnel junction consists of two metal electrodes separated by a nanometer-thick insulating barrier layer, as was first discussed by Frenkel in 1930 (*1*). Although forbidden by classical physics, an electron is allowed to traverse a potential barrier that exceeds the electron's energy. The electron therefore has a finite probability of being found on the opposite side of the barrier. A famous example is electron tunneling in superconducting tunnel junctions, discovered by Giaever, that allowed measurement of important properties of superconductors (*2*, *3*). In the 1970s, spin-dependent electron tunneling from ferromagnetic metal electrodes across an amorphous Al_2O_3 film was observed by Tedrow and Meservey (*4*, *5*). The latter discovery led Jullière to propose and demonstrate a magnetic tunnel junction in which the tunneling current depends on the relative magnetization orientation of the two ferromagnetic electrodes (*6*), the phenomenon nowadays known as tunneling (or junction) magnetoresistance (*7*). New kinds of tunnel junctions may be very useful for various technological applications. For example, magnetic tunnel junctions have recently attracted considerable interest due to their potential application in spin-electronic devices such as magnetic field sensors and magnetic random access memories.

The range of insulators for tunnel barriers is not limited to Al_2O_3, however. For example, De Teresa *et al*. studied tunnel junctions with epitaxial perovskite $SrTiO_3$ barriers to demonstrate the decisive role of interfaces in spin-dependent tunneling (*8*). Parkin *et al*. (*9*) and Yuasa *et al*. (*10*) found large magnetoresistance in crystalline tunnel junctions with MgO barriers. Despite the diversity of materials used in tunnel junctions, the common feature of almost all the existing tunnel junctions is that

E. Y. Tsymbal is in the Department of Physics and Astronomy, Nebraska Center for Materials and Nanoscience, University of Nebraska, Lincoln, NE 68588, USA. E-mail: tsymbal@unl.edu H. Kohlstedt is at the Institut für Festkörperforschung, Forschungszentrum Jülich, D-52425 Jülich, Germany, and the Department of Materials Science and Engineering, University of California, Berkeley, CA 94720, USA.

they are based on nonpolar barrier dielectrics.

Yet another concept is the ferroelectric tunnel junction (FTJ), which takes advantage of a ferroelectric as the barrier material. Ferroelectrics possess a spontaneous electric polarization that can be switched by an applied electric field. This adds a new functional property to a tunnel junction, which may lead to novel, yet undiscovered electronic devices based on FTJs. The discovery of ferroelectricity goes back to 1921 (*11*)—approximately when the principles of quantum mechanical electron tunneling were formulated (*1*). The basic idea of a FTJ (called a polar switch at that time) was formulated in 1971 by Esaki *et al*. (*12*).

The concept of a FTJ is illustrated in the figure, which shows the simplified band structure of a tunnel junction with a ferroelectric barrier. Owing to a reversible electric polarization, FTJs are expected to have current-voltage characteristics different from those of conventional tunnel junctions. The electric field–induced polarization reversal of a ferroelectric barrier may have a profound effect on the conductance of a FTJ, leading to resistive switching when the magnitude of the applied field equals that of the coercive field of the ferroelectric. Indeed, the polarization reversal alters the sign of the polarization charges at a barrier-electrode interface. Because of the incomplete screening (see figure, part 1), this reversal changes the depolarization field and hence the potential profile seen by the transport electrons (*13*). Interestingly, recent experimental (*14*) and theoretical (*15*) studies indicate that ionic displacements within the electrodes, in a few atomic monolayers adjacent to the ferroelectric, may affect the screening. The polarization switching alters positions of ions at the interfaces that influence the atomic orbital hybridizations at the interface and hence the transmission probability (see figure, part 2). Finally, the piezoelectricity of a ferroelectric barrier under an applied voltage produces a strain (see figure, part 3) that changes transport characteristics of the barrier such as the barrier width and the attenuation constant (*16*).

A crucial requirement for a FTJ is the existence of ferroelectricity in a nanometer-thick barrier film. Because ferroelectricity is a collective phenomenon, thin films are expected to sustain a spontaneous electric polarization only above some critical thickness. It has long been believed that the critical size for ferroelectricity is a few tens of nanometers. Such a property would render ferroelectrics useless as junction barriers. Triscone and his group in Geneva have, however, indicated that the critical size is much smaller than previously thought (*17*). They demonstrated the presence of a stable polarization in a 4-nm-thick epitaxial film of perovskite ferroelectric $Pb(Zr_{0.2}Ti_{0.8})O_3$. Unambiguous experimental evidence for ferroelectricity in ultrathin epitaxial $PbTiO_3$ films has been obtained by researchers at Argonne National Laboratory, where structural x-ray investigations demonstrated ferroelectric properties in these films down to 1.2 nm thickness (*18*). Theoretical studies based on density functional theory by Ghosez and his group in Liège also support the existence of ferroelectricity in ultrathin perovskite films (*19*). In addition, ferroelectricity has been observed in monomolecular layers of ferroelectric polymers such as polyvinylidene fluoride (PVDF) and its copolymers with trifluoroethylene (TrFE) (*20*). All these findings provide clear experimental and theoretical evidence for the viability of FTJs. As was recently pointed out by Dawber *et al.* (*21*), the idea of tunneling through a ferroelectric film is of considerable interest with respect to the fundamental science as well as device applications.

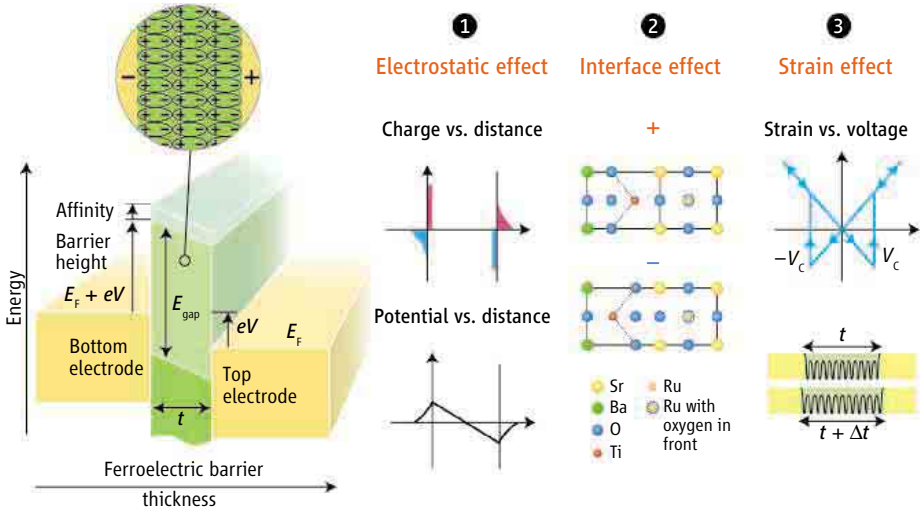

A ferroelectric tunnel junction. Schematic diagram of a tunnel junction, which consists of two electrodes separated by a nanometer-thick ferroelectric barrier layer. (E_{gap} is the energy gap. E_F is the Fermi energy, V is the applied voltage, V_c is the coercive voltage, t is the barrier thickness, and Δt is the thickness variation under an applied field.

Functional properties of FTJs can be extended by replacing normal metal electrodes with a ferromagnetic material that makes the junctions multiferroic (that is, simultaneously ferromagnetic and ferroelectric). The interplay between ferroelectric and ferromagnetic properties in a multiferroic tunnel junction (MFTJ) may affect the electric polarization of the ferroelectric barrier, the electronic and magnetic properties of the interface, and the spin polarization of the tunneling current. Such effects were observed by Ramesh and his group, who discovered the coupling between ferroelectric and ferromagnetic order parameters in $BaTiO_3$-$CoFe_2O_4$ nanostructures (*22*). These results indicate the potential to control the magnetization of the electrodes, and consequently the spin-dependent electronic transport properties of MFTJs, by electric fields.

Another type of MFTJ is feasible in which the barrier itself is made of a material that exhibits multiferroic properties in the bulk, such as $BiFeO_3$ or $BiMnO_3$. The research on bulk multiferroics that simultaneously display ferromagnetism and ferroelectricity began in the 1950s [for a review, see (*23*)]. The interest in such materials was recently renewed by the successful fabrication of multiferroic thin films as well as a deeper theoretical understanding of their properties (*24*). Recently, Gajek *et al*. (*25*) showed that $BiMnO_3$ tunnel barriers may serve as spin filters in magnetic tunnel junctions. This work was further advanced to demonstrate the presence of ferroelectricity in ultrathin $BiMnO_3$ films grown epitaxially on a half-metallic $La_{2/3}Sr_{1/3}MnO_3$ electrode (*26*).

These studies open an avenue for the development of novel electronic devices in which control of the ferroelectric polarization can be achieved by an external magnetic field via the magnetoelectric effect. Magnetoelectric properties of the barrier can also be used to produce an electrically controlled exchange-bias magnetic field (*27*), thereby affecting the resistance of MFTJs (*28*).

A number of obstacles must be overcome before ferroelectric and multiferroic tunnel junctions can be realized. In particular, parasitic effects such as local conductivity and transport via localized states must be eliminated. Also required is a greater understanding of the mechanisms of domain formation, nucleation and switching in nanoscale ferroelectrics, and tunneling transport across polar thin-film dielectrics. Achievements in the field of complex oxide epitaxy and ultrathin ferroelectric polymers, in addition to newly developed nanoscale characterization techniques, promise that all these problems can be solved and that the realization of FTJs is just a matter of time. The diversity of interesting physical phenomena that control the characteristics of these tunnel junctions and their multifunctional properties makes the research in this field challenging and promising.

References and Notes

1. J. Frenkel, *Phys. Rev.* **36**, 1604 (1930).
2. I. Giaever, *Phys. Rev. Lett.* **5**, 147 (1960).
3. I. Giaever, *Phys. Rev. Lett.* **5**, 464 (1960).
4. P. M. Tedrow, R. Meservey, *Phys. Rev. Lett.* **26**, 192 (1971).
5. P. M. Tedrow, R. Meservey, *Phys. Rev. B* **7**, 318 (1973).
6. M. Jullière, *Phys. Lett. A* **54**, 225 (1975).
7. J. S. Moodera *et al.*, *Phys. Rev. Lett.* **74**, 3273 (1995).
8. J. M. De Teresa *et al.*, *Science* **286**, 507 (1999).
9. S. S. P. Parkin *et al.*, *Nat. Mater.* **3**, 862 (2004).
10. S. Yuasa *et al.*, *Nat. Mater.* **3**, 868 (2004).
11. J. Valasek, *Phys. Rev.* **17**, 475 (1921).
12. L. Esaki, R. B. Laibowitz, P. J. Stiles, *IBM Tech. Discl. Bull.* **13**, 2161 (1971).
13. M. Ye. Zhuravlev *et al.*, *Phys. Rev. Lett.* **94**, 246802 (2005).
14. D. D. Fong *et al.*, *Phys. Rev. B* **71**, 144112 (2005).
15. G. Gerra *et al.*, *Phys. Rev. Lett*. **96**, 107603 (2006).
16. H. Kohlstedt *et al.*, *Phys. Rev. B* **72**, 125341 (2005).
17. T. Tybell, C. H. Ahn, J.-M. Triscone, *Appl. Phys. Lett.* **75**, 856 (1999).
18. D. D. Fong *et al.*, *Science* **304**, 1650 (2004).
19. J. Junquera, Ph. Ghosez, *Nature* **422**, 506 (2003).
20. A. V. Bune *et al.*, *Nature* **391**, 874 (1998).
21. M. Dawber, K. M. Rabe, J. F. Scott, *Rev. Mod. Phys.* **77**, 1083 (2005).
22. H. Zheng *et al.*, *Science* **303**, 661 (2004).
23. G. A. Smolenskii, I. E. Chups, *Sov. Phys. Usp.* **25**, 475 (1982).
24. N. A. Spaldin, M. Fiebig, *Science* **309**, 391 (2005).
25. M. Gajek *at al.*, *Phys. Rev. B* **72**, 020406 (2005).
26. H. Béa *et al.*, *Appl. Phys. Lett.* **88**, 062502 (2006).
27. P. Borisov *et al.*, *Phys. Rev. Lett.* **94**, 117203 (2005).
28. C. Binek, B. Doudin, *J. Phys. Condens. Matter* **17**, L39 (2005).

29. E.Y.T. thanks NSF (grants MRSEC DMR-0213808 and DMR-0203359) and the Nebraska Research Initiative for support of the research relevant to the subject of this article. H.K. thanks the Volkswagen-Stiftung under contract I/77737 and the Deutsche Forschungsgemeinschaft for financial support.

10.1126/science.1126230

SIGNAL TRANSDUCTION

Calcium Entry Signals—Trickles and Torrents

Two ion channels on the surface of cells control calcium influx, which is critical for cell signaling. One channel allows transient calcium entry and the other slower, more sustained flow.

Donald L. Gill, Maria A. Spassova, Jonathan Soboloff

The divalent cation calcium (Ca^{2+}) acts as an intracellular signal that controls a vast array of cellular processes that occur rapidly (such as secretory and contractile events) as well as on longer time scales (transcription, growth, and cell division) (*1*). In response to certain extracellular stimuli, the concentration of intracellular calcium rises, endures, and falls in patterns that affect specific signaling pathways. Ca^{2+} can enter the cytoplasm from two locations—outside the cell and from the endoplasmic reticulum (ER), an organelle that serves as the cell's calcium storage facility. Understanding how this influx of Ca^{2+} is managed has centered on characterizing the facilitating ion channels. As reported by Dellis *et al.* (*2*) on page 229 of this issue and in other recent work (*3*–*7*), two very distinct plasma membrane channels mediate Ca^{2+} entry. And a fascinating gating mechanism of one of these channels represents a new paradigm in intraorganelle communication.

Upon activation by ligands, certain cell surface receptors trigger phospholipase C enzymes to generate inositol 1,4,5-trisphosphate (IP_3). Considered a "second messenger" in transducing the signal elicited by the stimulus, IP_3 interacts with IP_3 receptors situated in the ER membrane. IP_3 receptors are well-established channels that permit the rapid release of Ca^{2+} from the ER, giving a fast initial rise in cytoplasmic Ca^{2+} concentration (*8*). But Ca^{2+} signals induced by cell surface receptors also have a second component: After rapid release of Ca^{2+}, a slower and more enduring entry of Ca^{2+} into the cytoplasm occurs, providing longer term Ca^{2+} signals (*9*). This latter Ca^{2+} entry process has been a mechanistic mystery. However, its understanding has received an enormous boost. Dellis *et al.* now show that one of the channels situated in the plasma membrane that facilitates this slow Ca^{2+} entry is the IP_3 receptor itself and its additional presence at the cell surface provides a remarkable new twist to understanding Ca^{2+} signaling events. Another cell surface Ca^{2+} channel that allows a slower influx is a hitherto unknown protein named Orai1 (or CRACM1). It is a tetraspanning channel whose gating involves the sensing of Ca^{2+} inside the ER (*3*–*7*).

The IP_3 receptor is a large-conductance, somewhat nonselective, cation channel whose opening is gated by specific binding of IP_3 molecules (*8*). Whereas its function to release Ca^{2+} from the ER is clearly established, its presence in the plasma membrane has long been the subject of speculation. Dellis *et al.* provide the first clear electrophysiological evidence for its operation in the plasma membrane. The authors engineered subtle mutations in the pore of the channel to pinpoint conductance across the plasma membrane. They also introduced a binding site for α-bungarotoxin, allowing pharmacological manipulation of channel activity from outside the cell. Although the vast majority of IP_3 receptors (>99%) are indeed within the ER, the new study reveals that cells allow just one or two of these channels to operate in the plasma membrane. Even huge overexpression of the IP_3 receptor does not increase appearance in the plasma membrane. This finding suggests that cells can "count" and accurately maintain just a very few IP_3 receptors at the cell surface. Strangely, although IP_3 is generated at the plasma membrane, the activation of IP_3 recep-

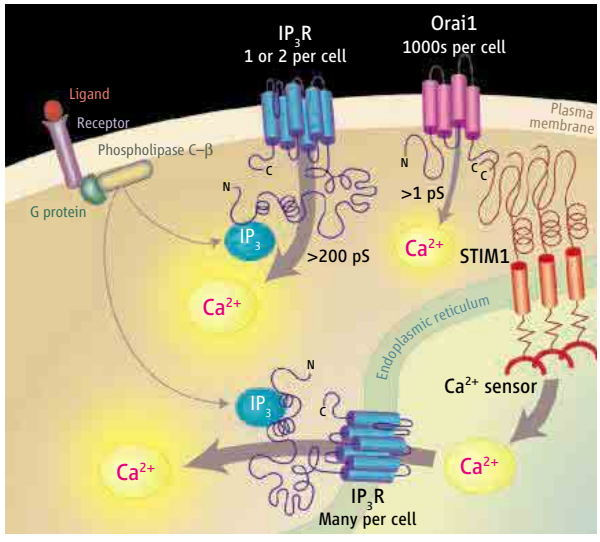

Receptor-mediated Ca^{2+} entry pathways. Binding of ligand to receptor at the cell surface activates phospholipase C–β via a G protein, producing IP_3 in the cytosol. IP_3 activates IP_3 receptors (IP_3R) in the endoplasmic reticulum (ER) and in the plasma membrane. Ca^{2+} release from the ER causes the Ca^{2+}-sensing STIM1 protein to aggregate in areas close to the plasma membrane and to interact with Orai1 in the plasma membrane, which is believed to be the store-operated channel. Many thousands of Orai1 channels are distributed across the plasma membrane, allowing substantial Ca^{2+} to "trickle" in all around the cell. In contrast, a few cell surface IP_3 receptors may allow Ca^{2+} to enter as a "torrent" at discrete points on the plasma membrane

The authors are in the Department of Biochemistry and Molecular Biology, University of Maryland School of Medicine, Baltimore, MD 21201, USA. E-mail: dgill@umaryland.edu

tors in the plasma membrane is slow. Application of intracellular IP_3 takes several minutes to activate plasma membrane IP_3 receptors; yet activation of Ca^{2+} release through ER IP_3 receptors is within a few seconds. Could this reflect a time-dependent insertion of IP_3 receptors into the plasma membrane or perhaps their time-dependent activation? Application of adenophostin, a nonmetabolizable, high-affinity IP_3 receptor agonist, gave a much faster effect, suggesting instead that some change in the metabolism of IP_3 occurs in the vicinity of the plasma membrane IP_3 receptors. This implies local regulation of IP_3 concentrations to control opening of these channels.

Ca^{2+} entry at the cell surface mediated by IP_3 receptors contrasts dramatically with another Ca^{2+} entry process occurring almost universally among cell types, known as "store-operated" Ca^{2+} entry (*9, 10*). Ca^{2+} stores have a finite release capacity, and activation of ER IP_3 receptors causes rapid Ca^{2+} store depletion. The decrease in luminal Ca^{2+} triggers store-operated channels (SOCs) present in the plasma membrane, which mediate the exceedingly Ca^{2+}-selective Ca^{2+} release–activated Ca^{2+} current (I_{CRAC}) observable in many cell types (*10*). Yet the identity of these channels, and the coupling process between the ER and the plasma membrane that triggers their activation, have eluded understanding. Novel high-throughput screens recently identified the single transmembrane-spanning ER protein STIM1 as the likely sensor of Ca^{2+} in the ER by virtue of its luminal-facing EF-hand domain, which binds to Ca^{2+} (*11–15*).

But STIM1 is not the only essential protein. New studies show that the Orai1 protein is also crucial for SOC activation (*3*, *4*, *7*). This revelation came from a combination of elegant studies including genome-wide RNA interference screening and modified linkage analysis identifying an Orai1 mutation as the cause of severe combined immune deficiency. T cells of the immune system in such patients have ablated Ca^{2+} entry which can be restored by Orai1 expression (*3*). Dramatically, coexpression of both Orai1 and STIM1 in any cell reconstitutes store-dependent coupling and I_{CRAC} function that is almost indistinguishable from that in normal T cells (*5–7*). Orai1 is expressed in the plasma membrane, and it seems certain to constitute the channel moiety itself. The structure of Orai1 does not appear to be a "typical" cation channel. For example, the IP_3 receptor has six transmembrane domains with a pore-forming loop between transmembrane segments 5 and 6, and exists as a tetramer. But the function of SOCs is itself rather unusual – highly inwardly rectifying, non–voltage-gated, and with a very small but exceedingly selective Ca^{2+} conductance. So the atypical structure of Orai1 may not be so surprising.

Whereas the IP_3 receptor and Orai1 both mediate receptor-induced Ca^{2+}entry signals, the function, appearance, and physiological significance of the two proteins provide some sharp distinctions (see the figure). The IP_3 receptor has a large single-channel conductance (in the 200-pS range under normal physiological conditions), and although its relative ion nonselectivity would predominantly facilitate Na^+ ion movement, substantial Ca^{2+} entry is predicted even though cells express only one or two in the plasma membrane (*2*). In contrast, Orai1-mediated I_{CRAC} has an estimated single-channel conductance at or below 1 pS (*16*). However, the high Ca^{2+} selectivity of Orai1 and the likely presence of thousands of these channels per cell predict an even larger entry of Ca^{2+} than through the IP_3 receptors. The scenario described by Dellis *et al.* is a torrent of Ca^{2+} through just one or two isolated IP_3 receptors in the plasma membrane, as opposed to a more evenly distributed trickle of Ca^{2+} through the many Orai1 channels across the cell surface. This may have profound consequences for Ca^{2+} signaling events in cells.

Certainly, uncovering the molecular identity of the Ca^{2+} entry machinery at the cell surface has crucial importance for pharmacological targeting to control cellular signaling. It would be premature to generalize about the universality of plasma membrane IP_3 receptors, because so far their function has been observed only in B cells of the immune system (*2*). However, the function and wide cellular distribution of the three mammalian *Orai* gene products and their ancillary coupling machinery, including the two mammalian STIM proteins, indicates that this process may have broad functional significance in the mediation of Ca^{2+} signal generation in many cell types.

References

1. M. J. Berridge, M. D. Bootman, H. L. Roderick, *Nat. Rev. Mol. Cell Biol.* **4**, 517 (2003).
2. O. Dellis *et al.*, *Science* **313**, 229 (2006).
3. S. Feske *et al.*, *Nature* **441**, 179 (2006).
4. M. Vig *et al.*, *Science* **312**, 1220 (2006); published online 27 April 2006 (10.1126/science.1127883).
5. C. Peinelt *et al.*, *Nat. Cell Biol.*, published online 30 May 2006 (10.1038/ncb1435).
6. J. Soboloff *et al.*, *J. Biol. Chem.*, published online 9 June 2006 (10.1074/jbc.C600126200).
7. S. L. Zhang *et al.*, *Proc. Natl. Acad. Sci. U.S.A.* **103**, 9357 (2006).
8. R. L. Patterson, D. Boehning, S. H. Snyder, *Annu. Rev. Biochem.* **73**, 437 (2004).
9. K. Venkatachalam, D. B. van Rossum, R. L. Patterson, H. T. Ma, D. L. Gill, *Nat. Cell Biol.* **4**, E263 (2002).
10. A. B. Parekh, J. W. Putney Jr., *Physiol. Rev.* **85**, 757 (2005).
11. J. Roos *et al.*, *J. Cell Biol.* **169**, 435 (2005).
12. J. Liou *et al.*, *Curr. Biol.* **15**, 1235 (2005).
13. S. L. Zhang *et al.*, *Nature* **437**, 902 (2005).
14. M. A. Spassova *et al.*, *Proc. Natl. Acad. Sci. U.S.A.* **103**, 4040 (2006).
15. J. Soboloff *et al.*, *Curr. Biol.*, in press.
16. M. Prakriya, R. S. Lewis, *J. Gen. Physiol.*, in press.

10.1126/science.1130811

PHYSICS

Controlling Friction

Robert W. Carpick

Nanometer-scale friction can be altered electronically or mechanically. The results may lead to more reliable nanometer-scale devices.

According to Plato, necessity is the mother of invention. Scientists and engineers working on small-scale mechanical devices may be relieved to find this idea starting to take effect at the nanometer scale. There is a critical need to control the effect of friction at this scale, and in this issue, two groups (*1*, *2*) provide independent and precise means of doing just that.

Control of tribological interactions—friction, adhesion, and wear—is desirable at all length scales. Estimated annual expenses attributable to friction and wear across the U.S. economy run up to hundreds of billions of dollars (*3*). But researchers working on small-scale devices such as micro- and nanoelectromechanical systems (MEMS/NEMS) are not even counting dollars yet. Devices with sliding interfaces, such as certain actuators, positioning devices, and microgears, cannot be commercialized because the surfaces of these devices wear out and seize too rapidly (*4*).

In these small-scale devices, many or even most atoms reside at surface and interface sites (rather than in the bulk of the material). Surface forces such as friction and adhesion therefore dominate over the available actuation and restoring forces; furthermore, the high friction and adhesiveness of silicon (a common MEMS material), coupled with its brittle nature, lead to high rates of wear and debris generation. Surface treatments, such as self-assembled monolayers, can overcome the adhesion problem and reduce friction, but wear persists, and device lifetimes and reliability remain inadequate (*5*).

On page 207 of this issue, Socoliuc *et al.* (*1*) show that friction can be reduced more than 100-fold in a nanometer-scale contact by

The author is in the Department of Engineering Physics, University of Wisconsin, Madison, WI 53706, USA. E-mail: carpick@engr.wisc.edu

applying a small vibrating normal force to the interface. The authors formed a contact between the silicon tip of an atomic force microscope (AFM) cantilever and atomically flat alkali halide surfaces under ultrahigh-vacuum conditions. When the sample is displaced laterally with respect to the cantilever, the tip sticks and slips in a series of instabilities. The effect, known as atomic-scale stick-slip friction (*6*), can be thought of as an atomic-scale analog to the macroscopic stick-slip effect responsible for squeaking door hinges and bowed violin strings.

The atomic-scale instability occurs because high static friction leads to a buildup of energy during sliding in the springlike elastic compliances of the system. This energy is partially stored in the elastic deformation of the cantilever, but some of it builds up at and around the interface. This elastic energy is suddenly released when the magnitude of the negative lateral force gradient in the sliding direction exceeds the combined lateral stiffness of the cantilever and the contact. Because the lateral interaction force is periodic by virtue of the symmetry of the crystal surfaces, the stick-slip behavior repeats once every lattice site, creating lateral-force images that match the lattice periodicity of the sample (see the figure). This leads to the buildup and dissipation of substantial amounts of energy.

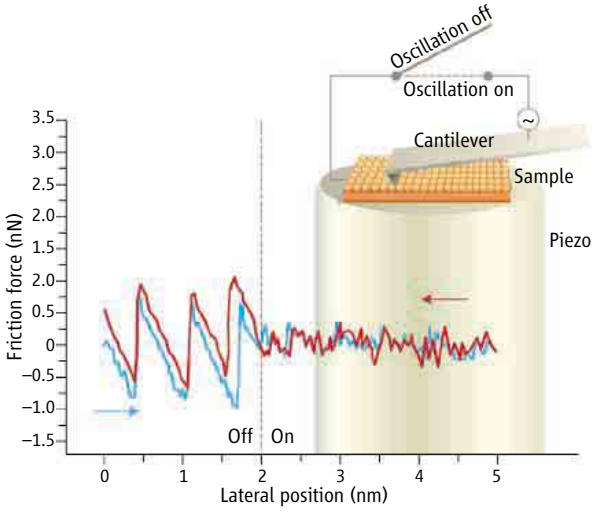

A method for reducing friction. Friction in a nanometer-scale contact, in the form of atomic-scale stick-slip instabilities (**left**), is dramatically reduced (**right**) when a modulation in the normal force is applied to the interface (sketch, top right).

This effect has been known for years (*7*) and was anticipated much earlier (*8*, *9*). What is new here is that the instability can be completely suppressed, and energy dissipation dramatically lowered, by cleverly navigating the available energy landscape. Socoliuc *et al*. have previously shown that the instability is suppressed when very small (tensile) normal forces are applied (*10*). This is because under tension, the separation between the tip and the sample is slightly increased even though they remain in contact. Consequently, the corrugation of the interfacial potential energy is reduced. The gentler slopes of this landscape ensure that the magnitude of the negative lateral force gradient never exceeds the lateral system stiffness, and hence, no instability occurs.

However, working at such small forces is not always practical. So instead, Socoliuc *et al.* have now used a range of higher (compressive) normal forces (*1*). A sinusoidal modulation of this normal force about its average value leads to brief periods where the gentler energy landscape is found; the tip takes advantage of this and smoothly slides over the next position in the laterally periodic system.

The process can be thought of in terms of a modified version of the story of Sisyphus, the tragic figure of Greek mythology who was condemned to push a rock up a mountainside, only to have it roll back to the bottom over and over again. Imagine that Sisyphus succeeded in pushing his rock to the top of the mountain. It would then begin to roll down the other side. Because the mountain is steep, he would not be able to keep up, and the rock would crash down to the next valley below. Sisyphus would then have to push the rock up the next mountain. This is like the stick-slip instability: Tremendous potential energy is built up (in the AFM, it is the elastic potential energy in the cantilever and contact; with Sisyphus, it is gravitational potential energy). Then, just as the landscape becomes easier to navigate at the top of the mountain, the energy is rapidly released and dissipated as the rock rolls down the steep downward slope. If the mountains were not so tall, Sisyphus could push the rock to the top of each one more easily, requiring less energy. Once at the top, he would be strong enough to hold on to the rock and control it as he continues down the gentle hill.

What Socoliuc *et al*. have done is to make the "mountain," that is, the corrugation of the lateral potential energy, less tall for brief periods of time. Because the corrugation is reduced at lower normal forces, oscillating the normal force will lead to short time spans when the tip can move forward in a stable manner without the stick-slip instability. The lateral force to slide, with the modulation turned on, is therefore reduced compared to the nonmodulated case by at least a factor of 100 (see the figure).

It is not clear whether the total amount of energy required to slide is reduced (because some energy is required to drive the cantilever), but smoother sliding unquestionably occurs. If this effect can be put to use in MEMS and NEMS devices with contacting interfaces, for example, by using actuators that are integrated into the devices, it could enable these devices to function reliably.

On page 186 of this issue, Park *et al.* (*2*) report another method for controlling friction in a nanometer-scale contact: the use of electric fields. The authors worked with a silicon sample with well-defined regions of n- and p-doping. The differently doped regions had distinct friction forces even when no bias voltage was applied between the sample and a conducting AFM tip. When a bias of +4 V was applied to the sample, an increase in friction by up to a factor of 2 was observed in the p-doped region. The mechanism for this increase is not clear, but estimates of the contribution due to electronic friction (the drag force that results when charge carriers move in an electric field) are far too low to explain the result.

Biases of a few volts can be easily applied in MEMS and NEMS devices. Thus, this also appears to be a feasible method to control friction. The frictional control knob in this case goes up and not down, but that, too, could be of use. Sliding MEMS actuators that depend on alternately holding and releasing interfaces have the potential for extremely high positional precision, but are limited by the ability to exert high enough friction to hold the device steady (*11*).

Both studies provide beautiful and enticing scientific insights into the origin of atomic-scale friction. At the Gordon Research Conference on Tribology (*12*), the conference chairman, J. Thomas Dickinson, commented that "these fascinating studies are examples of how nanotribology research is maturing from just investigating friction to now providing prescriptions to control it." Plato might be pleased to know that the discoveries were driven not only by necessity, but also by tremendous scientific curiosity, creativity, and skill.

References

1. A. Socoliuc *et al*., *Science* **313**, 207 (2006).
2. J. Y. Park, D. F. Ogletree, P. A. Thiel, M. Salmeron, *Science* **313**, 186 (2006).
3. H. P. Jost, *Wear* **136**, 1 (1990).
4. M. P. de Boer, T. M. Mayer, *MRS Bull.* **26**, 302 (2001).
5. E. E. Flater, A. D. Corwin, M. P. de Boer, R. W. Carpick, *Wear* **260**, 580 (2006).
6. S. Morita, S. Fujisawa, Y. Sugawara, *Surf. Sci. Rep.* **23**, 3 (1996).
7. C. M. Mate, G. M. McClelland, R. Erlandsson, S. Chiang, *Phys. Rev. Lett*. **59**, 1942 (1987).
8. L. Prandtl, Z. Angew, *Math. Mech*. **8**, 85 (1928).
9. G. A. Tomlinson, *Philos. Mag*. **7**, 905 (1929).
10. A. Socoliuc, R. Bennewitz, E. Gnecco, E. Meyer, *Phys. Rev. Lett*. **92**, 134301-1 (2004).
11. M. P. de Boer*et al.*, *J. Microelectromechanical Systems* **13**, 63 (2004).
12. The Gordon Research Conference on Tribology was held at Colby College, Waterville, ME, 18 to 23 June 2006; see www.grc.uri.edu/programs/2006/tribo.htm.

10.1126/science.1130420

Electronic Control of Friction in Silicon pn Junctions

Jeong Young Park,[1] D. F. Ogletree,[1] P. A. Thiel,[2] M. Salmeron[1]*

The nature of the fundamental processes that give rise to friction between sliding bodies in close proximity is a long standing question in tribology, both theoretically and experimentally (*1*, *2*). Ultimately energy is dissipated by conversion of kinetic energy of the moving bodies into lattice vibrations (heat). The vibrations of the surface atoms are damped by energy transfer to bulk phonon modes and in metals also by electronic excitations. Although excitation of electron-hole pairs has been invoked as a mechanism of frictional energy dissipation (*1*, *3*–*5*), the importance of this dissipation channel has not been ascertained experimentally in contacts between two solids.

Semiconductors offer the interesting possibility to test the effect of free charge carriers in the energy dissipation balance, because it is possible to reversibly change their density over many orders of magnitude. To test this idea, we used an atomic force microscopy (AFM) with a conductive TiN tip sliding on a silicon sample that was patterned with p and n regions of different doping levels (Fig. 1A). Friction was monitored as a function of carrier accumulation or depletion, which was controlled by the application of a voltage to the tip. Although the p and the n regions have different electronic properties, their chemical nature and structure is the same because of the oxide layer (~0.4 nm thick) that covers both regions. This layer also prevents Fermi-level pinning, which could obscure dopant-dependent contrast in the conductance (*6*). A remarkable dependence of the friction force on carrier concentration was found on doped silicon substrates. Charge depletion or accumulation resulted in a substantial difference in friction force.

The array of p-type stripes (concentration of 10^{18} cm^{-3}) was fabricated by B implantation at 190 keV into an n-type Si(100) substrate with a low dopant concentration of 1.6×10^{14} cm^{-3}. The normal force was kept constant during imaging while current and friction force were simultaneously recorded (*5*). No wear traces were observed in repeated high-resolution images, and the friction and adhesion measurements were reproducible.

When a voltage is applied between sample and tip, band bending changes the electrical character of the p and the n regions in opposite directions. When a positive voltage is applied to a p-type semiconductor, band bending causes accumulation of majority carriers (holes) near the semiconducting surface. When a negative voltage is applied, carriers are depleted near the surface. At a sample bias of +4 V, the highly doped p region is forward-biased and in strong accumulation, leading to a high carrier concentration near the surface. The n region is reverse-biased, causing depletion or weak inversion. As a result, the current was high in the p region (~50 μA) and low in the n region (~5 μA) (*7*). Friction was substantially higher in the p region than in the n region. Interestingly, no notable variation of friction force was observed between n and p regions at negative bias (*7*). Figure 1B shows a plot of the friction force versus load at +4 V sample bias. The line through the friction data is a fit to the Derjaguin-Müller-Toporov (DMT) contact model. Although the agreement with the DMT curve is very good in the n region, the p region shows a substantial "excess" friction. This difference is only observed for positive bias > +2 V. The Fig. 1B inset shows that the change in tip-sample pull-off force with bias increases in proportion to V^2 as expected, with no significant difference between p and n regions.

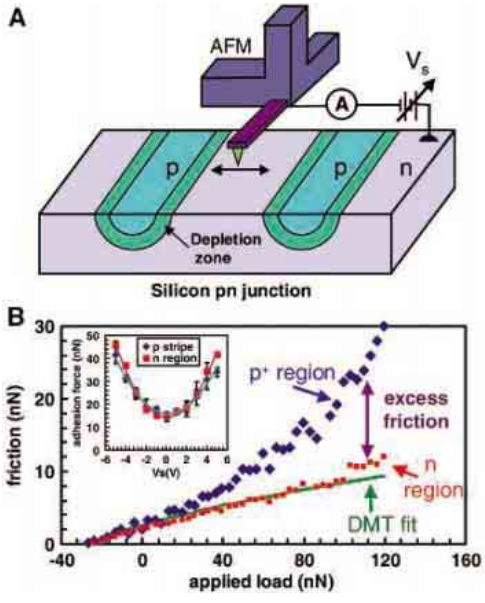

Fig. 1. (**A**) Schematic of AFM measurements on a silicon pn junction device. (**B**) Plot of friction force as a function of applied load at +4V sample bias. The scanning speed was 5 μm/s. (Inset) The pull-off force as a function of sample bias. The error scales represent the standard deviation from five independent measurements.

Although the excess friction in the p region during accumulation increases significantly with contact stress, it is not related to wear. It is not proportional to tip-sample current either, which excludes chemical effects as the potential origin. Previous calculations of electronic friction do not include the effects of localized strain under the AFM tip at ~GPa levels, and this may play a role in excess friction, perhaps by creating electronic surface states that are charged and then discharge upon release of the stress. In the pressure range of GPa, the band gap decreases, which in our geometry should produce an elastically induced quantum dot under the tip (*8*). This should lead to a substantial enhancement of electron-hole recombination, with the energy emitted in the form of phonons. Another possibility worth exploring is the enhancement of dislocation mobility (*9*) due to the increase in charge carrier density. The ability to modulate friction through control of doping levels and electric fields might have interesting technical applications for microelectromechanical (MEMS) devices and in the motion of nano-objects in patterned semiconductor substrates.

References and Notes

1. B. N. J. Persson, *Sliding Friction: Physical Principles and Applications* (Springer-Verlag, Berlin, 1998).
2. E. Gnecco, R. Bennewitz, T. Gyalog, E. Meyer, *J. Phys. Condens. Matter* **13**, R619 (2001).
3. G. Witte *et al.*, *Phys. Rev. Lett.* **80**, 121 (1998).
4. A. Dayo, W. Alnasrallah, J. Krim, *Phys. Rev. Lett.* **80**, 1690 (1998).
5. J. Y. Park *et al.*, *Science* **309**, 1354 (2005).
6. J. Y. Park, R. J. Phaneuf, D. F. Ogletree, M. Salmeron, *Appl. Phys. Lett.* **86**, 172105 (2005).
7. Materials and methods are available on *Science* Online.
8. X. J. Zhu, S. Fahy, S. G. Louie, *Phys. Rev.* **B39**, 7840 (1989).
9. J. R. Patel, L. R. Testardi, P. E. Freeland, *Phys. Rev.* **B13**, 3548 (1976).

10. This work was supported by the Director, Office of Energy Research, Office of Basic Energy Sciences, Materials Sciences Division, of the U.S. Department of Energy through the Lawrence Berkeley National Laboratory, contract no. DE-AC02-05CH11231, and through the Ames Laboratory, contract no. W-405-Eng-82. We thank R. J. Phaneuf (University of Maryland) for kindly providing the patterned Si samples.

Supporting Online Material

www.sciencemag.org/cgi/content/full/313/5784/186/DC1
Materials and Methods
SOM Text
Fig. S1
References and Notes

17 January 2006; accepted 15 May 2006
10.1126/science.1125017

[1]Materials Sciences Division, Lawrence Berkeley National Laboratory, University of California, Berkeley, CA 94720, USA. [2]Ames Laboratory and Department of Chemistry and Department of Materials Science and Engineering, Iowa State University, Ames, IA 50011, USA.

*To whom correspondence should be addressed. E-mail: mbsalmeron@lbl.gov

Crystal Structure of the Low-pH Form of the Vesicular Stomatitis Virus Glycoprotein G

Stéphane Roche,* Stéphane Bressanelli,* Félix A. Rey,† Yves Gaudin‡

The vesicular stomatitis virus has an atypical membrane fusion glycoprotein (G) exhibiting a pH-dependent equilibrium between two forms at the virus surface. Membrane fusion is triggered during the transition from the high- to low-pH form. The structure of G in its low-pH form shows the classic hairpin conformation observed in all other fusion proteins in their postfusion conformation, in spite of a novel fold combining features of fusion proteins from classes I and II. The structure provides a framework for understanding the reversibility of the G conformational change. Unexpectedly, G is homologous to gB of herpesviruses, which raises important questions on viral evolution.

Entry of enveloped viruses into host cells requires fusion of the viral envelope with a cellular membrane. This step is mediated by viral glycoproteins that undergo a dramatic fusogenic structural rearrangement induced by a specific trigger (e.g., low pH in the endosome or interactions with receptors).

Two classes of viral fusion proteins have been identified so far. The best characterized members of class I are the influenza virus hemagglutinin (HA) (*1*, *2*) and the fusion protein (F) of the paramyxoviruses (*3*–*5*). Class I also includes fusion proteins from retroviruses (*6*), filoviruses (*7*), and coronaviruses (*8*). The active fusogenic form is obtained by proteolytic cleavage of a precursor into two fragments and bears a hydrophobic fusion peptide at or near the amino terminus generated by this cleavage. The proteins are organized as trimers and their postfusion conformation contains a trimeric coiled-coil core, beginning near the carboxy-terminal end of the fusion peptide, against which are packed, in an antiparallel manner, the segments abutting the transmembrane region. The protein shape is thus an elongated hairpinlike structure bringing together the fusion peptide and the C-terminal transmembrane domain.

Class II contains the E protein of flaviviruses (*9*, *10*) and E1 of alphaviruses (*11*). They have an internal fusion peptide, located in a loop between two β strands, and are synthesized within a polyprotein. Folding takes place as a complex with a second viral envelope protein that plays a chaperone role. Proteolytic cleavage of the chaperone primes the fusion protein to trigger membrane merger. In their native conformation, they form dimers that lie flat at the viral surface and are organized with icosahedral symmetry (*11*). On exposure to low pH, the dimers dissociate, and the protomers reassociate to form trimers. Similarly to class I proteins, this transition results in a hairpin structure with the fusion loops and the transmembrane domains at the same end of an elongated molecule that is then perpendicular to the membrane (*12*–*14*).

A number of viral fusion proteins, from rhabdoviruses and herpesviruses, for instance, do not appear to fall within either of these classes. Among them, glycoprotein G of the vesicular stomatitis virus (VSV), from the *Rhabdoviridae* family, has been the most studied. Rhabdoviruses are bullet-shaped and are widespread among a great variety of organisms (including plants, insects, fishes, mammals, reptiles, and crustaceans). Their genome is a single RNA molecule (about 12 kb) of negative polarity encoding five or six proteins in total, among which is a single-transmembrane glycoprotein (G) that is trimeric and forms the spikes that protrude from the viral surface. G is both responsible for viral attachment to specific receptors and for low pH–induced membrane fusion after endocytosis of the virion. Most of the mass of G (446 amino acids out of 495 for VSV Indiana strain) is located outside the viral membrane and constitutes the N-terminal ectodomain, which is the target of neutralizing antibodies. The two most studied genera of rhabdoviruses are the lyssaviruses [prototype virus: rabies virus (RV)] and the vesiculoviruses (prototype virus: VSV).

Fusion of rhabdoviruses is optimal around pH 6 (*15*–*19*). Preincubation of the virus at low pH in the absence of a target membrane leads to inhibition of viral fusion. However, this inhibition is reversible, and readjusting the pH to above 7 leads to the complete recovery of the initial fusion activity (*20*). Low pH–induced conformational changes of G and their relations with the fusion activity have been studied by different biophysical and biochemical techniques (*16*, *21*–*26*). G can adopt at least three different conformational states (*15*, *16*): the native state detected at the viral surface above pH 7; the activated hydrophobic state, which interacts with the target membrane as a first step of the fusion process (*24*); and the fusion inactive, postfusion conformation that is antigenically distinct from both the native and activated states (*27*). There is a pH-dependent equilibrium between the different states of G that is shifted toward the inactive state at low pH (*27*). Thus, unlike fusogenic glycoproteins from other viral families, the native, prefusion conformation is not metastable. Furthermore, no α-helical coiled-coil motif characteristic of class I viral fusion proteins (*28*) is predicted from the amino acid sequence (*29*). Finally, although G contains an internal fusion domain (*24*), it is not cleaved from a polyprotein precursor or associated with a second envelope protein, as is the case for class II viral fusion proteins (*9*, *11*). All these characteristics suggest that the structure of G is distinct from the structure of any fusion protein described so far.

Here we describe the structure of the VSV-G ectodomain (residues 1 to 410), generated by limited proteolysis with thermolysin (G_{th}), under its postfusion conformation at 2.4 Å resolution.

Molecular architecture. The structure of the G_{th} trimer is depicted in Fig. 1. The overall shape of the molecule resembles an inverted cone (Fig. 1B). The length of the molecule is 125 Å, and the diameter at the head is 60 Å. The crystals that allowed the structural determination were grown at pH 7.0, but the same conformation was found in crystals grown at pH 6.0 (see Materials and Methods). The dimensions of the molecule—identical to those measured for RV G ectodomain low-pH form by electron microscopy (*16*)—and its hairpin-like organization (see below) indicate that this structure corresponds to the low-pH, postfusion conformation (i.e., the fusion inactive conformation). Thus, during crystal growth at pH 7.0, the minor fraction of G in the low-pH conformation was sequestered in the crystals, displacing the equilibrium between the different states of G (*27*).

G_{th} has an altogether different structural organization from those of both class I and class II viral fusion proteins described so far. The polypeptide chain of G_{th} folds into four distinct domains (Fig. 1, A and D, and fig. S1). A β sheet–rich lateral domain at the top of the molecule (domain I), a central, mostly α-helical

CNRS, Unité Mixte de Recherche (UMR) 2472, Institut Fédératif de Recherche (IFR) 115, Virologie Moléculaire et Structurale, 91198, Gif sur Yvette, France; Institut National de la Recherche Agronomique (INRA), UMR1157, Virologie Moléculaire et Structurale, 91198, Gif sur Yvette, France.

*These authors contributed equally to this work.
†Present address: Département de Virologie, Institut Pasteur, 25 rue du Docteur Roux, 75724 Paris cedex 15, France.
‡To whom correspondence should be addressed. E-mail: gaudin@vms.cnrs-gif.fr

domain that is involved in the trimerization of the top of the molecule (domain II), a neck domain that has the characteristic fold of pleckstrin homology (PH) domains (domain III), and the elongated fusion domain that makes the trimeric stem of the molecule (domain IV). Three of these compact domains are made from noncontiguous segments of the polypeptide chain (Fig. 1D). The single segment making the fusion domain is inserted into the PH domain, and the PH domain is inserted into domain II. The C-terminal part of G_{th} (411 to 422) is not ordered in either crystal form, and the polypeptide chain can be drawn up to residue 410 on one protomer and only to residue 408 on the other two. Nevertheless, the orientation of the chain after the end of domain II [residues 406 to 410 in magenta on Fig. 1A (right) and 1B] indicates that it is pointing toward the tip of the fusion domain. Thus, as in the postfusion conformation of other fusion proteins, the transmembrane domain and the fusion domains are located at the same end of the molecule.

Alignment of five G protein sequences from animal rhabdoviruses belonging to different genera is shown in fig. S2. Although the overall amino acid identity is very low, it remains significant, and all of them are predicted to display the same fold except possibly the C-terminal part of ephemeroviruses G.

Surprisingly, the structural organization of G is the same as that of herpesvirus gB that is described in this issue (*30*). This similarity extends from the N-terminal part to at least the end of helix G of domain II. It includes both the PH domain and the fusion domain [Dali score, $Z = 5.2$ for 109 residues of the fusion domain (*31*)], as well as part of the trimerization domain (fig. S3), and reveals a clear and unexpected homology between the two proteins.

Description of the domains. The top lateral domain I (Fig. 2A) contains about 90 residues in two segments (1 to 17 and 310 to 383). It is made of three antiparallel β sheets (astu, rsa′, and vwxys′) that are wrapped around the N-terminal β strands a to a′. β Strand s is also involved in the formation of β sheet rsa′ with the glycosylation site at position 320 on loop rs that is located at the very top of the molecule. Four other loops of this domain (vw, xy, s′t, and tu) are exposed at the surface of the molecule. It is noteworthy that an antigenic site has been reported in this domain, on loop s′t on the native conformation (*32*).

Domain II (Fig. 3A) is made of three segments (18 to 35, 259 to 309, and 384 to 405) and contains four helices (A, F, G, and H). In the trimer, the two longest helices F and H make a six-helix bundle, reminiscent of the structure found in class I fusion proteins in their postfusion conformation (*28*), in which helix F forms the trimerization region (Fig. 1C, Fig. 3C). As in class I proteins, the fusion domain is N-terminal to the central helix F, and the transmembrane domain is located at the C terminus of the antiparallel outer helix H. Helices F and H are zipped together by a small antiparallel β sheet formed by strands q and z. Helix F is linked by a disulfide bond (bridging cysteines C^{24} and C^{284}) (*33*) to the long extended N-terminal part of this domain, which is wound around the top of the molecule. The FG loop is exposed at the top of the domain. The segment delimited by P^{296} and P^{310}, which contains helix G, and the top of helix H (residues 384 to 391) are hydrophobically packed against domain I, interacting with strands s, r, v, w, and x.

Domain III is inserted within domain II. It is made of two segments (36 to 50 and 181 to 258) and has the fold of a PH domain (Fig. 2B). It contains two four-stranded β sheets (bjkl and pmno) and two helices D and E that are respectively located between strands j and k and strands o and p. The domain contains a disulfide bridge that stabilizes sheet pmno by bridging C^{219} and C^{253}. Numerous epitopes of the native prefusion conformation have been reported in this domain (*32*).

Domain IV (51 to 180) is inserted in a loop of the PH domain (Figs. 1D and 2B). It is an

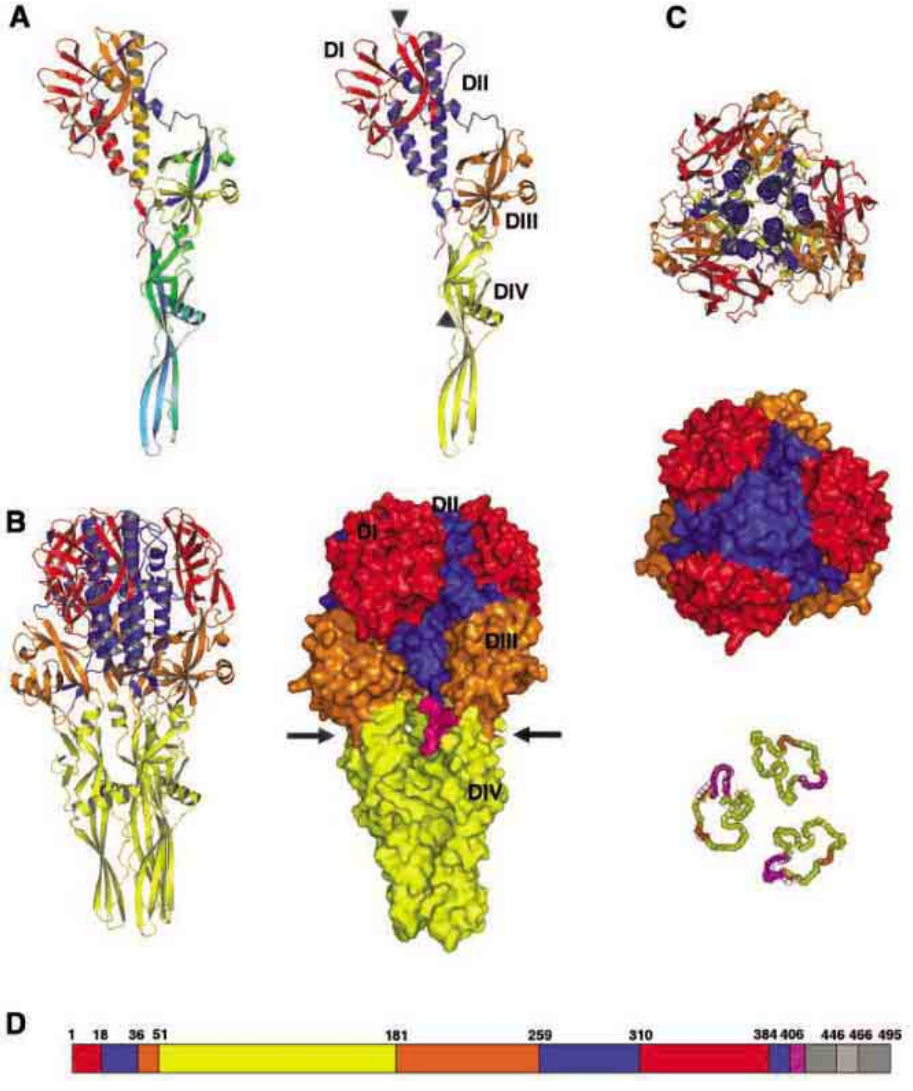

Fig. 1. Overall structure of glycoprotein G. (**A**) Ribbon diagram of the G protomer (residues 1 to 410). (Left) The chain is colored by residue number in a gradient from blue (N terminus) to red (C terminus); (right) the chain is colored by domain. The triangles indicate the glycosylation sites (on N^{163} and N^{320}). (**B**) (Left) Ribbon diagram of the G trimer, colored by domain; (right) surface representation of the G trimer, colored by domain. The arrows indicate the plane of the section shown in (C), bottom. (**C**) (Top) Top view of the trimer (ribbon diagram), colored by domain; (middle) top view of the trimer (surface representation); and (bottom) plane section of the G trimer, at the level of the C-terminal segment, showing the cavity inside the molecule. (**D**) Domain architecture of G. Domains observed in the crystal structure are colored as in (A), right. The C terminus, not observed in the structure, is in gray with the transmembrane segment hatched. All structural figures were generated with PYMOL (*38*).

extended β-sheet structure organized around two long antiparallel β strands [c and e in (Fig. 4A)] that contribute to the formation of a small six-stranded β barrel (cefghi) at one end, and at the other, to a three-stranded β sheet (dce) (Fig. 4A). The six-stranded β barrel exposes the glycosylation site at position 163 on loop hi. It is stabilized by the disulfide bridge linking C^{153} and C^{158}. The segments of the protein making the β barrel are the most conserved elements of the G amino acid sequence (fig. S2). Just before the junction of domain IV and the second segment of domain III is α helix C, which is covalently linked by a disulfide bond (bridging C^{177} and C^{226}) to loop lm of domain III (Fig. 4A).

Separating the top β barrel (cefghi) from the bottom sheet (dce), the horizontal helix B packs against strands c and e via hydrophobic interactions. Helix B is linked to strand c by the disulfide bond between C^{59} and C^{92}. After helix B, the chain adopts an elongated conformation through a $P^{107}GFPP^{111}$ motif that has a polyproline helix conformation. The very tip of the protomer is made of two loops (cd and Pe) containing aromatic residues and kept together by the disulfide bridge between C^{68} and C^{114} (Fig. 4A). As discussed below, these loops constitute the membrane-interacting motif of the G ectodomain.

The overall structural organization of this fusion domain, particularly the base of the stem, is strikingly similar to the one of class II fusion proteins (Fig. 4A). Nevertheless, these domains are not homologous: The topology of the strands making the sheet that exposes the fusion loops in VSG G is unrelated to the one in class II fusion proteins. Thus, this structural similarity appears as the result of convergent evolution.

The fusion loops. The tip of the trimeric stem has a bowllike concave shape similar to that already described for E protein of flaviviruses (Fig. 4B). Nevertheless, unlike these fusion proteins, the fusogenic motif of VSG G is made of both loops cd and Pe and, thus, is bipartite as already suggested for the viral hemorrhagic septicemia virus, another rhabdovirus (*19*). Indeed, four hydrophobic residues W^{72}, Y^{73} (both located on loop cd), Y^{116}, and A^{117} (both located on loop Pe) are fully exposed at the tip of VSV G (Fig. 4, A and C). Not surprisingly, replacement of A^{117} by lysine abolishes G fusion properties (*18*).

This "fusion patch" cannot penetrate deep into the membrane: Even if the hydroxyl of Y^{116} participates in a hydrogen bond with the carbonyl of W^{72}, the nitrogen of the indole ring of W^{72} and several carbonyls (e.g., those of Y^{73} and A^{117}) remain exposed and hinder penetration into the hydrophobic moiety of the membrane. R^{71} and D^{69}, located on the rim of the bowl, and K^{76}, which points toward the threefold axis, set an upper limit of about 8.5 Å for membrane insertion (Fig. 4C).

Sequence alignments reveal that all the rhabdoviral G proteins have at least one polar aromatic residue in their fusion loops (fig. S2). Tyrosines and tryptophans are residues typically found at the interface between the fatty acid chains and head-group layers of lipids (*34*). Such an interfacial interaction involving a large number of aromatic residues per trimer is probably sufficient to destabilize the membrane.

The trimeric interface. The buried interface between two subunits in the trimer is roughly 3860 $Å^2$ per protomer; the main part of it (2620 $Å^2$) is located in the top of the molecule (domain II) and the rest in the stem (domain IV). The core of the trimer in domain II is the six-helix bundle (Fig. 3C). The stabilizing interactions are mostly hydrophobic but also involve a salt bridge between E^{286} from one protomer and K^{290} from another. In domain IV, the trimer is stabilized by lateral interactions between the polyproline segment and strand d of the neighboring protomer. These interactions involve conserved residues P^{111}, I^{78}, and I^{82} (Fig. 4D), which keep together the fusion loops of the three protomers and thus ensure their correct positioning at the tip of the molecule. The other contacts between domains IV in the trimer involve the C terminus of helix B, which makes two hydrogen bonds (through the carboxyl group of K^{100} and the side chain of Q^{101}, respectively) with the relatively conserved H^{132} (on strand e) and H^{162} (on loop hi) of the neighboring protomer (Fig. 4D).

Inside the trimeric structure, there is a cavity (Fig. 1C, bottom) that is limited at the base of the stem by Q^{112}. The bottom of the cavity is a narrow channel flanked by the polyproline motif. It enlarges at the level of L^{106} into a chamber 5 nm long and up to 2 nm wide that ends at the base of helix F in domain II. This chamber has three large apertures delimited by the tops of domain IV of two protomers. These openings may be occluded by the C-terminal part of the ectodomain in the full-length protein.

This cavity, a relatively rare feature in proteins, is also found in the postfusion conformation of the flavivirus protein E (*12*, *14*). For both E and G, it certainly limits the stability of the trimeric organization of the fusion domains. Only a few bonds have to be broken (Fig. 4D) to allow the structure to adopt an open conformation such as the one that has been crystallized in the case of the low-pH form of the Semliki Forest Virus E1 protein (*13*). The versatility of the association of the fusion domains is probably necessary during the fusion process. Indeed, mutations in the polyproline motif (at positions 108, 109, and 111) result in a decrease of the fusion efficiency or a drastic shift of the pH threshold for fusion toward lower values (*17*, *18*).

Molecular basis for conformational change reversibility. It has been proposed that the reversibility of the low pH–induced conformational change is essential to allow G to be transported through the acidic compartments of the Golgi apparatus and to recover its native structure at the viral surface (*35*). The structure gives the clues to the molecular basis of this unusual property. Indeed, although one crystal form was grown at pH 7.0, it is clear that the structure of G_{th} that we have determined cannot be stable at high pH in solution.

Indeed, a large number of acidic amino acids are brought close together in the six-helix bundle (Fig. 3, A and D). These residues are clearly protonated and form hydrogen bonds (Fig. 3D), and therefore, the negative logarithm of acid constant (pK_a) for them is abnormally high. Their deprotonation at higher pH will induce strong repulsive forces that destabilize the trimer this step initiates the transition back toward the prefusion form. The regions that will thus be pushed apart include the bottom part of helix F from each protomer (through D^{268}), helices H and F from neighboring protomers (through D^{274} and D^{395}), and helices H and F within the same protomer (through

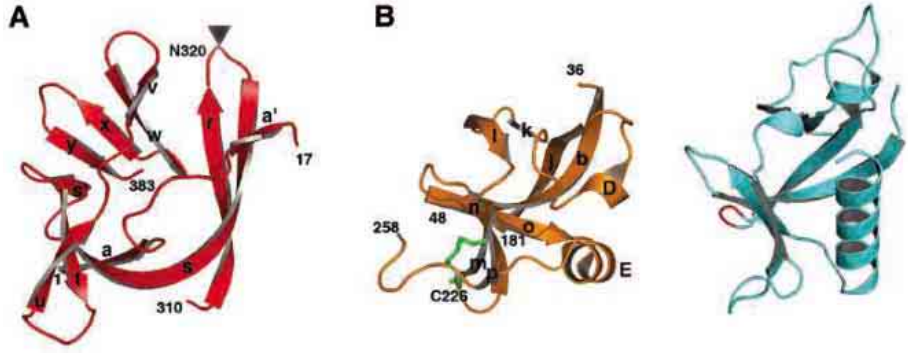

Fig. 2. Structural organization of domains I and III (PH domain). (**A**) Structure of domain I. The triangle indicates the glycosylation site. (**B**) Structure of domain III (left) and structure of the PH domain of the insulin receptor substrate 1, which is the best homolog found using Dali [Dali score Z = 4.8 (*31*)]. The loop of the PH domain in which G fusion domain is inserted is colored red. The disulfide bridge is indicated in green. Also shown is C^{226}, which makes a disulfide bond with C^{177} of domain IV.

E^{276} and D^{393}) (Fig. 3D). Although these amino acids are not conserved among the rhabdovirus family, helices F and H of all rhabdoviruses G contain numerous acidic residues (fig. S2). These residues are certainly involved in the destabilization of the low-pH form above pH 7.

The trimeric state of domain IV, as it is in the G_{th} low-pH structure, should be also affected at pH above 7, because, in its deprotonated form, H^{132} cannot maintain its interactions with both the carboxyl group of K^{100} of the neighboring protomer and the side chain of D^{145} (Fig. 4D).

Finally, D^{137}, Y^{139}, and the dipeptide $H^{407}P^{408}$, which are conserved among the rhabdovirus family, cluster together to interact with the tip of domain II qz zipper. They direct the C-terminal part of the ectodomain toward the base of the molecule (Fig. 3B). The salt bridge between D^{137} and H^{407} cannot exist after deprotonation of the histidine residue. Thus, a pH increase should also have a destabilizing effect on this small structural motif.

It is worth noting that the large number of protonated residues involved in the stability of the postfusion conformation explains the high cooperativity of the structural back transition upon deprotonation (*27*): An initial destabilization of the low-pH form at the qz zipper results in an increased solvent accessibility of acidic residues in domain II, a drop in their pK_a, and their concomitant deprotonation.

Mutations affecting the structural transition of G. For both VSV and rabies virus, mutant viruses have been selected for their ability to escape neutralization by antibodies directed against G in its low-pH conformation (*36*) or for their ability to infect cells at low pH (*37*). Seven mutations have been described that result in stabilization of the prefusion conformation (either kinetically or thermodynamically). Two of them ($Q^{285} \rightarrow R$ for VSV and $E^{282} \rightarrow K$ for RV) take place in the long helix F. Two others ($V^{392} \rightarrow G$ and $M^{396} \rightarrow T$ for RV) take place in the neighborhood of the small qz sheet and the conserved dipeptide $H^{397}P^{398}$ (residue numbering of RV G, fig. S2). These observations confirm that helix F and the cluster made by D^{137}, Y^{139}, and the dipeptide $H^{407}P^{408}$ are involved in the structural rearrangements of G. The phenotype linked to the last three mutations ($M^{44} \rightarrow$ V/I for RV and $F^{2} \rightarrow$ L for VSV) cannot be explained and may affect only other conformations of G.

Final remarks. In spite of having a novel fold, the low pH of G displays the classic hairpin conformation expected for the postfusion form of a fusogenic protein. It combines features of both class I and class II proteins. Together with gB of herpesviruses, it defines a new family of fusion proteins having a new fusion module: an elongated β structure inserted in a PH domain and carrying two fusion loops. This homology between G and gB invites us to reconsider the evolution of the *Mononegavirales* order: It suggests that *Mononegavirales* are able to steal genes, probably from their cellular host, likely by copying exogenous mRNA during genome synthesis.

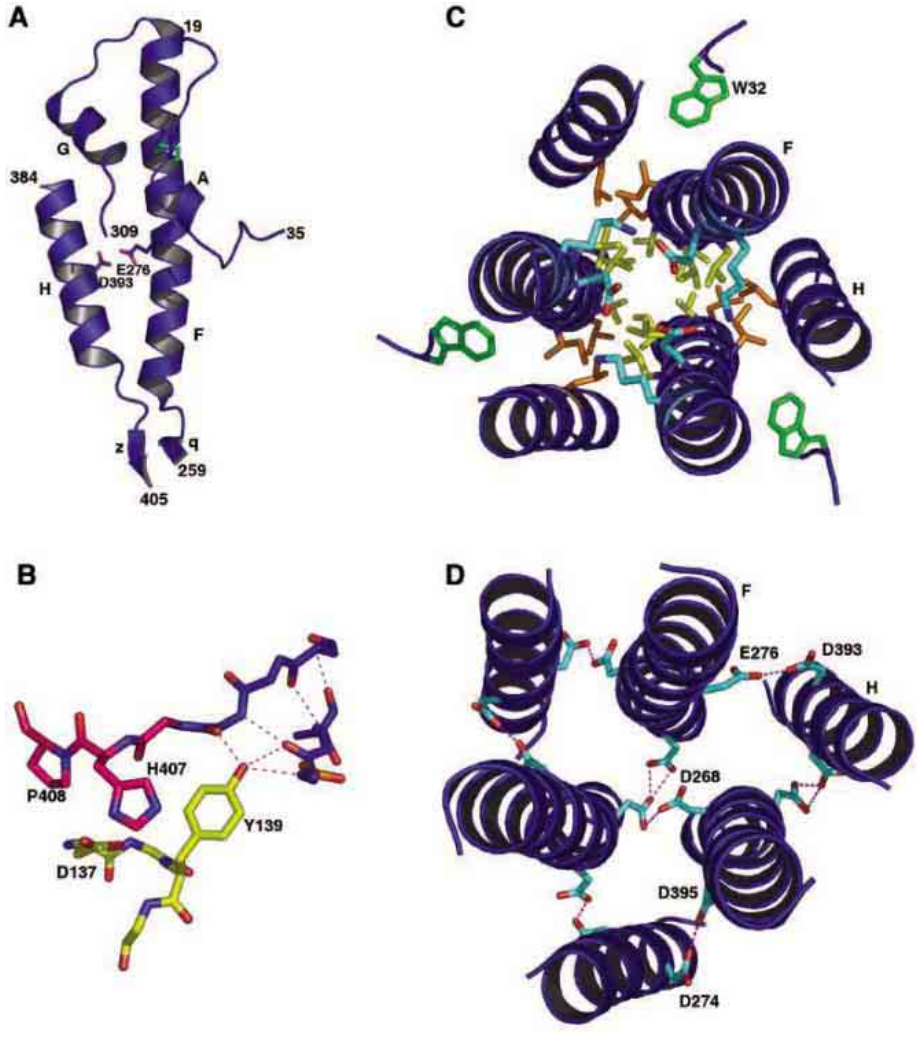

Fig. 3. Structural organization of domain II (trimerization domain). (**A**) Ribbon diagram of domain II. The disulfide bridge is indicated in green. Acidic residues E^{276} and D^{393}, which destabilize the domain at pH above 7, are also represented. (**B**) Close-up view of the qz sheet (in blue) and how it is stabilized by residues D^{137} and Y^{139} of domain IV and by the dipeptide $H^{407}P^{408}$. Hydrogen bonds are indicated as dotted lines in magenta. D^{137} makes a salt bridge with the imidazole ring of H^{407}, which is stacked against the aromatic group of Y^{139}. (**C**) Top view of the six-helix bundle (the helices labeled H and F and the residue labeled W^{32}, involved in lateral interactions, are from the same protomer). Aliphatic residues involved in interactions between helices F (I^{272}, V^{275}, L^{279}, L^{283}) are indicated in yellow; those involved in lateral interactions between two protomers (L^{271} and L^{278} in helix F and L^{392} in helix H) are indicated in orange; and E^{286} and K^{290}, which make a salt bridge, are indicated in cyan. (**D**) Top view of the six-helix bundle showing the cluster of acidic residues. Hydrogen bonds are indicated as dotted lines in magenta.

References and Notes

1. I. A. Wilson, J. J. Skehel, D. C. Wiley, *Nature* **289**, 366 (1981).
2. P. A. Bullough, F. M. Hughson, J. J. Skehel, D. C. Wiley, *Nature* **371**, 37 (1994).
3. H. S. Yin, X. Wen, R. G. Paterson, R. A. Lamb, T. S. Jardetzky, *Nature* **439**, 38 (2006).
4. H. S. Yin, R. G. Paterson, X. Wen, R. A. Lamb, T. S. Jardetzky, *Proc. Natl. Acad. Sci. U.S.A.* **102**, 9288 (2005).
5. L. Chen *et al.*, *Structure* **9**, 255 (2001).
6. D. Fass, S. C. Harrison, P. S. Kim, *Nat. Struct. Biol.* **3**, 465 (1996).
7. W. Weissenhorn, A. Carfi, K. H. Lee, J. J. Skehel, D. C. Wiley, *Mol. Cell* **2**, 605 (1998).
8. Y. Xu *et al.*, *J. Biol. Chem.* **279**, 30514 (2004).
9. F. A. Rey, F. X. Heinz, C. Mandl, C. Kunz, S. C. Harrison, *Nature* **375**, 291 (1995).
10. Y. Modis, S. Ogata, D. Clements, S. C. Harrison, *Proc. Natl. Acad. Sci. U.S.A.* **100**, 6986 (2003).
11. J. Lescar *et al.*, *Cell* **105**, 137 (2001).
12. Y. Modis, S. Ogata, D. Clements, S. C. Harrison, *Nature* **427**, 313 (2004).
13. D. L. Gibbons *et al.*, *Nature* **427**, 320 (2004).
14. S. Bressanelli *et al.*, *EMBO J.* **23**, 728 (2004).
15. M. J. Clague, C. Schoch, L. Zech, R. Blumenthal, *Biochemistry* **29**, 1303 (1990).

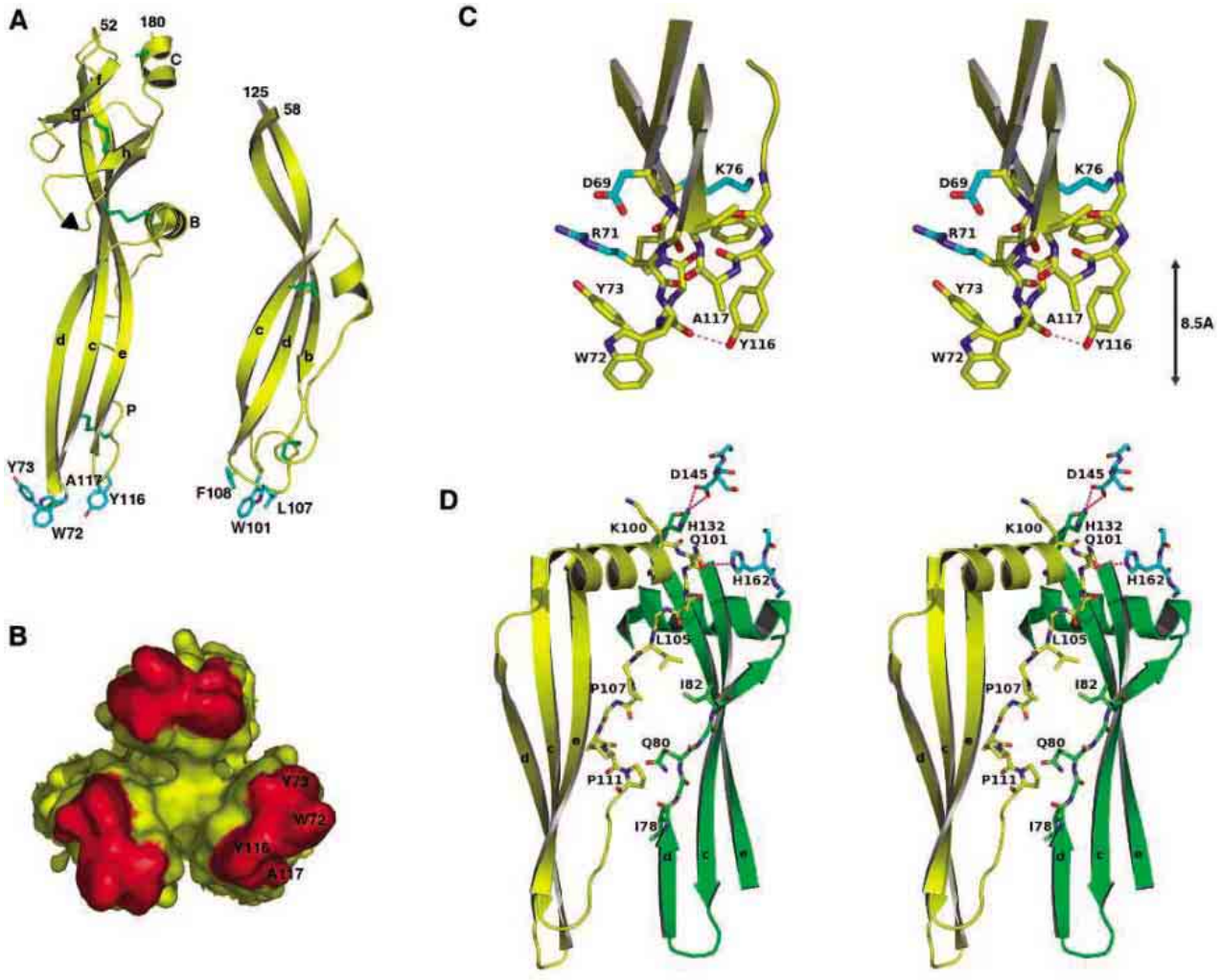

Fig. 4. Structural organization of domain IV (fusion domain). (**A**) Ribbon diagram of VSV G (left) and Dengue virus E (right) fusion domains showing their structural similarity. The disulfide bridges are indicated in green. Also shown is C^{177}, which makes a disulfide bond with C^{226} of domain III. The hydrophobic residues in the fusion loops are shown in cyan. The black triangle indicates the glycosylation site. (**B**) Surface representation of the tip of VSV G fusion domain. Hydrophobic residues inside the loops are shown in red. (**C**) Stereo view of the fusion loops of one protomer showing how charged residues (in cyan) limit the penetration of the fusion domain inside the membrane. (**D**) Stereo view showing the interactions between two protomers (one in yellow, the other in green) in the fusion domain. For clarity, only the side chains of residues playing a role in the stabilization have been drawn, and the polyproline segment of the green protomer has been omitted.

16. Y. Gaudin, R. W. Ruigrok, M. Knossow, A. Flamand, *J. Virol.* **67**, 1365 (1993).
17. L. Zhang, H. P. Ghosh, *J. Virol.* **68**, 2186 (1994).
18. B. L. Fredericksen, M. A. Whitt, *J. Virol.* **69**, 1435 (1995).
19. Y. Gaudin, P. de Kinkelin, A. Benmansour, *J. Gen. Virol.* **80**, 1221 (1999).
20. Y. Gaudin, *Subcell. Biochem.* **34**, 379 (2000).
21. B. L. Fredericksen, M. A. Whitt, *Virology* **217**, 49 (1996).
22. Y. Gaudin, C. Tuffereau, D. Segretain, M. Knossow, A. Flamand, *J. Virol.* **65**, 4853 (1991).
23. R. W. Doms, D. S. Keller, A. Helenius, W. E. Balch, *J. Cell Biol.* **105**, 1957 (1987).
24. P. Durrer, Y. Gaudin, R. W. Ruigrok, R. Graf, J. Brunner, *J. Biol. Chem.* **270**, 17575 (1995).
25. C. C. Pak, A. Puri, R. Blumenthal, *Biochemistry* **36**, 8890 (1997).
26. F. A. Carneiro, A. S. Ferradosa, A. T. Da Poian, *J. Biol. Chem.* **276**, 62 (2001).
27. S. Roche, Y. Gaudin, *Virology* **297**, 128 (2002).
28. J. J. Skehel, D. C. Wiley, *Cell* **95**, 871 (1998).
29. Y. Yao, K. Ghosh, R. F. Epand, R. M. Epand, H. P. Ghosh, *Virology* **310**, 319 (2003).
30. E. E. Heldwein *et al.*, *Science* **313**, 217 (2006).
31. L. Holm, J. Park, *Bioinformatics* **16**, 566 (2000).
32. S. B. Vandepol, L. Lefrancois, J. J. Holland, *Virology* **148**, 312 (1986).
33. Single-letter abbreviations for the amino acid residues are as follows: A, Ala; C, Cys; D, Asp; E, Glu; F, Phe; G, Gly; H, His; I, Ile; K, Lys; L, Leu; M, Met; N, Asn; P, Pro; Q, Gln; R, Arg; S, Ser; T, Thr; V, Val; W, Trp; and Y, Tyr.
34. W. C. Wimley, S. H. White, *Biochemistry* **31**, 12813 (1992).
35. Y. Gaudin, C. Tuffereau, P. Durrer, A. Flamand, R. W. Ruigrok, *J. Virol.* **69**, 5528 (1995).
36. Y. Gaudin, H. Raux, A. Flamand, R. W. Ruigrok, *J. Virol.* **70**, 7371 (1996).
37. I. Martinez, G. W. Wertz, *J. Virol.* **79**, 3578 (2005).
38. W. Delano, the PyMOL Molecular Graphics System (2002).

39. We thank A. Flamand for her constant support of this project; J. Lepault, R. Ruigrok, M. Knossow, A. Benmansour, C. Tuffereau, and D. Blondel for helpful discussions at different stages of this work; C. Maheu for virus purification; and S. Harrison and K. Heldwein for sharing information before publication. Data collection was performed in part at the Swiss Light Source, Paul Scherrer Institut, Villigen, Switzerland, and at the European Synchrotron Radiation Facility, Grenoble, France. We gratefully acknowledge the help in data collection of T. Tomizaki (beamline X06SA, SLS); C. Petosa (beamline ID14-1, ESRF); and S. Duquerroy, F. Ternois, and G. Squires. We thank B. Gigant and I. Gallay for the use of rotating anode sources for crystal testing. We acknowledge support from the CNRS and INRA, the CNRS program "Physique et Chimie du Vivant," the INRA Animal Health Department program "Les virus des animaux et leurs interactions avec la cellule," the Ministère de l'éducation nationale, de la recherche et de la technologie (MENRT) program "ACI blanche," and the Agence National de la Recherche (ANR) program.

Supporting Online Material

www.sciencemag.org/cgi/content/full/313/5784/187/DC1
Materials and Methods
SOM Text
Figs. S1 to S3
References and Notes

21 March 2006; accepted 17 May 2006
10.1126/science.1127683

Arginylation of β-Actin Regulates Actin Cytoskeleton and Cell Motility

Marina Karakozova,[1] Marina Kozak,[1] Catherine C. L. Wong,[2] Aaron O. Bailey,[2] John R. Yates III,[2] Alexander Mogilner,[3] Henry Zebroski,[4] Anna Kashina[1]*

Posttranslational arginylation is critical for mouse embryogenesis, cardiovascular development, and angiogenesis, but its molecular effects and the identity of proteins arginylated in vivo are unknown. We found that β-actin was arginylated in vivo to regulate actin filament properties, β-actin localization, and lamella formation in motile cells. Arginylation of β-actin apparently represents a critical step in the actin N-terminal processing needed for actin functioning in vivo. Thus, posttranslational arginylation of a single protein target can regulate its intracellular function, inducing global changes on the cellular level, and may contribute to cardiovascular development and angiogenesis.

Protein arginylation is an enigmatic posttranslational modification discovered more than 40 years ago (*1*) and poorly understood on the molecular level. Arginylation is mediated by Arg–transfer RNA (-tRNA) protein transferase (Ate1) (*2*, *3*), which transfers arginyl from tRNA onto the N terminus of proteins, forming a peptide bond. Three N-terminal residues, Asp, Glu, and Cys, can be arginylated, requiring prior posttranslational modification by Met-aminopeptidation or proteolysis.

Ate1 is an evolutionarily conserved enzyme that is essential for embryonic development. Ate1 knockout in mice results in embryonic lethality and severe defects in cardiovascular development and angiogenesis (*4*). Thus, arginylation is important for the regulation of the physiological functions of key proteins in vivo. However, its molecular effects and the identity of arginylated proteins are unknown.

We examined the role of protein arginylation in the regulation of a single protein target with effects on the molecular and cellular level.

β-actin is arginylated in vivo. Actin undergoes N-terminal processing in vivo by acetylation and removal of the first Met residue, followed by acetylation, and in some cases, removal of the second residue (*5*–*10*). This processing would result in N-terminal exposure of an arginylatable residue in all actin isoforms: Asp2 or Asp3 in β-actin, Glu2 or Glu3 in γ-actin, and Cys2 or Asp3 in α-actin, suggesting that actin could become a target for arginylation in vivo.

To find whether any of the actin isoforms could be arginylated in vivo, we fractionated whole lysates from mouse embryonic fibroblasts by two-dimensional (2D) gel electrophoresis, excised the spot corresponding to actin, and analyzed it by in-gel digestion followed by mass spectrometry (MS) (Fig. 1). This preparation predominantly contained a mixture of beta and γ-actin with a small amount of α-actin, which is consistent with the actin isoform composition reported for embryonic fibroblasts (*11*). Both beta and γ-actin were identified with >80% sequence coverage. We found peptides ending with N-terminal Met1, Glu2, and Glu3 of the γ-actin sequence, indicating that γ-actin had undergone sequential N-terminal removal of both first and second residues. However, we were unable to find any peptides corresponding to the N terminus of β-actin, suggesting that the β-actin N terminus was either undetectable by MS or had undergone additional N-terminal processing.

To test the hypothesis that actin had undergone arginylation, we introduced new sequences into the sequence database, adding Arg sequentially onto every arginylatable amino acid residue in the actin sequence for each identified isoform (Asp, Glu, Cys, and Asn deamidated to Asp, and Gln deamidated to Glu). We then repeated the search using the resulting database. This search yielded a new peptide, where an Arg residue was found on the N terminus of Asp3 of the β-actin sequence (Fig. 1A).

To confirm that the newly identified peptide was indeed arginylated, we compared its mass and tandem mass spectrum to the synthetic peptides corresponding to residues 1 to 17 of the actin N-terminal sequence (similar to the peptide yielded by cleavage with endopeptidase LysC), modified by the removal of Met1 and acetylation of Asp2 or the removal of Met1 and Asp 2 and arginylation of Asp3. Both peptides were found in actin preparations, confirming that both acetylated and arginylated forms of actin are found in vivo.

To make an estimate of what percentage of the intracellular actin was arginylated, we performed immunoprecipitation of actin from the lysates of wild-type mouse embryonic fibroblasts and fibroblasts from the knockout mice deficient in arginylation enzyme Ate1 [Ate1$^{-/-}$ mice (*4*)] and fractionated the resulting actin precipitates on 2D gels under conditions that allowed the separation of different actin isoforms (pH range 4 to 8). The addition of Arg onto β-actin would be expected to shift its isoelectric point (pI) into the more basic range without changing its molecular weight. Although in Ate1$^{-/-}$ cell extracts the majority of actin was found in two spots (spots 1 and 2 in Fig. 1C, consistent with the unmodified beta and γ-actin isoforms and containing beta and gamma N-terminal peptides, respectively), in the wild-type extracts there was a redistribution of protein toward the more basic pI range, resulting in the enlargement of the more basic (γ-actin) spot, reduction of the more acidic (β-actin) spot, and the appearance of an additional relatively major basic spot (spot 3 in Fig. 1C). The more basic spots 2 and 3 in the wild-type cells contained arginylated β-actin peptide, as confirmed by MS. The total shift of actin into the basic pI range in wild-type cells is likely to reflect the amount of actin arginylated in vivo, and corresponded to approximately 20% of total actin, which corresponds to approximately 40% of intracellular β-actin. Thus, we find that β-actin is arginylated in vivo.

Arginylation prevents actin filaments from clustering. To study which property of actin is affected by arginylation, we tested metabolic stability, the composition of actin-binding proteins, and polymerization properties of actin in the absence and presence of arginylation.

It has been suggested that N-terminal arginylation marks proteins for ubiquitin-dependent degradation by the N-end rule pathway (*12*). To check whether arginylation affects the metabolic stability of actin, we performed a cycloheximide chase of total actin and a pulse chase of β-actin in wild-type and Ate1$^{-/-}$ cells (Fig. 2A). In both cell types, total actin and β-actin remained stable over a time course of 6 hours, with no apparent changes in the kinetics or protein level in wild-type as compared to Ate1$^{-/-}$ cells. Moreover, we found no changes in the stationary level of β-actin in wild-type as compared to Ate1$^{-/-}$ cells, indicating that actin stability over longer times was probably not affected by arginylation. Thus, arginylation does not induce β-actin degradation.

To determine whether arginylation affects the ability of β-actin to bind other intracellular proteins, we performed immunoprecipitations of actin from wild-type and Ate1$^{-/-}$ cell extracts and analyzed the resulting preparations by MS. We found no major changes in the protein composition of the immunoprecipitates in either cell type.

To determine whether arginylation affects the ability of actin to form filaments, we performed polymerization assays in wild-type and Ate1$^{-/-}$ cell extracts, using a pyrenyl-actin assay (*13*, *14*) (Fig. 2B). Although the initial polymerization rate and kinetics were similar in both types of extracts, pyrenyl fluorescence in Ate1$^{-/-}$ extracts exhibited a sharp drop after the initial rapid increase, suggesting that actin filaments in

[1]Department of Animal Biology, University of Pennsylvania, Philadelphia, PA 19104, USA. [2]The Scripps Research Institute, La Jolla, CA 92037, USA. [3]University of California, Davis, CA 95616, USA. [4]The Rockefeller University, New York, NY 10021, USA.

*To whom correspondence should be addressed. E-mail: akashina@vet.upenn.edu

Ate1$^{-/-}$ extracts underwent aggregation. Similar results were obtained if actin polymerization in extracts was induced by the addition of seeds or of recombinant activator of the actin nucleator complex Arp2/3.

Because the addition of exogenous pyrenyl actin introduced wild-type actin protein into the extracts, it may have affected polymerization of the endogenous actin. To exclude this possibility, we performed spontaneous polymerization experiments in the cell extracts in the absence of exogenously added factors and then visualized the polymerized filaments by rhodamine-phalloidin staining followed by fluorescence microscopy (Fig. 2C). Actin filaments in the control extracts formed single filaments, whereas in Ate1$^{-/-}$ extracts the filaments appeared clustered, forming random filamentous aggregates (Fig. 2C).

To confirm that the observed filament clustering is the property of actin itself and not of other factors found in the extract, we incubated rhodamine-phalloidin–labeled filaments, pre-polymerized from purified rabbit skeletal muscle actin, in the Ate1$^{-/-}$ extracts. Such pre-polymerized filaments did not cluster or aggregate in Ate1$^{-/-}$ extracts (Fig. 2C), suggesting that the clustering was the property of the arginylation-free actin filaments and not of additional factors in the Ate1$^{-/-}$ extracts. Thus, the absence of protein arginylation causes actin to form aggregates in cell extracts by changing the properties of the nonarginylated actin filaments.

Arginylation regulates cell motility. To study the effect of arginylation on the intracellular functions of β-actin, we compared the morphology, motility, and actin cytoskeleton of wild-type and Ate1$^{-/-}$ cells. The majority of Ate1$^{-/-}$ cells appeared smaller than wild-type cells and were apparently unable to form a lamella during movement along the substrate (Fig. 3). Time-lapse imaging of single cells (Fig. 3A and videos S1 and S2) or of a fibroblast monolayer moving into the wound (Fig. 3C and videos S3 and S4) confirmed that although both types of cells were apparently motile, Ate1$^{-/-}$ cells failed to form normal lamellae during motility, resulting in their inability to cover the same distance or occupy the same area of the substrate as the control cells. In addition,

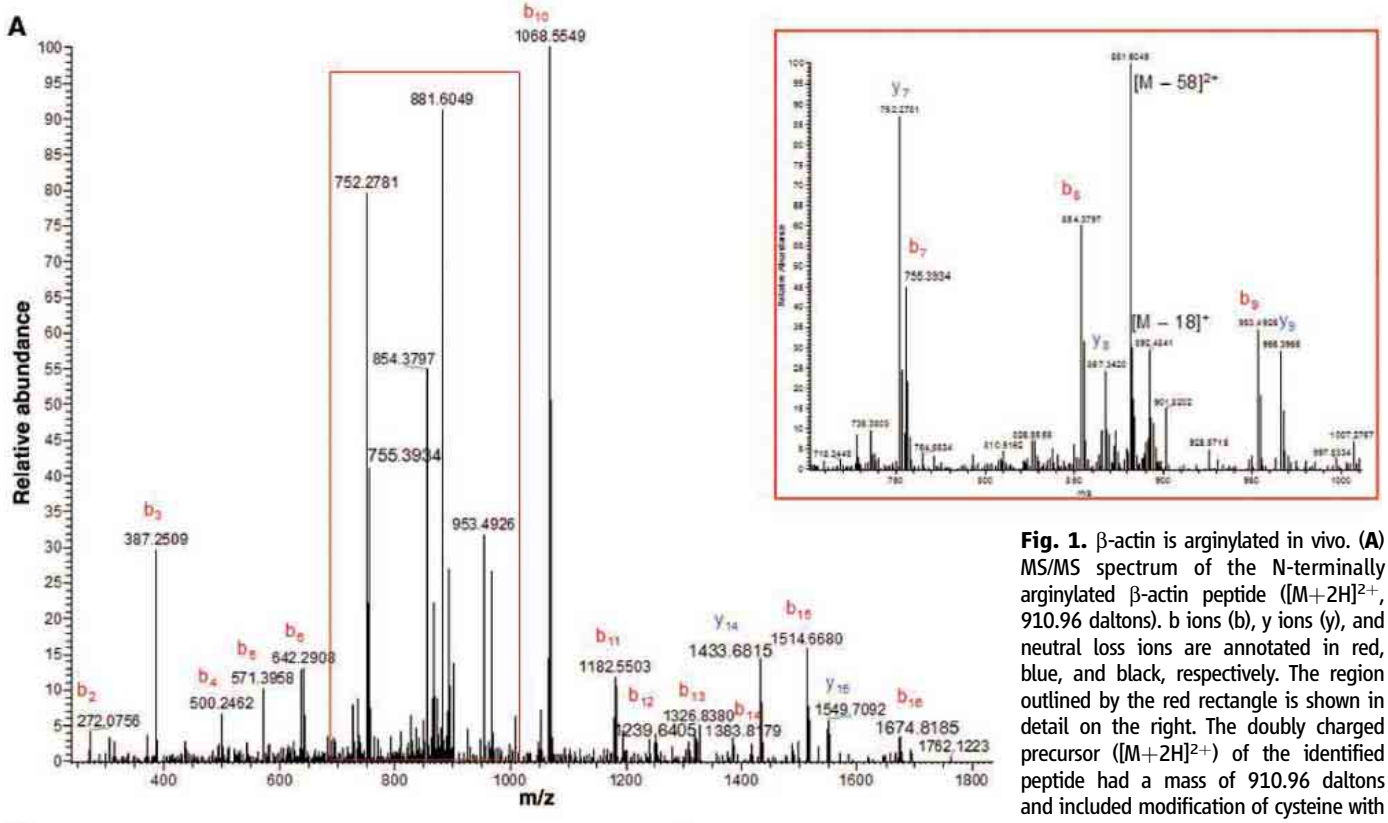

B

Seq	#	b ion (predicted)	b ion (observed)	difference (ppm)
R	1	-	-	
D	2	272.1359	272.0756	222
D	3	387.1628	387.2509	228
I	4	500.2469	500.2462	1.4
A	5	571.284	571.3958	196
A	6	642.3211	642.2908	47.1
L	7	755.4052	755.3934	15.6
V	8	854.4736	854.3797	110
V	9	953.542	953.4926	51.8
D	10	1068.5689	1068.5549	13.1
N	11	1182.6119	1182.5503	52.1
G	12	1239.6333	1239.6405	5.8
S	13	1326.6654	1326.838	130
G	14	1383.6868	1383.8179	94.7
M	15	1514.7273	1514.668	39.1
C	16	1674.758	1674.8185	36.1
K	17	-	-	

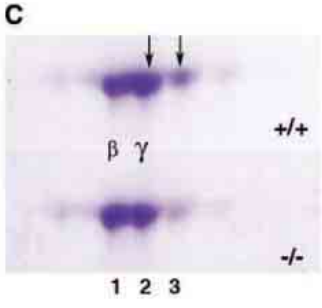

Fig. 1. β-actin is arginylated in vivo. (**A**) MS/MS spectrum of the N-terminally arginylated β-actin peptide ([M+2H]$^{2+}$, 910.96 daltons). b ions (b), y ions (y), and neutral loss ions are annotated in red, blue, and black, respectively. The region outlined by the red rectangle is shown in detail on the right. The doubly charged precursor ([M+2H]$^{2+}$) of the identified peptide had a mass of 910.96 daltons and included modification of cysteine with iodoacetamide (+57) (see also fig. S1). (**B**) Masses of predicted and observed b-fragment ions in the arginylated actin peptides, with differences in parts per million (ppm) listed on the right (see also table S1). (**C**) 2D gel electrophoresis of actin isoforms from wild-type (+/+) and Ate1$^{-/-}$ (–/–) cells (in 10% polyacrylamide gel with a pH range from 4 to 8, increasing from left to right). Major actin spots (approximate area of molecular weight 43 kD, pI 5.3) are marked 1, 2, and 3, and isoforms identified in the spots are marked as β (β-actin), and γ (γ-actin). Arrows indicate the spots that shifted into the more basic pI range in wild-type as compared to Ate1$^{-/-}$ cells, which contain arginylated β-actin and have been used to estimate the total arginylation-dependent gel shift described in the text and supporting online material.

Ate1$^{-/-}$ cells exhibited apparent defects in ruffling activity and cortical flow (videos S1 and S2).

To confirm that the apparently smaller size of the Ate1$^{-/-}$ cells was indeed due to the decreased spreading and not to a smaller volume, we compared the ratios of cell volume and area occupied by fully spread cells in wild-type and Ate1$^{-/-}$ fibroblasts (Fig. 3B). Although the volume ratio of the two cell types was approximately 1:1 [ratio of (+/+):(–/–) = 1: 1.06, n = 100 cells], the average area occupied by wild-type cells was more than 2 times larger [ratio of (+/+):(–/–) =

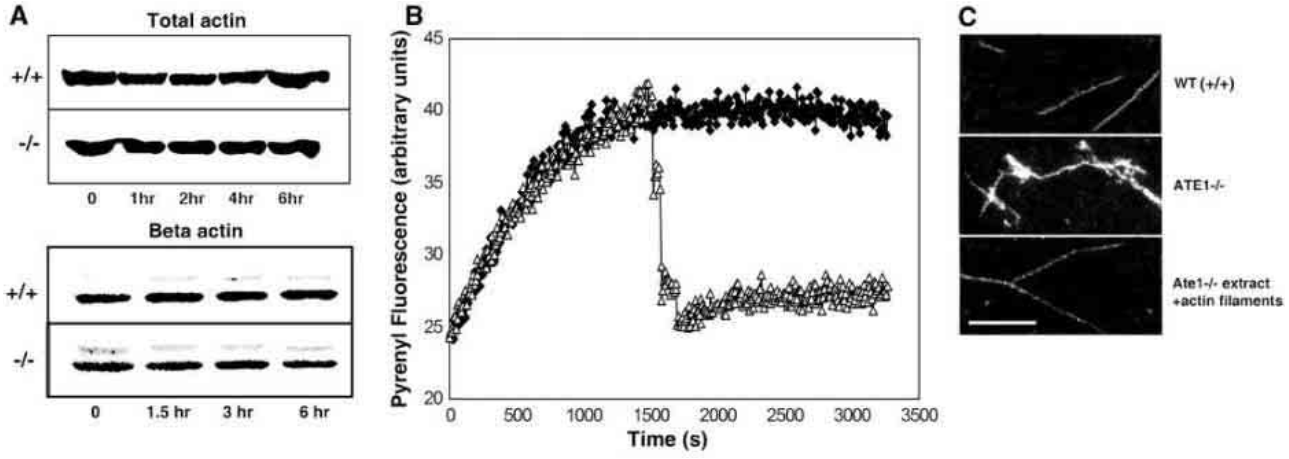

Fig. 2. Arginylation causes actin filament aggregation without affecting actin metabolic stability. (**A**) Cycloheximide chase of total actin (top) and pulse chase of β-actin (bottom) over a time course of 6 hours in wild-type (+/+) and Ate1$^{-/-}$ cells. (**B**) Polymerization curves in wild-type and Ate1$^{-/-}$ cell extracts measured by pyrenyl fluorescence of exogenous pyrenyl actin added to the extracts. Solid and open symbols indicate pyrenyl fluorescence in wild-type and Ate1$^{-/-}$ extracts, respectively. (**C**) Rhodamine-phalloidin–stained actin filaments spontaneously polymerized in wild-type (top) or Ate1$^{-/-}$ (middle) cell extracts or pre-polymerized from exogenous actin and added to the Ate1$^{-/-}$ extracts (bottom). Scale bar, 10 μm.

Fig. 3. Arginylation regulates cell spreading, lamella formation, and intracellular localization of β-actin. (**A**) Images of single cells in wild-type (+/+, left) and Ate1$^{-/-}$ (–/–, right) mouse fibroblast cultures visualized by phase contrast (top pair) or immunofluorescence staining for β-actin (middle pair) and rhodamine-phalloidin stain and rhodamine-phalloidin staining for filamentous actin (bottom pair). Scale bar, 10 μm. See also videos S1 and S2 for time-lapse images of cells shown in the phase-contrast photographs on top. (**B**) Quantification of cell volume, cell area, and lamella length in wild-type and Ate1$^{-/-}$ cells. (**C**) Images of monolayers of wild-type (+/+, top) and Ate1$^{-/-}$ (–/–, bottom) cells moving into a wound, visualized by phase contrast (left pair) or immunofluorescence staining for β-actin (middle pair) and rhodamine-phalloidin staining for filamentous actin (right pair). Scale bar, 10 μm. See also videos S3 and S4 for time-lapse images of cells shown in the phase-contrast photographs on the left.

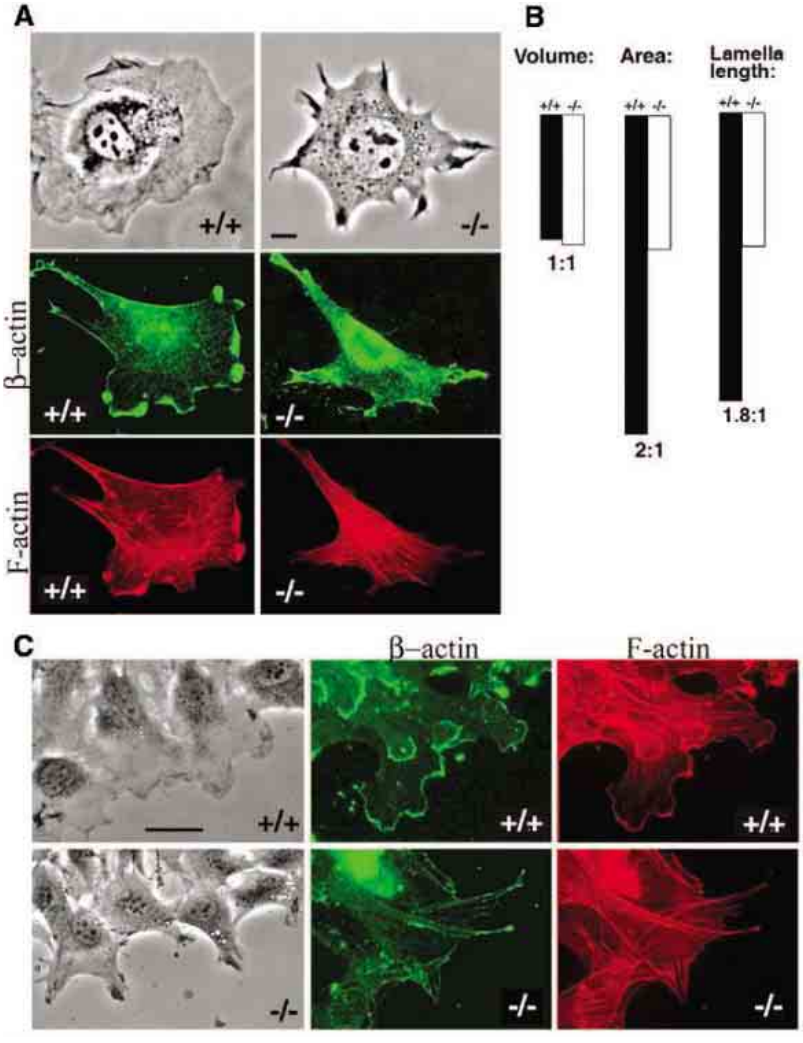

2.13:1, n = 75], and the average lamella length was almost 2 times larger [ratio of (+/+):(–/–) = 1.81:1, n = 55], confirming that Ate1$^{-/-}$ cells indeed exhibit defects in spreading and lamella formation.

We next compared the intracellular distribution of F-actin and β-actin in both cell types. Although the general appearance and distribution of F-actin were largely similar, β-actin in Ate1$^{-/-}$ cells formed patches and aggregates in the cytoplasm (Fig. 3A) and failed to localize to the leading edge of the fibroblasts moving into the wound (Fig. 3C), which is consistent with the in vitro evidence of actin aggregation in Ate1$^{-/-}$ cells.

Thus, the absence of actin arginylation causes defects in lamella formation and intracellular distribution of β-actin. To confirm that the lamella defects in Ate1$^{-/-}$ cells were indeed due to the absence of β-actin arginylation, we performed a "phenotype rescue" study by transiently transfecting Ate1$^{-/-}$ cells with a permanently arginylated β-actin construct, produced by a ubiquitin fusion technique (*12*), by replacing the Met1 and Asp2 of β-actin with Arg, followed by C-terminal fusion of the β-actin to green fluorescent protein (Arg-actin) (Fig. 4). Transfection with control constructs containing wild-type β-actin (Met-actin) caused no change in the morphology or motility of Ate1$^{-/-}$ cells, but transfection with permanently arginylated β-actin resulted in the cells forming normal lamellae [ratio of Arg:Met = 1.9:1, n = 46; compared to a 1.81:1 ratio of (+/+):(–/–)], without fully restoring the area on the substrate [ratio of Arg:Met = 1.52:1, n = 55, compared to a 2.1:1 ratio of (+/+):(–/–)], ruffling activity, or cortical flow, suggesting that other arginylated proteins may be responsible for additional phenotypes in Ate1$^{-/-}$ cells. Thus, arginylation of β-actin controls actin polymerization and lamella formation in motile cells.

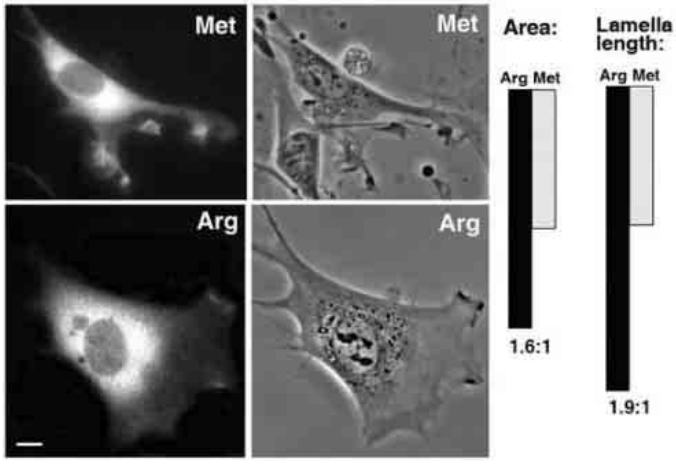

Fig. 4. Permanently arginylated β-actin restores lamella formation in Ate1$^{-/-}$ cells. (**Left**) Phase contrast (right) and fluorescence (left) images of Ate1$^{-/-}$ cells transfected with wild-type (Met) or permanently arginylated (Arg) β-actin constructs. (**Right**) Quantification of the ratios of cell area and lamella length between cells transfected with permanently arginylated (Arg) and wild type β-actin (Met). Scale bar, 10 μm. See also fig. S5 for construct details and videos S5 to S7 for the phenotype restoration seen in a single cell (video S5), a single cell moving next to an untransfected cell (video S6), and a cell moving in a monolayer during a wound healing assay (video S7).

Discussion. We found that protein arginylation can produce global effects on the molecular and cellular levels by regulating a single protein target. Arginylation apparently constitutes a next step in actin N-terminal processing, shown to be important for actin function in vivo (*9*, *10*). Indeed, the absence of N-terminal Arg caused severe effects on actin polymerization and induced filament aggregation in vitro and β-actin redistribution in vivo.

Based on the known crystal structure of the actin molecule and the information about the intracellular architecture of actin filaments, we propose a model of how arginylation regulates actin function at the leading edge (Fig. 5). Crystal structures of the actin monomers and oligomers suggest that the actin N terminus is exposed on the surface of the actin monomers (Fig. 5A) and actin filaments upon polymerization (*15*). In the absence of Arg, actin filaments are mildly negatively charged because of the presence of Asp/Glu side chains and N-terminal acetyl groups. The addition of Arg introduces a bulky positively charged group onto the filament surface. Assuming that each fifth subunit of actin is arginylated (corresponding to the 20% estimation found in our experiments), the assembly of actin filaments from such a mixture should produce filaments evenly coated with bulky positive charges (approximately one per half-turn of the helix of the actin filament; see the calculation in the supporting online material) (Fig. 5B). It is conceivable that such a coating would prevent arginylated filaments from coming together into bundles and aggregates, whereas the absence of such a coating would cause filaments to aggregate, producing the effects seen in vitro.

In vivo, the situation is more complex. β-actin mRNA localizes to the cell leading edge, where β-actin is rapidly produced to facilitate lamellar activity (*16*). β- and γ-actin in vivo are

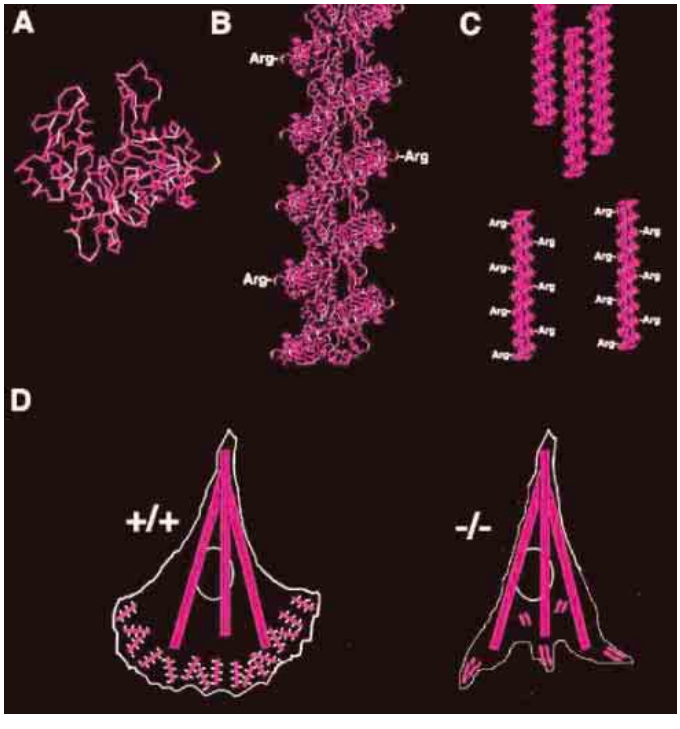

Fig. 5. Model of the role of arginylation in actin polymerization and in vivo assembly of intracellular actin networks. (**A**) Structure of bovine β-actin (downloaded from the CN3D structure database at www.ncbi.nlm.nih.gov, accession number 1HLU), with the arginylatable N-terminal Asp3 highlighted in yellow. (**B**) 2D structural model of an actin filament assembled in vitro from the monomers shown on the left, according to the model of actin polymerization by Lorenz *et al*. (*19*). Every fifth subunit in the filament is labeled with N-terminal Arg. (**C**) Structural model of actin filaments assembled from nonarginylated actin (top) or from a mixture of arginylated and nonarginylated actin in the ratio of 4:1. Filaments in the presence of Arg contain bulky charged groups of Arg residues on the surface that may prevent their side-to-side aggregation. (**D**) (Left) In a wild-type cell (+/+), arginylation of β-actin at the leading edge prevents filaments from aggregation, allowing the formation of a loose network; the absence of arginylation of γ-actin in the cell body allows the tight arrangement of the stress fibers. (Right) In the absence of arginylation (–/–), the β-actin filaments at the leading edge collapse into aggregates, causing the collapse of the lamella and the accumulation of the actin aggregates in the cell body. The γ-actin stress fibers remain unchanged (see also Fig. 3A for real cell images).

segregated, with γ-actin found predominantly in the stress fibers and β-actin predominantly at the leading edge (*16*–*18*). Because β-actin is arginylated to about 40% and γ-actin is not, the difference between β- and γ-actin–containing filaments in vivo should be quite substantial. Indeed, at the leading edge, β-actin–containing filaments are assembled from about 40% of arginylated subunits, which should prevent their side-to-side aggregation and induce the formation of a loose network, normally seen at the leading edge of locomoting cells. At the same time, the arrangement of arginylation-free γ-actin–containing filaments in the cell body favors the tightly packed stress fibers (Fig. 5D). Although other protein factors undoubtedly participate in this arrangement, the absence of arginylation in such cells should lead to bundling of β-actin at the leading edge, which would conceivably result in lamella collapse and the accumulation of β-actin aggregates in the cytoplasm, as seen in the Ate1$^{-/-}$ cells.

To further test these predictions, we have developed a mathematical model of actin assembly in vitro and in vivo in the presence and absence of arginylation (supporting online material). This model, in agreement with the experimental data and data from the literature, suggests that both β-actin arginylation and its targeting to the leading edge are essential to differentiate between actin isoform–specific networks in vivo and facilitate lamella formation in locomoting cells. The model also predicts that the effect of arginylation on actin assembly can be expected in a range of percentages of arginylated subunits as compared to nonarginylated ones, with effects that are substantial even when as little as 20% of the leading-edge actin is arginylated. Thus, our crude estimation of 40% arginylated β-actin does not need to be accurate to explain the observed effects in vivo and in vitro. In fact, the percentage of arginylated actin should vary in vivo, depending on the motile state of the cell.

Cell motility is critically important during cardiovascular development and angiogenesis. Our finding provides insights into the molecular events that lead to the impairment of these developmental events in Ate1$^{-/-}$ mice. Indeed, the defects in lamella formation observed in the Ate1$^{-/-}$ cells could result in reduced migration of the cells of cardiovascular lineages. Arginylation has been suggested to regulate many proteins; thus, other protein targets are likely to be responsible for additional arginylation defects on the molecular, cellular, and organismal levels.

References and Notes

1. H. Kaji, G. D. Novelli, A. Kaji, *Biochim. Biophys. Acta* **76**, 474 (1963).
2. H. Kaji, *Biochemistry* **7**, 3844 (1968).
3. E. Balzi, M. Choder, W. N. Chen, A. Varshavsky, A. Goffeau, *J. Biol. Chem.* **265**, 7464 (1990).
4. Y. T. Kwon *et al.*, *Science* **297**, 96 (2002).
5. P. A. Rubenstein, D. J. Martin, *J. Biol. Chem.* **258**, 3961 (1983).
6. P. A. Rubenstein, D. J. Martin, *J. Biol. Chem.* **258**, 11354 (1983).
7. D. J. Martin, P. A. Rubenstein, *J. Biol. Chem.* **262**, 6350 (1987).
8. D. R. Sheff, P. A. Rubenstein, *J. Biol. Chem.* **264**, 11491 (1989).
9. S. Schmitz *et al.*, *J. Mol. Biol.* **295**, 1201 (2000).
10. E. S. Hennessey, D. R. Drummond, J. C. Sparrow, *Eur. J. Biochem.* **197**, 345 (1991).
11. P. A. Rubenstein, J. A. Spudich, *Proc. Natl. Acad. Sci. U.S.A.* **74**, 120 (1977).
12. A. Bachmair, D. Finley, A. Varshavsky, *Science* **234**, 179 (1986).
13. J. A. Cooper, T. D. Pollard, *Methods Enzymol.* **85**, 182 (1982).
14. J. A. Cooper, S. B. Walker, T. D. Pollard, *J. Muscle Res. Cell Motil.* **4**, 253 (1983).
15. K. C. Holmes, M. Tirion, D. Popp, M. Lorenz, W. Kabsch, R. A. Milligan, *Adv. Exp. Med. Biol.* **332**, 15 (1993).
16. J. Condeelis, R. H. Singer, *Biol. Cell* **97**, 97 (2005).
17. C. A. Otey, M. H. Kalnoski, J. L. Lessard, J. C. Bulinski, *J. Cell Biol.* **102**, 1726 (1986).
18. D. Hofer, W. Ness, D. Drenckhahn, *J. Cell Sci.* **110**, 765 (1997).
19. M. Lorenz, D. Popp, K. C. Holmes, *J. Mol. Biol.* **234**, 826 (1993).

20. We are grateful to I. Sorokina from Midwest Bio Services for the original observation of the arginylated β-actin peptide and helpful suggestions throughout the project; S. Zigmond, J. Pehrson, and V. Rodionov for helpful discussions; D. Dong for assistance in preparation of the arginylated actin database; B. He from W. Guo's lab for his help with setting up the actin polymerization assays and a gift of recombinant VCA; Y. Wolf for his help with the analysis of the actin crystal structure and preparation of Fig. 5; M. Crawford and the staff of the W. M. Keck Facility at Yale for help with the analysis of actin samples; and S. Zigmond for critical reading of the manuscript. This work was supported by grant PC040372 from the U.S. Department of Defense Congressionally Directed Medical Research Programs to A.K. and by NIH grant P41 RR11823-09 to J.R.Y.

Supporting Online Material

www.sciencemag.org/cgi/content/full/1129344/DC1
Materials and Methods
SOM Text
Figs. S1 to S5
Table S1
References
Videos S1 to S7

13 March 2006; accepted 24 May 2006
Published online 22 June 2006;
10.1126/science.1129344
Include this information when citing this paper.

Massive-Star Supernovae as Major Dust Factories

Ben E. K. Sugerman,[1]* Barbara Ercolano,[2] M. J. Barlow,[2] A. G. G. M. Tielens,[3] Geoffrey C. Clayton,[4] Albert A. Zijlstra,[5] Margaret Meixner,[1] Angela Speck,[6] Tim M. Gledhill,[7] Nino Panagia,[1] Martin Cohen,[8] Karl D. Gordon,[9] Martin Meyer,[1] Joanna Fabbri,[2] Janet. E. Bowey,[2] Douglas L. Welch,[10] Michael W. Regan,[1] Robert C. Kennicutt Jr.[11]

We present late-time optical and mid-infrared observations of the Type II supernova 2003gd in the galaxy NGC 628. Mid-infrared excesses consistent with cooling dust in the ejecta are observed 499 to 678 days after outburst and are accompanied by increasing optical extinction and growing asymmetries in the emission-line profiles. Radiative-transfer models show that up to 0.02 solar masses of dust has formed within the ejecta, beginning as early as 250 days after outburst. These observations show that dust formation in supernova ejecta can be efficient and that massive-star supernovae could have been major dust producers throughout the history of the universe.

Millimeter observations of high-redshift ($z > 6$) quasars have revealed the presence of copious amounts of dust when the universe was as young as 700 million years (*1*). At the present day, dust in the interstellar medium of the Milky Way and other galaxies is generally thought to be injected mainly by the gentle winds of low-mass stars when they evolve onto the Asymptotic Giant Branch (*2*). However, stellar-evolution time scales of these low- to intermediate-mass stars are too long for them to have been a major contributor to the dust budget in the early universe (*3*). Instead, dust in the early universe must reflect the contribution from rapidly evolving (1 to 10 million years) massive stars, which return their nuclear ashes in explosive Type II supernova (SN) events. Theoretical studies have long suggested that dust can condense in the ejecta from core collapse (e.g., Type II) SNe (*4*), and calculations predict condensation of 0.08 to 1 solar mass ($M_\odot$) of dust within a few years, depending on metallicity and progenitor mass (*5*–*7*). There is also evidence for the origin of some dust in Type II

[1]Space Telescope Science Institute, 3700 San Martin Drive, Baltimore, MD 21218, USA. [2]Department of Physics and Astronomy, University College London, Gower Street, London WC1E 6BT, UK. [3]Kapteyn Astronomical Institute, Post Office Box 800, 9700 AV Groningen, Netherlands. [4]Department of Physics and Astronomy, Louisiana State University, Baton Rouge, LA 70803, USA. [5]School of Physics and Astronomy, University of Manchester, Post Office Box 88, Manchester M60 1QD, UK. [6]Department of Physics and Astronomy, University of Missouri, 316 Physics, Columbia, MO 65211, USA. [7]Department of Physics, Astronomy, and Maths, University of Hertfordshire, Hatfield AL10 9AB, UK. [8]Monterey Institute for Research in Astronomy, 200 Eighth Street, Marina, CA 93933, USA. [9]Steward Observatory, University of Arizona, 933 North Cherry Avenue, Tucson, AZ 85721, USA. [10]Department of Physics and Astronomy, McMaster University, Hamilton, Ontario L8S 4M1, Canada. [11]Institute of Astronomy, University of Cambridge, Madingley Road, Cambridge, CB3 0HA, UK.

*To whom correspondence should be addressed. E-mail: sugerman@stsci.edu

SNe on the basis of the isotopic composition of stardust isolated in meteorites (*8*).

Direct observational evidence for efficient dust formation in SN ejecta is, however, lacking, largely because SN explosions are rare and far apart. Dust formation was detected in the ejecta of SNe 1987A and 1999em, but only some 10^{-4} $M_{\odot}$ were inferred for each (*9*–*11*), a factor up to 10^3 smaller than typical SNe would have had to produce in order to contribute efficiently to the early-universe dust budget (*12*). Similarly low dust masses have been measured in evolving SN remnants with the recently launched Spitzer Space Telescope (*13*); however, its mid-infrared (mid-IR) instruments are most sensitive to warm (50 to 500 K) material, whereas dust in these remnants has almost certainly cooled to <30 K. Cold dust has been detected in remnants in the far-IR and sub-mm wavelengths; however, such observations risk strong contamination by cold, unrelated dust clouds along the line of sight (*14*). As such, the best way to demonstrate dust condensation in SN ejecta is to study them within a few years of their explosion, during the epoch of condensation when the ejecta are much hotter than interstellar dust. The high sensitivity of Spitzer's mid-IR detectors allows us to sample very young core collapse SNe within ~20 Mpc and opens up the whole nearby universe for such studies. Here we report on such a study of the Type II-P SN 2003gd in the galaxy NGC 628. A rare combination of contemporaneous optical and mid-IR observations of this well-studied SN with a known stellar progenitor mass of 8^{+4}_{-2} $M_{\odot}$ (*15*, *16*) provides an excellent test case for the efficiency of dust formation in SN ejecta.

Data in support of dust production. As dust condenses in SN ejecta, it increases the internal optical depth of the expanding ejecta, producing three observable phenomena: (i) a mid-IR excess; (ii) asymmetric blue-shifted emission lines, because the dust obscures more emission from receding gas; and (iii) an increase in optical extinction. All of these were observed from 1 to 3 years after outburst in SN 1987A (*9*, *10*). In this section, we present or confirm all three phenomena from SN 2003gd.

NGC 628 was observed by the Spitzer Infrared Nearby Galaxies Survey (SINGS) Legacy program (*17*) with Spitzer Space Telescope's Infrared Array Camera (IRAC) at 3.6, 4.5, 5.8, and 8.0 μm on 28 July 2004, or day 499 after outburst (*18*), and with the Multiband Imaging Spectrometer for Spitzer (MIPS) on 23 January 2005 (day 678) at 24 μm; the SN was also observed with IRAC as part of GO-3248 (P. I. W. P. Meikle) on 2005 Jan 15 (day 670). All data were acquired from the Spitzer archive, then spatially enhanced with the SINGS data pipelines to a final resolution of 0.″75 pixel^{-1}. A point source identified in all four IRAC bands from day 499 is consistent to within 0.″17 (0.2 IRAC pixels) with the position of the SN progenitor (Fig. 1), as measured by careful absolute and differential astrometry between the 3.6-μm IRAC image and the archival Hubble Space Telescope (HST) Wide Field and Planetary Camera 2 (WFPC2) data in which the progenitor was identified (*16*).

Photometry of the Spitzer data was performed with point-spread-function fitting techniques (*19*). The resulting flux densities are 20.8 ± 2.6 μJy at 3.6 μm, 73.8 ± 5.6 μJy at 4.5 μm, 64.9 ± 7.3 μJy at 5.8 μm, and 103 ± 22 μJy at 8.0 μm on day 499, and 106 ± 16 μJy at 24 μm on day 678; the SN is nearly undetectable in IRAC on day 670, with 3σ upper limits of 6.0, 10.6, 13.5, and 26.6 μJy at 3.6, 4.5, 5.8, and 8.0 μm, respectively (Fig. 2). An excess at 4.5 μm could be due to CO emitting at 4.6 μm (*10*). Otherwise, the rising 5.8- to 24-μm flux densities are not expected from the gaseous ejecta, which typically have temperatures of 3000 to 5000 K at these late times (*10*). It is unlikely that this emission is a thermal light echo, because the time variability of the IRAC fluxes is much faster than that expected for a typical circumstellar dust shell (*20*). Assuming that the mid-IR emission can be modeled with a single blackbody, the best fit to the 5.8- to 8.0-μm data from day 499 has a temperature of 480 K, which for an adopted distance to the SN of 9.3 Mpc (*18*) yields an integrated luminosity of 4.6×10^5 $L_{\odot}$ and an equivalent radius of 6.8×10^{15} cm. The size, temperature, and variability implied by the spectral-energy distributions (SEDs) are thus consistent with lower temperature ($T \sim 500$ K) dust that is cooling within the SN ejecta.

The first indication of such dust formation in SN 2003gd came in a comparison of broadband photometry and Hα spectra of the SN

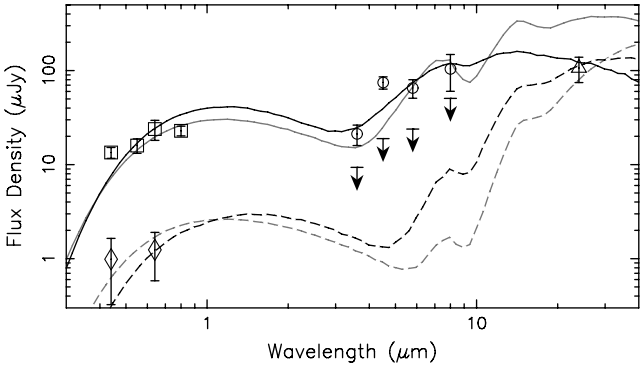

Fig. 2. Spectral-energy distribution of SN 2003gd, showing optical photometry on day 493 (squares) from (*18*) and extrapolated from day 632 (*21*) to day 678 (diamonds) based on the evolution of SN 1987A (*24*); IRAC data from day 499 (circles); upper limits to IRAC from day 670 (arrows); and the MIPS datum from day 678 (triangle). Error bars are computed with a Poisson-noise model that includes detector characteristics, and flat-field and profile uncertainties. Fluxes have been dereddened by $E(B - V) = 0.14$ (*18*). The curves are MOCASSIN radiative-transfer model fits to the data at day 499 (solid lines) and 678 (dashed lines) based on smoothly distributed (black) and clumpy (gray) dust. See text and Table 2.

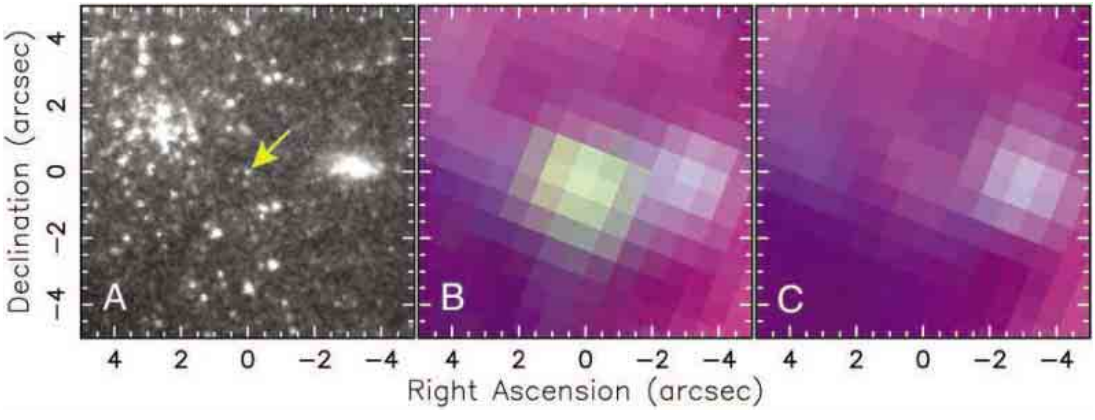

Fig. 1. Hubble and Spitzer Space Telescope images of a 10″by 10″ field centered on the position of SN 2003gd. (**A**) HST WFPC2 image taken in the F606W filter in which the SN progenitor (arrow) was identified (*15*, *18*), with a resolution of 0.″045 pixel^{-1}. (**B** and **C**) False-color SST IRAC images of the SN taken on (B) 28 July 2004 and (C) 15 January 2005, showing the 3.6-μm (blue), 4.5-μm (green), and 8.0-μm images (red). All IRAC images were processed by the SINGS collaboration to a final resolution of 0.″75 pixel^{-1}.

between days 124 and 493 (*18*), in which a small decline in the late-time luminosity was accompanied by a slight blueshift in the emission-line peaks. New spectroscopic observations of SN 2003gd were obtained in long-slit mode, covering ~4500 to 7000 Å with a spectral resolution of ~7 Å, by the Gemini Multi-Object Spectrograph (GMOS) on Gemini North on 19 August 2004 (day 521). Two spectra of SN 2003gd were obtained, which have been debiased, flattened, wavelength-calibrated, sky-subtracted, extracted, and then combined. The wavelength calibration is accurate to about 2 Å. The Hα and [O I] spectra from days 157 and 493 (*18*) are compared to the newer data in Fig. 3. Inspection of the lines confirms that the emission peak is indeed blueshifting, whereas the red high-velocity wing seen at the earliest epoch has diminished. Additionally, the most recent spectra show a clear asymmetry in the first few hundred km s^{-1} redward of each line peak. These blueshifted peaks and asymmetric profiles are consistent with a simple model in which dust with an increasing optical depth is located within an expanding sphere of uniform emission (*11*); in particular, the day 521 profiles suggest an optical extinction $A_R < 5$.

The *B*, *V*, and *R* light curves of SN 2003gd through day 493 (*18*) have been combined with the *B*- and *R*-band photometry from day 632 (*21*) in Fig. 4. Over this 500-day period, the SN is evolving almost identically to SN 1987A, with the exception that SN 2003gd is slightly subluminous in *V* and *R* around day 493. The close match between the light curves of these two SNe implies an increase in optical extinction of SN 2003gd as well.

The observed dust extinction is measured by comparing the change in photometry over time to a standard intrinsic luminosity. The internal extinction in SN 1987A is believed to have increased by $A_R = 0.8$ mag between days 525 and 700, as determined in broad-band photometry by comparing the light curve after day 525 to the best fit line through the data from days 450 to 525 (*9*). The slope of this line (Fig. 4) is extremely sensitive to the subset of the SN 1987A light curve used, and the resulting dust extinction can vary by >1 mag depending on the days included in the least-squares fit. Thus, we deem this a poor measure of the intrinsic luminosity.

The broad-band evolution of Type II SNe past ~500 days is poorly documented, because very few SNe have been observed beyond this epoch. At these late times, the light curve is dominated by the energy input of γ-rays from ^{56}Co decay, which decreases with an *e*-folding time of $\tau_{56} = 111.2$ days. The *R*-band photometry of the Type II SN 1990E (*22*) closely follows this evolution through 540 days (Fig. 4), suggesting that simple Co decay provides a good estimate of the unextinguished *R*-band light curve for at least that long. However, as the ejecta expand, their opacity to γ-rays is expected to decrease, which results in a modified light curve (*23*)

$$L_{56}(t) \propto e^{-t/\tau_{56}}[1 - e^{-\kappa_{56}\,\phi_0\,(t_0/t)^2}] \qquad (1)$$

where the term in brackets is the "effective opacity"; $\kappa_{56} = 0.033$ cm^2 g^{-1} is the average opacity to ^{56}Co-decay γ-rays, and $\phi_0 = 7 \times 10^4$ g cm^{-2} is the column depth at the fiducial time $t_0 = 11.6$ days, chosen to match the bolometric light curve of SN 1987A (*23*, *24*). Note that Eq. 1 begins fading relative to simple ^{56}Co decay around 500 days.

The Co-decay curves, both with and without the effective-opacity correction, are much more luminous than the aforementioned linear fit to SN 1987A at the time of dust formation (Fig. 4). The slopes of these Co-decay curves also closely resemble that of SN 1987A after day 775, when dust production is believed to have ended (*10*). Thus, Eq. 1 offers a more realistic standard luminosity for the unextinguished *R*-band light curve of SN 1987A. Comparison of L_{56} to the SN 1987A photometry yields extinctions of 1.5 mags around day 700 when effective opacity is included, and 2.5 mag when it is excluded. Because the evolution of SNe 1987A and 2003gd are so similar, Eq. 1 is also used to estimate the extinction of SN 2003gd at each epoch, as listed in Table 1.

Dust-mass analysis and interpretation. The observations presented above overwhelmingly point toward dust forming within the ejecta of SN 2003gd, beginning sometime between 250 and 493 days after outburst. To estimate the mass of dust present, we use the three-dimensional Monte Carlo radiative-transfer code MOCASSIN (*25*). Briefly, the paths of photon absorption, scattering, and escape are followed from a specified source through a given composition, grain-size distribution, and geometry of dust. The particular choices of these are either constrained a priori or are varied until the model emission and extinction match the observed values.

Because our hypothesis is that dust condenses within the ejecta, the radiative-transfer model is constructed under the initial assumption that the dust and source luminosity are mixed within a spherical, expanding shell with inner radius r_{in}, outer radius $Y \cdot r_{in}$, and $\rho \propto r^{-2}$ density profile, and with the illuminating radiation proportional to the dust density. Initial values for the shell size, source luminosity, and temperature are guided by the blackbody previously fit to the mid-IR data and by models

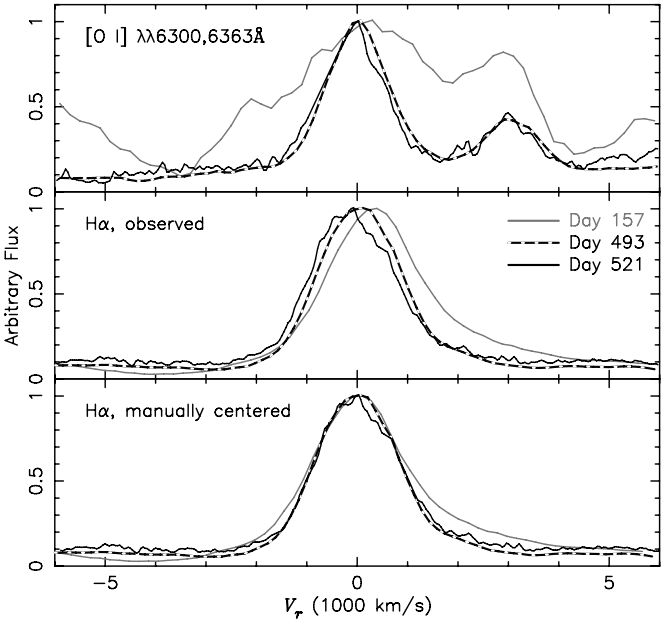

Fig. 3. Optical spectra of SN 2003gd showing [O I] λλ6300,6363 Å (**top**) and Hα (**middle** and **bottom**). Spectra have been corrected for the redshift $z = 0.00219$ of galaxy NGC 628. The gray curves are taken from the data presented in (*18*), showing the profiles at days 157 (solid line) and 493 (broken line). The solid black curve is from the new data taken on day 521 with GMOS-N on Gemini North. The profiles are normalized to an arbitrary flux scale. A monotonic blueshift in the Hα line peak, first reported by (*18*), is confirmed. The most recent spectra in all three lines also show a clear profile asymmetry redward of each line peak. This evolution is expected from dust forming homogeneously within the ejecta, which preferentially extinguishes emission from the receding (i.e., redshifted) gas.

Table 1. *R*-band extinction of SN 2003gd. Equation 1 is used with and without the effective opacity term to estimate the average and maximal extinction, respectively. The observed values are listed first, and these were used along with the *R*-band light curve of SN 1987A to extrapolate the extinction of the SN at the epochs of SST observation.

Day	A_R (mags)		
	Average	Maximal	Error
	Observed		
493	0.52	0.73	0.09
632	1.36	1.78	0.12
	Extrapolated		
499	0.53	0.74	0.14
678	1.51	2.13	0.20

of SN 1987A at similar epochs (*10*). There are numerous models for dust formation within SN ejecta [for a review, see (*26*)], most of which predict that grain sizes will remain small. We adopt a standard $a^{-3.5}$ size distribution (*27*), with grain radii between 0.005 and 0.05 μm, and the dust composition is taken to be 15% amorphous carbon and 85% silicates (*7*), with optical constants taken from (*28*, *29*). Finally, because there are very few optical and mid-IR data to constrain a given model, the source luminosity is restricted to evolve according to Eq. 1, whereas its temperature remains constant (*10*).

Two dust distributions are considered. In the first, "smooth" model, the dust is uniformly distributed throughout the shell according to the adopted density profile. However, as early as a few hours after outburst, postshock ejecta become Rayleigh-Taylor unstable (*30*, *31*), forming an inhomogeneous or "clumpy" distribution, which we model as a two-phase medium, in which spherical clumps with size $r_c = \delta \cdot (Y r_{in})$, volume filling factor f_c, and density contrast $\alpha = \rho_c/\rho$ are embedded within an interclump medium of density ρ. This is analogous to the mega-grains approximation (*32*) with the addition of a radial density profile. Only macroscopic mixing has been found in the clumpy ejecta of SN remnant Cas A (*33*), which suggests that elemental ejecta layers remain heterogeneous. We therefore assume that the source luminosity is completely separated from the dust clumps. For a given geometry, a clumpy model will always require more mass than a smooth one to fit a given SED, because clumping lowers the overall optical depth for a given mass of dust (*32*). Rather than explore the extensive parameter space of clumpy models, we study the limiting case where all dust is in clumps, i.e., $\alpha \to \infty$, which should provide upper mass limits, whereas the smooth models will provide lower mass limits. Finally, as suggested from hydrodynamic simulations (*31*), we fix $\delta = 0.025$.

Model results are summarized in Fig. 2 and Table 2. A good fit to the day 499 photometric and extinction data was achieved for the smooth model with $Y = 7$, $r_{in} = 5 \times 10^{15}$ cm, $L = 6.6 \times 10^5\ L_\odot$, and $T = 5000$ K, whereas fitting the day 678 data required changing r_{in} to 6.8×10^{15} cm and L to $9.2 \times 10^4\ L_\odot$. Clumpy models used these same parameters, with $f_c = 0.02$ on day 499, and $f_c = 0.05$ on day 678. A complete exploration of the model parameter space is beyond the scope of this work and will be presented elsewhere. In general, small changes to the model parameters have only modest effects. For example, including maximum grain sizes up to 0.25 μm (typical of dust in the interstellar medium) decreases the dust mass by less than 10%. A 10% change in δ or f_c results in a 1 to 5% change in mass for our adopted parameter ranges. Thus, the smooth and clumpy model results shown in Table 2 offer reasonably robust lower and upper mass limits, respectively.

Table 2. Dust masses and *R*-band extinction calculated by the radiative-transfer code MOCASSIN.

Day	Model	A_R	M_{dust} ($M_\odot$)
499	Smooth	0.40	2.0×10^{-4}
499	Clumpy	0.65	1.7×10^{-3}
678	Smooth	1.48	2.7×10^{-3}
678	Clumpy	1.22	2.0×10^{-2}

These clumpy-model masses, up to $2 \times 10^{-3}\ M_\odot$ on day 499 and $2 \times 10^{-2}\ M_\odot$ on day 678, are much higher than most analytic estimates of the dust mass for SN 2003gd. For example, when the same grain properties as those above are used, 5×10^{-4} and $2 \times 10^{-3}\ M_\odot$ of dust are required to produce the mid-IR emission at days 499 and 678, if all grains are visible and isothermal (*34*). When we use the mega-grains approximation for dust uniformly mixed with diffuse emission within a spherical shell (*32*), the *R*-band extinction yields masses of only 10^{-5} and $4 \times 10^{-4}\ M_\odot$ of smooth dust for days 499 and 678. In contrast, up to $5 \times 10^{-3}\ M_\odot$ of clumpy dust is deduced from the mega-grains model for day 499, which agrees well with our radiative-transfer model. However, once clumps become optically thick, only geometry (δ, f_c) determines their extinction, and thus an arbitrarily large mass of clumpy dust reproduces the extinction from day 678. This behavior of the mega-grains model makes it of limited use in determining dust masses when the observed optical depth reaches unity. We conclude that the most-often used analytic approximations can provide unreliable estimates of dust masses.

Observations similar to those presented here have demonstrated the condensation of dust in the ejecta of SN 1987A and 1999em, but the inferred masses for these SNe were only modest, on the order of $10^{-4}\ M_\odot$ (*10*, *11*). Asymmetric Hα line profiles have been detected for Type II SNe 1970G, 1979C, and 1980K (*35*); however, this phenomenon on its own is also consistent with an expanding ionization front shell of emission catching up with and passing through a preexisting dust shell and does not prove the presence of newly forming dust. For SN 1998S, asymmetric line profiles and near-IR ($\lambda < 4.7$ μm) excess emission also point toward dust condensation in the ejecta (*36*). In all these cases, the absence of contemporaneous mid-IR observations precluded a quantitative estimate of the condensation efficiency. In light of our quantitative clumpy-dust analysis, the amounts of dust believed to have formed in the ejecta of SN 1987A and 1999em—which were based upon analytical estimates—are being carefully revisited.

For a progenitor mass for SN 2003gd between 10 and 12 $M_\odot$ (*18*), roughly 0.16 to 0.42 $M_\odot$ of refractory elements are expected to form if the progenitor had solar metallicity (*37*). Assuming dust formation has finished by day 678, our derived dust mass of $2 \times 10^{-2}\ M_\odot$ for this progenitor translates into a condensation efficiency, defined here as (mass of refractory elements condensed into dust)/(mass of refractory elements in ejecta), of ≤0.12 for clumpy dust. Having found that analytic analyses of optical and IR observations tend to underestimate the dust mass by an order of magnitude or more, we deem it likely that dust formation in core-collapse SNe is much more efficient than previously believed. In particular, the efficiency implied by SN 2003gd is close to the value of 0.2 needed for SNe to account for the dust content of high-redshift galaxies (*12*). As noted earlier, too few SNe have been followed sufficiently in time and wavelength to establish the frequency with which SNe form dust. We are currently addressing this question through continued, long-term monitoring of a much larger sample of young, Type II SNe. If dust formation is found to be common in core-collapse SNe, then because most dust is expected to survive later passage through high-velocity SN shocks (*38*), we can conclude that

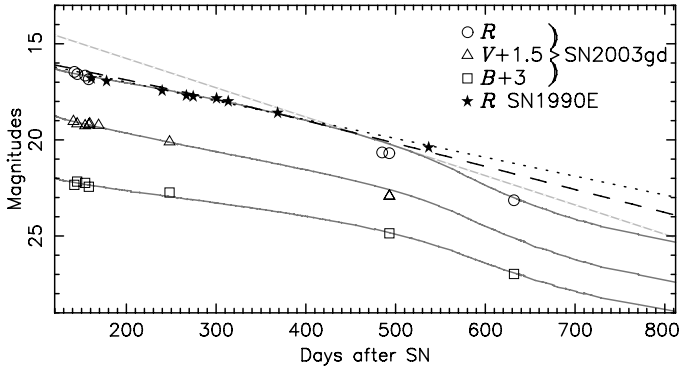

Fig. 4. Light curves of SN 2003gd, showing the increase of extinction with time. *B*, *V*, and *R* light curves of SN 2003gd compiled from (*18*) through day 493 after outburst, and (*21*) for day 632, are plotted and offset as marked. Error bars are all smaller than the point markers. For comparison, the corresponding light curves of SN 1987A (*24*) are also shown as thick gray lines, and the *R*-band light curve of SN 1990E is shown as filled stars. Also plotted in black are the light curves expected from Eq. 1 with (dashed) and without (dotted) the effective opacity term, as well as the linear fit to SN 1987A from days 450 to 525 (dashed gray) used by (*9*).

core-collapse SNe played an important role in the production of dust in the early universe.

References and Notes

1. F. Bertoldi *et al.*, *Astron. Astrophys.* **406**, L55 (2003).
2. A. G. G. M. Tielens, *Astrophys. J.* **499**, 267 (1998).
3. E. Dwek, *Astrophys. J.* **501**, 643 (1998).
4. F. Cernuschi, F. R. Marsicano, I. Kimel, *Ann. Astrophys.* **28**, 860 (1965).
5. E. Dwek, *Astrophys. J.* **329**, 814 (1988).
6. T. Kozasa, H. Hasegawa, K. Nomoto, *Astrophys. J.* **344**, 325 (1989).
7. P. Todini, A. Ferrara, *Mon. Not. R. Astron. Soc.* **325**, 726 (2001).
8. D. D. Clayton, S. Amari, E. Zinner, *Astrophys. Space Sci.* **251**, 355 (1997).
9. L. B. Lucy, I. J. Danziger, C. Gouiffes, P. Bouchet, in *Supernovae. The Tenth Santa Cruz Workshop in Astronomy and Astrophysics*, S. E. Woosley, Ed. (Springer-Verlag, New York, 1991), p. 82.
10. D. H. Wooden *et al.*, *Astrophys. J. Suppl. Ser.* **88**, 477 (1993).
11. A. Elmhamdi *et al.*, *Mon. Not. R. Astron. Soc.* **338**, 939 (2003).
12. H. L. Morgan, M. G. Edmunds, *Mon. Not. R. Astron. Soc.* **343**, 427 (2003).
13. D. C. Hines *et al.*, *Astrophys. J. Suppl. Ser.* **154**, 290 (2004).
14. O. Krause *et al.*, *Nature* **432**, 596 (2004).
15. S. D. Van Dyk, W. Li, A. V. Filippenko, *Publ. Astron. Soc. Pac.* **115**, 1289 (2003).
16. S. J. Smartt *et al.*, *Science* **303**, 499 (2004).
17. R. C. Kennicutt Jr. *et al.*, *Publ. Astron. Soc. Pac.* **115**, 928 (2003).
18. M. A. Hendry *et al.*, *Mon. Not. R. Astron. Soc.* **359**, 906 (2005).
19. P. B. Stetson, *Publ. Astron. Soc. Pac.* **99**, 191 (1987).
20. E. Dwek, *Astrophys. J.* **274**, 75 (1983).
21. B. E. K. Sugerman, *Astrophys. J.* **632**, L17 (2005).
22. S. Benetti *et al.*, *Astron. Astrophys.* **285**, 147 (1994).
23. S. E. Woosley, D. Hartmann, P. A. Pinto, *Astrophys. J.* **346**, 395 (1989).
24. N. B. Suntzeff, P. Bouchet, *Astron. J.* **99**, 650 (1990).
25. B. Ercolano, M. J. Barlow, P. J. Storey, *Mon. Not. R. Astron. Soc.* **362**, 1038 (2005).
26. D. D. Clayton, L. R. Nittler, *Annu. Rev. Astron. Astrophys.* **42**, 39 (2004).
27. J. S. Mathis, W. Rumpl, K. H. Nordsieck, *Astrophys. J.* **217**, 425 (1977).
28. B. T. Draine, H. M. Lee, *Astrophys. J.* **285**, 89 (1984).
29. M. S. Hanner, *NASA Conf. Pub.* **3004**, 22 (1988).
30. R. A. Chevalier, R. I. Klein, *Astrophys. J.* **219**, 994 (1978).
31. M. Herant, S. E. Woosley, *Astrophys. J.* **425**, 814 (1994).
32. F. Városi, E. Dwek, *Astrophys. J.* **523**, 265 (1999).
33. T. Douvion, P. O. Lagage, C. J. Cesarsky, *Astron. Astrophys.* **352**, L111 (1999).
34. S. D. Doty, C. M. Leung, *Astrophys. J.* **424**, 729 (1994).
35. R. A. Fesen *et al.*, *Astron. J.* **117**, 725 (1999).
36. M. Pozzo *et al.*, *Mon. Not. R. Astron. Soc.* **352**, 457 (2004).
37. S. E. Woosley, T. A. Weaver, *Astrophys. J. Suppl. Ser.* **101**, 181 (1995).
38. T. Nozawa, T. Kozasa, A. Habe, http://arxiv.org/abs/astro-ph/0605193.

39. We gratefully acknowledge M. Hendry for providing optical spectra of SN 2003gd, and E. Dwek and P. Ghavamian for useful discussions. This work is based in part on archival data obtained with the Spitzer Space Telescope, which is operated by the Jet Propulsion Laboratory, California Institute of Technology, under a contract with NASA; with the NASA/European Space Agency Hubble Space Telescope, obtained from the Data Archive at the Space Telescope Science Institute, which is operated by the Association of Universities for Research in Astronomy, Inc. (AURA), under NASA contract NAS 5-26555; and on observations obtained during the program GN-2004B-C-3 at the Gemini Observatory, which is operated by AURA under a cooperative agreement with the NSF on behalf of the Gemini partnership. Support for B.E.K.S. for this work was provided by Spitzer Space Telescope award GO-20320 issued by the Jet Propulsion Laboratory/California Institute of Technology (JPL/Caltech). D.L.W. acknowledges support from the Natural Sciences and Engineering Research Council of Canada. M.C.'s participation was supported by JPL contract 1269553 with the Monterey Institute for Research in Astronomy.

30 March 2006; accepted 30 May 2006
Published online 8 June 2006;
10.1126/science.1128131
Include this information when citing this paper.

REPORTS

Electric Fields at the Active Site of an Enzyme: Direct Comparison of Experiment with Theory

Ian T. Suydam, Christopher D. Snow, Vijay S. Pande, Steven G. Boxer*

The electric fields produced in folded proteins influence nearly every aspect of protein function. We present a vibrational spectroscopy technique that measures changes in electric field at a specific site of a protein as shifts in frequency (Stark shifts) of a calibrated nitrile vibration. A nitrile-containing inhibitor is used to deliver a unique probe vibration to the active site of human aldose reductase, and the response of the nitrile stretch frequency is measured for a series of mutations in the enzyme active site. These shifts yield quantitative information on electric fields that can be directly compared with electrostatics calculations. We show that extensive molecular dynamics simulations and ensemble averaging are required to reproduce the observed changes in field.

The organization of charged and polar groups in the folded state of proteins produces large electric fields that influence nearly every aspect of protein function. Electrostatics calculations suggest that these fields vary markedly from site to site in magnitude and direction (*1*–*3*). The consequence of such variations can be appreciated by considering a dipolar transition state that separates a unit charge over a distance of 1 Å. If this dipole were parallel to a field of 10 MV/cm, not atypical of fields that are estimated to be present in proteins, the energy of the transition state would be lowered by 9.6 kJ/mol; thus, the magnitude and direction of the field could have a substantial effect on the rate of reaction. Simulations on a large number of enzymes support this hypothesis and have shown that preorganized electric fields in active sites contribute substantially to transition-state stabilization (*4*).

Colorful maps of electrostatic potentials are routinely included in papers describing or analyzing protein structures and are often used to speculate on the electrostatic contributions to a variety of protein functions. However, there are relatively few experiments that can be used to test these calculations directly. Common benchmarks related to changes in free energies, such as pK_a shifts (where K_a is the acid dissociation constant), redox potential shifts, or binding constants, depend on a convolution of factors including electrostatic interactions, making direct comparisons to calculated potentials difficult. Similarly, electrostatic interactions can contribute substantially to the effect of mutations on the rates of enzyme-catalyzed reactions, but it is difficult to isolate their contribution.

In contrast, spectroscopic observables that relate directly to electric fields provide a straightforward connection to calculated potentials (*5*, *6*). The vibrational Stark effect, which describes the effect of an electric field on a molecular vibration, provides a particularly straightforward approach. The vibrational Stark tuning rate gives the sensitivity of a probe vibration to an electric field and can be calibrated by measuring the vibrational Stark spectrum in a known external electric field (*7*, *8*). Once calibrated, a probe vibration acts as a local reporter of its electrostatic environment; its frequency shifts in response to changes in nearby amino acids or protonation states, offering a direct measurement of the electric field change at specific sites. For many vibrations, the effect of an electric field on the stretching frequency is dominated by the projection of $\Delta\vec{\mu}_{probe}$, the change in dipole moment between the ground and excited states of the probe transition, along the electric field vector (*8*–*12*)

$$hc\Delta\bar{\nu}_{obs} = -\Delta\vec{\mu}_{probe} \cdot \Delta\vec{F}_{protein} \qquad (1)$$

Department of Chemistry, Stanford University, Stanford, CA 94305–5080, USA.

*To whom correspondence should be addressed. E-mail: sboxer@stanford.edu

where $\Delta\bar{\nu}_{obs}$ is the observed frequency shift in cm^{-1}, h is Planck's constant, c is the speed of light, and $\Delta\vec{F}_{protein}$ is the change in field at the probe location between two states of the protein—for example, two conformational states, two protonation states, or two mutants.

Previous vibrational Stark effect measurements in proteins have focused almost exclusively on the special case of diatomic ligands bound to heme cofactors, most notably carbon monoxide–bound myoglobin (*7*, *13*). Bound CO is an ideal vibrational probe because its frequency is isolated, the transition is intense, and one can obtain high-quality light-minus-dark difference spectra through CO photolysis. We sought to identify vibrational probes that could be applied more generally. The nitrile (-C≡N) stretching mode has nearly ideal properties for a vibrational probe, because its frequency is distinct from those of any protein absorption, it is quite intense, $\Delta\vec{\mu}_{probe}$ is relatively large, and $\Delta\vec{\mu}_{probe}$ lies along the nitrile bond in mononitriles, oriented from the nitrogen toward the carbon (*8*–*10*, *12*). The well-defined relationship between molecular structure and the direction of $\Delta\vec{\mu}_{probe}$ provides a straightforward connection between observed frequency shifts, $\Delta\bar{\nu}_{obs}$, and changes in field, $\Delta\vec{F}_{protein}$, along the nitrile bond. Aromatic nitriles can be incorporated into proteins through chemical and biosynthetic strategies, and individual nitrile vibrations can be observed in the background of a protein (*14*, *15*).

Here, we used vibrational Stark shifts to measure changes in electric fields caused by mutations in the active site of the enzyme human aldose reductase (hALR2) (Fig. 1). Aldose reductase catalyzes the first step in the polyol pathway, an alternative route of glucose metabolism that has been implicated in a number of diabetic complications (*16*). hALR2 has been the subject of numerous inhibition and structural studies, culminating recently in a collection of inhibitor-bound structures solved at ultrahigh resolution (*17*, *18*). This wealth of structural data provides an excellent starting point for the design of mutations anticipated to alter the field in the active site and electrostatics calculations at various levels of theory (*19*). In addition, the nitrile containing inhibitor IDD743 (indexed by the Institute for Diabetes Discovery) (Fig. 1C) had been described and shown to inhibit hALR2 with a median inhibitory concentration (IC_{50}) of 7 nM (*18*), providing a convenient method of delivering a nitrile probe vibration to the active site in a well-defined orientation. Ultrahigh-resolution crystal structures have been reported for hALR2 with two closely related inhibitors, IDD393 and IDD594 (Fig. 1C), bound in the active site (*17*, *20*). The orientations of IDD393 and IDD594 in these structures are very similar, and the IDD594 structure is of sufficient resolution (0.66 Å) to identify 77% of active-site hydrogens, clearly defining the protonation state of several titratable residues in the active site.

The vibrational Stark spectrum of the IDD743 nitrile stretch is similar to those obtained for other aromatic nitriles (*8*, *10*), and a fit to the vibrational Stark spectrum yields a magnitude for $\Delta\vec{\mu}_{probe}$ of 0.041 D (fig. S1). Defining the nitrile axis as pointing from carbon toward nitrogen, $\Delta\vec{\mu}_{probe}/hc = -0.69\ cm^{-1}/(MV/cm)$, leading to Eq. 2:

$$\Delta\bar{\nu}_{obs} = 0.69(cm^{-1}/(MV/cm)) \bullet \Delta F_{\parallel} \quad (2)$$

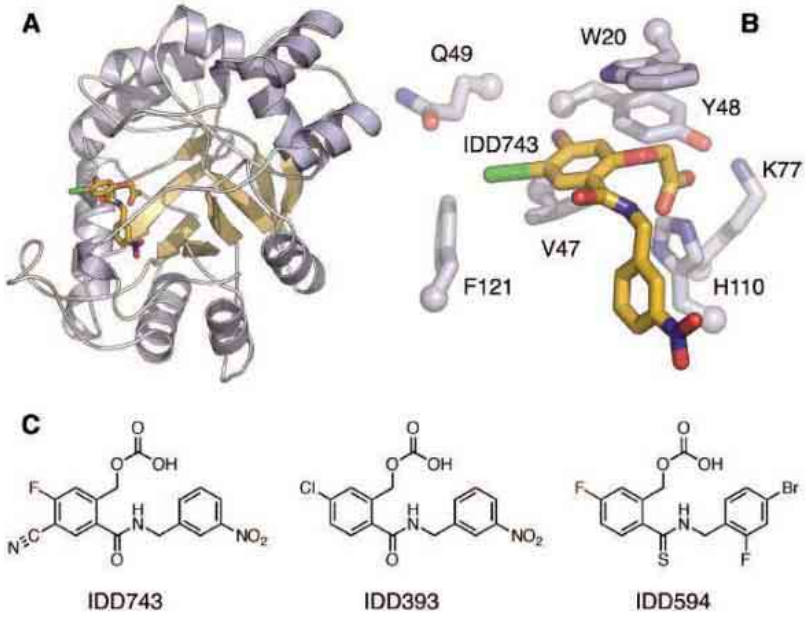

Fig. 1. Model of the hALR2/$NADP^+$/IDD743 structure. (**A**) Location of IDD743 in the tertiary structure. (**B**) Location of side chains mutated in this study relative to the nitrile of IDD743 (green). (**C**) Chemical structure of IDD743 and closely related inhibitors, IDD393 and IDD594, for which high-resolution structures are available (*17*, *20*).

where $\Delta\bar{\nu}_{obs}$ is the cm^{-1} change in nitrile stretching frequency observed in a mutant of hALR2 relative to the wild-type (WT) protein, $(\bar{\nu}_{mutant} - \bar{\nu}_{WT})$, and $\Delta F_{\parallel}$ is the MV/cm change in the electric field along the nitrile axis between the mutant and wild type $(F_{\parallel,mutant} - F_{\parallel,WT})$. According to this calibration, a mutation that causes a change in field of +1.0 MV/cm along the IDD743 nitrile would cause a shift in the nitrile stretching frequency of +0.69 cm^{-1}.

To demonstrate the ability of a nitrile vibration to report on electric field changes caused by mutation, we designed a series of mutants predicted to produce large changes in the field along the nitrile of IDD743. Mutations were initially screened by performing continuum electrostatics calculations on the wild-type protein and a large number of potential mutants [input structures were modeled from the available IDD393 and IDD594 structures (*21*)]. For the $V^{47}\rightarrow D^{47}$ (V47D) mutation (*22*), continuum calculations performed with the internal dielectric set to 4 predicted large changes in both electric potential at the nitrile and electric field projection along the nitrile (Fig. 2), giving rise to a predicted $\Delta\bar{\nu}$ of –6.8 cm^{-1}. From the mutations screened, eight were chosen for actual mutagenesis and infrared experiments, two of which made direct contacts with the inhibitor but were predicted to minimally perturb the field at the nitrile (Y48F and H110A), three of which were predicted to cause a measurable positive change in field at the nitrile (W20Y, V47N, and F121E), and three of which were predicted to cause a measurable negative change in field at the nitrile (V47D, Q49R, and K77M) (table S3). On the basis of the IDD393 and IDD594 structures, each mutated residue is expected to lie within 11 Å of the IDD743 nitrile, which is positioned at the active-site cleft of the enzyme. The selected mutations included buried (Y48F, K77M, and H110A), partially exposed (W20Y, V47D, and V47N), and fully solvated (Q49R and F121E) sites, and each either added or removed substantial charge or polarity.

Wild-type and mutant proteins were expressed and purified as described in the literature (*23*). Proper folds were confirmed by kinetic assay or by circular dichroism spectroscopy, and cofactor binding was confirmed by kinetic assay or by the spectral shift in the 340-nm absorption band of reduced nicotinamide adenine dinucleotide phosphate (NADPH) upon binding (*21*). Samples for infrared spectroscopy were prepared as 1:1:1 complexes of hALR2:$NADP^+$:IDD743, the state of the enzyme present in the IDD393 and IDD594 crystal structures [for details of mutant characterization, sample preparation, and infrared absorption experiments, see (*21*)]. Although the nitrile absorption band widths (Fig. 3A) were larger than the observed frequency shift for the mutations studied, frequency shifts measurable with our experimental resolution (0.5 cm^{-1}) were observed for several mutants

(table S2). The V47D mutation shifts the nitrile stretching frequency by –1.6 cm^{-1}, corresponding to a change in field along the nitrile bond of –2.3 MV/cm relative to the wild-type protein. This change in field is much smaller than that predicted from continuum electrostatics calculations on the initial model for V47D (–9.9 MV/cm). In general, the Stark shifts observed in the mutant spectra correlated poorly with predictions based on substitution of the calculated fields into Eq. 2 (Fig. 4).

Because the discrepancy between observed and expected frequency shifts was greatest for the two mutations closest to the nitrile, V47D and V47N, we explored the effect of side chain conformation on the calculated fields for these mutations. Conformational flexibility is a common problem in using continuum electrostatics calculations to predict changes in potential or field caused by mutations or protonation events (*24*). Uncertainty in side chain conformations is often modeled by choosing a slightly higher value for the internal dielectric, but such dielectric scaling is not expected to remove local errors (*25*, *26*). This problem was most evident for the V47N mutation. Here, reversing the orientation of the side chain amide led to a sign reversal of the predicted change in field, a particularly notable example of the importance of side chain orientation.

To evaluate the consequences of uncertainty and appropriate averaging in side chain positions, we used a large set of independent molecular dynamics (MD) simulations to relax the initial models toward an ensemble of structures more representative of equilibrium conformations. Techniques that combine MD simulations with electrostatics calculations have become increasingly popular and range in complexity from combined quantum mechanical and molecular mechanical methods to approxima-

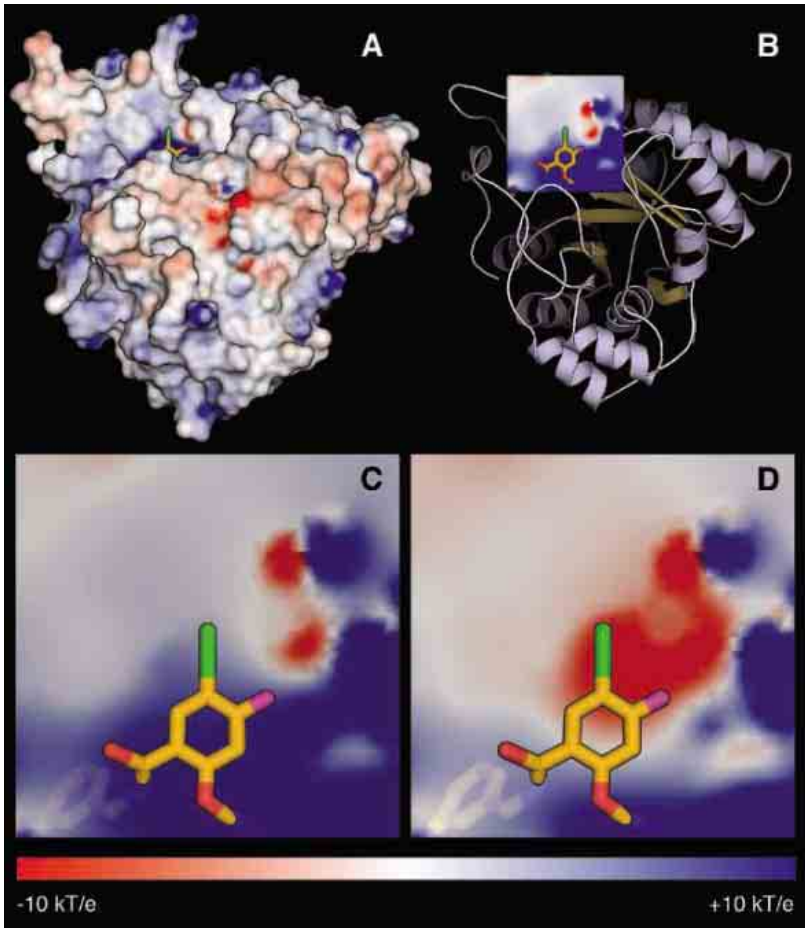

Fig. 2. (**A**) Result of continuum electrostatics calculation, with the interior dielectric set to 4, on the initial model of wild-type hALR2/$NADP^+$/IDD743. Electrostatic potentials are plotted on the surface of the enzyme from –10 *kT/e* (red) to +10 *kT/e* (blue), where *k* is the Boltzmann constant, *T* is temperature, and *e* is the charge of the electron. (**B**) Potentials from (A) plotted on a two-dimensional slice running through the nitrile of IDD743 (green). (**C**) Expanded view of slice in (B) in the vicinity of the nitrile probe. (**D**) Result of continuum electrostatics calculation, with the interior dielectric set to 4, on the initial model of V47D hALR2/$NADP^+$/IDD743. Electrostatic potentials are plotted on the same slice as in (C). The calculated change in field along the nitrile bond for the V47D mutation is –3.86 *kT/e*Å relative to the wild-type protein (1 *kT/e*Å = 2.57 MV/cm at 298 K).

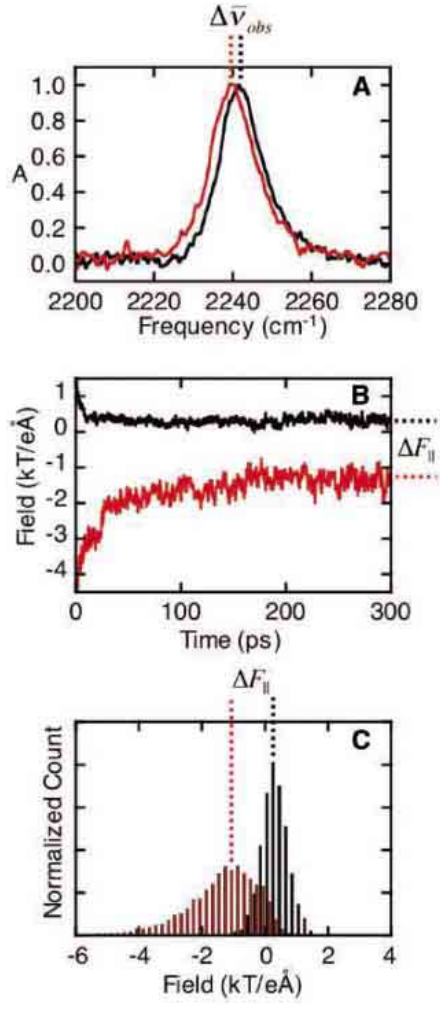

Fig. 3. (**A**) Infrared absorption spectra of IDD743 bound to wild-type (black) and V47D (red) hALR2 in the nitrile stretch region. Absorption spectra were scaled to an absorbance of 1.0 at the absorption maximum (typical absorption maxima were between 0.001 and 0.002). Nitrile stretching frequencies for the mutants studied were as follows (in cm^{-1}): wild type (2241.6), W20Y (2240.9), V47D (2240.0), V47N (2238.5), Y48F (2240.2), Q49R (2241.2), K77M (2239.4), H110A (2242.1), and F121E (2240.7) (**B**) Average trajectory of electric field along the nitrile bond of IDD7434 bound to wild-type (black) and V47D (red) hALR2. Each point is the average of continuum electrostatics calculations, with the interior dielectric set to 2, performed on multiple MD-generated structures. The predicted change in field relaxes from greater than –5 to –1.75 *kT/e*Å in the first 200 ps of the average trajectory. (**C**) Normalized distribution of electric field along the nitrile of IDD743 for wild-type (black) and V47D (red). Electric field values were obtained from continuum electrostatics calculations, with the interior dielectric set to 2, performed on structures obtained from MD trajectories at time points greater than 200 ps. Dotted lines in (B) and (C) represent the mean values of the distributions provided in (C).

tions of the continuum model such as the generalized Born method (*2*). The choice of method depends on the quality of the structural data available, the size of the system investigated, and the time scale of the motions of interest. Both structural reorganization and the consideration of a diverse thermal ensemble are crucial. Because structural data are not yet available for the mutations studied (and even with structures, the data are often not of sufficient resolution, especially for side chain orientations) we chose a simulation method that allows the long time-scale dynamics that might be required to observe side chain reorganization to the equilibrium ensemble. Dynamics simulations also allow an estimate of the distribution in electric field produced by thermal fluctuations about an equilibrium structure. This distribution of calculated electric fields should better represent the time-averaged environment reported in the infrared spectra.

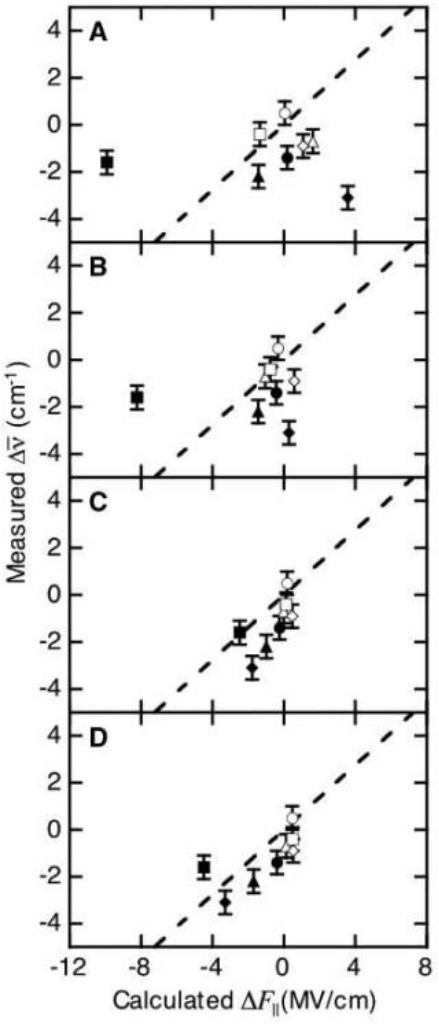

Fig. 4. Correlation between observed changes in frequency and calculated changes in electric field along the nitrile bond of IDD743, $\Delta F_{\parallel}$, for all mutants relative to wild-type: H110A (○), Q49R (□), W20Y (△), F121E (◇), Y48F (●), V47D (■), K77M (▲), and V47N (◆). (**A**) $\Delta F_{\parallel}$ calculated using initial structure models, with the interior dielectric set to 4. (**B**) $\Delta F_{\parallel}$ calculated using energy-minimized structure models, with the interior dielectric set to 4. (**C**) $\Delta F_{\parallel}$ calculated from the mean of electric field distributions. Distributions were generated by performing continuum electrostatics calculations on structures obtained from MD trajectories at time points greater than 200 ps. Each individual continuum electrostatics calculation was performed with the internal dielectric set to 4. (**D**) $\Delta F_{\parallel}$ calculated from the mean of field distributions as in (C), but with the internal dielectric of each continuum electrostatics calculation set to 2. The dashed lines in (A) to (D) represent the linear correlation expected from Eq. 2.

To obtain statistically meaningful values of the time-averaged fields, we simulated multiple MD trajectories for up to 500 ps. Each initial model was energy minimized, and 50 independent implicit-solvent MD simulations were initiated. Trajectories were calculated with the distributed computing platform Folding@Home (*27*) with structures saved every 0.5 ps (*21*). After the completion of these simulations, continuum electrostatics calculations were performed on each saved structure, providing the electric potentials and fields as a function of time along each trajectory. The potentials and fields for all structures were calculated using an interior dielectric value of 4 and repeated using an internal dielectric of 2 to test the dependence of the fields on this parameter. For each minimized mutant structure, we performed more than 5000 continuum calculations at time steps along multiple trajectories and then calculated the time-dependent ensemble average projections of the electric field along the nitrile bond (Fig. 3B).

The importance of relaxing initial models is evident from the predicted change in field as a function of time along these trajectories. Ensemble average field trajectories of this type were generated for each mutant (fig. S3) and the predicted field was stable within 200 ps for all mutants except V47N. For the V47N mutation, a very slow relaxation toward more negative field values was observed through 500 ps. Inspection of individual trajectories identified the flip of the Asn^{47} side chain amide as the origin of this slow relaxation, with the conformation aligning the side chain amide dipole with the nitrile bond vector accumulating in time. Comparative analysis of five additional V47N ensembles, each starting from a different initial conformation, suggested that the low-field Asn rotamer is favored at equilibrium. MD simulations initiated from models with the Asn^{47} side chain amide in the favored conformation led to stable values of the field by 100 ps (fig. S3). The orientation of side chain amides is a major source of uncertainty in electrostatics calculations because the vast majority of structures are of insufficient resolution to define their orientation. The Asn^{47} trajectories suggest that the barrier to rotation for side chain amides can be high, and that the orientation of side chain amides can have a profound effect on local fields. Thus, the observed negative frequency shift for the V47N mutation provides a strong prediction for the relative orientation of the Asn^{47} amide when IDD743 is bound.

To obtain relaxed values of the field along the IDD743 nitrile, we collected more than 2000 structures from trajectory time points longer than 200 ps for the wild-type protein and for each mutant; we then performed continuum calculations, first with an interior dielectric of 4 and then with an internal dielectric of 2, for each structure, generating field distributions past 200 ps (*21*) (Fig. 3C). The mean values of these distributions were then used to calculate the change in field between mutants and the wild-type protein (*28*). Using bootstrap analysis, we estimated that the statistical error for changes in field calculated from these distributions is at most 0.05 MV/cm, although we expect additional systematic error in the calculated fields to arise from MD and continuum electrostatics parameters that have not been optimized to reproduce electric field values.

The substantial improvement in the correlation relative to that obtained from the initial models demonstrates the importance of relaxing side chain conformations (a process that requires hundreds of picoseconds or more). Perhaps the most important aspect of the calculated distributions of field is that the width of these distributions is greater than the difference in means for any two mutants (fig. S4). These widths demonstrate that the sensitivity of the field to small structural changes can be much greater than the average change in field caused by mutation. For several of the mutants studied, the fields predicted from initial models and energy-minimized structures derived from those models fell in the far wings of the later calculated distribution, resulting in the poor frequency-to-field correlation (Fig. 4, A and B). Attempts to accurately calculate the time-averaged field from a single structure rely on obtaining a structure that represents the mean of these distributions, a challenge even when good structural data are available.

Continuum models are one of the most popular methods of calculating electrostatic properties of macromolecules. For many applications, the property of interest is a state of the system for which complete structural information is not available—for example, the effect of a mutation, side chain protonation, or the modification of functional groups in a bound ligand or inhibitor. Our results reinforce the importance of MD in calculating average electric fields or potentials. The observed frequency shifts also demonstrate the utility of nitrile vibrations as probes of electrostatic fields in proteins. Because obtaining high-quality nitrile absorption spectra in protein solutions is straightforward (*21*), this functional group should be widely applicable as a probe of electrostatics. For hALR2, the approach could be readily extended to measure changes in field at solvent-excluded sites in the

inhibitor binding pocket, where several mutations are predicted to produce much larger frequency shifts, including mutations at residues believed to be important for inhibitor specificity. Nitriles are a relatively common substituent in inhibitors and marketed drugs, and this method provides a strategy to probe the active sites of a large number of enzymes. Techniques to incorporate nitriles by means of nonnatural amino acids or chemical modification of amino acids have also been demonstrated and should allow similar measurements in a variety of protein systems. Direct comparison between experimental and computational field distributions should lead to improved electrostatics calculation methodology.

References and Notes

1. B. Honig, A. Nicholls, *Science* **268**, 1144 (1995).
2. T. Simonson, *Curr. Opin. Struct. Biol.* **11**, 243 (2001).
3. A. Warshel, A. Papazyan, *Curr. Opin. Struct. Biol.* **8**, 211 (1998).
4. J. Villa, A. Warshel, *J. Phys. Chem. B* **105**, 7887 (2001).
5. G. U. Bublitz, S. G. Boxer, *Annu. Rev. Phys. Chem.* **48**, 213 (1997).
6. E. Oldfield, *Annu. Rev. Phys. Chem.* **53**, 349 (2002).
7. E. S. Park, S. S. Andrews, R. B. Hu, S. G. Boxer, *J. Phy. Chem. B* **103**, 9813 (1999).
8. S. S. Andrews, S. G. Boxer, *J. Phys. Chem. A* **104**, 11853 (2000).
9. S. S. Andrews, S. G. Boxer, *J. Phys. Chem. A* **106**, 469 (2002).
10. I. T. Suydam, S. G. Boxer, *Biochemistry* **42**, 12050 (2003).
11. E. S. Park, S. G. Boxer, *J. Phys. Chem. B* **106**, 5800 (2002).
12. J. R. Reimers, J. Zeng, N. S. Hush, *J. Phys. Chem.* **100**, 1498 (1996).
13. H. Lehle *et al.*, *Biophys. J.* **88**, 1978 (2005).
14. K. Kirshenbaum, I. S. Carrico, D. A. Tirrell, *ChemBioChem* **3**, 235 (2002).
15. Z. Getahun *et al.*, *J. Am. Chem. Soc.* **125**, 405 (2003).
16. S. K. Srivastava, K. V. Ramana, A. Bhatnagar, *Endocr. Rev.* **26**, 380 (2005).
17. A. Podjarny, R. E. Cachau, T. Schneider, M. Van Zandt, A. Joachimiak, *Cell. Mol. Life Sci.* **61**, 763 (2004).
18. M. C. Van Zandt *et al.*, *Bioorg. Med. Chem.* **12**, 5661 (2004).
19. N. Muzet, B. Guillot, C. Jelsch, E. Howard, C. Lecomte, *Proc. Natl. Acad. Sci. U.S.A.* **100**, 8742 (2003).
20. E. I. Howard *et al.*, *Proteins Struct. Funct. Bioinform.* **55**, 792 (2004).
21. Materials and methods are available as supporting material on *Science* Online.
22. Single-letter abbreviations for the amino acid residues are as follows: A, Ala; C, Cys; D, Asp; E, Glu; F, Phe; G, Gly; H, His; I, Ile; K, Lys; L, Leu; M, Met; N, Asn; P, Pro; Q, Gln; R, Arg; S, Ser; T, Thr; V, Val; W, Trp; and Y, Tyr.
23. V. Lamour *et al.*, *Acta Crystallogr.* **55**, 721 (1999).
24. R. E. Georgescu, E. G. Alexov, M. R. Gunner, *Biophys. J.* **83**, 1731 (2002).
25. M. K. Gilson, B. H. Honig, *Biopolymers* **25**, 2097 (1986).
26. C. N. Schutz, A. Warshel, *Proteins Struct. Funct. Genet.* **44**, 400 (2001).
27. C. D. Snow, E. J. Sorin, Y. M. Rhee, V. S. Pande, *Annu. Rev. Biophys. Biomol. Struct.* **34**, 43 (2005).
28. This method of obtaining time-averaged electric fields is qualitatively similar to that used by Warshel and Oldfield to relate ^{19}F nuclear magnetic resonance chemical shifts in [5-^{19}F]tryptophan-labeled galactose binding protein to differences in electric field at each tryptophan position (*29*). That study calculated electric fields for a fluorine-substituted wild-type structure, whereas we wished to calculate fields for mutations for which structural information was unavailable. Our continuum solvent models are approximate in comparison to the Local Reaction Field method used in that study. However, distributed MD simulations allowed us to reach longer simulation times. These long time dynamics were required to converge the calculated fields for several of the mutants studied.
29. J. G. Pearson, E. Oldfield, F. S. Lee, A. Warshel, *J. Am. Chem. Soc.* **115**, 6851 (1993).

30. We thank M. Van Zandt and co-workers for providing the inhibitor IDD743 and for many helpful comments, A. Podjarny for structural information used to model IDD743 binding, and A. Fafarman for electronic structure calculations used to parameterize electrostatics calculations and MD simulations. Supported by grants from the NIH, NSF Chemistry Division, and Howard Hughes Medical Institute predoctoral fellowship program (C.D.S.).

Supporting Online Material

www.sciencemag.org/cgi/content/full/313/5784/200/DC1
Materials and Methods
Figs. S1 to S4
Tables S1 to S3
References
Databases S1 to S3

8 March 2006; accepted 5 June 2006
10.1126/science.1127159

Negative Coulomb Drag in a One-Dimensional Wire

M. Yamamoto,[1,2] M. Stopa,[3] Y. Tokura,[4,5] Y. Hirayama,[2,4] S. Tarucha[1,5]

We observed negative Coulomb drag for parallel coupled quantum wires, in which electrons flow in the opposite directions between the wires. This only occurred under the conditions of strong correlation in the wires, that is, low density, high magnetic field, and low temperature, and cannot be addressed by a standard theory of momentum transfer. We propose a Coulomb drag model in which formation of a Wigner crystal state in the drag wire and a particle-like state in the drive wire is taken into account.

Electrons experiencing strong Coulomb interaction in a homogeneous positive charge background tend to crystallize at low temperatures into a "Wigner crystal" state (*1*), and Wigner crystallization for two-dimensional (2D) electrons at a semiconductor hetero-interface and on liquid He surfaces (*2*) has been well studied. The interaction effect is expected to be stronger in lower dimensions, that is, in 1D rather than 2D, and also as the electron density becomes small, due to the relative dominance of Coulomb over kinetic energy and to reduced screening (*3*–*7*). Consequently, considerable effort has been devoted to the exploration of the electronic properties of dilute 1D electron systems, or "quantum wires." However, the experimental evidence for a Wigner crystal state in 1D has long been elusive. Measurement of Coulomb drag (*8*, *9*) is more relevant for studying electronic interaction effects and occurs for adjacent, current-carrying systems that exchange momentum and energy via Coulomb interactions (*10*, *11*). Because Coulomb drag is ultimately a probe of charge inhomogeneity (*12*–*15*), it can be used to investigate spontaneous charge fluctuations due to many-body correlation.

Consider two parallel coupled quantum wires. When coupling occurs via momentum-conserving Coulombic scattering (and the particles do not have negative mass such as at the top of a band), electrons in one of the wires (drag wire) are dragged in the same direction as the electron flow in the other wire (drive wire). This phenomenon is called positive Coulomb drag. By contrast, when the drag wire has a relatively low electron density and when the drive wire has a very low electron density, we observe negative Coulomb drag, in which electrons in the drag wire are pumped against the bias voltage direction in the drive wire. This negative drag is unexpected from existing theories of Coulomb drag. Because negative drag is enhanced in a high magnetic field and low temperature, electronic correlation is essential for this phenomenon. We propose a model of a 1D Wigner crystal state in the drag wire to account for our experimental data.

An *n*-AlGaAs/GaAs heterostructure was used to fabricate two configurations of coupled parallel wires in a 2D electron gas (2DEG) (Fig. 1). The first set of coupled wires (CW1) consisted of two wires with the same length, L_0, whereas the second set (CW2) had wires with differing lengths, L_s and L_l. We previously used CW1s with L_0 of 1, 2, and 4 μm to explore the locking of two Tomonaga-Luttinger liquids (*9*). In this work, we used the same CW1s but with a lower electron density and applied high magnetic fields perpendicular to the 2DEG plane to study the effects of strong correlation. CW2 with L_s of 2(4) μm and L_l of 4(8) μm were newly prepared for this work.

[1]Department of Applied Physics, University of Tokyo, Bunkyo-ku, Tokyo 113-8656, Japan. [2]SORST (Solution-Oriented Research for Science and Technology) Interacting Carrier Electronics, Kawaguchi-shi, Saitama 331-0012, Japan. [3]Center for Nanoscale Systems, Harvard University, Cambridge, MA 02138, USA. [4]NTT Basic Research Laboratories, Atsugi-shi, Kanagawa 243-0198, Japan. [5]ICORP (International Cooperative Research Project) Quantum Spin Information Project, Atsugi-shi, Kanagawa 243-0198, Japan.

In the Coulomb drag measurement, we injected a constant current I into the drive wire and measured the voltage drop V_{drag} along the drag wire. We used a low frequency (1 to 7 Hz) alternating current (AC) lock-in technique, but beforehand we confirmed the drag signal itself in a direct current (DC) measurement. The drag resistance, R_D, is defined as $R_D = -V_{drag}/I$, which is normally positive. The current I was set to be small enough ($\leq$ 1 nA) to suppress inter-subband coupling of electrons propagating in the drive wire. In this regime, the relationship between I and V_{drag} was linear. However, for a very small current (order pA) the I-V_{drag} relationship became nonlinear. Both the drive and drag wires showed a plateau-like conductance feature, which was lower than the quantized value, because of scattering in the lengthy wires [Supporting Online Material (SOM) Text]. Negative R_D was observed when the conductance was lower than the flat region of the lowest plateau for both wires. In this regime, electrons propagate through a single-mode 1D channel in the wire with transmission probability less than 1, and the electron density of each wire becomes small as the side gate voltage is made more negative.

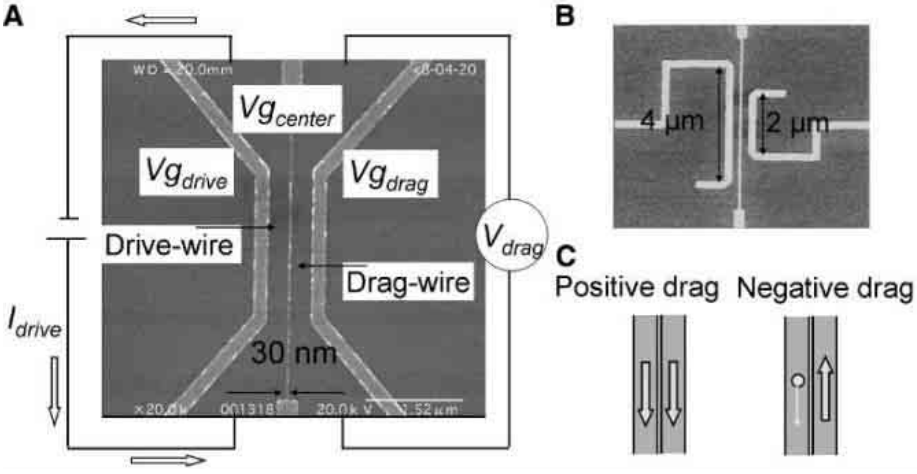

Fig. 1. (**A**) Scanning electron microscopy (SEM) image of CW1 and experimental setup. Devices were defined by three Schottky gates in an *n*-AlGaAs/GaAs 2DEG-based heterostructure (for *n*-AlGaAs/GaAs, 2DEG mobility was $\mu \cong 10^6$ cm^2 V^{-1} s^{-1}, electron density was $n_s \cong 3 \times 10^{11}$ cm^{-2}, and depth of 2DEG was 90 nm) using standard split-gate techniques. A sufficiently large negative voltage was applied to the center gate that the interwire tunneling resistance was much higher than 100 MΩ. In this condition the drag-wire voltage induced by the tunneling current is negligible. The electron density of each wire was varied by the voltage, Vg_{drive} and Vg_{drag}, applied to the side gate of the drive and the drag wires, respectively. (**B**) SEM image of CW2. (**C**) Schematic images of positive and negative electron drags. Arrows indicate the direction of electron flow. In the positive drag, direction of the electron flow in the drag wire was the same as that in the drive wire, whereas in the negative drag, direction of the electron flow in the drag wire was opposite to that in the drive wire.

Typical experimental data of R_D versus side gate voltage of the drive wire, Vg_{drive}, measured for a L_0 = 4 μm, CW1 wire are shown in Fig. 2A. The side gate voltage of the drag wire, Vg_{drag}, was fixed such that the conductance of the drag wire, G_{drag}, was around or less than the first plateau. For a magnetic field $B < 1.1$ T, R_D was positive in the whole Vg_{drive} range, as was the case for previous Coulomb drag experiments (*9*). On the other hand, for $B \geq 1.3$ T, R_D became negative in a Vg_{drive} range where the drive wire conductance, G_{drive}, was lower than the lowest plateau. This negative drag became stronger and appeared in a wider range of Vg_{drive} as the magnetic field was increased. At higher magnetic fields, a well-flattened spin-resolved plateau of conductance appeared for the drive wire, and then negative drag disappeared on this plateau but was still present below it (SOM Text). In some samples, we observed negative drag even at B = 0 T for the drive wire with very low electron density, whereas in other samples we only observed small or zero negative drag at $B \approx 0$ T. We conclude that sources of positive and negative drag, with independent origin, are competing and, in the less-correlated high-disorder regime, positive drag dominates. As already shown in Fig. 2A, net negative drag occurred as long as the drive conductance was below the first plateau (SOM Text). In addition, in Fig. 2B measured at B = 7 T, negative R_D appeared only in a limited range of drag gate voltages, i.e., -0.9 V $< Vg_{drag} < -0.5$ V. In this Vg_{drag} range, G_{drag} was also below the flat region of its (spin-resolved) plateau, and accordingly the drag wire electron density was relatively low but, as we discuss below, not too low. The negative drag in Fig. 2B became large as temperature was lowered, and interestingly the lower threshold gate voltage (at around –0.9 V) of the drag wire, below which the drag again becomes positive, was temperature-independent.

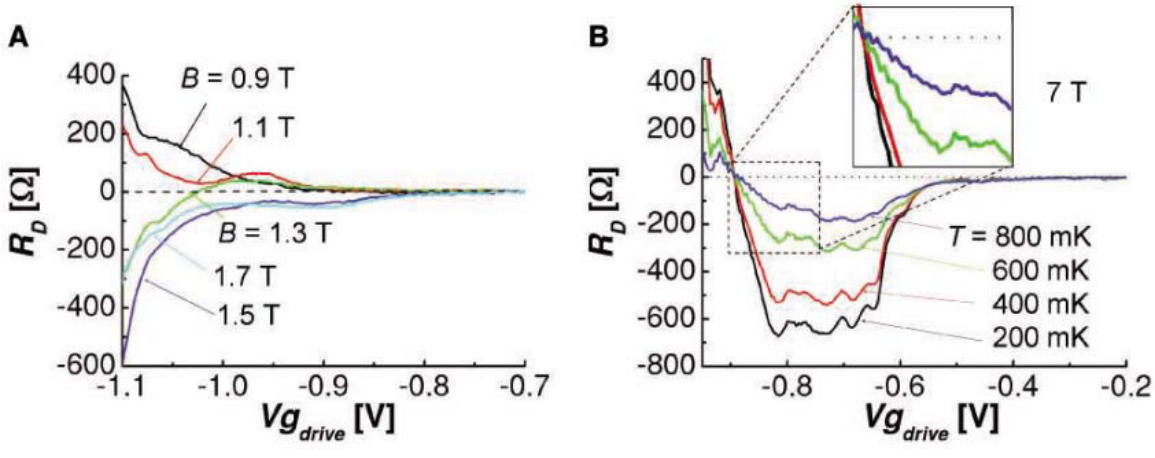

Fig. 2. (**A**) R_D versus Vg_{drive} of a CW1 sample with L_0 = 4 μm measured for $Vg_{center} = -0.9$ V, $Vg_{drag} = -0.92$ V, and I = 1 nA at T = 10 mK. The black, red, green, blue, and light blue lines are the data for B values of 0.9, 1.1, 1.3, 1.5, and 1.7 T, respectively. Negative drag was observed for $Vg_{drive} < -1.0$ V in a magnetic field of 1.3 T and for $Vg_{drive} < -0.8$ V in 1.7 T. (**B**) Drag resistance versus Vg_{drag} measured at a magnetic field of 7 T for $Vg_{center} = -0.9$ V, $Vg_{drive} = -0.8$ V, and I = 1 nA. Conductance of the drive wire was well below the first spin-resolved plateau but not very close to the pinch-off. The negative drag became small as the temperature was raised from 200 mK (black) to 400 mK (red), 600 mK (green), and 800 mK (blue).

In CW1 samples, the emergence of negative drag for low drive-wire electron density, a maximum at a relatively low drag-wire density, and the enhancing effect of high B and low T can all be associated with the effect of 1D Coulombic correlation. In this context, the negative R_D peak (Fig. 2B) can appear when the electron density in the drag wire is low enough that a particle-like state is formed but high enough that it is rigid and internal vibrational modes are difficult to excite. Note also that the negative drag appeared for CW1 wires even when the roles of the wires were exchanged. On the other hand, for wire set CW2 we observed the negative drag only when the short wire was used as the drag wire.

Typical data of R_D versus Vg_{drag} observed for a CW2 sample with L_s = 2 μm and L_l = 4 μm and with drive-wire current I = 1.0 nA are shown in Fig. 3. The negative drag appeared only when both wires had low electron densities and the longer wire was used as a drive wire. The conditions for observing the negative drag, such as low temperature, high magnetic field, and low electron density, are similar to CW1. When the shorter wire was used as a drive wire, only positive drag was observed. These results indicate that juxtaposition of the drive wire current with the drag wire leads is crucial for generating the negative drag. We also found that the drive-wire current is an important parameter for characterizing the negative drag. Negative drag became small and was finally overtaken by positive drag as the current became small (SOM Text). This indicates that negative drag is nonlinear, because we can assume that V_{drag} is linear with I for positive drag.

Negative drag was previously observed for coupled two 2D layers (*16*–*19*) as well as a coupled 3D and 2D system whose origin was argued to be inhomogeneous heating (Peltier effect) (*20*, *21*). Additionally, parallel arrays of tunnel junctions with direct (*22*) and slanted (*23*) couplings have been shown to produce current rectification via the so-called current mirror effect. These phenomena are different from the negative drag presented here. The negative drag in coupled 2D layers is linear with I, non-monotonically dependent on temperature as well as magnetic field (*19*), and assigned to electron-hole asymmetry of high Landau levels with different fillings between the layers, without intralayer correlation taken into account. Current mirror in parallel arrays of tunnel junctions originates from charging in quantum dots. Formation of dots or domains by disorder potential is not likely to cause the negative drag in our experiment, because negative drag disappears when the density is further reduced.

The preceding observations suggest a model for the negative drag behavior that we outline here and further substantiate in SOM Text. Isolated drive wire charges induce positive images in the drag wire leads, which attract the electrons in the drag wire (Fig. 4A) (*24*). We specifically designed the CW2 samples to verify that this interaction of the low density drive wire with the drag wire leads was essential to the negative drag. The assumed Wigner crystal in the drag wire responds rigidly by sliding (fig. S4). This "inductive" effect is stronger in the source than in the drain when the drive current is sufficiently beyond the linear regime to form a density gradient (Fig. 4B) (*25*, *26*). Thus, this induced current component is negative. Ordinary, momentum-conserving Coulombic scattering of the drag-wire electrons by drive-wire propagating point charges produces a competitive positive drag that is weaker when the correlated drag wire electrons are highly incompressible. The drag wire becomes compressible (and positive drag wins out) in the high density limit when the Wigner crystal makes a transition to a Fermi liquid. This occurs at high drag-wire density, ρ_{drag}, high T, and low B, all as observed. Additionally, there is a low density limit. The distance to the surface metal gates provides a cutoff screening length, L_{sc}, such that when $1/\rho_{drag} > L_{sc}$, the drag-wire electrons remain localized but the rigidity of the crystal vanishes. This T-independent cutoff explains the recovery of positive drag in Fig. 2B below $Vg_{drag} \approx -0.9$ V.

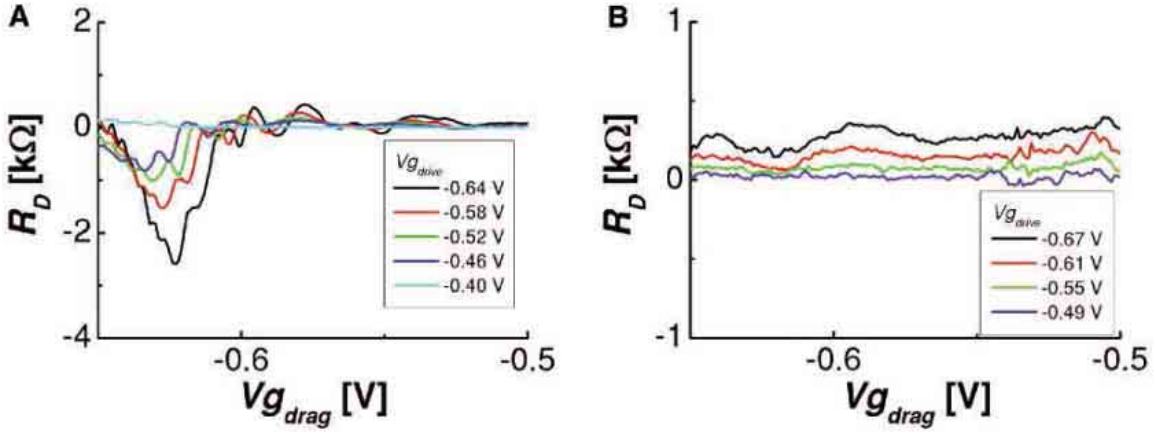

Fig. 3. R_D versus Vg_{drag} of a CW2 sample with L_s = 2 μm and L_l = 4 μm measured at 10 T for Vg_{center} = −0.95 V and I = 1 nA at T = 50 mK. (**A**) The longer wire was used as a drive wire. Negative drag was observed for Vg_{drag} < −0.60 V. (**B**) The shorter wire was used as a drive wire. No signature of negative drag was observed in the whole Vg_{drag} range.

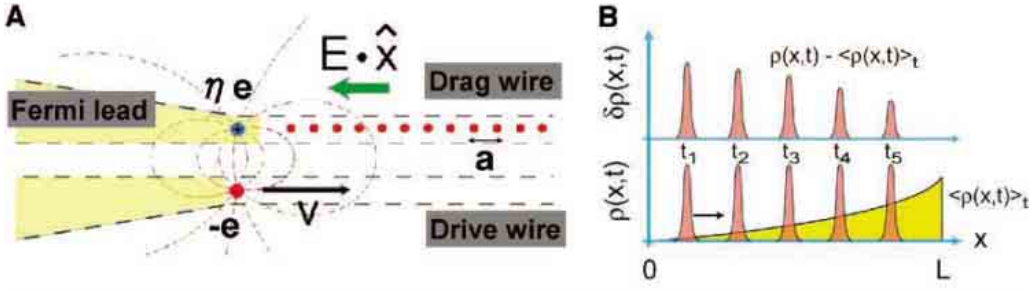

Fig. 4. (**A**) Electrons in the drive (lower) wire propagating from left to right are screened in the lead of the drag wire by a fraction η of a charge. The drive wire electron and this screening hole then induce the dipole field **E**, whose lateral component **E•x** is indicated by a green arrow. Lattice spacing a is 50 to 100 nm with wire width of a few 10 nm, and the distance between the wires is about 100 to 150 nm. (**B**) Effective driving force is time-dependent potential produced by drive charges (here represented as a moving Gaussian pulse at various times) minus the time-averaged density: $\delta\rho\ (x,t) = \rho(x,t) - \langle\rho(x,t)\rangle_t$, where $\rho(x,t)$ is given by a series of point pulses and $\langle\ldots\rangle_t$ denotes time averaging. Voltage drop within drive wire obviates the requirement of Onsager's relations and causes inhomogeneous average density.

Here, we only assume a condition that will meet our experiment, i.e., inhomogeneous screening of a disturbance produced by propagating point particles, which can induce a negative response. Our explanation is, as yet, qualitative. Further investigation will be necessary to quantify the observed negative drag.

References and Notes

1. E. P. Wigner, *Phys. Rev.* **46**, 1002 (1934).
2. C. C. Grimes, G. Adams, *Phys. Rev. Lett.* **42**, 795 (1979).
3. S. Tomonaga, *Prog. Theor. Phys.* **5**, 544 (1950).
4. J. M. Luttinger, *J. Math. Phys.* **4**, 1154 (1963).
5. H. J. Schultz, *Phys. Rev. Lett.* **71**, 1864 (1993).
6. M. D. Jones, D. M. Ceperley, *Phys. Rev. Lett.* **76**, 4572 (1996).
7. B. Tanatar, I. Al-Hayek, M. Tomak, *Phys. Rev. B* **58**, 9886 (1998).
8. P. Debray *et al.*, *J. Phys. Condens. Matter* **13**, 3389 (2001).
9. M. Yamamoto, M. Stopa, Y. Tokura, Y. Hirayama, S. Tarucha, *Physica E* **12**, 726 (2002).
10. V. I. Gurevich, V. B. Pevzner, E. W. Fenton, *J. Phys. Condens. Matter* **10**, 2551 (1998).
11. O. E. Raichev, P. Vasilopoulos, *Phys. Rev. B* **61**, 7511 (2000).
12. Y. V. Nazarov, D. V. Averin, *Phys. Rev. Lett.* **81**, 653 (1998).
13. V. V. Ponomarenko, D. V. Averin, *Phys. Rev. Lett.* **85**, 4928 (2000).
14. K. Flensberg, *Phys. Rev. Lett.* **81**, 184 (1998).
15. R. Klesse, A. Stern, *Phys. Rev. B* **62**, 16912 (2000).
16. J. G. S. Lok *et al.*, *Phys. Rev. B* **63**, 41305R (2001).
17. X. G. Feng, S. Zelakiewicz, H. Noh, T. J. Ragucci, T. J. Gramila, *Phys. Rev. Lett.* **81**, 3219 (1998).
18. F. von Oppen, S. H. Simon, A. Stern, *Phys. Rev. Lett.* **87**, 106803 (2001).
19. K. Muraki *et al.*, *Phys. Rev. Lett.* **92**, 246801 (2004).
20. P. M. Solomon, P. J. Price, D. J. Frank, D. C. La Tulip, *Phys. Rev. Lett.* **63**, 2508 (1989).
21. D. L. Maslov, *Phys. Rev. B* **45**, 1911 (1992).
22. D. V. Averin, Y. V. Nazarov, in *Single Charge Tunneling*, H. Grabert, M. H. Devoret, Eds. (Plenum, New York, 1992).
23. G. Y. Hu, R. F. O'Connell, J. Y. Ryu, *J. Appl. Phys.* **84**, 6713 (1998).
24. In our experiment, maximum negative drag did not increase dramatically with increasing magnetic field above 3 T. This indicates that there is no transition at higher magnetic field, so we assume the Wigner crystal state as the extreme of strongly correlated state.
25. The density gradient is induced only when G_{drive} is below the plateau and the driving current is not completely proportional to the bias voltage along the drive wire. This nonlinearity, i.e., current suppression at low bias voltage, indicates the charge accumulation toward the drain (*27*). The negative drag is generated by a nonlinear, hydrodynamic effect and that Onsager's relations are specifically invalid in this context.
26. M. Stopa, *Phys. Rev. B* **64**, 193315 (2001).

27. We acknowledge financial support from the Defense Advanced Research Project Agency grant no. DAAD19-01-1-0659 of the QuIST program, the Grant-in-Aid for Scientific Research A (no. 40302799), and Focused Research and Development Project for the Realization of the World's Most Advanced IT Nation, IT Program, MEXT. We acknowledge the National Nanotechnology Infrastructure Network Computation Project for support.

Supporting Online Material

www.sciencemag.org/cgi/content/full/313/5784/204/DC1
SOM Text
Figs. S1 to S4

23 February 2006; accepted 26 May 2006
10.1126/science.1126601

Atomic-Scale Control of Friction by Actuation of Nanometer-Sized Contacts

Anisoara Socoliuc,[1]* Enrico Gnecco,[1] Sabine Maier,[1] Oliver Pfeiffer,[1] Alexis Baratoff,[1] Roland Bennewitz,[2] Ernst Meyer[1]

Stiction and wear are demanding problems in nanoelectromechanical devices, because of their large surface-to-volume ratios and the inapplicability of traditional liquid lubricants. An efficient way to switch friction on and off at the atomic scale is achieved by exciting the mechanical resonances of the sliding system perpendicular to the contact plane. The resulting variations of the interaction energy reduce friction below 10 piconewtons in a finite range of excitation and load, without any noticeable wear. Without actuation, atomic stick-slip motion, which leads to dissipation, is observed in the same range. Even if the normal oscillations require energy to actuate, our technique represents a valuable way to minimize energy dissipation in nanocontacts.

Gears, bearings, and liquid lubricants can reduce friction in the macroscopic world, but the origins of friction for small devices such as micro- or nanoelectromechanical systems (NEMS) require other solutions. The much greater surface-to-volume ratios characteristic of these devices lead to serious adhesion and wear problems, and traditional liquid lubricants become too viscous when confined in layers of molecular thickness (*1*). This situation has led to a number of proposals for ways to reduce friction (*2*). Sliding with negligible friction is related to superlubricity, a term coined by Hirano *et al*. who, starting from Aubry's original ideas (*3*), predicted vanishing friction when two surfaces in contact are laterally stiff and incommensurate (*4*). Dienwiebel *et al*. have observed superlubricity while dragging a graphite flake out of registry over a graphite surface (*5*). Dry friction also decreases when the sliding speed is reduced below a critical velocity that increases with temperature. This effect is related to thermally activated jumps occurring in the contact area and has therefore been called thermolubricity (*6*).

A third way to achieve ultralow friction has recently been demonstrated for a sharp tip sliding over an atomically flat surface. When the normal load acting on the tip decreases below a critical threshold, the characteristic stick-slip motion is suppressed and sliding occurs smoothly without abrupt jumps and dissipation while contact is maintained (*7*). This transition was observed by our group on ionic crystals in ultrahigh vacuum (UHV) (*8*), but the basic idea can be traced back to Prandtl (*9*).

Unfortunately, these techniques to achieve superlubricity cannot be easily applied in practical situations. The first method requires accurate control in the preparation and relative orientation of the two surfaces; the second is efficient only at very slow speeds; and the third requires detecting and maintaining constant, very small, normal loads that are almost comparable to the instrumental noise level. Furthermore, none of these methods allows fast switching between a superlubricated state and a usual state, in which friction is nonzero.

We report on achieving superlubricity in a dynamic way on the atomic scale. Our technique is based on the modulation of the normal force acting between two contacting bodies at well-defined frequencies corresponding to normal resonances of the combined system. The experiments were performed with the use of a friction force microscope (FFM) in UHV (*10*). In our FFM, a sharp silicon tip slid on a flat surface, and both the normal load F_N and the lateral force F_x between tip and surface were monitored by a doped silicon cantilever integrated with the tip. F_N and F_x are proportional to the bending and the torsion at the end of the cantilever, which were quantified by a light beam reflected from the back of the cantilever into a four-quadrant photodiode. We present results obtained on single crystals (~1 mm thick) of NaCl and KBr cleaved along their (100) plane in UHV and in air, respectively; the crystals were heated in UHV for 30 min to 120°C to remove surface charges and contaminants. The spring constants of the cantilever used on NaCl were k_n = 0.12 N/m for bending and k_t = 68 N/m for torsion, whereas k_n = 0.03 N/m and k_t = 18 N/m were the constants associated with bending and torsion for the cantilever used on KBr.

The effect of a sinusoidal excitation at f = 56.7 kHz on atomic-scale friction on NaCl is shown (Fig. 1, A and B). When the excitation is switched on, the characteristic hysteresis loop

[1]Department of Physics and Astronomy, University of Basel, Switzerland. [2]Department of Physics, McGill University, Montreal, Quebec, Canada.

*To whom correspondence should be addressed. E-mail: a.socoliuc@unibas.ch

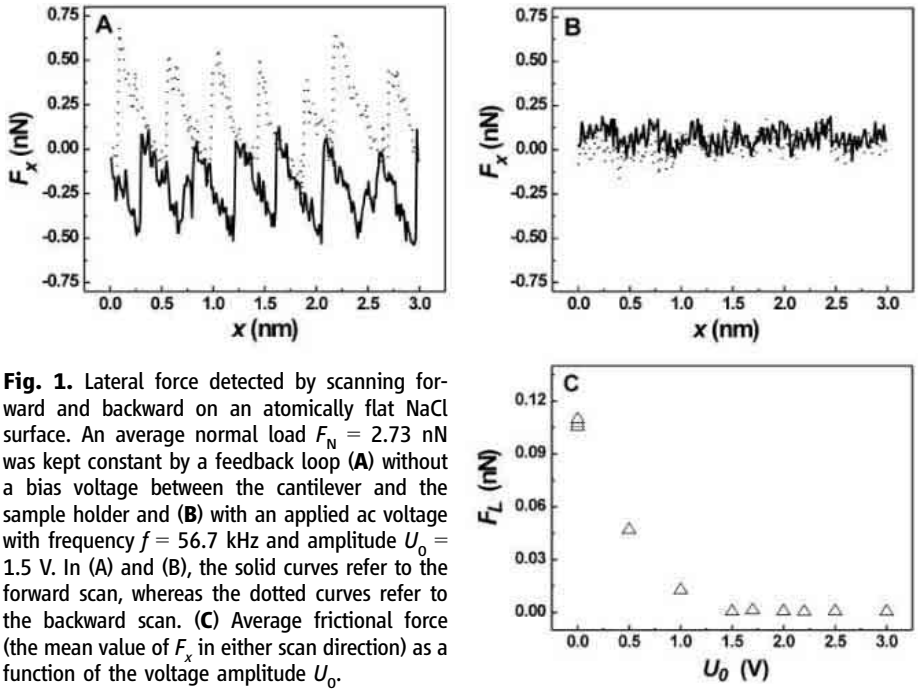

Fig. 1. Lateral force detected by scanning forward and backward on an atomically flat NaCl surface. An average normal load F_N = 2.73 nN was kept constant by a feedback loop (**A**) without a bias voltage between the cantilever and the sample holder and (**B**) with an applied ac voltage with frequency f = 56.7 kHz and amplitude U_0 = 1.5 V. In (A) and (B), the solid curves refer to the forward scan, whereas the dotted curves refer to the backward scan. (**C**) Average frictional force (the mean value of F_x in either scan direction) as a function of the voltage amplitude U_0.

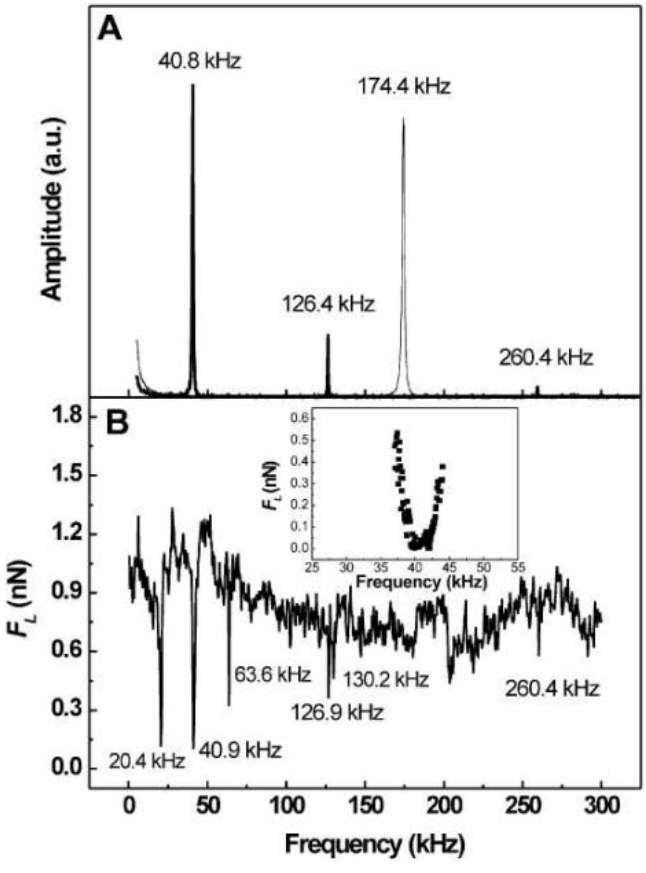

Fig. 2. (**A**) Thermal noise spectrum of the bending (thick line) and torsional (thin line) oscillations of the silicon cantilever in contact with a KBr (001) surface. a.u., arbitrary units. (**B**) Average value of the frictional force recorded while applying a modulated bias voltage with frequencies between 0 and 300 kHz. (Inset) Friction recorded at a low sweeping rate falls below the sensitivity of our instrument around the resonance frequency f_{n1} = 40.8 kHz.

of the lateral force recorded in opposite directions disappears, and energy dissipation and hence net friction become negligible. The transition is fully reversible, as observed when the oscillations are switched off. The force modulation was provided by an ac voltage applied between the cantilever and the sample holder plate. The average friction force F_L rapidly drops and vanishes with increasing modulation amplitude (Fig. 1C), until wear and high friction suddenly set in. (Similar behavior was observed on the more compliant KBr crystals, albeit over a smaller load range). The mechanical resonances of the cantilever in contact were determined from a frequency analysis of the thermal noise spectra in the normal and lateral force signals.

On KBr, the peak at f_{n1} = 40.8 kHz (Fig. 2A) corresponds to the first bending mode, which is shifted upward from 8.0 kHz upon contact formation with respect to the free cantilever; this result is in good agreement with theoretical predictions (*11*). The peaks at f_{n2} = 126.4 and f_{n3} = 260.4 kHz correspond to higher bending modes. The first torsional resonance peak observed at f_{t1} = 174.4 kHz is only weakly shifted. All of the resonances remained sharp, although their quality factors decreased by factors of 10^2 to 10^3 upon contact formation, which is in agreement with recent observations and modeling (*12*). Figure 2B shows the mean frictional force versus the frequency f of the applied voltage. Friction is reduced below the noise level (~10 pN) when this frequency matches one of the normal resonance frequencies of the lever or half of those values. When the torsional mode of the cantilever was excited, no such effects were observed.

At adequately low normal loads, the motion of a sharp tip sliding on a crystal surface is determined by the local interactions and by the combined elastic deformations of the materials in contact (*13*). The elastic deformation is represented in two dimensions by a parabola of curvature k equal to the effective lateral stiffness. The interaction between the tip and sample can be described by a potential having the spatial periodicity of the crystal and a lateral corrugation $E_0(F_N)$ increasing with normal load (*8*). We introduce the parameter $\eta = 2\pi^2 E_0/ka^2$, where a is the lattice constant of the crystal; the condition for the disappearance of stick-slip motion is $\eta < 1$ (*8*). When the ac voltage is switched on, the ionic crystal acts as a dielectric medium placed between two conductors. Because the thickness of the sample is much larger than the tip height, the capacitive interaction occurs mainly between the cantilever body and the sample holder. This interaction results in a capacitive force, F_U, proportional to the square of the applied voltage. The attractive force F_U oscillates with twice the excitation frequency f. Besides F_U, any charge trapped at the tip or any charge layer at the surface results in a nonzero contact potential and in an additional force F_Q, which oscillates at the actuation frequency f (*14*). Thus, when one of the frequencies f or $2f$ matches a bending resonance of the pinned lever, the oscillation amplitude causes the normal force F_N and the energy corrugation E_0 to vary between two extreme values (*15*). We represent the effect of the normal modulation on the lateral tip motion by assuming that the corrugation energy changes with time as $E(t) = E_0\,(1 + \alpha\cos 2\pi ft)$, where the parameter α is proportional to the amplitude of the applied voltage and exhibits maxima at the bending resonances.

An important result of previous measurements (*8*, *12*) is that the effective stiffness k is

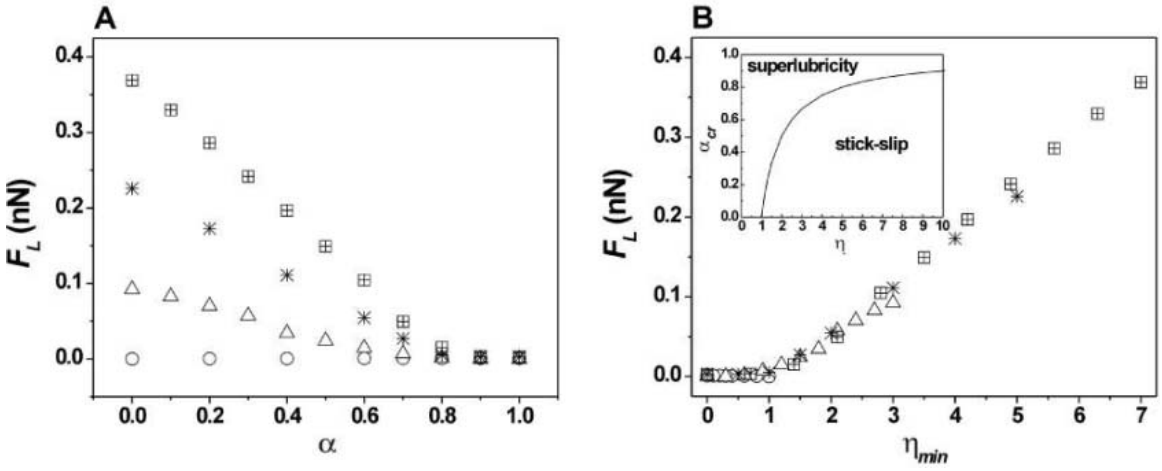

Fig. 3. (**A**) Numerical evaluation of the frictional force as a function of the normalized excitation amplitude α. The four symbols correspond to $\eta = 7$ (squares), 5 (asterisks), 3 (triangles), and 1 (circles). (**B**) The same values as in (A) as a function of the parameter η_{min}. (Inset) Depending on the values of η and $\alpha(\eta_{min})$, two sliding regimes are possible.

typically ~1 N/m (i.e., much lower than k_t). This finding strongly suggests that the entity that mainly slips is a "nanotip" at the tip apex rather than the cantilever. In order to clarify the observed suppression of friction, we ignored the lateral deflection of the cantilever and considered the equation of motion of the nanotip connected by a spring of lateral stiffness k = 1 N/m to an essentially rigid object (the remainder of the tip plus the lever) pulled along the scan direction at a low velocity v = 10 nm/s across an oscillating sinusoidal potential with spatial periodicity a = 0.5 nm. The mass and damping of the nanotip are difficult to determine (*12*). Nevertheless, we expect that the corresponding resonance frequency f_{nt} and damping rate Γ_{nt} considerably exceed those of the cantilever. The simple adiabatic approximation, in which the inertia and damping of the nanotip are neglected, explains our observations. In that limit, the forces acting on the nanotip are in balance at every instant, and all of the equations derived in the quasistatic case ($\alpha = 0$) (*8*) then hold, provided that $E(t)$ replaces E_0. Because $f \gg v/a$, the nanotip experiences the minimum corrugation $E_0(1 - \alpha)$ many times as the rigid tip slowly crosses the distance that separates adjacent potential minima, and hence slides smoothly once $\eta_{min} = 2\pi^2 E_0 (1 - \alpha)/ka^2 < 1$, even if friction is finite ($\eta > 1$) when $\alpha = 0$. In other words, the parameter η_{min} replaces η in the condition for the occurrence of superlubricity.

This simple criterion is confirmed by numerical calculations as long as the conditions

$$f_{nt} \gg f \gg v/a, f\Gamma_{nt} \ll 4\pi f_{nt}^2 \qquad (1)$$

are satisfied. For the particular case f_{nt} = 178 kHz, $\Gamma_{nt}/(4\pi)$ = 100 kHz, f = 567 Hz, and v/a = 20 Hz (Fig. 3A), the computed average frictional force $F_L \equiv \overline{F}_x$ decreases linearly with α and becomes negligible beyond a critical value α_{cr}. The dependence calculated for $\eta = 3$ is near that shown in Fig. 1C, where η = 3.1 was determined from an independent fit to the friction loops measured without ac modulation. F_L values for different η essentially collapse on the universal adiabatic curve when plotted versus η_{min}. The curve $\alpha = \alpha_{cr}$, where

$$\alpha_{cr} = 1 - \eta^{-1} \qquad (2)$$

divides the (η, α) plane in two regions (Fig. 3B, inset). Below the critical curve, normal oscillations do not remove the instabilities that lead to stick-slip motion and dissipation. In the upper region, such oscillations prevent hysteresis and friction becomes negligible.

A partial reduction in friction has previously been achieved by exciting oscillations perpendicular to the sliding direction in different situations, such as in force microscopy of transition-metal chalcogenides (*16*, *17*), wide contact areas subject to ultrasonic excitation (*18*), in the presence of confined lubricant films (*19*), or between glassy polymers (*20*). In those investigations, however, the reduction of friction remained unexplained (*16*) and was attributed to an induced lateral motion of the tip (*17*) or to an increase in the mean separation between the two surfaces (*18*, *19*), as confirmed in simulations (*20*–*22*). In some of these cases, friction was suppressed only if the excitation was so strong that the slider lost contact over a fraction of each oscillation cycle. The model of Rozman *et al*. (*23*) showed that it was possible to switch a sliding state on and off with reduced friction by means of a feedback scheme to control the normal load, albeit at high velocities that violate the second condition in Eq. 1. In our model, the second condition in Eq. 1 can be satisfied in a range where the nanotip motion is overdamped ($f_{nt} < \Gamma_{nt}/4\pi$). If this condition is poorly satisfied, then the reduction of F_L is rather inefficient, as in previous cases where friction was studied as a function of the amplitude of normal oscillations (*18*, *20*). Furthermore, Bureau *et al*. (*20*) could fit their measurements only after including a stiffness value analogous to our k in their phenomenological equations, describing the average behavior of a typical asperity in a sheared multicontact interface.

Riedo *et al*. observed a partial reduction of friction when the contact between a conventional FFM tip and a mica surface in humid air was laterally excited at 20 kHz, in the low-velocity range where F_L is reduced by thermal activation (*24*). The actual torsional resonance in contact was not measured in that experiment. In our study, reduced friction is expected if the displacement of the nanotip, induced by lateral excitation, reaches roughly half of a lattice constant. Taking into account that the quality factor decreases by a factor of at least 100 upon contact, it is perhaps not surprising that in our experiment the stick-slip motion was maintained and that no substantial reduction of friction was observed under torsional excitation.

Our results indicate that the problem of stiction in microdevices may be overcome. Parts in physical contact within NEMS are usually small enough to constitute single-asperity contacts, and their structure favors the development of distinct normal resonances. In macroscopic bodies, the wide distribution of contact resonances makes our technique difficult to apply, but resonance-induced superlubricity occurs in many natural phenomena, such as in biological systems or, on much larger scales, in the motion of tectonic plates.

References and Notes

1. Y. Z. Hu, S. Granick, *Trib. Lett.* **5**, 81 (1998).
2. M. Urbakh, J. Klafter, D. Gourdon, J. Israelachvili, *Nature* **430**, 525 (2004).
3. S. Aubry, *Phys. D* **7**, 240 (1983).
4. M. Hirano, K. Shinjo, *Phys. Rev. B* **41**, 11837 (1990).
5. M. Dienwiebel *et al.*, *Phys. Rev. Lett.* **92**, 126101 (2004).
6. S. Y. Krylov, K. B. Jinesh, H. Valk, M. Dienwiebel, J. W. M. Frenken, *Phys. Rev. E* **71**, R65101 (2005).
7. The zero normal force is defined as the position where the cantilever is not bent.
8. A. Socoliuc, R. Bennewitz, E. Gnecco, E. Meyer, *Phys. Rev. Lett.* **92**, 134301 (2004).
9. A. Nadai, *Theory of Flow and Fracture of Solids* (McGraw Hill, New York, 1950), chap. 7.
10. L. Howald *et al.*, *Appl. Phys. Lett.* **63**, 117 (1993).
11. U. Rabe, K. Janser, W. Arnold, *Rev. Sci. Instrum.* **67**, 3281 (1996).
12. S. Maier *et al.*, *Phys. Rev. B* **72**, 245418 (2005).
13. E. Gnecco, R. Bennewitz, T. Gyalog, E. Meyer, *J. Phys. Condens. Matt.* **13**, R619 (2001).

14. M. R. Weaver, D. Abraham, *J. Vac. Sci. Technol. B* **9**, 1559 (1991).
15. The quick variation of the electrostatic forces cannot be followed by the distance-controlling feedback, which keeps the mean value of the total normal force constant over several lattice constants.
16. T. Schimmel *et al.*, Eds. *Forces in Scanning Probe Methods* (North Atlantic Treaty Organization–Advanced Study Institute Series, Kluwer, Dordrecht, Netherlands, 1995).
17. J. Kerssemakers, J. T. M. De Hosson, *Surf. Sci.* **417**, 281 (1998).
18. F. Dinelli, S. K. Biswas, G. A. D. Briggs, O. V. Kolosov, *Appl. Phys. Lett.* **71**, 1177 (1997).
19. M. Heuberger, C. Drummond, J. Israelachvili, *J. Phys. Chem. B* **102**, 5038 (1998).
20. L. Bureau, T. Baumberger, C. Caroli, *Phys. Rev. E* **62**, 6810 (2000).
21. J. P. Gao, W. D. Luedtke, U. Landman, *J. Phys. Chem. B* **102**, 5033 (1998).
22. V. Zaloj, M. Urbakh, J. Klafter, *Phys. Rev. Lett.* **82**, 4823 (1999).
23. M. G. Rozman, M. Urbakh, J. Klafter, *Phys. Rev. E* **57**, 7340 (1998).
24. E. Riedo, E. Gnecco, R. Bennewitz, E. Meyer, H. Brune, *Phys. Rev. Lett.* **91**, 084502 (2003).
25. This work was supported by the Swiss National Science Foundation, the National Center of Competence in Research on Nanoscale Science, the Kommission zur Förderung von Technologie und Innovation, and the European Science Foundation Nanotribo program. M. T. Cuberes is gratefully acknowledged for discussions and advice.

6 February 2006; accepted 25 May 2006
10.1126/science.1125874

Dynamic Forces Between Two Deformable Oil Droplets in Water

Raymond R. Dagastine,[1,2] Rogério Manica,[1,3] Steven L. Carnie,[1,3] D. Y. C. Chan,[1,3] Geoffrey W. Stevens,[1,2] Franz Grieser[1,4]*

The understanding of static interactions in colloidal suspensions is well established, whereas dynamic interactions more relevant to biological and other suspended soft-matter systems are less well understood. We present the direct force measurement and quantitative theoretical description for dynamic forces for liquid droplets in another immiscible fluid. Analysis of this system demonstrates the strong link between interfacial deformation, static surface forces, and hydrodynamic drainage, which govern dynamic droplet-droplet interactions over the length scale of nanometers and over the time scales of Brownian collisions. The results and analysis have direct bearing on the control and manipulation of suspended droplets in soft-matter systems ranging from the emulsions in shampoo to cellular interactions.

Much of the ability to produce advanced materials relies on a well-developed understanding of surface forces. Static interactions between surfaces have been studied for decades (*1*–*3*), but a comprehensive quantitative understanding of dynamic interactions in biological and other suspended soft-matter systems is still being developed. These dynamic forces are the basis behind manipulating and controlling soft-matter systems, such as complex fluids or emulsions, in formulation and processing. The challenge in understanding lies in both the quantitative measurement and the ability to predict dynamic droplet-droplet interactions, which are more complicated than the analogs in solid particulate suspensions. The experimental and theoretical analyses presented in this work describe the dynamic interactions between two deformable oil droplets. The general methodology presented in this study is applicable to all soft-matter systems and opens another dimension to the observable forces in collisions arising from Brownian motion.

The interactions between droplets common to emulsions with droplet radii, between 10 and 100 μm, have been difficult to measure experimentally. Atomic force microscopy (AFM) has been used to examine the equilibrium interactions between a rigid probe particle and a single bubble or droplet in this size range (*4*–*6*). In addition, one study has examined the hydrodynamic interaction between a single oil droplet and a rigid probe particle with a semiquantitative analysis (*7*). However, these studies lack a specific relevance to the dynamic interactions between soft matter, such as emulsion droplets, where every interface is deformable. Recent developments have allowed for direct force measurement of the interactions between droplets with radii of the order of 40 μm (*8*) and the development of a quantitative model for these systems (*9*, *10*). By comparing the model to experimental observations on these intermediate-size drops, this study has developed an understanding of dynamic droplet-droplet interactions in a region where deformation, hydrodynamic drainage, and interaction forces are all important.

The droplet size range in this study is bracketed by droplet sizes that have largely decoupled deformation, surface forces, and hydrodynamic drainage effects. For droplet radii below 10 μm, the droplet internal pressure is large enough that equilibrium surface forces dominate the interaction over deformation and hydrodynamic effects. For droplet radii above 100 μm, there is a large body of work that uses interferometry to measure interfacial profiles, with time (*11*) between approaching capillaries at either constant velocity (*12*) or constant force (*13*). The deformation and hydrodynamic drainage effects in this larger droplet regime are mostly decoupled from equilibrium surface forces in a two-stage process (*14*). The results of the present study provide considerable insight into how to quantitatively model droplet-droplet interactions for this intermediate droplet size and, more important, how the traditional concepts of drainage as a two-stage process are not appropriate for droplet sizes relevant to real emulsions. This may have considerable implications with respect to improving the design and operation of emulsion processing equipment.

Two decane droplets with radii of 43 and 90 μm, in solutions of an anionic surfactant, sodium dodecyl sulfate (SDS), and 1 mM sodium nitrate, were immobilized on an AFM cantilever and substrate (Fig. 1A). The dynamic interaction force between these oil droplets as a function of piezo drive motion of the substrate for a series of approach and retract velocities of the piezo actuator is shown in Fig. 1, B to D. The SDS adsorbed at the oil-water interface controls both the interfacial tension and the surface charge at the interface, where both of these effects are well characterized for the decane-SDS-water system (*15*). It is not possible to decouple interfacial deformation and separation distance from these data without interpretation through modeling. Therefore, it is standard practice to assign an arbitrary origin for piezo motion; in this case, the origin is set at the highest measured force (*16*, *17*).

The approach and subsequent retracting curves show a strong dependence on the piezo velocity. The approach curves show a hydrodynamic repulsion due to film drainage between the surfaces with a dynamic behavior slower than the time scale of the measurement. The magnitude of the attractive well in the retracting curve is a function of velocity. The time required for the oil droplets to restore upon retraction is a result of the fluid film thickening and the pressure profile between the droplets resisting fluid flow on a time scale longer than the time scale of the measurement. The velocity range spans the likely velocities of an emulsion droplet of comparable size undergoing Brownian motion. For example, the root mean square velocity due to Brownian motion of an oil droplet with a radius of 40 μm is

[1]Particulate Fluids Processing Center, [2]Department of Chemical and Biomolecular Engineering, [3]Department of Mathematics and Statistics, [4]School of Chemistry, University of Melbourne, Victoria 3010, Australia.

*To whom correspondence should be addressed. E-mail: franz@unimelb.edu.au

approximately 7 μm/s in water at room temperature (*9*). The measurements demonstrate that hydrodynamic interactions between droplets in this size range are not insignificant even when describing emulsion stability, where equilibrium forces are commonly assumed to dominate.

A quantitative analysis of these data and determination of the interfacial separation require development of an approach based on the augmented Young-Laplace equation and the methods developed for static or equilibrium force measurements between a rigid particle and droplet (*17*) or between two droplets (*18*). The dynamic problem contains three disparate length scales: the droplet radii, on the order of 50 μm; the axial length scale of the interaction forces, from 10 to 100 nm; and the radial length scale of the interaction, on the order of 1 to 5 μm. A more robust model is required to treat these disparate length scales and incorporate the static forces with the hydrodynamic drainage behavior at a deformable interface (*7*, *9*, *10*). The lubrication approximation is used to describe the forces across the thin film between the droplets and neglects the hydrodynamic drag on the droplet outside this lateral interaction area. This requires low capillary numbers ($Ca = \mu V/\sigma$), which span 10^{-6} to 10^{-8} for this system, where V is the droplet velocity, σ is the interfacial tension, and μ is the viscosity.

The two main coupled partial differential equations are the standard Reynolds drainage equation and the normal stress balance:

$$\frac{\partial h}{\partial t} = \frac{1}{12\mu r}\frac{\partial}{\partial r}\left(rh^3\frac{\partial p}{\partial r}\right)$$

$$p + \Pi(h) = \frac{2\sigma}{R_o} - \frac{2\sigma}{r}\frac{\partial}{\partial r}\left(r\frac{\partial h}{\partial r}\right) \quad (1)$$

where $h(r,t)$ is the interdroplet separation, p is the hydrodynamic pressure, Π is the equilibrium disjoining pressure, and R_o is the harmonic mean of the unperturbed droplet radii on the cantilever, R_1, and the substrate, R_2. The position of the interfacial profile must be calculated for each droplet. A no-slip boundary condition is employed at the aqueous solution–oil interface for the drainage between the droplets in the presence of surfactant, SDS. This assumption is supported by a number of theoretical and experimental studies (*15*, *19*, *20*) that suggest that the adsorption of surfactant molecules on the interface is sufficient to arrest momentum transfer across the interface and prevent any internal flow in the droplets.

This study differs from previous work in two respects. First, one droplet is immobilized on a cantilever that has an added degree of freedom and that must be incorporated into the drainage equations (*9*, *10*). Second, the treatment of the boundary conditions for the velocity of the interface at large radial distances is far more rigorous in accounting for changes in interfacial deformation. The traditional approach assumes that the velocity matches the velocity of the drive actuator (in this case, the piezo) at a large radial distance, r_{max}, where the interaction forces are insignificant (*12*, *20*). The previous studies do not account for the constant volume constraint of the droplet in the velocity calculation. A dynamic interaction results in a time-dependent deformation of the droplet's inner region, which results in a time-dependent bulge of the droplet's outer region and changes the velocity at r_{max} (*9*, *10*). Details on the calculations, methods, and boundary conditions are presented elsewhere (*21*).

For a comparison of experimental data of the AFM measurable quantities, force and piezo drive motion, with theoretical calculations, several independently measured experimental parameters are required, including the interfacial tension and the contact angles of the droplets on the piezo drive and the cantilever (*21*). The disjoining pressure for this system was calculated on the basis of the numerical solution to the Poisson-Boltzmann equation to describe the electrostatic double-layer repulsion between the negatively charged surfactant-laden interfaces. The surface potential required for this calculation was previously measured for the decane-SDS-water system to be –100 mV from an electrokinetic study (*15*).

The comparison of the model output and the experimental data is shown in Fig. 1, B to D. The one parameter determined from the fit of the

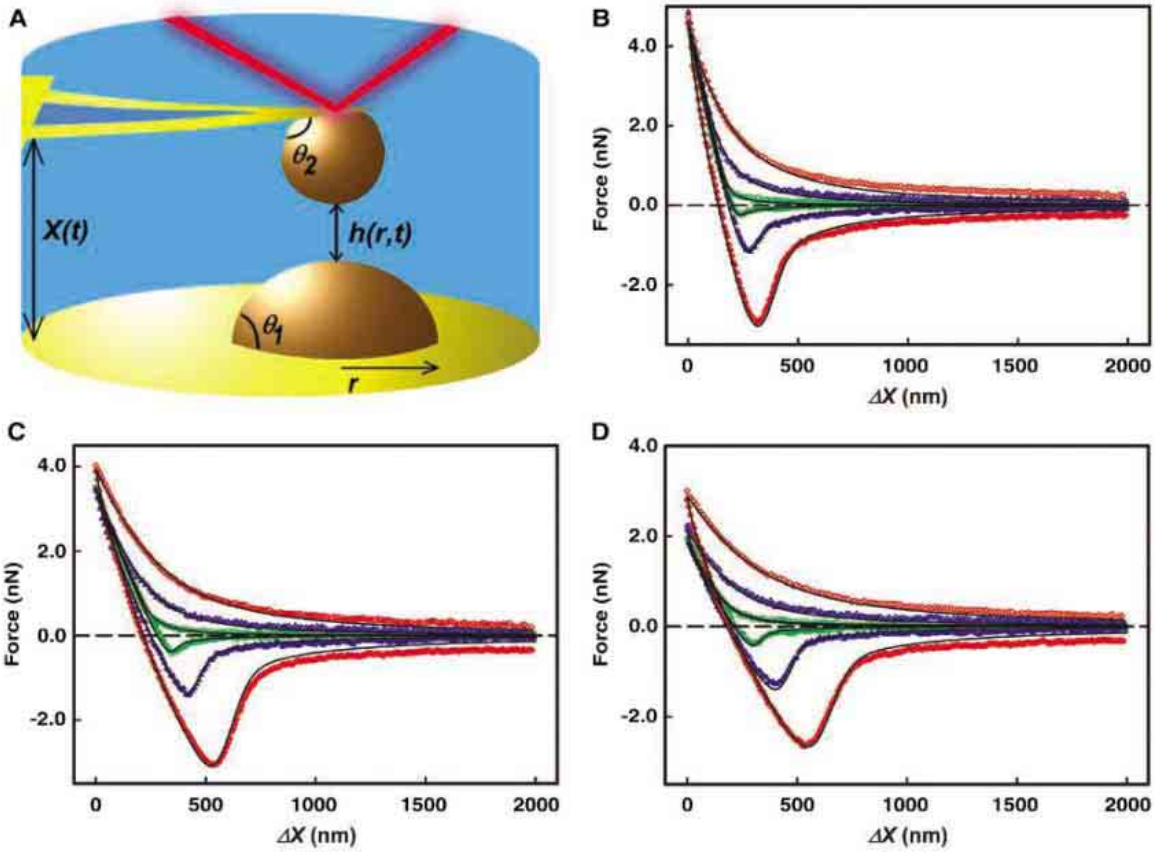

Fig. 1. (**A**) A schematic of the experiment between two oil droplets, one immobilized on the cantilever and the other immobilized on the substrate of an atomic force microscope. (**B** to **D**) The dynamic interaction force F versus piezo drive motion ΔX between two decane droplets in aqueous solution in the presence of SDS at a series of approach (open symbols) and retract (filled symbols) velocities (green circles, 2 μm/s; blue triangles, 9.3 μm/s; red diamonds, 28 μm/s) over a range of SDS concentrations: (B) 0.1 mM, (C) 3 mM, and (D) 10 mM. The points refer to the experimental data, and the solid lines are the calculated force curves from a comprehensive model of the dynamic droplet interactions.

model to the data is the only unknown in the system, the initial starting separation distance h_o. Each force curve is an independent measurement, and the starting distances vary from 20 to 50 nm at a given SDS concentration, as shown in Fig. 1, B to D, where the total piezo drive is 2 μm and h_o ranges from 1.75 μm to 1.89 μm. A sensitivity study shown in fig. S1 demonstrates that a 100-nm change in initial starting distance results in a 20% change in the maximum measured force and the position of the minimum. This analysis leads to a resolution in the determined distance of ~20 nm over 2 μm, or an accuracy better than 1% in separation.

Although the agreement is notable, a discussion of the impact of the experimental error on the comparison with the theory is warranted. The independently measured parameters mentioned above all have an experimental uncertainty, but the largest source of error on these force data is the experimental error in the calibration of the cantilever spring, constant with an accuracy of 10% (*22*). A sensitivity study has shown that the theory is sensitive to statistically significant errors in each of the above parameters, but a comparison of the impact of all these errors on the theoretical calculations offers a more practical comparison to the experimental data. The gray regions in Fig. 2, A and B, are bounded by the maximum and minimum experimental uncertainties for all these parameters for a velocity of 28 μm/s. The agreement shown for the 3 mM SDS case is typical for all the concentrations and velocities where the experimental data are centered on the theoretical predictions. The only exception is the 10 mM case, where the data are on the edge of the parameter bounds. The critical micelle concentration for SDS is approximately 8 mM. The disjoining pressure calculation only accounts for the effect of micelles on the solution ionic strength and not any possible additional effect on the disjoining pressure.

Two features of these force data can now be explained by using the validated model to develop a larger understanding of what occurs at the interface during the drainage process. First, drop coalescence caused by an ever-present van der Waals force is not observed, even though a significant attractive force is observed between these droplets. Second, the smoothly varying minima exhibit a strong dependence on the approach and retract velocities.

It has been shown for the static interactions for these droplet sizes that repulsive forces are always observed experimentally for all SDS concentrations (*18*). Modeling of the static system has shown that the interface flattens at the radial center of the film as the interdroplet disjoining pressure approaches the Laplace pressure of the droplets (*18*). The phenomenon limits to a finite separation distance according to the relation $\Pi(h_l) = 2\sigma/R_o$, where h_l is this limiting distance, which is commonly on the order of nanometers for the experimental systems studied (*18*). For this static system, the limiting distance is always larger than the length scale of the van der Waals attraction; therefore, attraction is never observed. For the dynamic case, the flattening of the droplet occurs on the approach curve whenever the normal pressure is on the order of the droplet Laplace pressure, regardless of the contribution to the pressure

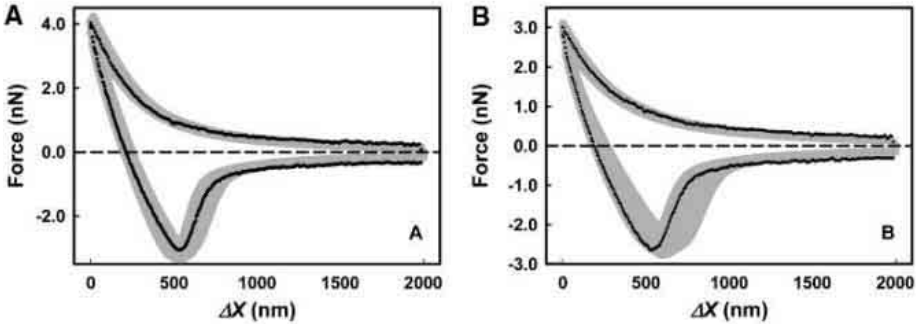

Fig. 2. The dynamic interaction force F versus piezo drive motion ΔX between two decane droplets in aqueous solution in the presence of SDS at approach and retract velocities of 28 μm/s at (**A**) 3 mM and (**B**) 10 mM SDS concentrations. The gray region represents the impact of the uncertainties in the theoretical calculations from independently measured parameters required for the calculations compared with the experimental data (points) plotted on the same graph.

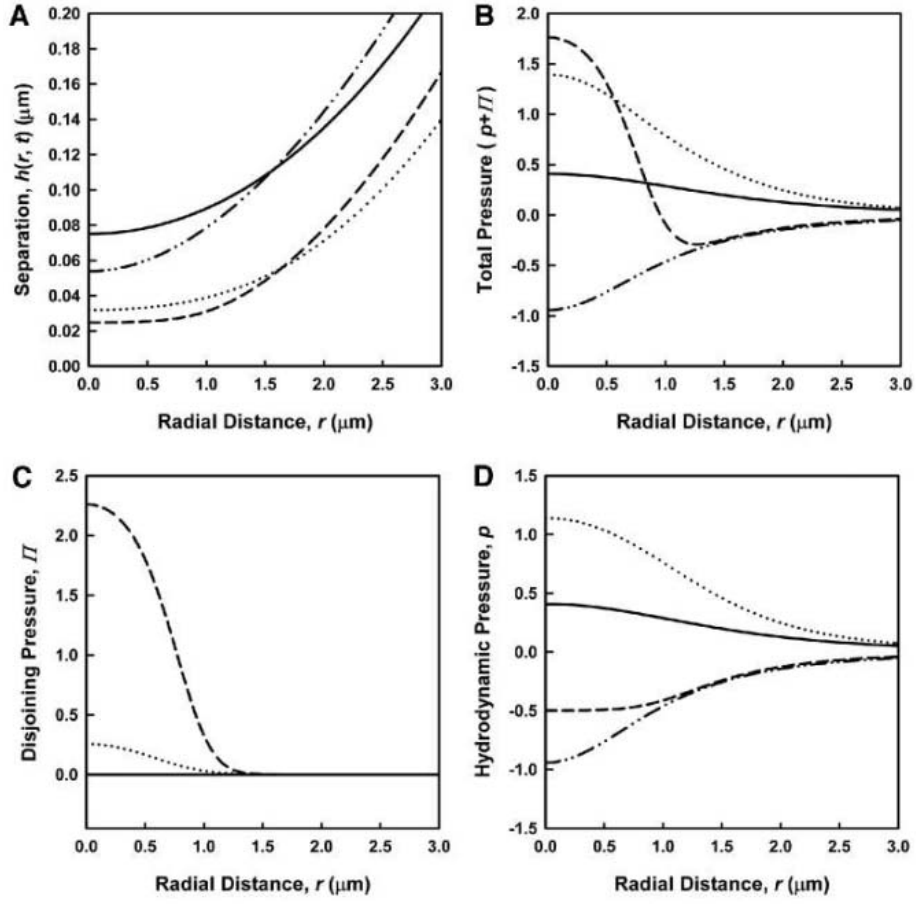

Fig. 3. Model calculations of droplet and pressure profiles for the 9.3 μm/s approach and retract velocity for 0.1 mM SDS concentration at four times, t_1 through t_4, in a 430.2-ms measurement. The four times are t_1 = 199.6 ms (solid line), t_2 = 215.1 ms (dotted line), t_3 = 223.7 ms (dashed line), and t_4 = 240.9 ms (dotted and dashed line). (**A**) The interfacial separation h as a function of radial distance r. (**B**) The total pressure between the droplets as a function of radial distance. Pressure is in dimensionless units, scaled by σ/R_o. (**C**) The disjoining pressure, Π, from only the equilibrium or static forces between the droplets as a function of radial distance. (**D**) The pressure p from only the hydrodynamic drainage effects as a function of radial distance.

from either equilibrium surface forces or hydrodynamic drainage. This is shown in Fig. 3A for the 10 mM SDS case at a series of times in the measurement conducted at a speed of 9.3 μm/s. The interdroplet separation in Fig. 3A flattens at the time closest to the largest repulsive force, marked t_2, 215.1 ms into a 430.2-ms measurement. The total pressure in Fig. 3B is a combination of the component contributions shown in Fig. 3, C and D. The strong positive pressure in Fig. 3B at time t_2 corresponds to the flat region in the interface profile in Fig. 3A.

The closest approach for the entire dynamic interaction event occurs in the retraction as shown at time t_3, 223.7 ms. The total radial pressure profile exhibits more features than any other curve in the time sequence in Fig. 3B, with a reversal from positive pressure at small radii to negative pressure at larger radii. This is due to the combination of pressure with different length scales from a positive equilibrium surface force at these interfacial separations and the negative hydrodynamic drainage pressure, as shown in Fig. 3, C and D. In contrast to the case involving only equilibrium interactions, for the dynamic interaction situation the closest approach, and hence opportunity for droplet coalescence to occur, can take place as the droplets move apart.

Ultimately it is clear that at velocities similar to those experienced through the Brownian motion of these droplets in solution, the contributions from hydrodynamic and surface forces are strongly coupled, and the relative length scales of these forces will influence which component dominates the interaction. The absence of a dimple in the interfacial profile when compared to drainage studies for larger droplets (*12*, *14*, *20*, *23*, *24*) is a product of both smaller droplet size and low deformation. The control of the velocity and interfacial tension in the experiment allows one to vary the relative effects so as to probe the situation where either surface force or hydrodynamic drainage can dominate the interactions behavior. For example, at even higher velocities, about twice those of the Brownian motion, the interfacial profile looks similar, but the contribution to the total pressure is then dominated by hydrodynamic drainage.

The thinning of the film in the radial center between the droplets at higher forces creates a remarkable coupling of the motion of the two droplets, which enhances the development of the smoothly varying minimum in the retract curve. The droplet velocity as a function of time at the axial and the edge positions of the droplet on the cantilever, for the 10 mM SDS concentration at 28 μm/s, is shown in fig. S2. As the two droplets approach, the displacement of the center of the interface slows as the film thins, and the two interfaces become stationary for small radial distances near the turnaround point. The axial center of the top droplet continues to lag behind the motion of the rest of the droplet, even at the beginning of the retract motion. The axial center of the top droplet then decouples its motion from the other droplet and accelerates to a velocity faster than the piezo drive with a recoiling motion before returning to rest. This behavior is described in the validated model without invoking interfacial rheological effects.

The agreement between the experimental data and the quantitative model identifies a number of important points related to describing interaction dynamics in liquid-liquid systems. This agreement is achieved by using the traditional no-slip boundary condition. This is contrary to what might be expected on the basis of some experimental observations of liquid drainage between rigid hydrophobic surfaces. One possible explanation is that the surface roughness of the oil-water interface is much smaller than that on a rigid surface, where deviations between theory and experiments have led to a heuristic correction to drainage models, referred to as a slip length. The quantitative visualization of the interfacial and pressure profiles provides a means of understanding the dynamic contributions from individual components in the physics of the interactions. The behavior of the droplet profile, pressure, and velocity upon the retraction presents an opportunity to probe systems possessing interfacial rheological characteristics and the impact of these on dynamic droplet-droplet interactions.

References and Notes

1. R. J. Hunter, *Foundations of Colloid Science* (Clarendon, Oxford, 1995).
2. J. N. Israelachvili, *Intermolecular and Surface Forces* (Academic Press, New York, 1992).
3. W. B. Russel, D. A. Saville, W. R. Schowalter, *Colloidal Dispersions* (Cambridge Univ. Press, New York, 1989).
4. H.-J. Butt, *J. Colloid Interface Sci.* **166**, 109 (1994).
5. W. A. Ducker, Z. G. Xu, J. N. Israelachvili, *Langmuir* **10**, 3279 (1994).
6. P. Mulvaney, J. M. Perera, S. Biggs, F. Grieser, G. W. Stevens, *J. Colloid Interface Sci.* **183**, 614 (1996).
7. D. E. Aston, J. C. Berg, *Ind. Eng. Chem. Res.* **41**, 389 (2002).
8. R. R. Dagastine, G. W. Stevens, D. Y. C. Chan, F. Grieser, *J. Colloid Interface Sci.* **273**, 339 (2004).
9. S. L. Carnie, D. Y. C. Chan, C. Lewis, R. Manica, R. R. Dagastine, *Langmuir* **21**, 2912 (2005).
10. S. L. Carnie, D. Y. C. Chan, R. Manica, *ANZIAM J.* **46(E)**, C808 (2005).
11. I. Ivanov, D. Dimitrov, *Surfact. Sci. Ser.* **29**, 379 (1988).
12. S. Abid, A. K. Chesters, *Int. J. Multiphase Flow* **20**, 613 (1994).
13. S. G. Yiantsios, R. H. Davis, *J. Fluid Mech.* **217**, 547 (1990).
14. A. K. Chesters, *Chem. Eng. Res. Des.* **69**, 259 (1991).
15. S. A. Nespolo, M. A. Bevan, D. Y. C. Chan, F. Grieser, G. W. Stevens, *Langmuir* **17**, 7210 (2001).
16. D. Bhatt, J. Newman, C. J. Radke, *Langmuir* **17**, 116 (2001).
17. D. Y. C. Chan, R. R. Dagastine, L. R. White, *J. Colloid Interface Sci.* **236**, 141 (2001).
18. R. R. Dagastine, T. T. Chau, D. Y. C. Chan, G. W. Stevens, F. Grieser, paper presented at the 7th World Congress of Chemical Engineering, Glasgow, Scotland, 10–14 July 2005.
19. J. C. Baygents, D. A. Saville, *J. Chem. Soc. Faraday Trans.* **87**, 1883 (1991).
20. E. Klaseboer, J. P. Chevaillier, C. Gourdon, O. Masbernat, *J. Colloid Interface Sci.* **229**, 274 (2000).
21. Materials and methods are available as supporting material on *Science* Online.
22. J. L. Hutter, J. Bechhoefer, *Rev. Sci. Instrum.* **64**, 1868 (1993).
23. J. N. Connor, R. G. Horn, *Faraday Discuss.* **123**, 193 (2003).
24. D. G. Goodall, M. L. Gee, G. Stevens, J. Perera, D. Beaglehole, *Colloids Surf. A* **143**, 41 (1998).

25. This work was supported by the Australian Research Council and by the National Science Foundation under Grant No. INT-020267.

Supporting Online Material

www.sciencemag.org/cgi/content/full/313/5784/210/DC1
Materials and Methods
Figs. S1 and S2

30 January 2006; accepted 1 June 2006
10.1126/science.1125527

Tyrannosaur Life Tables: An Example of Nonavian Dinosaur Population Biology

Gregory M. Erickson,[1]* Philip J. Currie,[2] Brian D. Inouye,[1] Alice A. Winn[1]

The size and age structures for four assemblages of North American tyrannosaurs—*Albertosaurus*, *Tyrannosaurus*, *Gorgosaurus*, and *Daspletosaurus*—reveal a pronounced, bootstrap-supported pattern of age-specific mortality characterized by relatively high juvenile survivorship and increased mortality at midlife and near the maximum life span. Such patterns are common today in wild populations of long-lived birds and mammals. Factors such as predation and entrance into the breeding population may have influenced tyrannosaur survivorship. This survivorship pattern can explain the rarity of juvenile specimens in museum collections.

Little is known about the population biology of nonavian dinosaurs. Did these animals show survivorship patterns akin to extant living dinosaurs—the birds, like the dinosaurs' cousins the crocodilians, or were they similar to more distantly related ecological analogs? Here, we use the age and size distribution from a death assemblage of the North American tyrannosaur *Albertosaurus sarcophagus* to produce an age-standardized ecological life table for a nonavian dinosaur population.

[1]Department of Biological Science, Florida State University, Tallahassee, FL 32306, USA. [2]Department of Biological Sciences, University of Alberta, Alberta T6G 2E, Canada.

*To whom correspondence should be addressed. E-mail: gerickson@bio.fsu.edu

We analyzed specimens from a monospecific assemblage found in 1910 by Brown (*1*) in sediments from the Horseshoe Canyon Formation along the Red Deer River, near Dry Island Buffalo Jump Provincial Park, Alberta, Canada. Renewed excavation of the site by the Royal Tyrrell Museum of Palaeontology, Drumheller, shows that 22 individuals are represented at the site (Table 1), making it the largest known aggregation of nonavian theropods from the Cretaceous Period and second only to the Cleveland Lloyd allosaur quarry (n = 40+) for a large species (*2*). Taphonomic analysis (*1*, *3*) reveals that the assemblage represents an attritional sampling (i.e., it is not representative of standing crop; fig. S2) from the local population (a group of coexisting individuals of the same species, whether a pack or individuals drawn from the area). The animals succumbed over a short period of time, perhaps through drought or starvation.

We selected fibulae and/or metatarsals from individuals representing 27% of the assemblage and used growth line counts to estimate ages at death (*3*–*6*). The smallest individual was included, as were some of the largest (Table 1). A regression of these data, along with age estimates for four other *A. sarcophagus* specimens from nearby sites within the formation (*7*) on femoral length, yielded $\text{Age}_{(\text{years})} = 0.033(\text{Femoral length}_{(\text{mm})}) - 9.765$, $r^2 = 0.919$ (fig. S1). The ages of the remaining individuals from the bone bed were estimated from this equation. Femoral lengths ranged from 0.32 to 1.16 m, and corresponding total lengths ranged from 2.2 to 10.1 m (table S1). Estimated ages for the dinosaurs spanned 2 to 28 years (Table 1). A life table (Table 1) (*3*, *8*) was constructed using these data, and a graph of age (x) versus survivorship (log l_x) was made (Fig. 1). We found a convex pattern of survivorship, with annual mortality ($q_{x(\text{year})}$) varying between 2 and 7% (mean = 3.7%) from ages 2 through 13, and between 10 and 33% (mean = 22.9%) from ages 14 through 23. (Note: 14 years is a plausible estimate for the typical age of sexual maturation in this taxon; see below.) Individuals surviving to 2 years of age had an average life expectancy of 16.60 years [6207 days divided by the 374 days in an early Maastrichtian year (*9*)]. A 90% confidence interval based on 10,000 bootstrap samples of these data supports the convex shape of the survivorship curve (Fig. 1 and fig. S4) (*3*).

Given that wild vertebrate populations, including carnivores, show high neonate mortality rates [e.g., a range of 50 to 80% per year is common in living crocodilians (*10*), birds (*11*), and mammals (*12*, *13*) despite major life history differences], this suggests similar rates in Dry Island *A. sarcophagus* and their complete survivorship curve resembling the sigmoidal type B_1 pattern (*14*) [a blend of Deevey type I and type III survivorship (*15*)] in which high neonate mortality gives way to high juvenile survivorship followed by increased rates of attrition later in development. Of the major survivorship patterns used to characterize populations for heuristic purposes (Fig. 2), types II and III can be ruled out as competing hypotheses in that they show linear and concave patterns, respectively. The remaining type I pattern is convex but is untenable because it occurs only in captive animals and humans from developed countries, where medical care and an absence of predation yield low neonate mortality.

The observed Dry Island *A. sarcophagus* survivorship pattern may be characteristic of tyrannosaurs as a whole, or it may reflect adaptation to local selective factors. Similar-sized single-population aggregations are not available for comparison. However, we surveyed a number of tyrannosaur fossils collected throughout specific North American formations (multipopulation sampling) and constructed composite life tables for these populations for comparison (tables S2 to S4) (*3*). Survivorship curves were constructed for *Tyrannosaurus rex* (n = 30) from the Hell Creek, Scollard, Willow Creek, and Frenchman formations; *Gorgosaurus libratus* (n = 39) from the Dinosaur Park and Two Medicine formations; and *Daspletosaurus* (n = 14) from the Dinosaur Park, Two Medicine, Oldman, and Lower Kirtland formations (*3*). As for the *A. sarcophagus* analysis, age was determined from growth line counts for 23% of the *T. rex* (n = 7), 13% of the *G. libratus* (n = 5), and 21% of the *Daspletosaurus* specimens (n = 3).

Like the Dry Island albertosaur population, survivorship in the outgroup tyrannosaurs—including *T. rex*, an animal with five times the body mass of *A. sarcophagus* (*7*)—was characterized by a convex pattern (Fig. 2). Post-neonate mortality rates averaging 2.5% (range 2.4 to 2.7%) were followed by increases in mortality averaging 20.9% (range 15.2 to 30.0%) before the demise of the cohorts. Maximum life span was 28 years for *T. rex*, 22 years for *G. libratus*, and 26 years for *Daspletosaurus*. Bootstrapped confidence in-

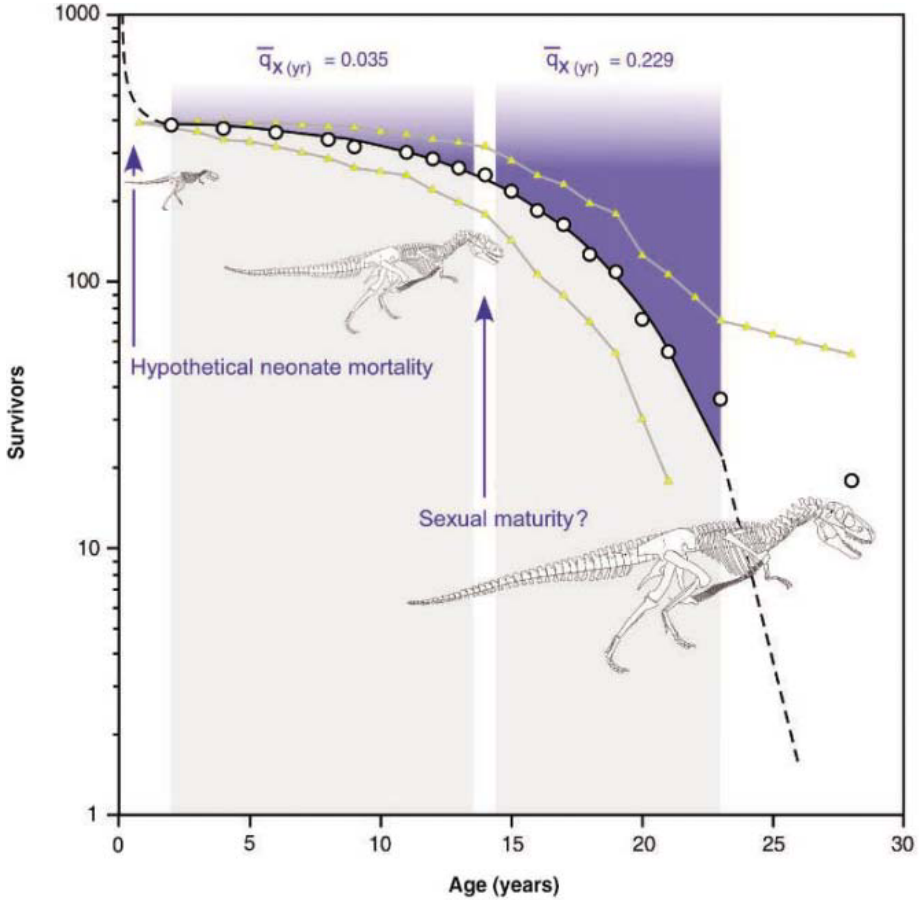

Fig. 1. Survivorship curve for a hypothetical cohort of 1000 *Albertosaurus sarcophagus* individuals, based on the Dry Island assemblage. Hypothesized neonate mortality is 60%. A period of relatively low mean mortality rates ($\overline{q}_{x(\text{year})}$) followed by a period of higher rates is indicated by the shaded regions. The progressive entrance of individuals into the breeding population may be reflected by the initial increases. A possible second increase in mortality late in development is denoted by dashed lines. Skeleton sizes during development at 2, 13, and 28 years are drawn in relative proportions to the maximal adult size of 10.1 m. The equation for the Gompertz curve is $n_x = n_0 \exp[(0.0073/0.1870)[1 - \exp(0.1870x)]]$, r^2 = 0.996, where n_x is the number of individuals alive at year x. Triangles show the 90% confidence interval based on 10,000 bootstrap samples of these data.

tervals supported the convex pattern in each taxon (fig. S4). Hence, it is unlikely that these samples could have come from populations with survivorship characteristics different from those of Dry Island *A. sarcophagus*, and this pattern appears to be characteristic of the entire group.

The ecological factors that contribute to the expression of type B_1 survivorship in extant vertebrate populations are well understood (*11*, *12*, *14*–*16*). High neonate mortality rates due to predation alone (disease, starvation, accidents, adverse climatic conditions, etc., also contribute) subside once a threshold size is reached. It appears that such a threshold was reached by age 2 in *A. sarcophagus*, when these animals had attained total lengths of 2 m, rivaling all other carnivorous theropods (deinonychosaurs, oviraptors, and ornithomimosaurs) in the Horseshoe Canyon Formation. It is here that *A. sarcophagus* survivorship diverged from patterns exhibited by their living archosaurian relatives, the crocodilians (Fig. 2), as well as other large ectothermal reptiles (*17*). Crocodilians, unlike nonavian dinosaurs such as tyrannosaurs (*6*, *7*), grow slowly, and their young remain susceptible to predation relatively late into development (*10*, *18*). Poor survivorship is further attenuated in crocodilians by rampant cannibalism that does not subside until they approach adult size (*10*). The relatively earlier decline in mortality and the evidence for gregariousness in tyrannosaurs (*1*, *19*), along with the rarity of postcranial bite marks from tyrannosaurs feeding on other tyrannosaurids (*20*), suggest that the rampant cannibalism seen in some theropods (*21*) was not a major factor in *A. sarcophagus* attrition. The *A. sarcophagus* survivorship pattern is also unlike that of most small birds, which do not show precipitous declines in mortality with attainment of adult size. This is because they remain highly susceptible to predation throughout life (*15*). In addition, adult size is often reached in a fraction of a year, so high neonate mortality rates contribute minimally to the first-year survivorship pattern (*11*, *15*). The hypothesized type B_1 survivorship pattern of tyrannosaurs is, however, similar to that seen in long-lived, typically large birds and mammals (*11*–*13*, *15*, *16*, *22*), which reach threshold sizes more rapidly than do ectothermal reptiles because of their relatively rapid growth rates (*23*), rates that are shared by tyrannosaurs (*7*).

The relatively low mortality rates among postneonate *A. sarcophagus* were maintained through about the 13th year of life, at which point they reached total lengths of ~6 m or 60% of their maximum recorded size (Fig. 1). A consequence of such low attrition is that ~70% of the animals surviving to 2 years of age were still alive at age 13. The taphonomic implications of this are intriguing. Neonate dinosaur remains are rarely recovered, either because they go unnoticed in the field or because their bones were consumed in their entirety or were completely broken down by the environment, hence they were unlikely to survive the vagaries of diagenesis to become fossilized (*12*, *13*, *15*). It seems unlikely that such considerations apply to the

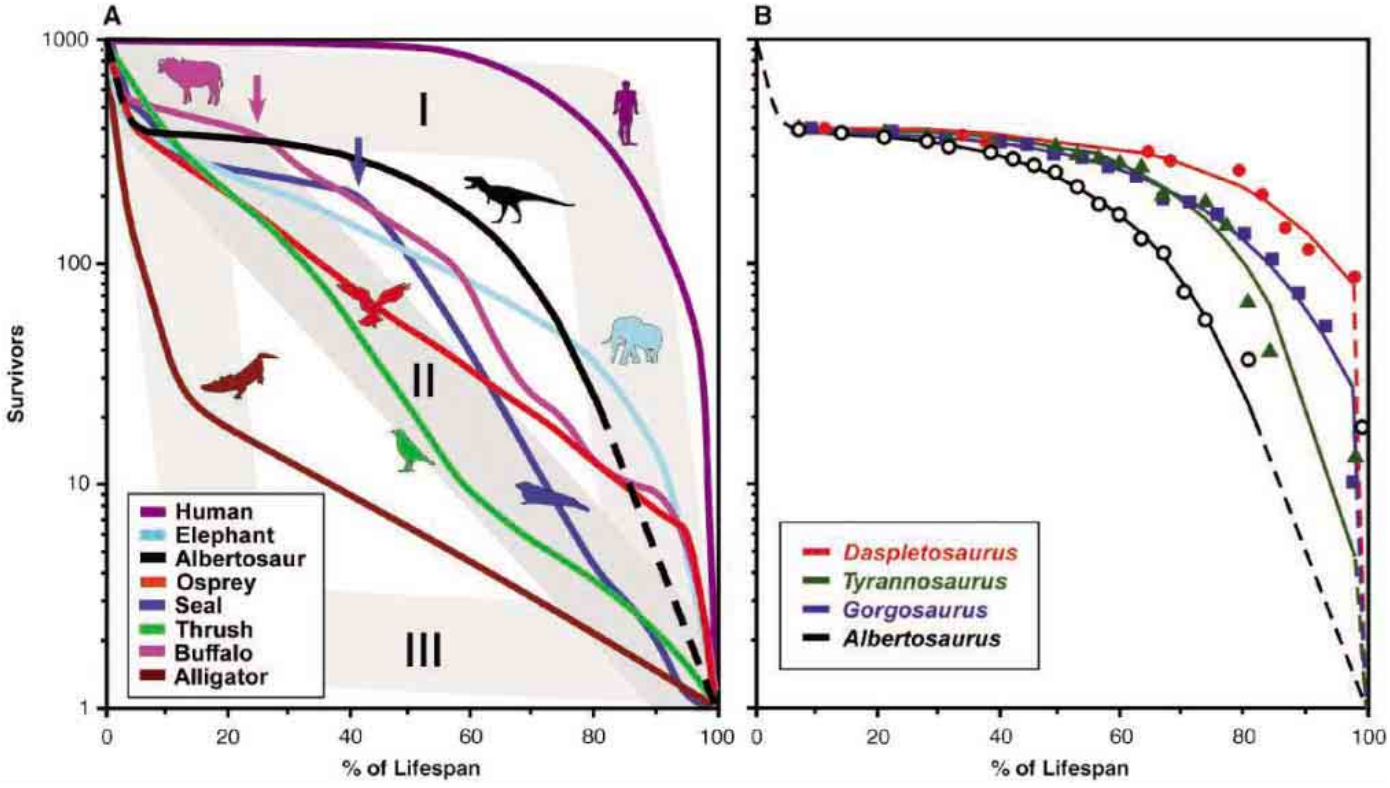

Fig. 2. *Albertosaurus* survivorship compared with patterns in living mammals, archosaurian relatives, and outgroup tyrannosaurs. The data are standardized according to ecological convention, with survivorship plotted on a logarithmic scale with respect to percent of maximum life span (*12*, *13*, *15*). (**A**) The shaded backgrounds show hypothetical ecological extremes used to characterize and contrast survivorship patterns (*15*). The convex type I pattern seen in some captive animals and in humans from developed countries (*8*, *15*) shows relatively low initial mortality followed by massive, senescence-driven die-offs as maximal life span is approached. The diagonal type II pattern [characteristic of small, short-lived birds, mammals, and lizards (*8*, *11*, *15*)] occurs in animals whose mortality is relatively constant throughout life. Populations showing the concave type III pattern [approached in crocodilians (*10*, *18*) and other large, long-lived reptiles (*17*)] experience high, early attrition; the few survivors that reach threshold sizes are likely to experience low mortality and to reach maximal life span. Long-lived, typically moderate to large birds (*22*) and mammals (*12*)—and presumably the tyrannosaur—show a sigmoidal type B_1 (*14*) pattern with high initial mortality rates, subsequent lower mortality, and increased mortality before extinction of the cohort. Note: Midlife, non–senescence-driven increases in mortality rates (arrows) often correspond to the onset of sexual maturity and breeding competition (*12*, *16*, *26*). (**B**) Survivorship in outgroup tyrannosaurs from multipopulation samples. All three outgroup species show bootstrap-supported (*3*) patterns of survivorship like that of the Dry Island *A. sarcophagus* population. Gompertz equation ($n_x = n_0 \exp[(a/g)[1 - \exp(gx)]]$) parameter values and fits: for *A. sarcophagus*, $a = 0.0073$, $g = 0.1870$, $r^2 = 0.9961$; for *Daspletosaurus* sp., $a = 0.0018$, $g = 0.2006$, $r^2 = 0.9669$; for *G. libratus*, $a = 0.0059$, $g = 0.2072$, $r^2 = 0.9944$; and for *T. rex*, $a = 0.002$, $g = 0.2214$, $r^2 = 0.9822$.

Table 1. Life table for Dry Island *A. sarcophagus*. TMP, Royal Tyrrell Museum of Palaeontology, Drumheller, Alberta, Canada; AMNH, American Museum of Natural History, New York City. Specimen numbers reflect elements definitively attributed to separate individuals from the assemblage. Mean length of life = 16.60 years. l_x values are the proportion of individuals alive at the beginning of each age class.

Specimen number	Age (years)	d_x (proportion dying)	l_x (proportion surviving)	q_x (interval mort. rate)	$q_{x(year)}$ (annual mort. rate)†
TMP 2002.5.46*	2	0.0455	1.000	0.0455	0.0455
(Age not represented)	3	—	—	—	0.0241
TMP 2000.45.15	4	0.0455	0.9545	0.0477	0.0241
(Age not represented)	5	—	—	—	0.0254
TMP 1999.50.19	6	0.0455	0.9090	0.0501	0.0254
(Age not represented)	7	—	—	—	0.0267
AMNH 5229*	8	0.0455	0.8635	0.0527	0.0267
TMP 2000.45.7	9	0.0455	0.8180	0.0556	0.0556
(Age not represented)	10	—	—	—	0.0299
AMNH 5233*	11	0.0455	0.7725	0.0589	0.0299
TMP 1999.50.28	12	0.0455	0.7270	0.0626	0.0626
TMP 1999.50.26	13	0.0455	0.6815	0.0668	0.0668
TMP 2004.56.43, 2001.45.60	14	0.0909	0.6360	0.1429	0.1429
AMNH 5234,* AMNH 5218i	15	0.0909	0.5451	0.1668	0.1668
TMP 2001.45.49	16	0.0455	0.4542	0.1002	0.1002
AMNH 5235,* 5228	17	0.0909	0.4087	0.2224	0.2224
AMNH 5218ay	18	0.0455	0.3178	0.1432	0.1432
AMNH 5232,* 5231	19	0.0909	0.2723	0.3338	0.3338
AMNH 5218ac	20	0.0455	0.1814	0.2508	0.2508
TMP 1999.50.2	21	0.0455	0.1359	0.3348	0.3348
(Age not represented)	22	—	—	—	0.2952
TMP 2000.45.9	23	0.0455	0.0904	0.5033	0.2952
(Age not represented)	24 to 27	—	—	—	—
TMP 2004.56.48	28	0.0455	0.0449	1.000	1.000

*Specimens for which longevity was directly determined from growth line counts. †Values for the missing cohorts (ages 3, 5, 7, 10, 22) were calculated assuming constant annual mortality over the interval spanning missing ages (*3*).

relatively large juveniles and subadults of North American tyrannosaurs, and yet their remains (even partial remains) are rare (tables S2 to S4) (*24*, *25*). Some have speculated, on the basis of an implicit assumption of a constant rate of mortality, that tyrannosaurs must have rocketed to adult size in a few years or less (*25*), thereby leaving only a small fraction of development from which juveniles could have contributed to the fossil record. However, this notion is inconsistent with our growth curve (*7*). Instead, we suggest that these young animals simply had low mortality, just like older juveniles and subadults of most large terrestrial mammals today.

Midlife increases in mortality rate among extant vertebrates are not uncommon (*8*, *12*, *13*, *15*). Some of these increases reflect intermittent adverse environmental perturbation or human intervention. Those reflecting life history often coincide with the onset of sexual maturity and/or entrance into the breeding population, at which time the physiological demands of oviposition and fasting, increased injuries and stress from agonistic activity in competition for mates, and heightened exposure to predators take their toll. Notable examples of decreased survival associated with attainment of sexual maturity include some birds (*11*), large ungulates (*12*, *26*), and marine mammals (*16*). Given these considerations, it is plausible that the doubling of interval mortality rates and the quadrupling of annual mortality rates predicted between ages 11 and 15 reflect one or more of these same selective factors (Table 1). Horrific cranial bite scars attest that agonistic encounters with conspecifics were commonplace in tyrannosaurs (*19*). Schweitzer *et al*. (*27*) have found medullary bone deposits indicating sexual maturity in a young *T. rex*. The corresponding developmental stage in *A. sarcophagus* occurs at 14 to 16 years (fig. S3), approximately the age at which growth rates begin to slow in *A. sarcophagus* in association with somatic maturity (*7*). Slowing of somatic growth also signals the onset of sexual maturity in living reptiles (*28*).

If *A. sarcophagus* typically matured no later than 14 to 16 years of age, the survivorship curve indicates that ~25% of *A. sarcophagus* hatchlings reached reproductive maturity; the proportion that successfully reproduced is indeterminable. Among this group, few would have had long reproductive life spans because mortality rates escalated thereafter to greater than 23% per year.

In most long-lived vertebrates, mortality rates accelerate late in life. Such acceleration may reflect the debilitating effects of physiological senescence that promote greater susceptibility to disease, predation, and injury (*29*, *30*). Substantial declines in survival late in life are difficult to document because large sample sizes are required and few older individuals remain to be sampled. Although our samples contained only one or two large individuals, the largest and oldest known *T. rex*—the 28-year-old FMNH PR 2081—derives from a late (stationary) developmental stage (*7*) and shows numerous signs of senescence in the form of age-related disease (*31*). Similarly, the giant 10.1-m *A. sarcophagus* individual in our analysis is the largest (and presumably oldest) known for the taxon. It also was in the late stationary phase of development (*7*) and, like FMNH PR 2081, appears to be an outlier in the size distribution (fig. S2) and thus may have been of similar physiological condition at the time of its demise. As is true for the paucity of subadult specimens in museums, the estimated survivorship curve also provides a possible explanation for the rarity of such giants; just 2% of the population lived long enough to attain maximal size and age for the species.

References and Notes

1. P. J. Currie, *Gaia* **15**, 271 (1998).
2. J. H. Madsen Jr., *Bull. Utah Geol. Min. Surv.* **109**, 1 (1976).
3. See supporting material on *Science* Online.
4. P. M. Sander, *Ann. Sci. Natur. Zool. Paris* **13**, 213 (1990).
5. A. Chinsamy-Turan, *The Microstructure of Dinosaur Bone* (Johns Hopkins Univ. Press, Baltimore, MD, 2005).
6. G. M. Erickson, *Trends Ecol. Evol.* **20**, 677 (2005).
7. G. M. Erickson *et al.*, *Nature* **430**, 772 (2004).
8. T. A. Ebert, *Plant and Animal Populations: Methods in Demography* (Academic Press, San Diego, CA, 1999).
9. J. W. Wells, *Nature* **197**, 948 (1963).
10. G. Webb, C. Manolis, *Crocodiles of Australia* (Reed, French's Forest, New South Wales, Australia, 1989).
11. I. Newton, Ed., *Lifetime Reproduction in Birds* (Academic Press, London, 1989).
12. C. A. Spinage, *Ecology* **53**, 645 (1972).
13. B. Kurtén, *On the Evolution of Fossil Mammals* (Columbia Univ. Press, New York, 1988).
14. R. Pearl, J. R. Miner, *Q. Rev. Biol.* **10**, 60 (1935).
15. E. S. Deevey Jr., *Q. Rev. Biol.* **22**, 283 (1947).
16. J. R. Flowerdue, *Mammals: Their Reproductive Biology and Population Ecology* (Edward Arnold, London, 1987).
17. J. B. Iverson, *Can. J. Zool.* **69**, 385 (1991).
18. C. L. Abercrombie, K. G. Rice, C. A. Hope, in *Crocodilian Biology and Evolution*, G. C. Grigg, F. Seebacher, C. E. Franklin, Eds. (Surrey Beatty, Chipping Norton, New South Wales, Australia, 2000), pp. 409–418.
19. D. Tanke, P. J. Currie, *Gaia* **15**, 167 (1998).
20. A. R. Jacobsen, *Hist. Biol.* **13**, 17 (1998).
21. R. R. Rogers, D. W. Krause, K. C. Rogers, *Nature* **422**, 515 (2003).
22. S. Postupalsky, in *Lifetime Reproduction in Birds*, I. Newton, Ed. (Academic Press, London, 1989), pp. 297–313.
23. G. M. Erickson, K. Curry-Rogers, S. Yerby, *Nature* **412**, 429 (2001).
24. T. D. Carr, *J. Vertebr. Paleontol.* **19**, 497 (1999).
25. P. Larson, K. Donnan, *Rex Appeal* (Invisible Cities Press, Montpelier, VT, 2002).
26. R. D. Estes, *Behavioral Guide to African Mammals: Including Hoofed Mammals, Carnivores, Primates* (Univ. of California Press, Berkeley, CA, 1991).
27. M. H. Schweitzer, J. L. Wittmeyer, J. R. Horner, *Science* **308**, 1456 (2005).
28. R. M. Andrews, in *Biology of the Reptilia, Physiology D, Vol. 13*, C. Gans, F. H. Pough, Eds. (Academic Press, New York, 1982).
29. D. Promislow, *Evolution* **45**, 1869 (1991).
30. R. E. Ricklefs, A. Scheurlein, *Exp. Gerontol.* **36**, 845 (2001).

31. C. A. Brochu, *J. Vertebr. Paleontol. Mem.* **22**, 1 (2003).
32. We thank M. Norell and C. Mehling of the American Museum of Natural History and J. Gardner of the Royal Tyrrell Museum of Palaeontology for access to specimens in their care, and P. Larson and the Black Hills Institute of Geological Research Inc. for providing graphics for our use. Supported by NSF Division of Earth Sciences grant EAR 0207744 (G.M.E.).

Supporting Online Material
www.sciencemag.org/cgi/content/full/313/5784/213/DC1
Materials and Methods
Figs. S1 to S4
Tables S1 to S4
References

2 February 2006; accepted 1 June 2006
10.1126/science.1125721

Crystal Structure of Glycoprotein B from Herpes Simplex Virus 1

Ekaterina E. Heldwein,[1,2]* Huan Lou,[4] Florent C. Bender,[4] Gary H. Cohen,[4] Roselyn J. Eisenberg,[5] Stephen C. Harrison[1,2,3]

Glycoprotein B (gB) is the most conserved component of the complex cell-entry machinery of herpes viruses. A crystal structure of the gB ectodomain from herpes simplex virus type 1 reveals a multidomain trimer with unexpected homology to glycoprotein G from vesicular stomatitis virus (VSV G). An α-helical coiled-coil core relates gB to class I viral membrane fusion glycoproteins; two extended β hairpins with hydrophobic tips, homologous to fusion peptides in VSV G, relate gB to class II fusion proteins. Members of both classes accomplish fusion through a large-scale conformational change, triggered by a signal from a receptor-binding component. The domain connectivity within a gB monomer would permit such a rearrangement, including long-range translocations linked to viral and cellular membranes.

Herpes simplex virus type 1 (HSV-1) is the prototype of the diverse herpesvirus family, which includes such notable human pathogens as cytomegalovirus (CMV), Epstein-Barr virus (EBV), and Kaposi's sarcoma–associated herpesvirus (KSHV). Herpesviruses have an envelope, an outer lipid bilayer, bearing 12 surface glycoproteins. To deliver the capsid containing the double-stranded DNA genome into the host cell, HSV-1 must fuse its envelope with a cellular membrane. Among viral glycoproteins, only gC, gB, gD, gH, and gL participate in viral cell entry, and only the last four are required for fusion (*1*–*4*). All herpesviruses have gB, gH, and gL, which constitute the core fusion machinery (*5*). Of these, gB is the most highly conserved.

The virus attaches to a cell through a nonessential interaction of gC with heparan sulfate proteoglycan and through an essential interaction of gD with one of three cellular receptors: nectin-1, herpesvirus entry mediator (HVEM), or a specifically modified heparan sulfate (*6*). Crystal structures of the soluble ectodomain of gD, unbound and in complex with the ectodomain of HVEM (*7*, *8*), show that binding of gD and receptor causes the former to undergo a conformational change in which a C-terminal segment of the ectodomain polypeptide chain is released from a strong intramolecular contact. The liberated C-terminal segment may interact with gB or the gH/gL complex to trigger molecular rearrangements and, ultimately, fusion. The precise functions of gB and gH/gL are unknown. Both are required for entry, and either or both presumably receive the signal from gD and respond by undergoing a conformational change; gD itself is thought not to participate in the fusion process (*9*, *10*). Neither gB nor gH/gL has an obvious fusion peptide, but an indication that gB might be a fusion effector comes from the notable syncytial phenotype caused by certain mutations within the cytoplasmic domain of gB (*1*, *11*–*13*).

HSV-1 gB is a 904-residue protein. In the work reported here, we determined the crystal structure of a nearly full-length ectodomain of gB, residues Asp^{103} to Ala^{730} (*14*) (Fig. 1). Various features of the structure suggest that it is a fusion effector, an inference strengthened by its notable and unanticipated similarity to the structure of the fusion glycoprotein Gr of vesicular stomatitis virus (VSV), described in an accompanying paper (*15*). Domains that

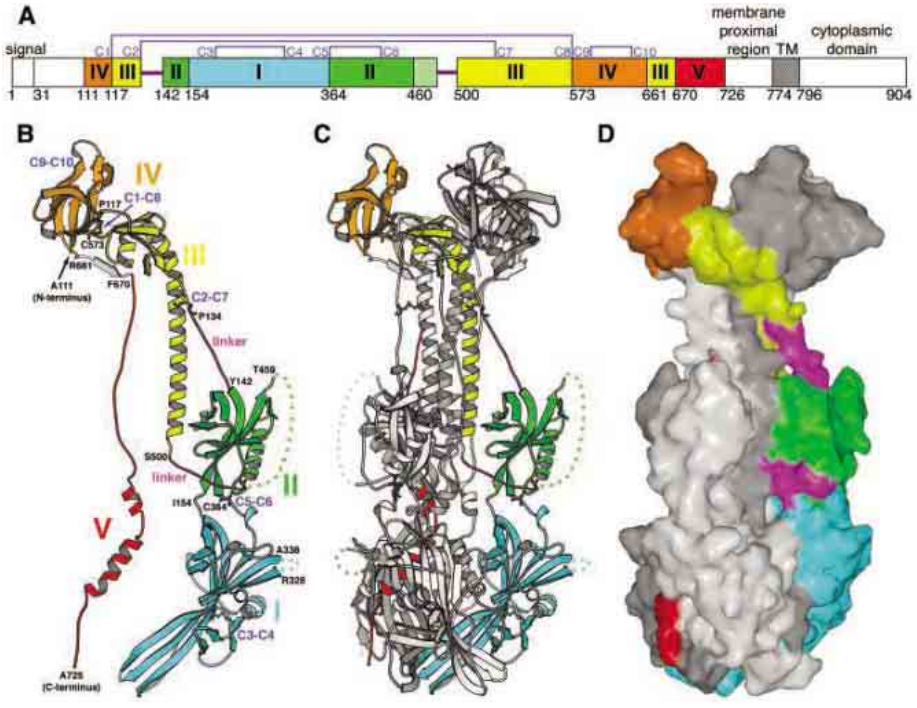

Fig. 1. (**A**) Domain architecture of gB. Domains observed in the crystal structure are highlighted in different colors, and their corresponding first residue positions are shown. (**B**) Ribbon diagram of a single gB protomer. The domains are rendered in colors corresponding to (A). Labeled residues (*26*) indicate the limits of individual domains and the disordered loop in domain I. Residues Arg^{661} to Thr^{669} of the shown protomer are in gray because they belong to domain III of a neighboring protomer. Residues Arg^{661} to Thr^{669} of the other neighboring protomer are included here and shown in yellow, because they contribute to a sheet in domain III of the shown protomer. Disordered segments are shown as dots of appropriate color. Disulfides are shown in ball-and-stick representation. Cysteines are numbered according to (A) and fig. S2. (**C**) gB trimer. Protomer A is the same as in (B). Protomer B is shown in white and protomer C in gray. (**D**) Accessible surface area representation of gB trimer. The coloring scheme is the same as in the rest of Fig. 1. Images were generated with the use of MOLSCRIPT (*27*) and SPOCK (*28*).

[1]Department of Biological Chemistry and Molecular Pharmacology, Harvard Medical School, [2]Laboratory of Molecular Medicine, [3]Howard Hughes Medical Institute, Children's Hospital, 320 Longwood Avenue, Boston, MA 02115, USA. [4]Department of Microbiology, School of Dental Medicine, [5]Department of Pathobiology, School of Veterinary Medicine, University of Pennsylvania, 240 South 40th Street, Philadelphia, PA 19104, USA.

*To whom correspondence should be addressed. E-mail: heldwein@crystal.harvard.edu

cover the lateral surfaces of the gB spike are suspended by extended segments of polypeptide chain from the membrane-distal end of the molecule (Fig. 1), suggesting a mechanism for a fusogenic conformational change.

The crystal structure of the HSV-1 gB ectodomain, refined at 2.1 Å resolution, contains three protomers designated A, B, and C. Disordered regions correspond to ~10% of the polypeptide chain. Trimeric gB is a spike with approximate dimensions of 85 Å by 80 Å by 160 Å. The bulk of each protomer, residues Ala^{111} to Thr^{669}, coils around the others with a left-handed twist (Fig. 1). Each protomer extends a C-terminal arm from one end of the molecule to the other, inserting it into the junction between the other two protomers (Fig. 1). There is no trimerization domain per se; instead, multiple contacts between protomers throughout the molecule contribute to trimer stability. The 10 cysteines per subunit form five disulfide bonds, all intramolecular. Their pairwise assignments in our structure agree with those previously determined by mass spectrometry for a homologous HSV-2 gB (*16*).

Each protomer can be divided into five distinct regions or domains: I, base; II, middle; III, core; IV, crown; and V, arm (Fig. 1 and fig. S1). Residues Pro^{134} to Asn^{141} and Val^{492} to Ser^{499} are linkers between domains II and III.

Domain I is composed of a continuous polypeptide chain, residues Ile^{154} to Val^{363} (Fig. 1). It has the fold characteristic of a pleckstrin-homology (PH) domain (*17*, *18*), a β sandwich composed of two nearly orthogonal β sheets of four and three strands, respectively (Fig. 2). In cytoplasmic signaling pathways, proteins with this fold serve as scaffolds to allow phosphoinositide and peptide binding. The helix that in a canonical PH domain normally covers one opening of the β sandwich is replaced in domain I by a long loop and short helix. An insertion of residues Tyr^{165} to Ile^{272} between strands β4 and β11 creates a curving subdomain at the base of the trimer (Fig. 2). This latter subdomain consists of a four-strand β sheet (with three long strands and one short strand), the convex side of which is covered with an α helix, a β hairpin, and a short two-strand β sheet. This subdomain has no previously described structural relatives (*19*).

Domain II comprises two discontinuous segments, residues Tyr^{142} to Asn^{153} and Cys^{364} to Thr^{459} (Fig. 1). At its center is a six-strand β barrel reminiscent of the PH superfold, with strand β5 of the canonical PH domain missing (Fig. 2). In its place, there is a helix-strand insert on the outer face of the barrel. The entire domain I is inserted between strands β3 and β17, the first and second strands of domain II. Residues Leu^{460} to Ser^{491} in protomers A and C and residues Glu^{462} to Ser^{491} in protomer B are disordered. Tryptic cleavage between Arg^{474} and Lys^{475} has probably destabilized this loop, which lies on the outer margin of domain II and which is the locus of a posttranslational cleavage in some herpesviruses, such as HCMV (*20*). The loop is at least partially ordered in crystals of uncleaved gB ectodomain (*14*).

Domain III contains three discontinuous segments, residues Pro^{117} to Pro^{133}, Ser^{500} to Thr^{572}, and Arg^{661} to Thr^{669} (Fig. 1). It has a long, 44-residue α helix followed by a short helix and a small, four-strand mixed β sheet. The long helix and its trimeric counterparts form the central coiled-coil. Residues Arg^{661} to Thr^{669} of the outer β strand do not belong to the same polypeptide chain but instead to a neighboring protomer. This region, which is not a domain in the strict sense of an independent folding unit, contributes many of the essential trimer contacts.

Domain IV comprises two discontinuous segments, residues Ala^{111} to Cys^{116} and Cys^{573} to Ser^{660} (Fig. 1). These segments are linked by a disulfide bond, C1 to C8. This domain has no previously described structural relatives (*19*).

Domain V, residues Phe^{670} to Ala^{725}, stretches from top to bottom of the molecule as a long extension (Fig. 1). Residues in this segment have no contact with the rest of the polypeptide chain of the same protomer but rather fit into the groove between the core domains of the other two protomers, probably reinforcing the trimer interactions.

gB is the most conserved herpesvirus entry glycoprotein (fig. S2). Our structure accounts well for the regions of high and low sequence variation. Thus, the structure of HSV-1 gB can be taken to represent the structure of all herpesvirus gB proteins, and in analyzing properties such as antigenicity, we can map results from various herpesviruses onto it. Figure 3 shows several epitopes of neutralizing monoclonal antibodies against HSV and HCMV. All epitopes map to the surface, along the lateral faces of the spikes and on the tip of the crown. Although the majority of the epitopes are located far from either end of the molecule, two virus-neutralizing monoclonal antibodies to HSV, both of which recognize the same epitope, map to domain IV, directly on the crown end (*21*) (Fig. 3). In addition, residues Pro^{575} to Gln^{658} are homologous to antigenic domain 1 in HCMV gB, which is a dominant neutralizing epitope (*22*). Thus, we propose that on the surface of the virions, gB is oriented such that domain IV is fully exposed.

The gB ectodomain fragment we have analyzed lacked residues Ala^{31} to Arg^{102} and Met^{731} to Asn^{773}. Trypsin cleavage before crystallization separates residues Ala^{31} to Arg^{102}, which are poorly conserved and relatively unstructured, from the rest of the molecule, probably because this segment, which contains a heparan sulfate interaction site (*23*), is not firmly anchored. We have determined a lower resolution (3.5 Å) structure of an uncleaved ectodomain trimer, residues Ala^{31} to Ala^{730} (*14*); the conformation of residues Thr^{109} to Ala^{725} is essentially the same as in the crystals of trypsin-treated ectodomain, and the residues Ala^{31} to Asn^{108} are disordered. The membrane-proximal region of the intact ectodomain, residues Met^{731}

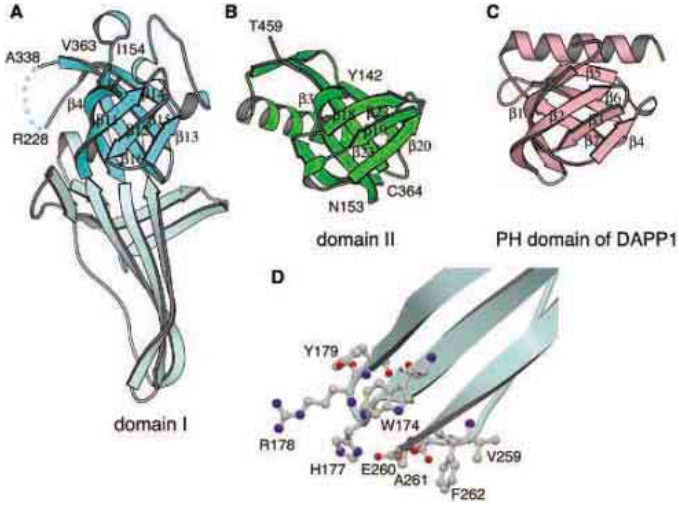

Fig. 2. Side-by-side comparison of domains I and II with a PH domain from the B-lymphocyte adaptor protein DAPP1 (PDB identification number 1fao). The three domains are shown in the same orientation. The alignment was carried out with the use of LSQMAN (*29*). (**A**) Domain I. PH-like subdomain, residues Ile^{154} to Thr^{162} and Glu^{275} to Val^{363}, is shown as a cyan ribbon. Disordered residues Asp^{329} to Thr^{337} are shown as dots. Residues that do not belong to the PH-like subdomain, Met^{163} to Glu^{274}, are shown in a lighter color. (**B**) Domain II. Disordered residues Leu^{460} to Ser^{491} are not shown. (**C**) PH domain of DAPP1. The numbering scheme for the β strands follows PH domain convention. Strands β4-β11-β12-β13-β14-β15 of domain I and β3-β18-β19-β20—β22-β23 of domain II correspond to strands β1-β2-β3-β4-β5-β6-β7 of the PH domain in DAPP1. Domain I residues Ile^{154} to Asp^{167} and Cys^{271} to Val^{363} superimpose on DAPP1 residues Pro^{162} to Trp^{250}, with a root mean square deviation (RMSD) of 2.0 Å between 39 structurally equivalent Cα atoms. Domain II residues Tyr^{142} to Lys^{151} and Cys^{364} to Asn^{458} superimpose on DAPP1 residues Pro^{162} to Trp^{250}, with a RMSD of 1.68 Å between 41 structurally equivalent Cα atoms. Domain I and domain II superimpose with a RMSD of 1.77 Å between 41 structurally equivalent Cα atoms. (**D**) Close-up of the tip of domain I, as if viewing from the right the lower part of the structure in (A). Selected residues (labeled) are shown in ball-and-stick representation.

to Asn^{773}, is very hydrophobic. This characteristic suggests that it lies against the membrane, perhaps forming a pedestal for the rest of the trimeric ectodomain.

The complex architecture of the gB ectodomain identifies it as a homolog of VSV G, described in the accompanying paper (*15*). The VSV G ectodomain is smaller and more compact than gB, but the individual domains are structurally homologous (fig. S3) and their spatial relations correspond remarkably closely. The most obvious similarities include the elongated structural element that includes domains I and II of gB (corresponding to domains IV and III, respectively, in VSV G), the PH domain–like fold of domain II (domain III in VSV G), the central helix of domain III of gB (domain II of VSV G), the order of strands of gB domain IV (domain I of VSV G), and the location of the C terminus adjacent to the putative fusion loops.

G, the sole surface protein on VSV, is the viral fusogen. It contains an internal fusion loop, identified by membrane photolabeling experiments (*24*) as the segment corresponding to the tip of our domain I. G undergoes a reversible, fusion-activating conformational change at low pH; the structural correlates of this change have not yet been mapped. The similarity to VSV G strongly suggests that gB is the effector of fusion in herpesviruses and that aspects of the fusion mechanisms proposed for other viral fusion proteins apply. The two loops at the tip of domain I, corresponding to the fusion peptide segments in VSV G, contain hydrophobic residues, including an exposed phenylalanyl side chain and a tryptophanyl side chain that could rotate into an exposed position (Fig. 2). This tip could insert into the interface between head groups and hydrocarbons in a lipid bilayer, in the same way that the class II viral fusion loops insert (*25*). Nevertheless, the conformation of the fusion loops appears suboptimal for membrane insertion, and we anticipate that local conformational changes will expose more hydrophobic residues.

An important characteristic of viral fusion effectors is triggered conformational rearrangement. In most cases, the transition is irreversible, and the structural change dramatic. Because the VSV G transition appears to be reversible and because the protein is a trimer in both states, the structural differences between the two states might be less striking. The structure of VSV G described in the accompanying paper is probably the postfusion form. Which state of gB does our structure represent? The epitopes for neutralizing antibodies all map to the surface of the protein in the conformation present in our crystals (Fig. 3). In particular, the major neutralizing epitope for HCMV gB lies on the outer face of the crown (domain IV). Neutralizing antibodies should recognize the prefusion conformation of gB, and we might expect that at least some of the epitopes would be absent from the surface of the protein in a postfusion conformation. Nonetheless, a number of other features suggest that our structure represents a postfusion state, consistent with its similarity to the low-pH form of VSV G. The critical characteristic of all postfusion structures, in both class I and class II fusion proteins, is adjacency of the fusion peptide and the C-terminal transmembrane anchor. The fusion peptide inserts into the target-cell membrane; the transmembrane anchor crosses the viral membrane, and the transition to proximity forces the two membranes together. The putative gB fusion loops are indeed adjacent to the C-termini of the polypeptide chains of the fragment we have crystallized, but there are about 45 additional residues not present in the expressed fragment that intervene between its terminus and the transmembrane segment. Uncertainty about the disposition of this intervening peptide thus makes it difficult to conclude where the transmembrane anchor will be relative to the tip of domain I. The peptide could be analogous to the stem of flavivirus fusion proteins: a hydrophobic element that forms a pedestal against the membrane in the prefusion state and zips up along the trimer in the transition to a postfusion state.

Some unusual features of the gB structure suggest that it has evolved to unfold and refold like other viral fusion proteins. Do-

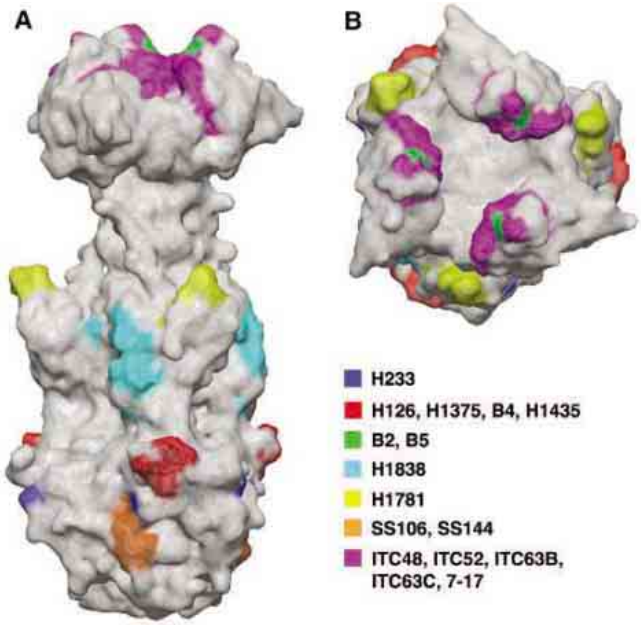

Fig. 3. Accessible surface of the gB ectodomain in semitransparent rendering in a side view (**A**) and a top view (**B**). The underlying polypeptide chains are shown as white worms. Three groups of epitopes of the neutralizing antibodies are shown. Group 1 contains epitopes in HSV-1 gB identified by isolating single–amino acid monoclonal antibody (mAb) resistance mutants. These are residues Ala^{315} and Arg^{328} (mAb H233), shown in blue; residues Tyr^{303} (mAb H126), Arg^{304} (mAb H1375), Glu^{305} (mAb B4), and His^{308} (mAb H1435), shown in red; and residue Gly^{594} (mAbs B2 and B5), shown in green (*21*, *30*–*32*). Group 2 contains epitopes in HSV-1 gB identified by peptide mapping using enzyme-linked immunosorbent assays (ELISAs). These are residues Ala^{390} to Gly^{410} (mAb H1838), shown in cyan; residues Pro^{454} to Ser^{473} (mAb H1781), shown in yellow; and residues Ser^{697} to Ala^{725} (mAbs SS106 and SS144), shown in orange (*14*). Group 3 contains epitopes in HCMV gB identified by peptide mapping using ELISAs. These correspond to HSV-1 residues Pro^{593} to Val^{602}, Ala^{629} to Thr^{642} (mAbs ITC48, ITC52, ITC63B, and ITC63C), and Glu^{631} to Val^{648} (mAb 7-17), all shown in purple (*33*, *34*). The orientations were chosen to show all the epitopes and were derived from the orientation in Fig. 1 by rotating the molecule about the vertical axis by ~45° to the left.

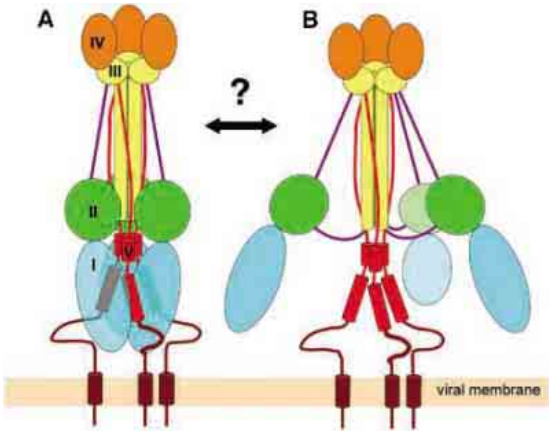

Fig. 4. Schematic model of gB, illustrating how it could refold in a umbrellalike fashion. (**A**) Structure determined in this work. Domains are shown schematically by using the color scheme in Fig. 1. The membrane-proximal regions are shown as brown lines. Transmembrane regions are shown as brown cylinders. (**B**) The linkers leading into and out of the domain I-II module would permit a large-amplitude rotation. The structure described here might represent either the starting point or the endpoint of such a translocation, and thus it might have either a prefusion or a postfusion conformation (double-headed arrow).

mains I and II, which decorate the lateral surface of the trimer, are suspended from the rest of the molecule by curiously extended polypeptide segments (Fig. 1 and Fig. 4). Moreover, they trap the almost fully extended domain V of another monomer. The segment that leads downward into domain II is anchored at the top by a disulfide bond to the coiled-coil, C2 to C7. The segment that leads out of domain II and into the coiled-coil contains the long disordered loop that is cleaved in CMV. These two linker segments would permit large motions of the domain I-II fusion module, as suggested in the diagram (Fig. 4). The putative fusion loops at the tip of this module could swing through a substantial arc.

Despite the notable homology between gB and VSV G, the two proteins have some functional differences. Unlike VSV G, gB alone is not sufficient for viral entry; all herpesviruses also require gH and gL. The trigger for HSV fusion is, at least in part, the rearrangement of gD induced by receptor binding. Receptor-mediated release of the gD C terminus would allow it to contact another HSV glycoprotein involved in entry, e.g., the peripherally located, PH-like domains I and II of gB. It is possible that gH/gL restrains gB in a prefusion state; the exposed gD C terminus might then interrupt this inhibitory contact at least in the case of alphaherpesviruses. Whatever the mechanism, the structure of gB identifies it as the fusogen and shows it to have the properties needed for a fusion-promoting conformational rearrangement.

References and Notes

1. W. H. Cai, B. Gu, S. Person, *J. Virol.* **62**, 2596 (1988).
2. M. W. Ligas, D. C. Johnson, *J. Virol.* **62**, 1486 (1988).
3. A. Forrester *et al.*, *J. Virol.* **66**, 341 (1992).
4. C. Roop, L. Hutchinson, D. C. Johnson, *J. Virol.* **67**, 2285 (1993).
5. P. G. Spear, R. Longnecker, *J. Virol.* **77**, 10179 (2003).
6. P. G. Spear, *Cell. Microbiol.* **6**, 401 (2004).
7. A. Carfi *et al.*, *Mol. Cell* **8**, 169 (2001).
8. C. Krummenacher *et al.*, *EMBO J.* **24**, 4144 (2005).
9. N. A. Jones, R. J. Geraghty, *Virology* **324**, 213 (2004).
10. F. Cocchi *et al.*, *Proc. Natl. Acad. Sci. U.S.A.* **101**, 7445 (2004).
11. P. J. Gage, M. Levine, J. C. Glorioso, *J. Virol.* **67**, 2191 (1993).
12. T. P. Foster, J. M. Melancon, K. G. Kousoulas, *Virology* **287**, 18 (2001).
13. D. J. Bzik, B. A. Fox, N. A. DeLuca, S. Person, *Virology* **137**, 185 (1984).
14. Materials and methods are available as supporting material on *Science* Online.
15. S. Roche, S. Bressanelli, F. A. Rey, Y. Gaudin, *Science* **313**, 187 (2006).
16. N. Norais *et al.*, *J. Virol.* **70**, 7379 (1996).
17. N. Blomberg, E. Baraldi, M. Nilges, M. Saraste, *Trends Biochem. Sci.* **24**, 441 (1999).
18. M. A. Lemmon, K. M. Ferguson, *Biochem. J.* **350**, 1 (2000).
19. L. Holm, C. Sander, *Trends Biochem. Sci.* **20**, 478 (1995).
20. M. Vey *et al.*, *Virology* **206**, 746 (1995).
21. S. L. Highlander *et al.*, *J. Virol.* **63**, 730 (1989).
22. W. J. Britt, M. A. Jarvis, D. D. Drummond, M. Mach, *J. Virol.* **79**, 4066 (2005).
23. S. Laquerre *et al.*, *J. Virol.* **72**, 6119 (1998).
24. P. Durrer, Y. Gaudin, R. W. H. Ruigrok, R. Graf, J. Brunner, *J. Biol. Chem.* **270**, 17575 (1995).
25. S. C. Harrison, *Adv. Virus Res.* **64**, 231 (2005).
26. Single-letter abbreviations for the amino acid residues are as follows: A, Ala; C, Cys; D, Asp; E, Glu; F, Phe; G, Gly; H, His; I, Ile; K, Lys; L, Leu; M, Met; N, Asn; P, Pro; Q, Gln; R, Arg; S, Ser; T, Thr; V, Val; W, Trp; and Y, Tyr.
27. P. J. Kraulis, *J. Appl. Crystallogr.* **24**, 946 (1991).
28. More information is available online (http://quorum.tamu.edu/Manual/Manual/Manual.html).
29. G. J. Kleywegt, T. A. Jones, *Acta Crystallogr.* **D52**, 826 (1996).
30. P. E. Pellett, K. G. Kousoulas, L. Pereira, B. Roizman, *J. Virol.* **53**, 243 (1985).
31. K. G. Kousoulas, B. Huo, L. Pereira, *Virology* **166**, 423 (1988).
32. L. Pereira, M. Ali, K. Kousoulas, B. Huo, T. Banks, *Virology* **172**, 11 (1989).
33. U. Utz, W. Britt, L. Vugler, M. Mach, *J. Virol.* **63**, 1995 (1989).
34. M. Ohlin, V. A. Sundqvist, M. Mach, B. Wahren, C. A. Borrebaeck, *J. Virol.* **67**, 703 (1993).

35. We thank M. Berne of the Tufts Protein Chemistry Facility for N-terminal sequencing, D. King of the University of California at Berkeley for mass spectrometry, E. Settembre for the x-ray data collection, E. M. Vogan for help with crystallographic software, and L. Pereira for providing several antibodies to gB. This work was funded by NIH grants AI065886 (to E.E.H.), AI049980 (to S.C.H.), and AI056045 and NS36731 (to R.J.E.). S.C.H. is an investigator in the Howard Hughes Medical Institute. Coordinates and structure factors have been deposited with the Research Collaboratory for Structural Bioinformatics (RCSB) Protein Data Bank (PDB) with accession code 2gum.

Supporting Online Material

www.sciencemag.org/cgi/content/full/313/5784/217/DC1
Materials and Methods
Figs. S1 to S3
Tables S1 and S2
References

22 February 2006; accepted 16 May 2006
10.1126/science.1126548

A Bacterial Virulence Protein Suppresses Host Innate Immunity to Cause Plant Disease

Kinya Nomura,[1] Sruti DebRoy,[1] Yong Hoon Lee,[1] Nathan Pumplin,[1] Jonathan Jones,[2] Sheng Yang He[1]*

Plants have evolved a powerful immune system to defend against infection by most microbial organisms. However, successful pathogens, such as *Pseudomonas syringae*, have developed countermeasures and inject virulence proteins into the host plant cell to suppress immunity and cause devastating diseases. Despite intensive research efforts, the molecular targets of bacterial virulence proteins that are important for plant disease development have remained obscure. Here, we show that a conserved *P. syringae* virulence protein, HopM1, targets an immunity-associated protein, AtMIN7, in *Arabidopsis thaliana*. HopM1 mediates the destruction of AtMIN7 via the host proteasome. Our results illustrate a strategy by which a bacterial pathogen exploits the host proteasome to subvert host immunity and causes infection in plants.

Many plant and human pathogenic bacteria rely on an essential virulence system—the type III secretion system—to inject virulence effector proteins into the host cell to cause infection (*1*–*3*). Recent research has documented the ability of effector proteins of mammalian pathogenic bacteria to modulate host cytoskeleton dynamics, membrane composition, vesicle trafficking, and host immunity (*4*). In contrast, very little is known about the molecular mechanisms by which bacterial effector proteins induce disease in plants. Emerging evidence suggests that a major function of these effector proteins is to suppress host immune responses in susceptible plants (*5*–*11*). However, the mechanisms by which effector proteins subvert host immune responses are poorly understood at the molecular level.

Pseudomonas syringae infects a wide range of economically important plant species. All of the examined *P. syringae* strains contain a common genomic pathogenicity island, which is composed of type III secretion–associated *hrp*/*hrc* genes, an exchangeable effector locus, and a conserved effector locus (*12*). A partial deletion of the conserved effector locus in the ΔCEL mutant of *Pst* DC3000 resulted in a notable reduction of the bacterial population and the complete elimination of disease symptoms (necrosis and chlorosis) in infected tomato and *Arabidopsis* plants (*12*, *13*). The severe virulence defect in the ΔCEL mutant bacteria is caused by the deletion of the functionally redundant

[1]Department of Energy Plant Research Laboratory, Department of Plant Biology, Michigan State University, East Lansing, MI 48824, USA. [2]Sainsbury Laboratory, John Innes Centre, Norwich Research Park, Norwich NR4 7UH, UK.

*To whom correspondence should be addressed. E-mail: hes@msu.edu

effector genes *hopM1* (formerly *hopPtoM*) and *avrE* (*13*). pORF43, a plasmid expressing only HopM1 and its cognate chaperone ShcM, is sufficient to fully complement the virulence defect of the ΔCEL mutant in *Arabidopsis* (*13*).

HopM1 is a 712–amino acid protein that is translocated into the host cell (*14*). In this study, we investigated whether HopM1, expressed inside the host cell, could restore the virulence of the ΔCEL mutant. Plant-expressed full-length HopM1 almost fully complemented the virulence defect of the ΔCEL mutant (Fig. 1A). Moreover, the complementation was specific to the ΔCEL mutant because the multiplication of the type III secretion–defective *hrcC* mutant (*15*), which does not secrete any effector proteins, was increased only slightly (Fig. 1A). Subcellular fractionation experiments revealed that HopM1 was enriched in the endomembrane fraction in the transgenic plants (Fig. 1B). Taken together, these results suggest that HopM1 acts in a host's endomembrane compartment or compartments to promote bacterial pathogenesis.

To define the regions important for the virulence function of HopM1, we produced transgenic *Arabidopsis* plants expressing a series of C- and N-terminally truncated derivatives of HopM1. $HopM1_{101–712}$, which lacks the first 100 amino acids, partially restored bacterial multiplication and the chlorotic symptom of the ΔCEL mutant (Fig. 1C and fig. S1). None of the other 11 truncated derivatives could complement the virulence defect of the ΔCEL mutant (Fig. 1C and fig. S1). However, further analysis showed that the N terminus of HopM1 ($HopM1_{1–200}$ and $HopM1_{1–300}$) exerted a dominant negative effect on the function of full-length HopM1 delivered from the ΔCEL mutant (pORF43) (Fig. 1C and fig. S1). Necrosis, chlorosis, and bacterial multiplication were significantly reduced in these plants, compared with those in Col-0 *gl1* or transgenic plants expressing other HopM1 truncated derivatives (Fig. 1C and fig. S1). The dominant negative effect was specific to HopM1 because $HopM1_{1–200}$ and $HopM1_{1–300}$ plants were still susceptible to *Pst* DC3000, which produces AvrE, in addition to HopM1 (Fig. 1C and fig. S1). These results suggest that the N-terminal 200 to 300 amino acids of HopM1 can function as an independent domain in vivo, interfering with the virulence function of the full-length HopM1 delivered from bacteria.

The dominant negative effect in a cellular process is often caused by unproductive protein-protein interactions (*16*, *17*). We therefore reasoned that $HopM1_{1–200}$ and $HopM1_{1–300}$ may compete with full-length HopM1 for interaction with host proteins. To test this hypothesis, we performed yeast two-hybrid (Y2H) screens of an *Arabidopsis* cDNA library using $HopM1_{1–300}$ and full-length HopM1 as baits. We did not recover any interactors with full-length HopM1, but we obtained 21 strong interactors of $HopM1_{1–300}$, which were named AtMIN (*Arabidopsis thaliana* HopM interactors). AtMIN proteins interacted not only with $HopM1_{1–300}$ (Fig. 2A) but also with $HopM1_{1–200}$ (fig. S2A). Furthermore, the interaction between $HopM1_{1–300}$ and AtMIN proteins could also be observed in plant cells, based on transient expression experiments in *Nicotiana benthamiana* after conducting pull-down assays (Fig. 2B for AtMIN7).

The failure to isolate interacting host proteins by means of full-length HopM1 was unexpected, but subsequent immunoblot analysis of yeast cells expressing each of the 21 AtMIN proteins revealed a notable result: eight AtMIN proteins (AtMIN2, 3, 4, 6, 7, 9, 10, and 11) (table S1) either disappeared or were present in much smaller amounts in yeast cells expressing full-length HopM1, compared with yeast cells expressing $HopM1_{1–300}$ (AtMIN2, 7, and 10) (fig. S2B). This result explains why these AtMIN proteins could not be isolated when full-length HopM1 was used in Y2H screening. The amounts of the remaining AtMIN proteins, most of which are predicted to be chloroplast or mitochondrial proteins, did not differ between the two yeast strains (AtMIN12 in fig. S2B). Because HopM1 is localized in the plant endomembranes (Fig. 1B) and does not contain any organelle-targeting signature sequences, we reasoned that organelle-targeted AtMINs identified in Y2H experiments would not be physiological targets.

The HopM1-dependent destabilization of AtMIN proteins was observed not only in yeast cells but also in *N. benthamiana* leaves transiently expressing HopM1 and AtMIN proteins (fig. S2C) and, most important, in *Arabidopsis* leaves during bacterial infection [see Fig. 2C for AtMIN7, which is a low-abundance ~200-kilodalton (kD) protein in *Arabidopsis*]. Reduction of the AtMIN protein level (for example, AtMIN7) was not accompanied by a corresponding reduction of the *AtMIN* transcript level (Fig. 2C). Consistent with the specific dominant negative effects of $HopM1_{1–200}$ and $HopM1_{1–300}$ on HopM1, but not on AvrE (Fig. 1C and fig. S1), AvrE did not destabilize AtMIN proteins (AtMIN7 in fig. S2D). Subcellular fractionation analysis of AtMIN10-hemagglutinin (HA) transgenic plants, in which AtMIN10-HA is localized in both soluble and membrane fractions, showed that membrane-associated AtMIN10-HA was preferably destabilized by HopM1 during bacterial infection (fig. S2E). Collectively, these results suggest that HopM1 acts in the host endomembranes to destabilize AtMIN proteins by means of a posttranscriptional mechanism.

The HopM1-dependent destabilization of AtMIN proteins (such as AtMIN7) in *N. benthamiana* leaves was not affected by a cocktail of inhibitors of serine-, cysteine-, aspartic-, and metallo-proteases and aminopeptidases (Fig. 2D). However, proteasome inhibitors (e.g., MG132 and epoxomicin) completely blocked HopM1-mediated destabilization of AtMIN7 (Fig. 2D). Furthermore, immunoblot analysis of total leaf extract revealed that transiently expressed HopM1 greatly enhanced the protein ubiquitination in *N. benthamiana* leaves, as evidenced by the increased accumulation of the characteristic ubiquitin smear of >200 kD (Fig. 2E). Nonfunctional $HopM1_{1–300}$ and $HopM1_{301–712}$ did not enhance protein ubiquitination (fig. S3). The polyubiquitinated AtMIN7-

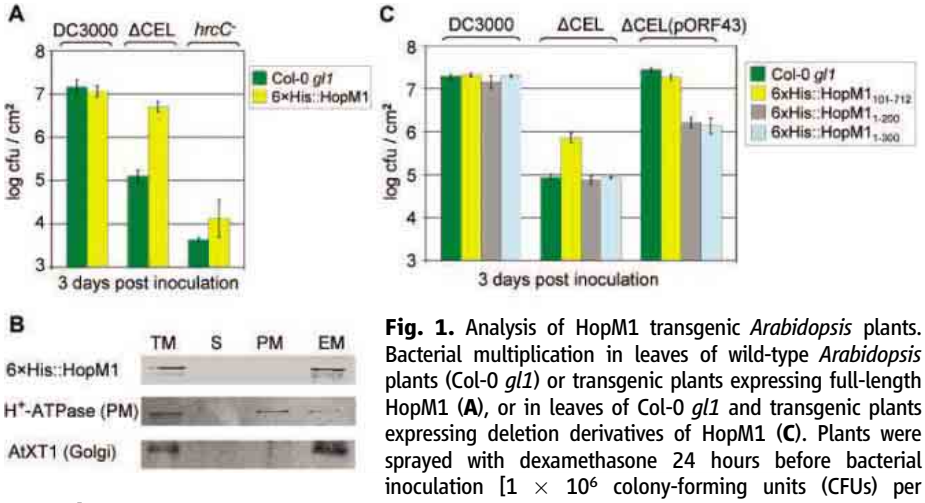

Fig. 1. Analysis of HopM1 transgenic *Arabidopsis* plants. Bacterial multiplication in leaves of wild-type *Arabidopsis* plants (Col-0 *gl1*) or transgenic plants expressing full-length HopM1 (**A**), or in leaves of Col-0 *gl1* and transgenic plants expressing deletion derivatives of HopM1 (**C**). Plants were sprayed with dexamethasone 24 hours before bacterial inoculation [1×10^6 colony-forming units (CFUs) per milliliter]. Bacterial populations were determined at day 3 after inoculation. Error bars indicate SD. (**B**) Immunoblot analysis of HopM1, plasma membrane–localized H^+ adenosine triphosphatase, and Golgi-localized xyloglucan xylosyltransferase AtXT1 after total leaf proteins of HopM1 transgenic *Arabidopsis* plants were separated into the indicated subcellular fractions. TM, total membrane; S, soluble fraction; PM, plasma membrane; EM, endomembrane.

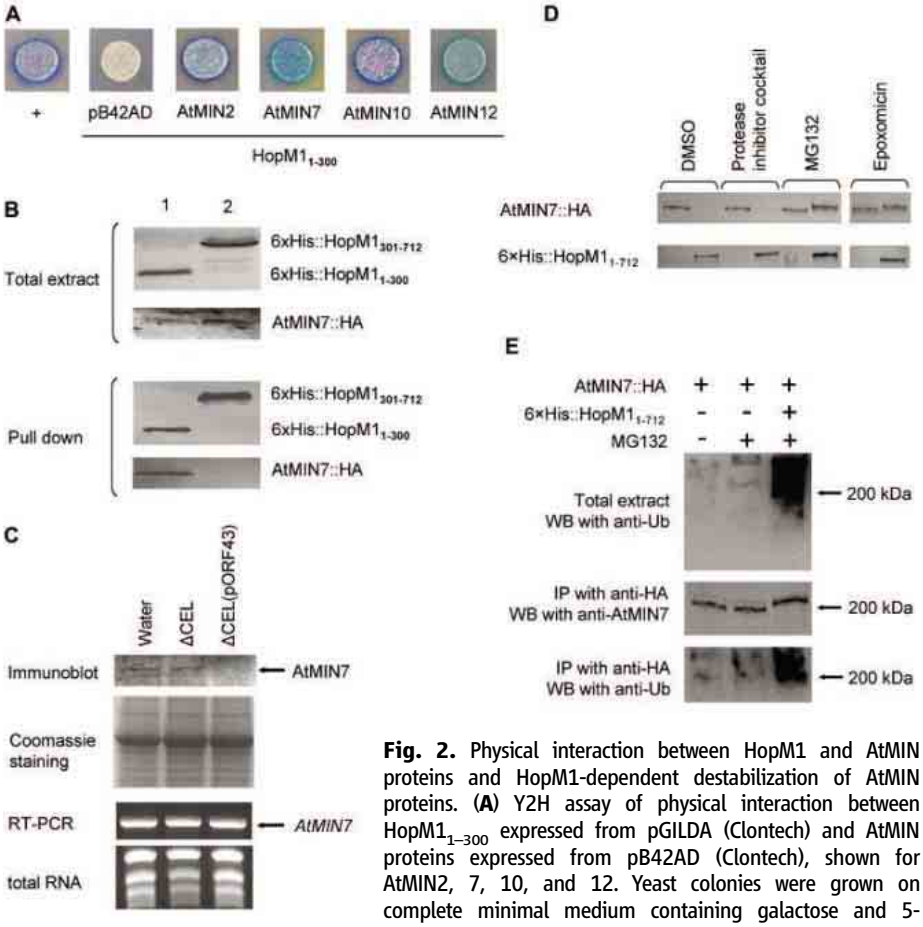

Fig. 2. Physical interaction between HopM1 and AtMIN proteins and HopM1-dependent destabilization of AtMIN proteins. (**A**) Y2H assay of physical interaction between $HopM1_{1–300}$ expressed from pGILDA (Clontech) and AtMIN proteins expressed from pB42AD (Clontech), shown for AtMIN2, 7, 10, and 12. Yeast colonies were grown on complete minimal medium containing galactose and 5-bromo-4-chloro-3-indoxyl-β-D-galactopyranoside. Blue indicates interaction and white indicates no interaction. +, positive control strain containing pLexA-p53 and pB42AD-T. (**B**) Immunoblot analysis of the physical interaction between AtMIN7-HA and 6xHis-$HopM_{1–300}$ (1) or between AtMIN7-HA and 6xHis-$HopM_{301–712}$ (2) in *N. benthamiana* leaves with a protein pull-down assay (*27*). AtMIN-HA and 6xHis-HopM1 proteins were detected with the HA and 6xHis epitope antibodies, respectively. AtMIN7-HA was pulled down with $HopM_{1–300}$ but not with 6xHis-$HopM_{301–712}$. (**C**) Western blot and reverse transcription polymerase chain reaction analyses of HopM1-dependent destabilization of AtMIN7 in *Arabidopsis* plants. Leaves of Col-0 *gl1* plants were infiltrated with water or 1×10^8 CFUs per milliliter of ΔCEL mutant bacteria with or without pORF43 and harvested 10 hours later. The endogenous AtMIN7 protein—detected with the use of a rabbit polyclonal AtMIN7 antibody—was absent in leaves infiltrated with ΔCEL mutant bacteria (pORF43) that produce HopM1; however, the *AtMIN7* transcript level was not reduced. (**D**) Proteasome inhibitors (MG132 and epoxomicin) blocked the HopM1-mediated destabilization of AtMIN7 in *N. benthamiana* leaves, whereas a cocktail of inhibitors of serine-, cysteine-, aspartic-, and metallo-proteases did not. AtMIN7::HA and 6xHis::$HopM1_{1–712}$ proteins were detected with HA and 6xHis epitope antibodies, respectively. (**E**) Detection of polyubiquitination of AtMIN7 in plants. AtMIN7::HA and 6xHis-$HopM_{1–712}$ proteins were transiently coexpressed in 1% dimethyl sulfoxide (-)- or in MG132-treated *N. benthamiana* leaves. AtMIN7 was immunoprecipitated (IP) with the use of an epitope antibody to HA (*27*). Ubiquitinated proteins were detected by Western blot (WB) with a polyclonal ubiquitin (Ub) antibody (Sigma). HopM1 induced the polyubiquitination of AtMIN7::HA in vivo.

HA protein could be precipitated with either the HA epitope antibody or the polyclonal AtMIN7 antibody (Fig. 2E and fig. S3). Together with the observed physical interaction between the N terminus of HopM1 and the AtMIN7 protein in vivo (Fig. 2B), these results suggest a mechanism for HopM1 action: HopM1 recruits AtMIN7, or an AtMIN7-containing complex, via its N terminus and promotes the subsequent ubiquitination and degradation of AtMIN7 via the host proteasome.

To address the critical question of whether destabilization of a specific AtMIN protein or proteins is necessary for HopM1-mediated promotion of *Pst* DC3000 pathogenesis in *Arabidopsis*, we analyzed *Arabidopsis* SALK lines (*18*) carrying transferred DNA (T-DNA) insertions in each of the AtMIN genes listed in table S1. When infected with the ΔCEL mutant, all of the AtMIN knockout (KO) lines, except for the AtMIN7 KO line, restricted the growth of the ΔCEL mutant in a manner similar to the wild-type Col-0 plants. AtMIN7 KO plants (fig. S4) infected by the ΔCEL mutant showed increased bacterial multiplication and enhanced chlorotic and necrotic disease symptoms, compared with Col-0 plants (Fig. 3, A and B). AtMIN7 KO plants remained resistant to the nonpathogenic *hrcC* mutant bacteria and responded to *Pst* DC3000 similarly to wild-type Col-0 plants (Fig. 3, A and B). This result demonstrates that the increased susceptibility in AtMIN7 KO plants is specific to ΔCEL mutant bacteria, mirroring the results shown in Fig. 1A, and is therefore biologically relevant to the virulence function of HopM1. Thus, a host-target mutation specifically increased the virulence of a plant-pathogen mutant lacking the cognate effector protein.

AtMIN7 encodes one of the eight members of the *Arabidopsis* adenosine diphosphate (ADP) ribosylation factor (ARF) guanine nucleotide exchange factor (GEF) protein family (*19*) (fig. S5A). HopM1 did not act on all *Arabidopsis* ARF GEFs. For example, HopM1 interacted strongly with and destabilized only AtMIN7, but not At1g13980 or At4g35380 in yeast (fig. S5, B and C).

The ARF GEF proteins are key components of the vesicle trafficking system in eukaryotic cells and are the primary molecular targets of Brefeldin A (BFA), a well-known inhibitor of vesicle trafficking (*20*, *21*). If the virulence function of HopM1 (i.e., destabilization of AtMIN7) is to inhibit host vesicle traffic, we reasoned that BFA treatment might substitute for HopM1 and restore the virulence of this bacterial mutant. Indeed, BFA treatment significantly enhanced the virulence (both bacterial multiplication and disease symptoms) of the ΔCEL mutant in wild-type Col-0 *gl1* plants (Fig. 3C). Notably, the restoration of bacterial virulence by BFA was also specific to the ΔCEL mutant, because there were no significant differences in bacterial multiplication or disease symptoms caused by *Pst* DC3000 or the *hrcC* mutant in Col-0 *gl1* plants treated with water or BFA (Fig. 3C). The restoration of the virulence of the ΔCEL mutant in BFA-treated leaves was even more complete than that in the AtMIN7 KO plants, suggesting that BFA and HopM1 target other host components in addition to AtMIN7.

The HopM1-mediated destruction of AtMIN7 and the ability of BFA to restore the virulence of the ΔCEL mutant suggest that HopM1 may be involved in the inhibition of a host vesicle trafficking pathway. Accelerated vesicle traffic is associated with a polarized cell wall–associated defense in plants (*22*, *23*), and our previous study showed that a major function of HopM1 is the suppression of this defense (*13*). To assess the requirement of AtMIN7 for the cell wall–associated defense, we examined the callose

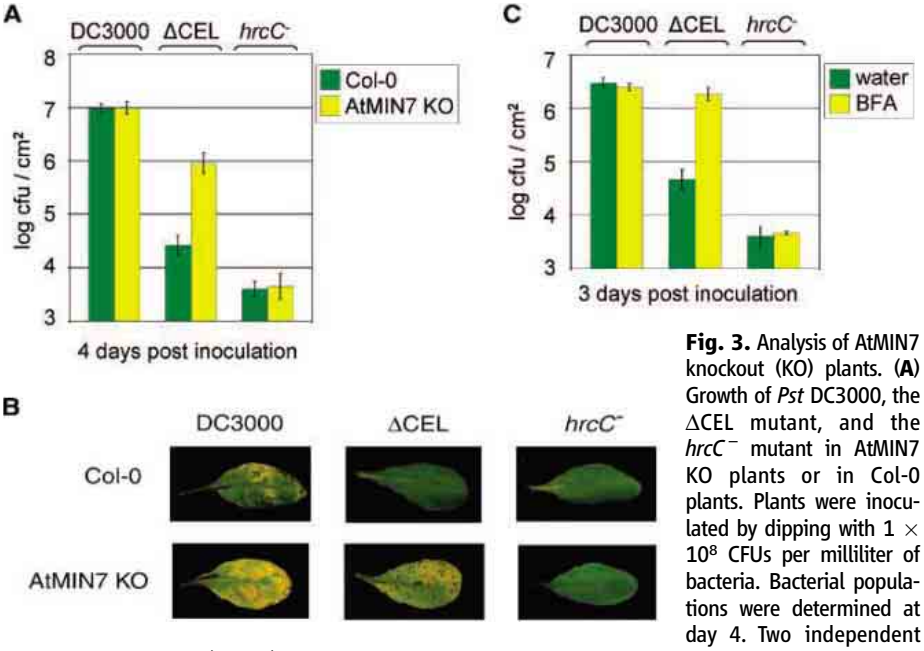

Fig. 3. Analysis of AtMIN7 knockout (KO) plants. (**A**) Growth of *Pst* DC3000, the ΔCEL mutant, and the *hrcC*⁻ mutant in AtMIN7 KO plants or in Col-0 plants. Plants were inoculated by dipping with 1×10^8 CFUs per milliliter of bacteria. Bacterial populations were determined at day 4. Two independent T-DNA insertion lines (fig. S4) were analyzed with similar results; results from line #1 are shown here. (**B**) Disease symptoms (chlorosis and necrosis) in Col-0 plants and AtMIN7 KO plants at day 4. (**C**) Effect of BFA treatment on bacterial multiplication.

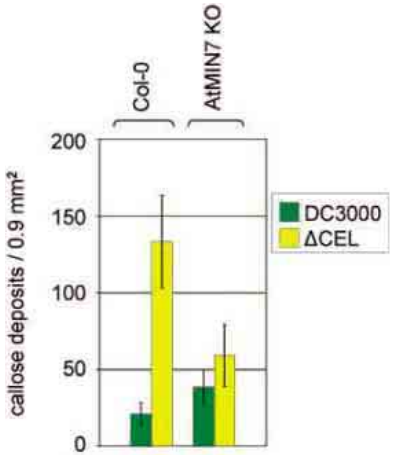

Fig. 4. Callose deposition in leaves of Col-0 and AtMIN7 KO plants. *Arabidopsis* Col-0 and AtMIN7 KO leaves (line #1) were stained to show callose deposition 7 hours after inoculation with 1×10^8 CFUs per milliliter of DC3000 and ΔCEL mutant bacteria. Average numbers of callose depositions per field of view (0.9 mm²) are presented with standard deviations displayed as error bars.

deposition (a cellular marker of this defense) in the leaves of Col-0 and AtMIN7 KO plants infected by *Pst* DC3000 or the ΔCEL mutant. Col-0 leaves accumulated a high number of polarized callose deposits in response to the ΔCEL mutant, whereas *Pst* DC3000 suppressed callose deposition in Col-0 leaves (*13*) (Fig. 4). The leaves of AtMIN7 KO plants were reduced in the ability to mount an active polarized callose response to the ΔCEL mutant (i.e., the remaining callose deposition was mostly not polarized), whereas their response to *Pst* DC3000 was similar to that of Col-0 plants (Fig. 4). This result and the increased susceptibility of AtMIN7 KO plants to the ΔCEL mutant (Fig. 3) are both consistent with an active role of AtMIN7 in the host immune response.

The HopM1-dependent destabilization of a host ARF GEF family protein via the host proteasome is interesting in light of the recent findings that a *P. syringae* effector protein, AvrPtoB, has intrinsic E3 ligase activity (*24*) and that vesicle trafficking and extracellular secretion play important roles in plant immune response (*23*, *25*). HopM1 does not show any sequence similarity to AvrPtoB, nor does it contain any known structure motifs present in various components of the ubiquitination/proteasome system, including various types of E3 ligases. Therefore, HopM1 probably functions as an adaptor protein that targets AtMIN7 to the host ubiquitination/proteasome system.

The majority of plant pathogenic bacteria, including *P. syringae*, are extracellular pathogens, living outside the plant cell wall. Our results suggest that *P. syringae* has evolved a mechanism to eliminate a component of a putative vesicle traffic pathway as an effective strategy of suppressing the extracellular cell wall–associated host defense (fig. S6). The intracellular human pathogen *Salmonella enterica* also uses effector proteins to interfere with host vesicle trafficking, although in this case the purpose is for the biogenesis and maintenance of a specialized membrane-bound compartment in which bacteria live (*4*, *26*). Despite the difference, our results suggest that modulation of host vesicle trafficking serves a common final purpose for plant and human pathogens, creating a host environment favorable for bacterial survival and multiplication.

References and Notes

1. S. T. Chisholm, G. Coaker, B. Day, B. J. Staskawicz, *Cell* **124**, 803 (2006).
2. S.-Y. He, K. Nomura, T. S. Whittam, *Biochim. Biophys. Acta* **1694**, 181 (2004).
3. D. Buttner, U. Bonas, *EMBO J.* **21**, 5313 (2002).
4. P. Cossart, P. J. Sansonetti, *Science* **304**, 242 (2004).
5. R. B. Abramovitch, G. B. Martin, *Curr. Opin. Plant Biol.* **7**, 356 (2004).
6. K. Nomura, M. Melloto, S.-Y. He, *Curr. Opin. Plant Biol.* **8**, 361 (2005).
7. J. R. Alfano, A. Collmer, *Annu. Rev. Phytopathol.* **42**, 385 (2004).
8. M. B. Mudgett, *Annu. Rev. Plant Biol.* **56**, 509 (2005).
9. D. Mackey, B. F. Holt, A. Wiig, J. L. Dangl, *Cell* **108**, 743 (2002).
10. M. J. Axtell, B. J. Staskawicz, *Cell* **112**, 369 (2003).
11. M. G. Kim *et al.*, *Cell* **121**, 749 (2005).
12. J. R. Alfano *et al.*, *Proc. Natl. Acad. Sci. U.S.A.* **97**, 4856 (2000).
13. S. DebRoy, R. Thilmony, Y. B. Kwack, K. Nomura, S.-Y. He, *Proc. Natl. Acad. Sci. U.S.A.* **101**, 9927 (2004).
14. J. L. Badel, K. Nomura, S. Bandyopadhyay, A. Collmer, S.-Y. He, *Mol. Microbiol.* **49**, 1239 (2003).
15. J. Yuan, S.-Y. He, *J. Bacteriol.* **178**, 6399 (1996).
16. E. D. Shpak, M. B. Lakeman, K. U. Torii, *Plant Cell* **15**, 1095 (2003).
17. X. Wang *et al.*, *Dev. Cell* **8**, 855 (2005).
18. J. M. Alonso *et al.*, *Science* **301**, 653 (2003).
19. A. A. Sanderfoot, N. V. Raikhel, in *The Arabidopsis Book*, C. R. Somerville, E. M. Meyerowitz, Eds. (American Society of Plant Biologists, Rockville, MD, 2002), http://dx.doi.org/10.1199/tab.0098.
20. E. Mossessova, R. A. Corpina, J. Goldberg, *Mol. Cell* **12**, 1403 (2003).
21. T. Steinmann *et al.*, *Science* **286**, 316 (1999).
22. C. S. Bestwick, M. H. Bennett, J. W. Mansfield, *Plant Physiol.* **108**, 503 (1995).
23. N. C. Collins *et al.*, *Nature* **425**, 973 (2003).
24. R. Janjusevic, R. B. Abramovitch, G. B. Martin, C. E. Stebbins, *Science* **311**, 222 (2006).
25. D. Wang, N. D. Weaver, M. Kesarwani, X. Dong, *Science* **308**, 1036 (2005).
26. L. A. Knodler, O. Steele-Mortimer, *Mol. Biol. Cell* **16**, 4108 (2005).
27. Materials and methods are available as supporting material on *Science* Online.

28. We thank members of the He laboratory for stimulating discussions and critical reading of the manuscript. *Arabidopsis* SALK lines were obtained from the Ohio State University *Arabidopsis* Biological Resource Center, which is sponsored by NSF. W. Underwood was involved in the initial analysis of SALK lines. J. Callis, G. Martin, and R. Vierstra advised us on ubiquitination experiments. K. Bird edited the manuscript. This work was supported by funding from the Department of Energy, NSF, and NIH to S.Y.H. Y.H.L was supported by a Korean Government long-term Fellowship.

Supporting Online Material

www.sciencemag.org/cgi/content/full/313/5784/220/DC1
Materials and Methods
Figs. S1 to S6
Table S1
References

4 May 2006; accepted 1 June 2006
10.1126/science.1129523

Evolution of Character Displacement in Darwin's Finches

Peter R. Grant* and B. Rosemary Grant

Competitor species can have evolutionary effects on each other that result in ecological character displacement; that is, divergence in resource-exploiting traits such as jaws and beaks. Nevertheless, the process of character displacement occurring in nature, from the initial encounter of competitors to the evolutionary change in one or more of them, has not previously been investigated. Here we report that a Darwin's finch species (*Geospiza fortis*) on an undisturbed Galápagos island diverged in beak size from a competitor species (*G. magnirostris*) 22 years after the competitor's arrival, when they jointly and severely depleted the food supply. The observed evolutionary response to natural selection was the strongest recorded in 33 years of study, and close to the value predicted from the high heritability of beak size. These findings support the role of competition in models of community assembly, speciation, and adaptive radiations.

Character displacement (*1*, *2*) is an evolutionary divergence in resource-exploiting traits such as jaws and beaks that is caused by interspecific competition (*3*–*5*). It has the potential to explain nonrandom patterns of co-occurrence and morphological differences between coexisting species (*6*–*10*). Supporting evidence has come from phylogenetic analyses (*11*) and from experimental studies of sticklebacks, in which the role of directional selection in character divergence has been demonstrated (*12*). The process of character displacement occurring in nature, from the initial encounter of competitors to the evolutionary change in one or more of them as a result of directional natural selection, has not previously been investigated.

The situation on the small Galápagos island of Daphne Major (0.34 km^2) has been referred to as the classical case of character release (*1*, *2*, *13*), which is the converse of character displacement. Here, in the virtual absence of the small ground finch (*Geospiza fuliginosa*; weighing ~12 g) and released from competition, the medium ground finch (*G. fortis*; ~18 g) is unusually small in beak and body size. Lack (*14*) proposed that its small size reflects an evolutionary shift enabling *G. fortis* to take maximum advantage of small seeds made available by the absence of its competitor. Subsequent field studies demonstrated an association, previously only inferred, between beak sizes and seed diets (*13*, *15*). In 1977, a drought on Daphne revealed that small seeds are preferred when they are abundant, but when they are scarce, finches turn increasingly to large and hard seeds that only the large-beaked members of the population can crack (*13*, *15*). Most finches died that year, and mortality was heaviest among those with small beaks (*13*, *16*, *17*). Thus, a population's mean beak size is determined by the tradeoff in energetic rewards from feeding on small and large seeds, and the tradeoff is affected by variation in beak morphology and rates of seed depletion and replenishment (*7*, *18*, *19*). Competitors can modify the tradeoff (*7*).

The situation on Daphne changed in 1982 with the arrival of a new competitor species, setting up the potential for character displacement to occur. Between 1973 and 1982, a few individuals of the large ground finch (*G. magnirostris*; ~30 g) visited the island for short periods in the dry season but never bred (*15*). In late 1982, a breeding population was established by two females and three males at the beginning of an exceptionally strong El Niño event that brought abundant rain to the island (1359 mm) (*20*–*22*). *G. magnirostris* is a potential competitor as a result of diet overlap with *G. fortis* (Table 1), especially in the dry season when food supply is limiting (*9*, *23*). The principal food of *G. magnirostris* is the seeds of *Tribulus cistoides*, contained within a hard mericarp and exposed when a finch cracks or tears away the woody outer covering (Fig. 1). Large-beaked members of the *G. fortis* population are capable of this maneuver—indeed, survival in the 1977 drought to a large extent depended on it (*13*, *16*)—but on average they take three times longer than *G. magnirostris* to gain a seed reward (*13*, *24*). The smallest *G. fortis* never attempt to crack them (*18*, *24*). *G. magnirostris* compete with *G. fortis* by physically excluding them from *Tribulus* feeding sites and by reducing the density of *Tribulus* fruits to the point at which it is not profitable for *G. fortis* to feed on them, owing to handling inefficiencies in relation to search and metabolic costs (*7*, *13*, *18*, *24*). By depleting the supply of *Tribulus* fruits, *G. magnirostris* was predicted to cause a selective shift in *G. fortis* in the direction of small beak size.

The predicted shift occurred in 2004 (Fig. 2). Initially, the population size of *G. magnirostris* was too small in relation to the food supply to have anything but a mild competitive effect on *G. fortis*. Their numbers gradually increased as a result of local production of recruits, augmented by additional immigrants (*22*, *25*), and reached a maximum of 354 ± 47 (SE) in 2003 (Fig. 3). Little rain fell in 2003 (16 mm) and 2004 (25 mm), there was no breeding in either year, numbers of both species declined drastically, and from 2004 to 2005 *G. fortis* experienced strong directional selection against individuals with large beaks (*26*).

Selection differentials in *G. fortis* were uniformly negative for both males and females treated separately (Table 2). Average selection differentials in standard deviation units for the six measured traits that quantify bill size and shape and body size were 0.774 for males and 0.649 for females. Compared with values reported in other studies elsewhere (*27*), they are unusually large. The six traits are positively correlated to varying degrees. Selection gradient analysis helps to identify which particular traits were subject to selection independent of correlations among traits (*28*). However, bill depth and width are so strongly correlated in these samples (r = 0.861 for males, 0.946 for females) that their independent effects on survival cannot be distinguished. Selection gradient analysis without these two variables shows bill length to be the only significant entry into the gradient, for both males [partial regression coefficient (β) = –0.931 ± 0.334 SE, P = 0.0079; R^2 = 0.190] and females (β = –0.814 ± 0.295, P =

Table 1. Proportions of seeds in the diets of three finch species. Small seeds are a composite group of 22 species, medium seeds are *O. echios*, and large seeds are *T. cistoides*. *N* is the number of observations. There is strong heterogeneity in the *G. fortis* feeding data (X^2_6 = 30.979, P < 0.0001). The reduction in *G. fortis* feeding on *Tribulus* in 2004 makes a significant contribution (X^2_1 = 3.912, P < 0.05). Data were obtained by observations in the first 3 months of each year. In 1977 (only), when *G. fortis* experienced directional selection against small bill size, the proportion of large seeds in the diet rose to 0.304 (June) and 0.294 (December) (*15*).

Year	*N*	Small	Medium	Large
		G. fortis		
1977	216	0.731	0.102	0.167
1985	205	0.805	0.000	0.195
1989	628	0.771	0.051	0.162
2004	97	0.804	0.113	0.082
		G. magnirostris		
1985	27	0.185	0.000	0.815
1989	68	0.059	0.118	0.823
2004	110	0.045	0.264	0.691
		G. scandens		
1977	115	0.852	0.148	0.000
1985	96	0.771	0.219	0.000
1989	145	0.234	0.697	0.000
2004	98	0.174	0.826	0.000

Department of Ecology and Evolutionary Biology, Princeton University, Princeton, NJ 08544–1003, USA.

*To whom correspondence should be addressed: E-mail: prgrant@princeton.edu

0.0130; R^2 = 0.455). Inclusion of either bill depth or bill width made no difference to these results. Overall bill size rather than bill length is identified as the most important factor distinguishing survivors from nonsurvivors in each year, by the fact that $PC1_{bill}$ (bill size) was a selected trait in both sexes, whereas $PC2_{bill}$ (bill shape) was not selected in either. There was little effect on body size, unlike in the 1977 episode. In contrast to *G. fortis*, the heavy mortality experienced by *G. magnirostris* was apparently not selective: Four surviving males did not differ from 32 nonsurvivors in any of the six measured traits (all $P > 0.1$), and only 1 of 38 measured females survived.

Thus, character displacement in *G. fortis* occurred in 2004–2005. Four lines of evidence support the causal role of *G. magnirostris*. First, the potential impact of *G. magnirostris* was greatest at the beginning of 2004 because their numbers (150 ± 19) were closer to those of *G. fortis* (235 ± 46) than at any other time (Fig. 3), and their population biomass was about the same, because a *G. magnirostris* individual was approximately twice the mass of a *G. fortis* individual.

Second, *G. magnirostris* are largely dependent on an important food resource, *Tribulus* seeds, which are not renewed during droughts. *G. magnirostris* deplete the *Tribulus* seed supply faster than do *G. fortis*. The seeds that are consumed by a *G. magnirostris* individual each day are sufficient for two *G. fortis* individuals if they feed on nothing else (*13*). Moreover, a much higher fraction of *G. magnirostris* than *G. fortis* feed on *Tribulus*, as inferred from feeding observations (Table 1). As a result of their joint reduction of seed biomass, *G. fortis* fed on *Tribulus* in 2004 only half as frequently as in other years (Table 1). We did not quantify food supply; nevertheless, food scarcity was evident from the exceptionally low feeding rates of *G. magnirostris*. In 2004, a minimum of 90 individuals were observed foraging for *Tribulus* mericarps for 200 to 300 s, and none obtained seeds from more than two mericarps; whereas under the more typical conditions prevailing in the 1970s, a total of eight birds observed for the same length of time fed on 9 to 22 mericarps, with an average interval between successive mericarps of only 5.5 ± 0.5 s (SE) (*24*).

Third, numbers of *G. fortis* declined to a lower level (83) in 2005 than at any time since the study began in 1973, and numbers of *G. magnirostris* declined so strongly from the 2003 maximum that by 2005, only four females and nine males were left. The population was almost extinct, apparently as a result of exhaustion of the standing crop of large seeds and subsequent starvation. Of the 137 *G. magnirostris* that disappeared in 2004–2005, 13.0% were found dead, and so were 21.7% of 152 *G. fortis*. Consistent with the starvation hypothesis, the stomachs of all dead birds (23 *G. magnirostris* and 45 *G. fortis*, banded and not banded individuals combined) were empty.

The principal alternative food for both species is the seeds of *Opuntia* cactus, but production in 2004 was low, the fourth lowest since records were first kept systematically in 1982 (*23*). Not only were cactus seeds insufficient for the two granivore species to escape the dilemma of a diminishing supply of their preferred foods, they were insufficient for the cactus specialist *G. scandens* (~20 g), whose numbers, like those of *G. fortis*, fell lower (to 50) than in any of the preceding 32 years. The only escape was available to the smallest, most *G. fuliginosa*–like, members of the *G. fortis* population, which are known to feed like *G. fuliginosa* on small seeds with little individual energy reward (*13*, *18*). We have no feeding observations to indicate that they survived as a result of feeding on the typical components of the *G. fuliginosa* diet: the very small seeds of *Sesuvium edmonstonei* and *Tiquilia fusca* (*13*, *15*, *23*). Nevertheless, it may be significant that two *G. fuliginosa* individuals were present on the island in 2004 and both survived to 2005.

The fourth line of evidence is the contrast between the directions of strong selection on the *G. fortis* population in the presence (2004) and near absence (1977) of *G. magnirostris*. In 1977, a year of only 24 mm of rain and no

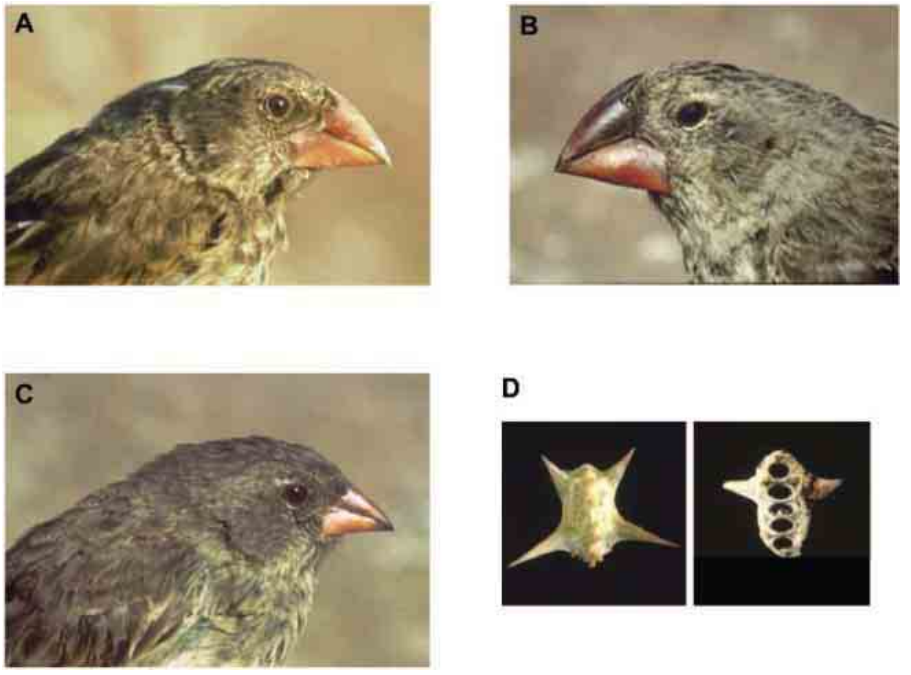

Fig. 1. Large-beaked *G. fortis* (**A**) and *G. magnirostris* (**B**) can crack or tear the woody tissues of *T. cistoides* mericarps (**D**), whereas small-beaked *G. fortis* (**C**) cannot. Five mericarps constitute a single fruit. In (D), the left-hand mericarp is intact. The right-hand mericarp, viewed from the other (mesial) side, has been exploited by a finch, exposing five locules from which seeds have been extracted. Mericarps are ~8 mm long and are shown at twice the magnification of the finches. [Photos are by the authors]

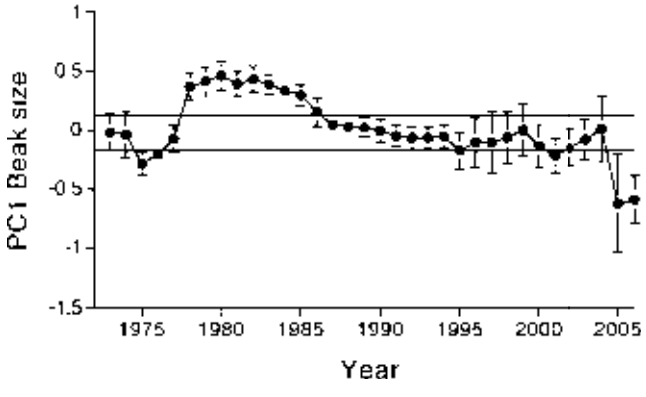

Fig. 2. Mean beak size $PC1_{bill}$ of adult *G. fortis* (sexes combined) in the years 1973 to 2005. Vertical lines show 95% confidence intervals for the estimates of the mean. Horizontal lines mark the 95% confidence limits on the estimate of the mean in 1973 to illustrate subsequent changes in the mean. Sample sizes vary from 29 (in 2005) to 950 (in 1987). Signs of the PC values are reversed so that mean size increases from the origin.

breeding, body size and beak size of both male and female *G. fortis* considered separately were subject to selection (Table 2). Average selection differentials were 0.642 for males and 0.668 for females, and they were uniformly positive. In the intervening years, 1978–2003, there was a weaker selection episode favoring *G. fortis* with small beaks when the food supply changed toward a predominance of small seeds and scarcity of large ones after the El Niño event of 1982–1983 (*20*, *21*, *23*). At that time, *G. magnirostris* were rare (*22*, *25*); numbers varied from 2 to 24. The selection events of 1977 and 2004 stand out against a background of relative morphological stability (*29*) (Fig. 2). Immediately before 2004 there was no unusual rainfall to cause a change in the composition of the food supply and no other unusual environmental factor such as temperature extremes or an invasion of predators, yet with the same amount of rain as in 1977, and with the same community of plants in the environment, large finches survived at a high frequency in 1977 but survived at a low frequency in 2004. The conspicuous difference between these years was the number of *G. magnirostris*: 2 to 14 occasional visitors in 1977 (*15*) versus 150 ± 19 residents at the beginning of 2004.

Given the high heritability of beak size of *G. fortis* (*30*, *31*), an evolutionary response is to be expected from strong directional selection against large size (*32*). This was observed. The mean beak size ($PC1_{bill}$) of the 2005 generation measured in 2006 was significantly smaller than that in the 2004 sample of the parental generation before selection ($t_{176} = 4.844$, $P < 0.0001$). The difference between generations is 0.70 SD, which is exceptionally large (*27*, *29*). It may be compared with the range of values predicted from the breeders equation, namely the product of the average selection differential of the two sexes and the 95% confidence intervals of the heritability estimate. The observed value of 0.70 SD falls within the predicted range of 0.66 to 1.00 SD. Although a small component of the response is probably attributable to environmental factors [food supply and finch density (*30*, *32*)], the major component is genetic. This is the strongest evolutionary change seen in the 33 years of the study.

The evolutionary changes that we observed are more complex than those envisaged by Lack. Nevertheless, they provide direct support for his emphasis on the ecological adjustments that competitor species make to each other, specifically in the final stages of speciation and more generally in adaptive radiations (*9*–*12*, *14*). They also support models of ecological community assembly that incorporate evolutionary effects of interspecific competition, in contrast to null or neutral models (*6*, *9*). Replicated experiments with suitable organisms are needed to demonstrate definitively the causal role of competition, not only as an ingredient of natural selection of resource-exploiting traits (*12*) but as a factor in their evolution (*33*). Our findings should prove useful in designing realistic experiments, by identifying ecological context (high densities at the start of an environmental stress) and by estimating the magnitude of natural selection.

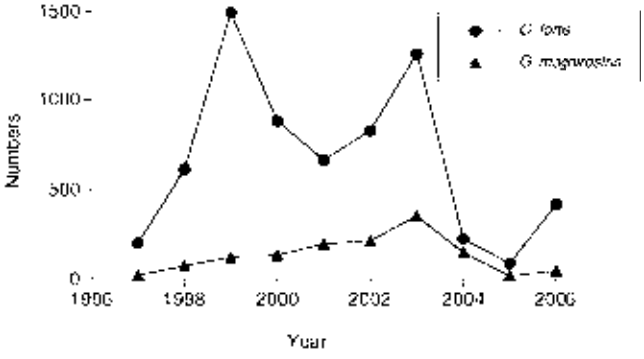

Fig. 3. Numbers of *G. fortis* and *G. magnirostris*. Breeding was extensive in 1997–1998 and 2002, and as a result finch numbers were elevated in the following years. There was no breeding in 2003 and 2004. Numbers before 1997 have been omitted because *G. magnirostris* were scarce (≤13 pairs) (*25*).

Table 2. Selection differentials for *G. fortis* in the presence (2004) and absence (1977) of *G. magnirostris*. Statistical significance at $P < 0.05$, <0.01, <0.005, and <0.001 is indicated by *, **, ***, and ****, respectively.

	2004		1977	
	Males	Females	Males	Females
Weight	−0.62*	−0.63	0.88****	0.84***
Wing length	−0.66*	−0.60	0.47***	0.71**
Tarsus length	−0.48	0.01	0.24	0.27
Beak length	−1.08****	−0.95*	0.75****	0.88***
Beak depth	−0.94***	−0.91*	0.80****	0.69*
Beak width	−0.87***	−0.81*	0.71****	0.62*
PC1 body	−0.67*	−0.52	0.69****	0.73**
PC1 beak	−1.02****	−0.92*	0.80****	0.74**
PC2 beak	−0.34	−0.26	0.23	0.29
Sample size	47	24	164	55
Proportion of survivors	0.34	0.54	0.45	0.42

References and Notes

1. W. L. Brown Jr., E. O. Wilson, *Syst. Zool.* **5**, 49 (1956).
2. P. R. Grant, *Biol. J. Linn. Soc.* **4**, 39 (1972).
3. B. W. Robinson, D. S. Wilson, *Am. Nat.* **144**, 596 (1994).
4. D. C. Adams, F. J. Rohlf, *Proc. Natl. Acad. Sci. U.S.A.* **97**, 4106 (2000).
5. D. W. Pfennig, P. J. Murphy, *Ecology* **84**, 1288 (2003).
6. T. W. Schoener, in *Ecological Communities: Conceptual Issues and the Evidence*, D. R. Strong, L. G. Abele, A. B. Thistle, Eds. (Princeton Univ. Press, Princeton, NJ, 1984), pp. 254–281.
7. D. Schluter, T. Price, P. R. Grant, *Science* **227**, 1056 (1985).
8. J. B. Losos, *Proc. Natl. Acad. Sci. U.S.A.* **97**, 5693 (2000).
9. P. R. Grant, *Ecology and Evolution of Darwin's Finches* (Princeton Univ. Press, Princeton, NJ, 1999).
10. D. Schluter, *Am. Nat.* **156**, S4 (2002).
11. J. B. Losos, *Evolution* **44**, 588 (1990).
12. D. Schluter, *Science* **266**, 798 (1994).
13. P. T. Boag, P. R. Grant, *Biol. J. Linn. Soc.* **22**, 243 (1984).
14. D. Lack, *Darwin's Finches* (Cambridge Univ. Press, Cambridge, 1947).
15. P. T. Boag, P. R. Grant, *Ecol. Monogr.* **54**, 463 (1984).
16. P. T. Boag, P. R. Grant, *Science* **214**, 82 (1981).
17. T. D. Price *et al.*, *Nature* **309**, 787 (1984).
18. T. Price, *Ecology* **68**, 1015 (1987).
19. C. W. Benkman, *Ecol. Monogr.* **57**, 251 (1987).
20. H. L. Gibbs, P. R. Grant, *J. Anim. Ecol.* **56**, 797 (1987).
21. H. L. Gibbs, P. R. Grant, *Nature* **327**, 511 (1987).
22. P. R. Grant, B. R. Grant, *Evolution* **49**, 229 (1995).
23. P. R. Grant, B. R. Grant, in *Long-Term Studies of Vertebrate Communities*, M. L. Cody, J. A. Smallwood, Eds. (Academic Press, New York, 1996), pp. 343–390.
24. P. R. Grant, *Anim. Behav.* **29**, 785 (1981).
25. P. R. Grant, B. R. Grant, K. Petren, *Genetica* **112-113**, 359 (2001).
26. See methods in supporting material on *Science* Online.
27. J. G. Kingsolver *et al.*, *Am. Nat.* **157**, 245 (2001).
28. R. Lande, S. Arnold, *Evolution* **37**, 1210 (1983).
29. P. R. Grant, B. R. Grant, *Science* **296**, 707 (2002).
30. P. T. Boag, *Evolution* **37**, 877 (1983).
31. L. F. Keller *et al.*, *Heredity* **87**, 325 (2001).
32. P. R. Grant, B. R. Grant, *Evolution* **49**, 241 (1995).
33. P. R. Grant, *Science* **266**, 802 (1994).

34. We thank K. T. Grant, L. F. Keller, K. Petren, and U. Reyer for help with recent fieldwork, and the Charles Darwin Research Station and Galápagos National Park Service for permission and support. The research was supported by grants from NSF.

Supporting Online Material

www.sciencemag.org/cgi/content/full/313/5784/224/DC1
Methods
References

5 April 2006; accepted 25 May 2006
10.1126/science.1128374

Teaching in Wild Meerkats

Alex Thornton* and Katherine McAuliffe

Despite the obvious benefits of directed mechanisms that facilitate the efficient transfer of skills, there is little critical evidence for teaching in nonhuman animals. Using observational and experimental data, we show that wild meerkats (*Suricata suricatta*) teach pups prey-handling skills by providing them with opportunities to interact with live prey. In response to changing pup begging calls, helpers alter their prey-provisioning methods as pups grow older, thus accelerating learning without the use of complex cognition. The lack of evidence for teaching in species other than humans may reflect problems in producing unequivocal support for the occurrence of teaching, rather than the absence of teaching.

Teaching is ubiquitous in human societies, but although social learning is widespread in other species (*1*, *2*), it is not yet clear how commonly teaching is involved. Teaching is characterized by the active involvement of experienced individuals in facilitating learning by naïve conspecifics (*3*, *4*). The focus of definitions of teaching ranges from cognitive mechanisms (*5*, *6*) to evolutionary function (*3*, *7*). In this paper, we use a widely accepted (*2*, *4*, *8*–*10*) functional definition developed by Caro and Hauser (*3*). This definition comprises three criteria: (i) an individual, A, modifies its behavior only in the presence of a naïve observer, B; (ii) A incurs some cost or derives no immediate benefit; and (iii) as a result of A's behavior, B acquires knowledge or skills more rapidly or efficiently than it would otherwise, or that it would not have learned at all. Teaching is thought to allow faster and more efficient information transfer than passive forms of social learning (*11*), but evidence for its existence in nonhuman animals is equivocal (*3*, *4*, *8*–*10*, *12*, *13*). To date, only one study provides firm evidence for teaching (*10*), and its occurrence in the wild remains unconfirmed.

We investigated whether teaching occurs in wild meerkats (*Suricata suricatta*), a species living in demanding environments where food acquisition involves considerable skill. Meerkats are obligate cooperative breeders living in groups of 2 to 40 individuals in the arid regions of southern Africa. Groups comprise a dominant male and female, who are the parents of over 80% of the pups in the group, and a variable number of helpers of both sexes that aid in rearing the young (*14*). Hereafter, all individuals over 3 months old are referred to as helpers. Pups are initially incapable of finding their own prey. They begin to follow foraging groups at around 30 days of age and are provisioned by all group members in response to begging calls (*15*, *16*) until they reach nutritional independence at around 90 days of age.

Department of Zoology, University of Cambridge, Downing Street, Cambridge CB2 3EJ, UK.

*To whom correspondence should be addressed. E-mail: jant2@cam.ac.uk

Meerkats are opportunistic generalists, feeding on a range of vertebrate and invertebrate prey (*15*), many of which are difficult to handle and potentially dangerous to young pups. Scorpions of the genera *Parabuthus* and *Opistophthalamus*, which form up to 4.5% of total prey biomass for meerkats (*15*), may be particularly dangerous; the former possess neurotoxins potent enough to kill a human, whereas the latter have milder toxins but are more aggressive, defending themselves with large, powerful pincers (*17*).

Helpers typically kill or disable prey with rapid bites to the head or abdomen before provisioning pups. Scorpions are normally disabled by removing the sting. Helpers adjust the frequency with which they kill or disable mobile prey according to pup age, gradually introducing pups to live prey. The proportion of highly mobile prey fed when dead or disabled decreased with pup age (Fig. 1, A and B) while the proportion of prey fed intact increased (Fig. 1C) (controlling for characteristics of the pups, helpers, and prey) (*18*) (table S1). Scorpions were more likely to be provisioned dead or disabled (Fig. 1, A and B) and less likely to be provisioned intact (Fig. 1C) than were other items.

Helpers often fed pups that were out of sight (mean distance to pup = 5.4 m, range = 0 to 50 m, N = 1399 feeds), but pup begging calls can generally be heard by all individuals in the group (*16*). The acoustic parameters of begging calls are known to change with age (*19*). To investigate whether helpers modify prey in response to begging calls, we conducted playback experiments in which we broadcast begging calls of old pups (71 to 86

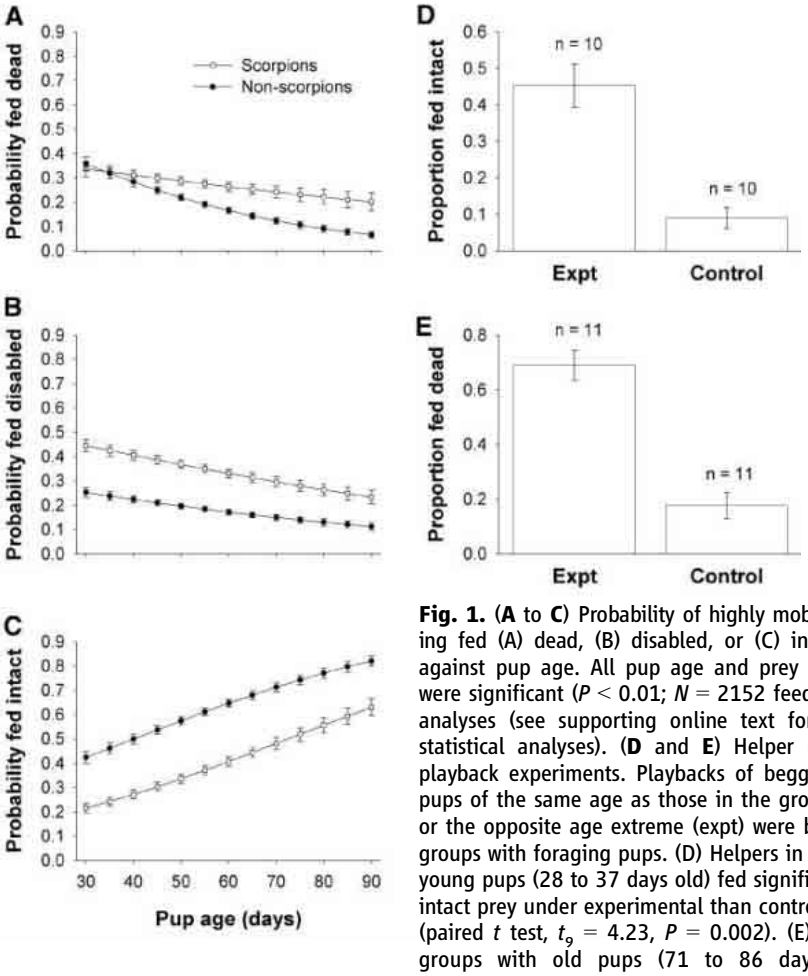

Fig. 1. (**A** to **C**) Probability of highly mobile prey being fed (A) dead, (B) disabled, or (C) intact plotted against pup age. All pup age and prey type effects were significant ($P < 0.01$; N = 2152 feeds) in GLMM analyses (see supporting online text for details of statistical analyses). (**D** and **E**) Helper response to playback experiments. Playbacks of begging calls of pups of the same age as those in the group (control) or the opposite age extreme (expt) were broadcast to groups with foraging pups. (D) Helpers in groups with young pups (28 to 37 days old) fed significantly more intact prey under experimental than control playbacks (paired t test, t_9 = 4.23, P = 0.002). (E) Helpers in groups with old pups (71 to 86 days old) fed significantly more dead prey under experimental than control playbacks (paired t test, t_{10} = 4.81, P = 0.001).

days old) to groups with young pups (28 to 37 days old) or vice versa (*18*). Begging calls of pups of the same age as those in the group were broadcast as controls. Helpers in groups with young pups fed significantly more intact prey when calls of older pups were broadcast than in control playbacks, and helpers in groups with old pups fed significantly more dead prey under experimental than control playbacks (Fig. 1, D and E).

After a helper gave a pup a food item, it normally remained with the pup and monitored its handling of the prey (87.5% of recorded feeds; N = 10,479 feeds). If pups did not attempt to handle a prey item, helpers sometimes nudged the item repeatedly with their nose or paws (8.3% of occasions; N = 5343 feeds). After nudging occurred, pups normally consumed the prey successfully (99% of occasions; N = 446 feeds). The duration of monitoring and the probability of nudging both declined with pup age [monitoring, analyzed with a generalized linear mixed model (GLMM), gave the following results: $\chi^2 = 142.04$, df = 1, $P < 0.001$ (Fig. 2A and table S2); nudging (GLMM): $\chi^2 = 80.23$, df = 1, $P < 0.001$ (table S3)], suggesting that helpers modify their behavior in response to improvements in pup competence. Nudging was more common when rare prey types were presented to pups [prey abundance (GLMM): $\chi^2 = 13.65$, df = 1, $P < 0.001$ (Fig. 2B and table S4)], suggesting that it may direct pups' attention toward unfamiliar food.

Helpers' killing or disabling prey before feeding a pup probably has few costs to helpers as compared to the post-provisioning costs of feeding live prey. Controlling for prey type and size (*18*), there was no significant difference between pre-provisioning handling times for prey provisioned dead, intact, or disabled [generalized linear model (GLM): $F_{2,93} = 1.67$, $P = 0.195$], suggesting that the time costs of modifying prey rather than feeding it intact are low. In contrast, there were clear post-provisioning costs involved in feeding pups live prey. These included longer times spent monitoring pups handling prey (Fig. 2A), the risk of pups losing prey (Fig. 2C and table S5), and the investment in retrieving and further modifying items lost by pups. Among 731 feeds where pups lost the prey initially, helpers retrieved prey and returned it to pups on 192 occasions (26.3%). On around 7% of occasions, helpers further modified the prey before returning it.

Helpers appear to facilitate pup skill acquisition by creating opportunities for pups to handle live prey. Young pups encounter live, highly mobile prey almost exclusively when provisioned by helpers. As pups grow older, they increasingly find such items themselves, but the mean number of items found remained below 50% of the total encountered (found by pups and fed by helpers), even for pups approaching nutritional independence (Fig. 2D). The presence of a helper after provisioning appears to have an important effect on the likelihood that pups will attempt to handle live prey. When we presented live scorpions to helpers, they removed the sting and fed the scorpion to a pup on 13 occasions. In all cases, the pup then bit the scorpion. In contrast, when we presented stingless scorpions directly to 13 littermates when no helpers were within 2 m (*18*), 7 did not bite the prey (Fisher's test: $P = 0.005$).

As pups grew older, they were less likely to lose live prey (Fig. 2C) and time taken to handle scorpions declined (Fig. 2E). To examine the effect of experience with live prey on pup handling skills, rather than age per se, we trained three littermates on 3 consecutive days by directly provisioning them each day with (i) four dead scorpions; (ii) four live, stingless scorpions; or (iii) an equivalent mass of hard-boiled egg, as a control. On the fourth day, we tested the handling abilities of all three pups by provisioning each with one live, stingless scorpion (*18*). We conducted the experiment on six litters in four groups. All pups trained on live scorpions successfully handled the scorpion on the fourth day, whereas those trained on dead scorpions lost the scorpion in two out of six tests and control pups lost their scorpions on four occasions. In all six trials, the pup trained on live scorpions was either the only pup to handle the scorpion successfully or had the fastest handling time (*18*) (Friedman test: S = 10.38, df = 5, $P = 0.006$). Moreover, all control pups and all pups trained on dead scorpions were pincered or pseudo-stung (struck by the stingless tail) by the scorpion during the test with a live scorpion, whereas this occurred only once in tests with pups trained on live scorpions (Fisher's test: $P < 0.001$).

The results of this study provide strong evidence that the provisioning behavior of meerkat helpers constitutes a form of "opportunity teaching," in which teachers provide pupils with opportunities to practice skills, thus facilitating learning (*3*, *7*). Helpers modified their behavior in the presence of pups, gradually introducing them to live prey, monitoring their handling behavior, nudging prey, and retrieving and further modifying prey if necessary. Dan-

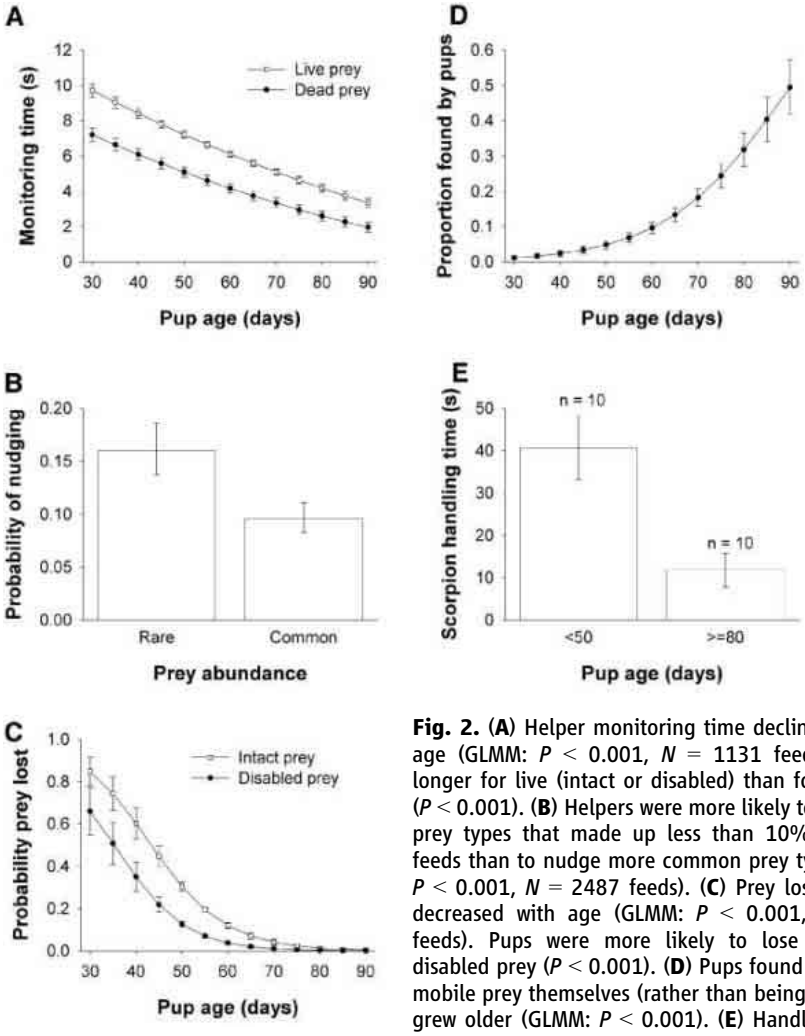

Fig. 2. (**A**) Helper monitoring time declined with pup age (GLMM: $P < 0.001$, N = 1131 feeds) and was longer for live (intact or disabled) than for dead prey ($P < 0.001$). (**B**) Helpers were more likely to nudge rare prey types that made up less than 10% of all pup feeds than to nudge more common prey types (GLMM: $P < 0.001$, N = 2487 feeds). (**C**) Prey losses by pups decreased with age (GLMM: $P < 0.001$, N = 3046 feeds). Pups were more likely to lose intact than disabled prey ($P < 0.001$). (**D**) Pups found more highly mobile prey themselves (rather than being fed) as they grew older (GLMM: $P < 0.001$). (**E**) Handling time for pups experimentally provisioned with stingless scorpions was higher for pups <50 days old than for pups ≥80 days old (paired t test: $t_9 = 3.98$, $P = 0.003$).

gerous items were more likely to be killed or disabled than other mobile prey. Helpers gained no direct benefits from their provisioning behavior and incurred costs through giving pups prey that was difficult to handle and might escape. Finally, there was strong evidence that helper provisioning behavior plays an important role in promoting the development of pup handling skills.

It is often assumed that teaching requires awareness of the ignorance of pupils and a deliberate attempt to correct that ignorance (*5*, *6*, *20*), but viewed from a functional perspective (*3*), teaching can be based on simple mechanisms without the need for intentionality and the attribution of mental states. By differentially responding to the calls of pups of different ages, helpers may accelerate pups' learning of handling skills without the need for complex cognitive processes. Additional post-provisioning behavior, such as nudging and retrieving prey, may then further enhance skill acquisition.

Evidence from ants (*10*) and meerkats suggests that teaching, as defined by Caro and Hauser (*3*), may have evolved independently in many unrelated taxa. Where individuals must acquire critical skills or information but individual learning is costly or opportunities to practice are lacking, selection may favor mechanisms whereby experienced individuals actively facilitate learning by naïve conspecifics. The paucity of evidence for teaching is likely to reflect difficulties in producing unequivocal support for strict criteria rather than an absence of teaching per se. As evidence for teaching in nonhuman animals emerges, research will be in a position to look in more detail at the conditions under which teaching is likely to evolve and to relate forms of teaching found in humans and other animals in a broad framework.

References and Notes

1. C. M. Heyes, B. G. Galef Jr., Eds., *Social Learning in Animals: The Roots of Culture* (Academic Press, San Diego, CA, 1996).
2. D. M. Fragaszy, S. Perry, Eds., *The Biology of Traditions: Models and Evidence* (Cambridge Univ. Press, Cambridge, 2003).
3. T. M. Caro, M. D. Hauser, *Q. Rev. Biol.* **67**, 151 (1992).
4. D. Maestripieri, *Hum. Nat.* **6**, 361 (1995).
5. A. T. Pearson, *The Teacher: Theory and Practice in Teacher Education* (Routledge, New York, 1989).
6. M. Tomasello, A. C. Kruger, H. H. Ratner, *Behav. Brain Sci.* **16**, 495 (1993).
7. R. F. Ewer, *Nature* **222**, 698 (1969).
8. B. G. Galef, E. E. Whiskin, G. Dewar, *Anim. Behav.* **70**, 91 (2005).
9. L. Rendell, H. Whitehead, *Behav. Brain Sci.* **24**, 309 (2001).
10. N. R. Franks, T. Richardson, *Nature* **439**, 153 (2006).
11. R. Boyd, P. Richerson, *Culture and the Evolutionary Process* (Univ. of Chicago Press, Chicago, 1985).
12. C. Boesch, *Anim. Behav.* **41**, 530 (1991).
13. T. M. Caro, *Cheetahs of the Serengeti Plains: Grouping in an Asocial Species* (Univ. of Chicago Press, Chicago, 1994).
14. T. H. Clutton-Brock *et al.*, *Science* **291**, 478 (2001).
15. S. P. Doolan, D. W. Macdonald, *J. Zool.* **239**, 697 (1996).
16. M. B. Manser, G. Avey, *Behav. Ecol. Sociobiol.* **48**, 429 (2000).
17. J. Leeming, *Scorpions of Southern Africa* (Struik, Cape Town, South Africa, 2003).
18. Materials and methods are available as supporting material on *Science* Online.
19. S. M. White, thesis, University of Cambridge, Cambridge, UK (2001).
20. D. Cheney, R. Seyfarth, *How Monkeys See the World: Inside the Mind of Another Species* (Univ. of Chicago Press, Chicago, 1990).

21. H. and J. Kotze kindly allowed us to work on their land, and the Northern Cape Conservation Authority granted permission to conduct the research. We are grateful for the support of the Mammal Research Institute at the University of Pretoria and for the help of N. Jordan, T. Flower, N. Tayar, and volunteers who contributed to data collection. L. Hollén allowed us the use of some begging call recordings. We thank T. Clutton-Brock for supervision and access to the meerkats and S. Hodge, J. Gilchrist, K. Isvaran, A. Radford, N. Raihani, S. English, and A. Young for discussion and advice. The work was funded by a Natural Environment Research Council studentship to A.T.

Supporting Online Material

www.sciencemag.org/cgi/content/full/313/5784/227/DC1
Materials and Methods
Tables S1 to S5
Reference

13 April 2006; accepted 2 June 2006
10.1126/science.1128727

Ca^{2+} Entry Through Plasma Membrane IP_3 Receptors

Olivier Dellis, Skarlatos G. Dedos, Stephen C. Tovey, Taufiq-Ur-Rahman, Stefan J. Dubel, Colin W. Taylor*

Inositol 1,4,5-trisphosphate receptors (IP_3Rs) release calcium ions, Ca^{2+}, from intracellular stores, but their roles in mediating Ca^{2+} entry are unclear. IP_3 stimulated opening of very few (1.9 ± 0.2 per cell) Ca^{2+}-permeable channels in whole-cell patch-clamp recording of DT40 chicken or mouse B cells. Activation of the B cell receptor (BCR) in perforated-patch recordings evoked the same response. IP_3 failed to stimulate intracellular or plasma membrane (PM) channels in cells lacking IP_3R. Expression of IP_3R restored both responses. Mutations within the pore affected the conductances of IP_3-activated PM and intracellular channels similarly. An impermeant pore mutant abolished BCR-evoked Ca^{2+} signals, and PM IP_3Rs were undetectable. After introduction of an α-bungarotoxin binding site near the pore, PM IP_3Rs were modulated by extracellular α-bungarotoxin. IP_3Rs are unusual among endoplasmic reticulum proteins in being also functionally expressed at the PM, where very few IP_3Rs contribute substantially to the Ca^{2+} entry evoked by the BCR.

Most IP_3R in most cells are in the endoplasmic reticulum (ER) (*1*–*3*), but IP_3-evoked Ca^{2+} release also occurs from other intracellular organelles (*2*, *3*). Receptors that evoke Ca^{2+} release from intracellular stores usually also stimulate Ca^{2+} entry across the PM (*1*). This is often through store-operated Ca^{2+} entry (SOC), where depletion of intracellular stores activates a Ca^{2+}-permeable channel in the PM (*4*–*6*). The SOC channel is not itself an IP_3R, although IP_3R within the ER may interact with it (*4*). Non-SOC pathways, often regulated by signals derived from diacylglycerol, also contribute to Ca^{2+} entry (*7*), but these channels are not formed from IP_3R proteins. Cell-surface labeling, immunolocalization, subcellular fractionation, and whole-cell patch-clamp recording (*8*) have suggested the presence of IP_3R in the PM (*9*). The patch-clamp results are disputed because the most thoroughly characterized current activated by IP_3, Ca^{2+} release–activated current (CRAC) (*10*, *11*), is also activated by store depletion, has properties distinct from IP_3R, and is probably activated when IP_3R within ER mediate loss of Ca^{2+} from intracellular stores. The only clear evidence for functional IP_3R in the PM comes from cilia of olfactory neurons, but these IP_3R differ from those in ER (*12*, *13*). The only IP_3-gated channels detected in the PM are thus not obviously related to IP_3R in the ER.

SOC evoked by emptying intracellular Ca^{2+} stores with thapsigargin occurred in cells lacking IP_3R (Fig. 1A) (*9*, *14*). The whole-cell current evoked by store depletion in DT40 cells (I_{CRAC}) is likewise independent of IP_3R (*15*). SOC was completely blocked by low concentrations of Gd^{3+} [half-maximal inhibitory concentration (IC_{50}), 69 ± 9 nM (Fig. 1C)] (*5*). Antibody to immunoglobulin M (anti-IgM) (5 μg/ml), which stimulates phospholipase Cγ2 through the B cell receptor (BCR), predictably failed to increase the intracellular Ca^{2+} concentration ($[Ca^{2+}]_i$) in cells lacking IP_3R, but it caused release of Ca^{2+} from intracellular stores and Ca^{2+} entry in normal DT40 cells (Fig. 1B) (*16*). The latter was only partially inhibited (55 ± 4%) by a concentration of Gd^{3+} (300 nM) that abolished SOC (Fig. 1D). Activation of the BCR, but not SOC, stimulates Ba^{2+} entry and requires IP_3R, leading to an earlier suggestion that IP_3R might directly mediate Ca^{2+} entry

Department of Pharmacology, Tennis Court Road, Cambridge, CB2 1PD, UK.

*To whom correspondence should be addressed. E-mail: cwt1000@cam.ac.uk

(*9*). Our results establish that the Ca^{2+} entry evoked by the BCR requires IP_3R and cannot be mediated by SOC alone (*17*).

In whole-cell patch-clamp recordings from wild-type DT40 cells using K^+ as a charge carrier, IP_3 (10 μM) (*16*) stimulated opening of cation-selective channels with a slope conductance (γ_K) of 213 ± 7 pS (n = 27) (Fig. 2, A to C). At the peak of their activity, mean channel open (t_o) and closed (t_c) times were 11.0 ± 0.8 ms and 11.1 ± 1.5 ms, respectively. The channel was inactive in the absence of IP_3 (Fig. 2A). The effect of IP_3 was inhibited by intracellular heparin (100 μg/ml), a competitive antagonist of IP_3, and by high extracellular concentrations of 4-aminopyridine (1 mM) or tetraethylammonium (≥10 mM) (fig. S1). Both are blockers of K^+ channels but also inhibit IP_3R (*18*). Inhibition of Cl^- channels had no effect on IP_3-activated currents (fig. S1), nor did extracellular Gd^{3+} (≤1 μM) (fig. S2).

The maximal open probability (P_o) of the PM channels was 0.54 ± 0.03 (n = 7) (Fig. 2B), similar to that observed for IP_3R1 expressed in the nuclear envelope from COS (*19*) or DT40 cells (Fig. 3B and table S1). In >30 recordings from DT40 cells lacking IP_3R (DT40-KO) (*9*, *14*), we never detected IP_3-evoked currents (Fig. 3A). As expected, IP_3 stimulated

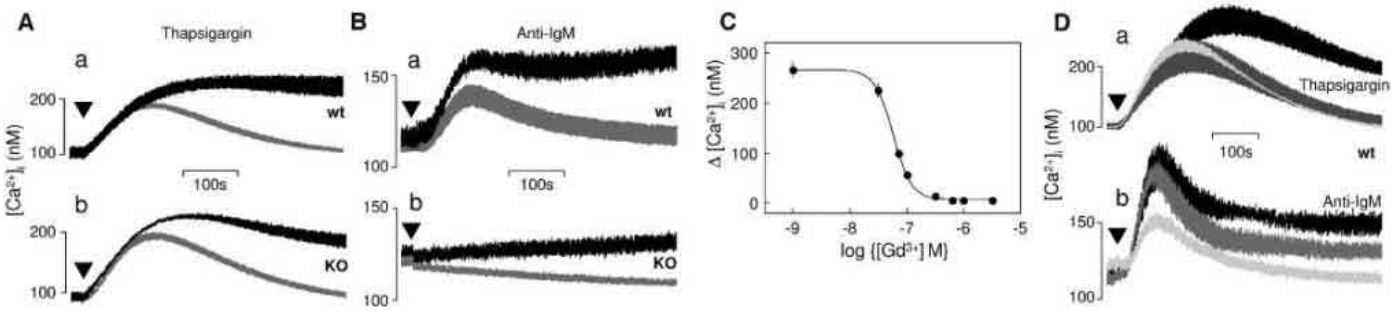

Fig. 1. Ca^{2+} entry in DT40 cells with and without IP_3R. Ca^{2+} signals evoked by (**A**) thapsigargin (0.5 μM, from arrowhead) or (**B**) anti-IgM (5μg/ml, from arrowhead) in the presence (black) or absence (gray) of extracellular Ca^{2+} in (a) DT40 wild-type cells and (b) DT40-KO cells. Traces are shown with fluorescence collected at 1.5-s intervals and with SEM shown at each point. (**C**) Concentration-dependent inhibition of thapsigargin-evoked Ca^{2+} entry by Gd^{3+} in DT40 wild-type cells, with inhibition calculated as the difference between the average increase in $[Ca^{2+}]_i$ recorded 350 to 450 s after restoration of extracellular Ca^{2+} in the presence and absence of Gd^{3+}. (**D**) Ca^{2+} signals in DT40 wild-type cells evoked by (a) thapsigargin or (b) anti-IgM (each from arrowhead) in the presence (gray) or absence (black) of 300 nM Gd^{3+}; palest lines show responses in absence of extracellular Ca^{2+}. (**E**) Time course of the Gd^{3+}-insensitive Ca^{2+} entry evoked by anti-IgM in DT40-R1 cells (fig. S4Ab) compared with that for P_o (as percentage of maximum) recorded using perforated patches in the presence of anti-IgM (Fig. 2F). Results are means ± SEM; $n \geq 3$.

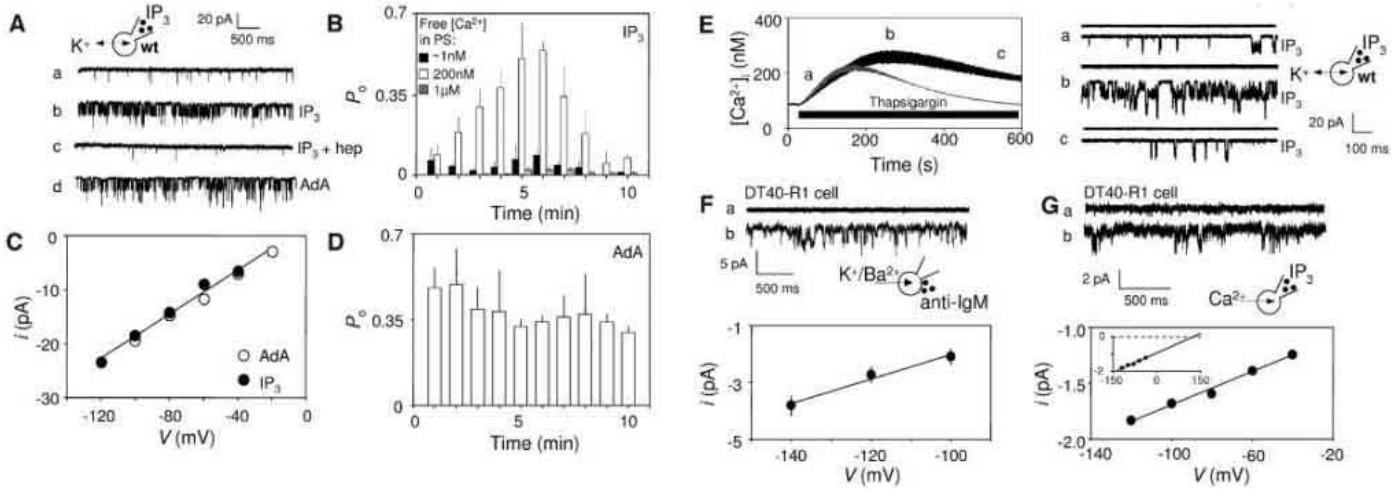

Fig. 2. Plasma membrane channels activated by IP_3. (**A**) Whole-cell recordings (5 to 6 min after break-in, with K^+ as charge carrier) from DT40 wild-type cells held at 0 mV and stepped to −100 mV for current recordings (a) over 15 s, (b) with added IP_3 (10 μM), (c) with IP_3 and heparin (100 μg/ml), or (d) with adenophostin A (0.5 μM) in pipette solution. (**B**) P_o is shown during stimulation with IP_3 (10 μM) during 15-s periods sampled at 1-min intervals after establishing whole-cell recording and with the intracellular free $[Ca^{2+}]$ buffered at 1 nM (solid), 200 nM (open), or 1 μM (gray) bars. Records that included only a single channel are shown. (**C**) *i-V* relationship for the IP_3-stimulated (filled circles) and adenophostin A–stimulated (open circles) currents. (**D**) P_o measured as in (B), but with 0.5 μM adenophostin A in the pipette. (**E**) Thapsigargin-evoked (0.5 μM) Ca^{2+} signals in intact DT40 cells in the absence (gray trace) or presence (black) of extracellular Ca^{2+}. Whole-cell recordings (at −100 mV) are shown at the indicated times (a, b, and c) from cells treated with only thapsigargin (upper traces) or with thapsigargin and IP_3 (lower traces). Results are means ± SEM, $n \geq 5$. (**F**) Perforated-patch recordings (at −100 mV) from DT40-R1 cells with Ba^{2+} as a major charge carrier (a) without and (b) with anti-IgM (5 μg/ml in bath solution), and *i-V* relationship for the anti-IgM–activated current. (**G**) *i-V* relationship for IP_3-activated whole-cell current in DT40-R1 cells (at −120 mV) with Ca^{2+} as the only charge carrier (50 mM $CaCl_2$ in BS, 200 nM free $[Ca^{2+}]$ in pipette solution; details in table S2). Inset shows data extrapolated to the reversal potential. Traces recorded in the (a) absence or (b) presence of IP_3 (10 μM in pipette solution).

Ca^{2+} release from the intracellular stores of DT40 wild-type cells but not from DT40-KO cells (table S1). In all DT40 wild-type cells on which gigaseals were established (n = 135), IP_3 stimulated opening of PM channels, but in recordings that lasted up to 20 min, we never detected more than five simultaneous openings and typically detected only one to three (mean: 1.9 ± 0.2). With so few channels, it is unsurprising that we never (n = 19) detected IP_3-gated currents in isolated inside-out membrane patches. Nor could we detect biotinylation of PM IP_3R in DT40-KO cells stably expressing rat IP_3R1 (DT40-R1), in which the total number of IP_3R was more than 20 times as much as that in DT40 wild-type cells (table S1 and fig. S6). In perforated-patch recordings of DT40-R1 cells with Ba^{2+} as a major charge carrier, anti-IgM caused sustained activation of 2.3 ± 0.3 channels per cell (P_o = 0.24 ± 0.02, n = 3) (Fig. 3E), and their conductance (γ = 43 ± 6 pS) (Fig. 3F) was the same as that from whole-cell recording with IP_3 as the stimulus (table S2). In three similar recordings without anti-IgM, there was no response. Gd^{3+}-insensitive Ca^{2+} entry (detected with the Ca^{2+}-sensitive indicator, fluo 4) and opening of PM cation channels (in perforated-patch recordings) proceeded with similar time courses after addition of anti-IgM (Fig. 1E). IP_3 and the BCR thus stimulate opening of the same PM channels.

An unexpected feature was the delay of several minutes between intracellular dialysis with IP_3 and maximal channel activity (Fig. 2B). This is too long to result from diffusion of IP_3, but it could reflect slow intervening steps between IP_3 binding to an IP_3R and activation of PM channels or slow loss of enzymes that degrade IP_3. Results with adenophostin A, a nonmetabolized agonist of IP_3R (*20*), support the second possibility. With adenophostin A (0.5 μM) in the pipette, channels with the same properties as those activated by IP_3 were activated without detectable latency and remained active for at least 10 min (γ = 210 ± 9 pS, P_o = 0.49 ± 0.14, t_o = 10.6 ± 1.9 ms, t_c = 12.7 ± 2.1 ms, n = 8) (Fig. 2, A, C, and D). A much higher concentration of IP_3 (100 μM in pipette solution) or another nonmetabolized agonist of IP_3R, dimeric IP_3 (*21*), also activated the channels with reduced (IP_3, ≤2 min) or undetectable (dimeric IP_3) latency. These results establish that IP_3 need not be metabolized for it to activate PM cation channels.

Cytosolic Ca^{2+} biphasically regulates IP_3-evoked Ca^{2+} release from intracellular stores (*22*). The PM channels activated by IP_3 were inhibited when $[Ca^{2+}]_i$ was reduced to 1 nM or increased to 1 μM (Fig. 2B). In both cases, channel activity peaked after 5 to 6 min, but P_o was reduced from 0.54 ± 0.03 to 0.09 ± 0.04 and 0.02 ± 0.01 (n = 5), respectively. Adenosine triphosphate (ATP) potentiates the effects of IP_3 on IP_3R (*23*). Our IP_3-activated currents were recorded with 500 μM ATP (but no Mg^{2+}) in the pipette, but in the absence of ATP, P_o was reduced by 90% to 0.057 ± 0.04 (n = 5). The requirement for ATP, but not Mg^{2+}, is noteworthy because only MgATP supports the activities of Ca^{2+} pumps and protein kinases, whereas Mg^{2+} is not required for ATP to modulate IP_3R (*23*).

DT40-KO cells never responded to IP_3, but DT40-R1 cells were responsive. IP_3 stimulated release of Ca^{2+} from the intracellular stores of permeabilized DT40-R1 cells (table S1) and stimulated opening of single channels in the nuclear envelope (γ_K = 117 ± 5 pS, P_o = 0.38 ± 0.06, t_o = 12.3 ± 1.6 ms, t_c = 11.9 ± 2.9 ms) and cation channels in whole-cell recordings with properties (γ_K = 214 ± 17 pS, P_o = 0.52 ± 0.06) (Fig. 3, A to D) indistinguishable from those of DT40 wild-type cells. The similarities included detection of only 1 to 3 PM channels per cell (mean, 1.7 ± 0.2) and a latency of 5 to 6 min before P_o peaked. With Ca^{2+} as the only charge carrier, γ_{Ca} was 9.1 ± 1.3 pS (Fig. 2G), and again there were only 3.2 ± 0.2 channels per cell (table S2).

In mouse B cells, in which IP_3R3 is the major subtype (fig. S3), IP_3 invariably activated PM channels (2.0 ± 0.3 channels per cell) with two major K^+ conductances (γ_K = 147 ± 11 and 75 ± 6 pS, n = 8) (Fig. 3, E and F). After expression of rat IP_3R3 in DT40-KO cells, IP_3 activated channels in the PM (2.6 ± 0.5 channels/cell) and nuclear membrane. IP_3R3 displayed subconductances; a major γ_K in the PM (132 ± 5 pS) and nuclear envelope (130 ± 6 pS) (Fig. 3, F and G) was indistinguishable from that in B cells (147 ± 11 pS). We conclude that small numbers of IP_3-activated channels are expressed also in the PM of B cells. Our results demonstrate that IP_3 interacts with an intracellular IP_3R to stimulate opening of a PM cation channel, but is that channel itself an IP_3R?

SOC in DT40 cells is mediated by I_{CRAC}, which is inwardly rectifying, is highly Ca^{2+}-selective (P_{Ca}/P_{Na} ~1000), and has a very low unitary Ca^{2+} conductance (γ_{Ca} < 20 fS) (*10*). The current activated by IP_3 is totally different: It is nonrectifying, γ_{Ca} is much greater (Fig.

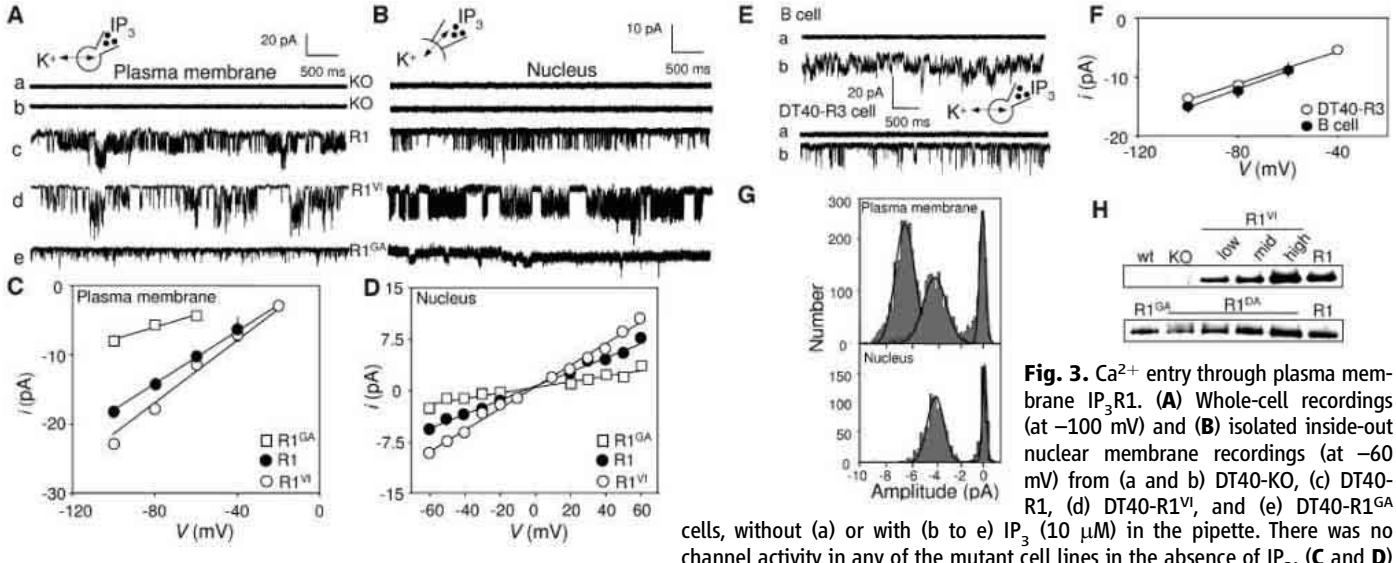

Fig. 3. Ca^{2+} entry through plasma membrane IP_3R1. (**A**) Whole-cell recordings (at −100 mV) and (**B**) isolated inside-out nuclear membrane recordings (at −60 mV) from (a and b) DT40-KO, (c) DT40-R1, (d) DT40-$R1^{VI}$, and (e) DT40-$R1^{GA}$ cells, without (a) or with (b to e) IP_3 (10 μM) in the pipette. There was no channel activity in any of the mutant cell lines in the absence of IP_3. (**C** and **D**) *i-V* relationship for the IP_3-stimulated currents for (C) whole-cell and (D) nuclear membrane recordings from DT40-R1 (filled circles), DT40-$R1^{VI}$ (open circles), and DT40-$R1^{GA}$ (squares) cells. (**E**) Whole-cell recordings from mouse B cells and DT40-R3 cells with K^+ as charge carrier, (a) without or (b) with IP_3 (10 μM in pipette solution). (**F**) *i-V* relationship for the IP_3-activated currents in B cells (filled circles) and DT40-R3 cells (open circles). (**G**) All-points current amplitude distribution for whole-cell and nuclear recordings at −40 mV from DT40-R3 cells stimulated with 10 μM IP_3. (**H**) Expression of IP_3R1 in different cell lines (10 μg protein per lane), determined using Ab1, which recognizes mammalian IP_3R1 but not endogenous IP_3R of DT40 cells.

2G), and it is not as selective as I_{CRAC} (table S2). PM IP_3R are permeable to Ba^{2+} and Ca^{2+} (Fig. 2, F and G) and, consistent with previous analyses of IP_3R1 in the nuclear envelope ($P_{Ca}/P_K = 4$) (*19*) and lipid bilayers ($P_{Ba}/P_K = 6$) (*24*), they are poorly selective for bivalent over monovalent cations (table S2). Because Ca^{2+}, but not Ba^{2+}, inhibits IP_3R (*25*), it is notable that P_o is decreased when Ca^{2+} is a major charge carrier and reduced further when it is the sole charge carrier but the number of channels detected in the PM is similar whether Ca^{2+}, Ba^{2+}, or K^+ is the charge carrier (table S2). Feedback inhibition by cytosolic Ca^{2+} cannot therefore limit the number of active channels detected in our recordings.

Over a period when thapsigargin (0.5 μM) stimulated SOC in recordings of $[Ca^{2+}]_i$, it had no effect on whole-cell currents or those evoked by IP_3 (Fig. 2E). These results and the Gd^{3+}-insensitivity of the channels (fig. S2) establish that the channels activated by IP_3 do not result from IP_3 causing more complete emptying of intracellular stores and consequent activation of a SOC pathway. To eliminate any possibility that the effects of IP_3 might be a consequence of activating IP_3R within intracellular stores, we introduced point mutations into the IP_3R1 pore. Mutation of V^{2548} to I (IP_3R1^{VI}) increases γ_K (*19*), whereas mutation of D^{2550} to A (IP_3R1^{DA}) creates an impermeant channel (*26*), and mutation of G^{2547} to A (IP_3R1^{GA}) is expected to decrease γ (*27*). IP_3 failed to stimulate Ca^{2+} release from permeabilized DT40-KO cells or those expressing IP_3R1^{DA} (table S1). In inside-out patches from nuclear membrane, IP_3 stimulated the opening of channels and γ_K was increased by 27 ± 4% in IP_3R1^{VI} and reduced by 60 ± 15% in IP_3R1^{GA} (Fig. 3, B and D). In whole-cell recordings, γ_K of the PM channels activated by IP_3 was increased by 22 ± 8% for IP_3R1^{VI} and decreased by 58 ± 9% for IP_3R1^{GA} (Fig. 3, A and C, and table S1). In four DT40 lines stably expressing different amounts of IP_3R1^{DA} (Fig. 3H and table S1), stimulation of the BCR never evoked Ca^{2+} signals, IP_3 never evoked Ca^{2+} release from intracellular stores, and in whole-cell recordings we detected no IP_3-activated Ca^{2+} currents (fig. S5). These results are inconsistent with a suggestion that Ca^{2+} entry evoked by the BCR requires the IP_3R but not its functional pore (*26*).

We introduced an α-bungarotoxin–binding site (*16*, *28*) into the loop linking the final pair of transmembrane domains of IP_3R1 close to the pore (Fig. 4A) and expressed it in DT40-KO cells. In whole-cell recordings from these cells, IP_3 stimulated the opening of 2.5 ± 0.2 channels per cell, and both their conductance and P_o were lower than for normal IP_3R (Fig. 4, B and C). The channels were not activated by α-bungarotoxin alone, but in the presence of intracellular IP_3, extracellular (but not intracellular) α-bungarotoxin increased both P_o and γ_K (Fig. 4, B and C) without changing the total number of channels detected (3.0 ± 0.3 channels/cell). These results establish that IP_3 directly activates an IP_3R in the PM and that Ca^{2+} entry occurs via its pore. The IP_3R is unusual in that the same protein is expressed in the ER and the PM and functions in both as an IP_3-gated channel. Our results challenge the notion that ER-resident proteins cannot progress to the PM (*29*).

Because we invariably detected very few (~2 per cell) PM IP_3R, despite considerable differences in overall levels of IP_3R expression (Fig. 3H and table S1), trafficking of IP_3R to the PM is probably precisely regulated. Indeed DT40-R1 cells expressed >20 times as much IP_3R as did DT40 wild-type cells, but both cell lines express only ~2 IP_3R at the PM (table S1). Furthermore, although the intracellular stores of cells with more IP_3R^{VI} were more sensitive to IP_3, the number of IP_3-gated channels in the PM never exceeded that in DT40 wild-type cells (table S1). In DT40 wild-type cells, the density of IP_3R at the PM is only ~3% of that in the nuclear envelope, and <0.5% of all IP_3R are expressed at the PM (fig. S6). Nevertheless, two IP_3R with the properties revealed by our whole-cell recordings would allow more than sufficient Ca^{2+} entry to cause the Gd^{3+}-insensitive Ca^{2+} signal detected after activation of the BCR (fig. S6).

The same IP_3R1 has almost twice the γ_K when expressed in the PM relative to the nuclear envelope (table S1), and although a major γ_K for IP_3R3 was similar in both membranes, the distribution between subconductance states differed (Fig. 3G). Different membranes may selectively stabilize different subconductances of the IP_3R, such that the same IP_3R behaves differently in the two membranes.

We conclude that most IP_3R are expressed in intracellular stores but that a tiny fraction is reliably directed to the PM, where they contribute substantially to the Ca^{2+} entry evoked by the BCR. Different Ca^{2+}-regulated processes are likely to respond very differently to Ca^{2+} dribbling into the cell from huge numbers (possibly >10,000) of I_{CRAC} channels (*10*) or gushing into the cell through only two IP_3R.

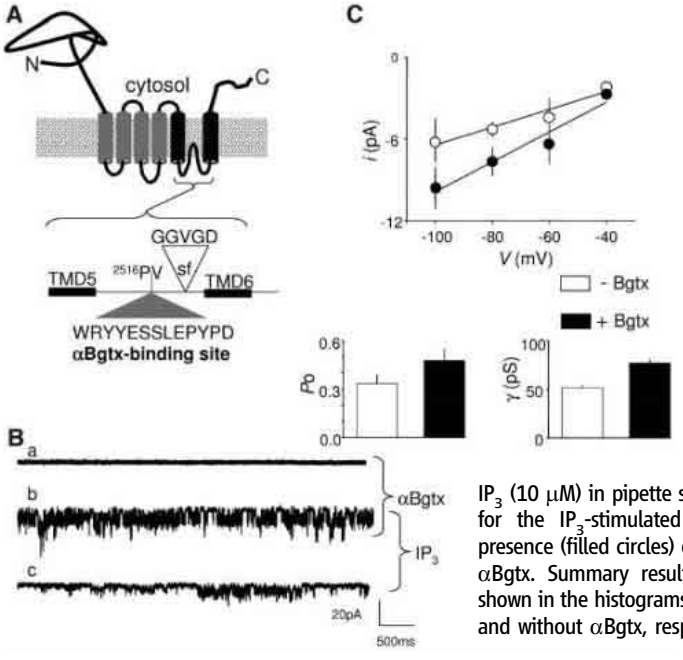

Fig. 4. Regulation of plasma membrane IP_3R through an extracellular α-bungarotoxin binding site. (**A**) Structure of IP_3R1 containing an α-bungarotoxin (αBgtx) binding site; sf denotes the selectivity filter, and TMD5 and 6 the surrounding transmembrane regions. (**B**) Whole-cell recordings from DT40-R1αBgtx cells with K^+ as charge carrier in the presence of (a and b) αBgtx in bath solution (100 nM) and/or (b and c) IP_3 (10 μM) in pipette solution. (**C**) *i-V* relationship for the IP_3-stimulated current recorded in the presence (filled circles) or absence (open circles) of αBgtx. Summary results for P_o and the γ_K are shown in the histograms (n = 4 and 8 for cells with and without αBgtx, respectively).

References and Notes

1. M. J. Berridge, *Nature* **361**, 315 (1993).
2. C. W. Taylor, A. A. Genazzani, S. A. Morris, *Cell Calcium* **26**, 237 (1999).
3. W. Echevarria, M. F. Leite, M. T. Guerra, W. R. Zipfel, M. H. Nathanson, *Nat. Cell Biol.* **5**, 440 (2003).
4. K. Kiselyov, G. A. Mignery, M. X. Zhu, S. Muallem, *Mol. Cell* **4**, 423 (1999).
5. A. B. Parekh, J. W. Putney, *Physiol. Rev.* **85**, 757 (2005).
6. S. Feske *et al.*, *Nature* **441**, 179 (2006).
7. C. W. Taylor, *Cell* **111**, 767 (2002).
8. L. Vaca, D. L. Kunze, *Am. J. Physiol.* **269**, C733 (1995).
9. G. Vazquez, B. Wedel, G. S. J. Bird, S. K. Joseph, J. W. Putney, *EMBO J.* **21**, 4531 (2002).
10. A. Zweifach, R. S. Lewis, *Proc. Natl. Acad. Sci. U.S.A.* **90**, 6295 (1993).
11. M. Hoth, R. Penner, *J. Physiol.* **465**, 359 (1993).
12. D. A. Fadool, B. W. Ache, *Neuron* **9**, 907 (1992).
13. D. L. Kalinoski *et al.*, *Biochem. J.* **281**, 449 (1992).
14. H. Sugawara, M. Kurosaki, M. Takata, T. Kurosaki, *EMBO J.* **16**, 3078 (1997).
15. M. Prakriya, R. S. Lewis, *J. Physiol.* **536**, 3 (2001).
16. Materials and methods are available as supporting material on *Science* Online.
17. T. Morita, A. Tanimura, A. Nezu, T. Kurosaki, Y. Tojyo, *Biochem. J.* **382**, 793 (2004).
18. P. Palade, C. Dettbarn, P. Volpe, B. Alderson, A. S. Otero, *Mol. Pharmacol.* **36**, 664 (1989).
19. D. Boehning, D.-O. Mak, J. K. Foskett, S. K. Joseph, *J. Biol. Chem.* **276**, 13509 (2001).
20. M. Takahashi, K. Tanzawa, S. Takahashi, *J. Biol. Chem.* **269**, 369 (1994).
21. A. M. Riley, A. J. Laude, C. W. Taylor, B. V. L. Potter, *Bioconjugate Chem.* **15**, 278 (2004).
22. C. W. Taylor, A. J. Laude, *Cell Calcium* **32**, 321 (2002).

23. I. Bezprozvanny, B. E. Ehrlich, *Neuron* **10**, 1175 (1993).
24. I. Bezprozvanny, B. E. Ehrlich, *J. Gen. Physiol.* **104**, 821 (1994).
25. I. C. B. Marshall, C. W. Taylor, *Biochem. J.* **301**, 591 (1994).
26. D. B. van Rossum *et al.*, *Proc. Natl. Acad. Sci. U.S.A.* **101**, 2323 (2004).
27. G. G. Du, D. H. MacLennan, *J. Biol. Chem.* **273**, 31867 (1998).
28. Y. Sekine-Aizawa, R. L. Huganir, *Proc. Natl. Acad. Sci. U.S.A.* **101**, 17114 (2004).
29. R. E. Dalbey, G. Von Heijne, *Protein Targeting, Transport, and Translocation* (Academic Press, San Diego, 2002).

30. We thank S. Lummis (Cambridge) for use of her Flexstation and T. Kurosaki (Kansai Medical University Japan) for providing DT40 cells. Supported by the Wellcome Trust (072084), Biotechnology and Biological Sciences Research Council, and a Jameel Family Studentship (to T-U-R).

Supporting Online Material
www.sciencemag.org/cgi/content/full/313/5784/229/DC1
Materials and Methods
Figs. S1 to S7
Tables S1 to S3
References

20 January 2006; accepted 24 May 2006
10.1126/science.1125203

Biomineralization of Gold: Biofilms on Bacterioform Gold

Frank Reith,[1,2]* Stephen L. Rogers,[1,4] D. C. McPhail,[1,2] Daryl Webb[3]

Bacterial biofilms are associated with secondary gold grains from two sites in Australia. 16*S* ribosomal DNA clones of the genus *Ralstonia* that bear 99% similarity to the bacterium *Ralstonia metallidurans*—shown to precipitate gold from aqueous gold(III) tetrachloride—were present on all DNA-positive gold grains but were not detected in the surrounding soils. These results provide evidence for the bacterial contribution to the authigenic formation of secondary bacterioform gold grains and nuggets.

The origin of secondary gold grains is controversial and widely debated in the scientific community; the two main theories are that they are detrital or are formed by chemical accretion (*1*). However, there is growing evidence pointing to the importance of microbial processes in the cycling of gold (*2*, *3*). Common soil bacteria (*Bacillus megaterium*, *Pseudomonas fluorescens*, *Bacterium nitrificans*) are able to solubilize several milligrams of gold per liter of medium under in vitro conditions (*2*, *4*). A recent microcosm study of auriferous soils from the Tomakin Park Gold Mine in southeastern New South Wales, Australia (35°48′51.9″S, 150°10′26.4″E) showed that resident microbiota solubilized up to 80 wt % [i.e., 1100 ng per g (dry weight, soil)] of

[1]Cooperative Research Centre for Landscape Environments and Mineral Exploration, Post Office Box 1130, Bentley, Western Australia 6102, Australia. [2]Department of Earth and Marine Sciences, [3]Research School of Biological Sciences, Electron Microscopy Unit, Australian National University, Acton, ACT 0200, Australia. [4]Commonwealth Scientific and Industrial Research Organisation (CSIRO) Land and Water, PMB2, Glen Osmond, South Australia 5064, Australia.

*To whom correspondence should be addressed. E-mail: frank.reith@csiro.au

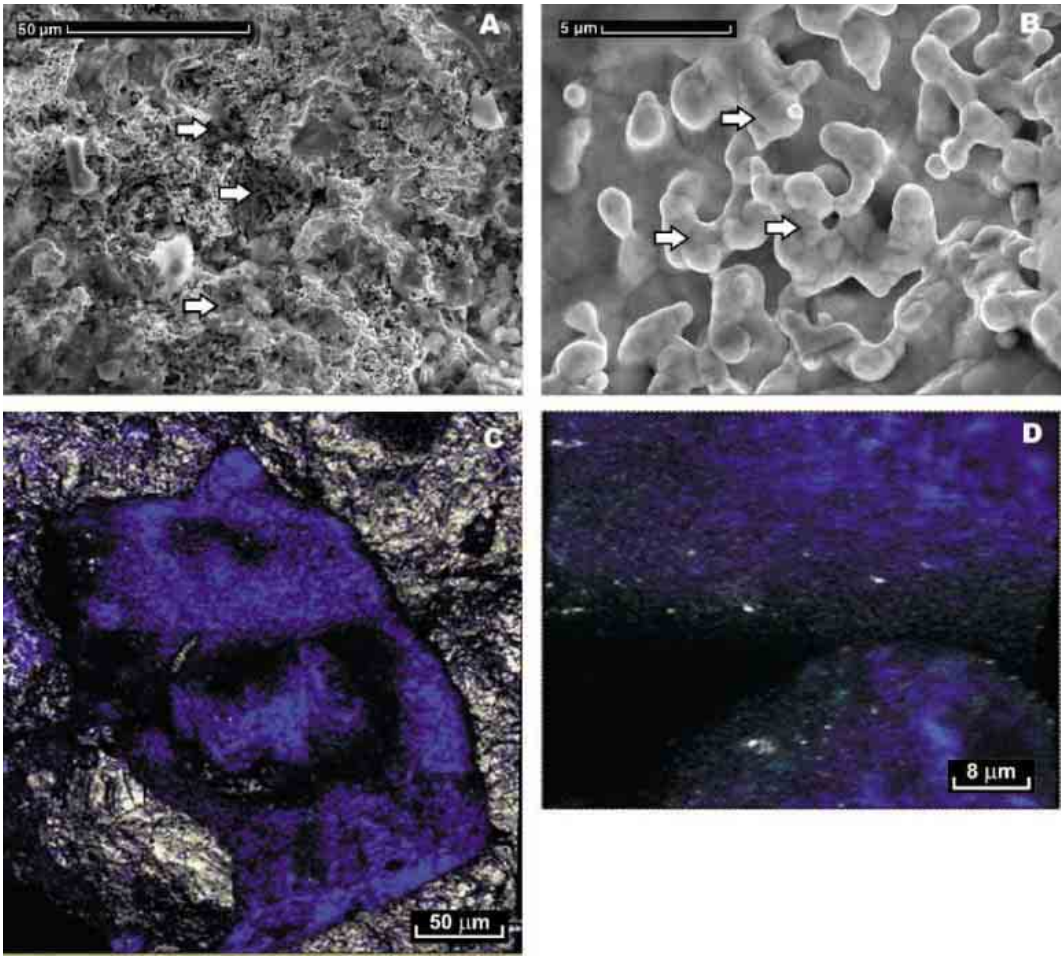

Fig. 1. Secondary electron micrographs of bacterioform gold (**A** and **B**) and confocal stereo laser microscope images (**C** and **D**) of fluorescently stained biofilms on gold grains from the Hit or Miss Gold Mine in Queensland, Australia. (A) Bacterioform gold with apparent exopolymers (white arrows) possibly derived from a microbial biofilm. (B) Detailed view of branching network of rounded and oval budding cell-like structure with apparently preserved cell wall structures (white arrows). (C) Biofilm covering an area of 200 μm by 100 μm of underlying bacterioform gold. (D) Detailed view into a small crevice in the biofilm, showing cells or cell clusters (in blue) separated by unstained interstices. Fluorescent cells are spreading predominantly over the surface of the bacterioform gold and are not present at the base of the crevice.

native gold within 45 days of incubation (*5*). In other studies, bacteria, actinomycetes, archaea, and fungi have been shown to precipitate Au(I/III) complexes under a wide range of experimental conditions (*6*–*13*). For example, *Bacillus subtilis* and *Pseudomonas aeruginosa* precipitate gold colloids intracellularly and extracellularly from $AuCl_4^-$ solutions (*8*, *9*). Lengke and Southam (*11*) have shown active intracellular precipitation of gold particles from $Au(S_2O_3)_2^{3-}$ by *Acidothiobacillus thiooxidans*; they observed irregular, rounded gold particles and octahedral gold crystals that formed several months after bacterial growth had stopped. In field studies, structures resembling gold-encrusted microfossils observed on numerous gold grains from the Americas and Australia have suggested that microbial processes contribute to the formation of secondary gold grains (*14*–*18*). However, after producing similar structures with natural and artificial gold amalgams by hot nitric acid dissolution, Watterson and others concluded that the observed morphologies alone could not be considered adequate proof of the microbial origin of these grains (*19*, *20*). Thus, the evidence to date for an association of bacteria with gold grains and their contribution to the formation of secondary grains is at best equivocal.

Gold grains for this study were obtained from soils overlying the mineralized zones at the Tomakin Park Gold Mine and the Hit or Miss Gold Mine, the latter of which is located in tropical northern Queensland, Australia (16°03′32″S, 144°19′09″E). Primary mineralization at both sites is submicroscopic and is associated with arsenopyrite and pyrite hosted in quartz (*21*, *22*). In soils overlying mineralized zones, secondary gold grains (99.2 wt % fineness; table S1) ranging in size from 0.1 to 2.5 mm were obtained (fig. S1). These findings indicate that gold dissolution from the host material, transport of gold [possibly as Au(I/III)-organic complexes or colloids], and accumulation and secondary gold grain formation had occurred in the weathering zone (*23*).

Scanning electron microscopy (SEM) of gold grains revealed micrometer-sized bacterioform pseudomorphs (Fig. 1, A and B) (*23*). Bacterial pseudomorphs detected on 5 of 10 grains from Tomakin Park Gold Mine and 7 of 10 from the Hit or Miss Gold Mine were spheroidal, cell-like structures with seemingly conserved cell walls (Fig. 1, A and B). Dried organic matter was observed in areas of bacterioform gold centered on surfaces of several grains (Fig. 1A) by means of SEM combined with spot energy-dispersive x-ray (EDX) analysis that showed carbon, oxygen, and nitrogen (fig. S2) (*23*). It is thus likely that the observed organic matter originated from extracellular polymeric substances of bacterial biofilms. Nucleic acid staining with 4′,6′-diamidino-2-phenylindole (DAPI) combined with confocal stereo laser microscopy confirmed the presence of extensive biofilms on gold grains covered with bacterial pseudomorphs (Fig. 1, C and D) (*23*). High-resolution imagery showed an uneven distribution of DAPI within the biofilm, indicating staining of nucleic acids within individual cells (Fig. 1D), whereas zones without cellular structures did not stain positive with DAPI.

Twenty gold grains from each site were used as templates for polymerase chain reactions, and 16*S* ribosomal DNA (rDNA) was amplified from 80% of these grains (*23*). Denaturing gradient gel electrophoresis (DGGE) and SYBR-Gold (Invitrogen) staining were used to separate and visualize the 16*S* rDNA bands, respectively (*23*). The number of detected bands points to the presence of up to 30 different bacterial species on the individual grains (Fig. 2). Analyses of DGGE fingerprints and 16*S* rDNA clone libraries of the bacterial communities associated with the bacterioform gold grains show that they are distinct and differ from those dominating the surrounding soils (Fig. 2 and table S2) (*23*). One 16*S* rDNA sequence was associated with all DNA-positive gold grains, irrespective of the site, but was not detected in the surrounding soils (Fig. 2). 16*S* rDNA clones from this band (TG1.1 to 1.3, PG1.1 and 1.2; Fig. 2) displayed 99% similarity to *Ralstonia metallidurans* (fig. S3 and table S2).

R. metallidurans is a Gram-negative, non–spore-forming β-proteobacterium that is highly resistant to metals, grows in the presence of

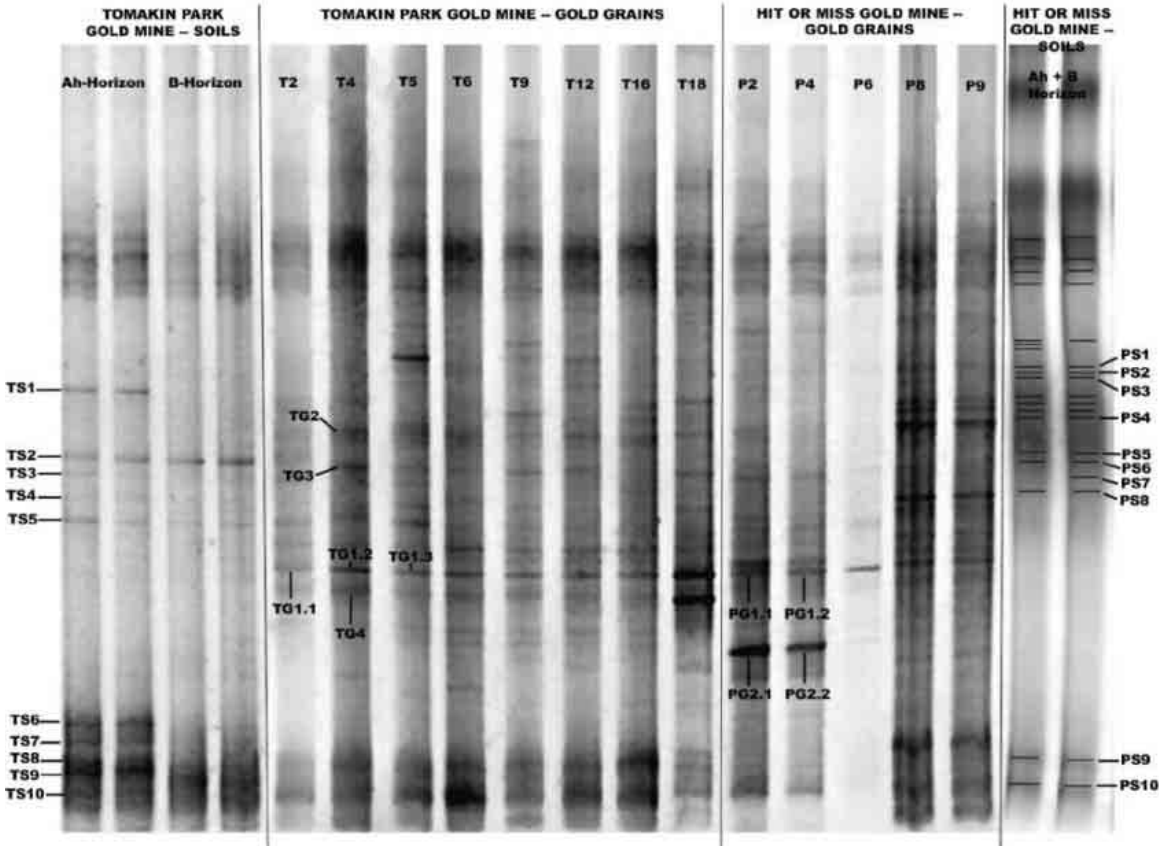

Fig. 2. DGGE patterns obtained after amplifying the V3 region of the 16*S* rDNA extracted from gold grains and surrounding soils collected at the Tomakin Park (T) and Hit or Miss (P) gold mines. Bands designated with acronyms were excised from the gels, reamplified, and sequenced. The banding of the Hit or Miss soil samples was visually enhanced with Adobe Photoshop.

millimolar concentrations of dissolved heavy metals such as Ag(I), Zn(II), Cd(II), Co(II), Pb(II), Hg(II), Ni(II), and Cr(VI), and has also been shown to reductively precipitate some of these metals [i.e., Ag(I), Cd(II), and Zn(II)] (*24*, *25*). Thus, in a first set of experiments, the ability of *R. metallidurans* to precipitate gold by reducing soluble, toxic $AuCl_4^-$ complexes was tested (*23*, *26*). In an unamended growth medium, *R. metallidurans* multiplied exponentially for 16 hours from the start of the incubation before reaching a stationary phase, where viable cell numbers increased from the original inoculum of 4.2×10^4 cells/ml to 1.5×10^8 cells/ml (fig. S4) (*23*). In the growth medium amended with 50 μM $AuCl_4^-$, viable cell numbers declined to 10^3 cells/ml at 4 hours after inoculation and then increased to 1.8×10^7 cells/ml after 72 hours (fig. S4). Initial gold precipitation by *R. metallidurans* was rapid, and after 8 hours of incubation, about 3 μM gold had been precipitated. Subsequently, the precipitation of gold was slower, and at the end of the experiment, after 72 hours, 5.5 μM gold had been precipitated (fig. S4). These results show that gold toxicity initially led to the death of more than 90% of viable cells from the original inoculum. The remaining cells were able to grow in the $AuCl_4^-$-amended medium, indicating that *R. metallidurans* harbors a resistance to $AuCl_4^-$ toxicity and is able to adapt to high gold concentrations. In a second set of experiments, the precipitation of gold by viable and lysed cells was assessed (*23*). Lysed, metabolically inactive *R. metallidurans* cells accumulated less than 50 wt % of gold relative to biologically active cells, indicating that *R. metallidurans* may be able to actively reduce $AuCl_4^-$ and accumulate metallic gold (fig. S5).

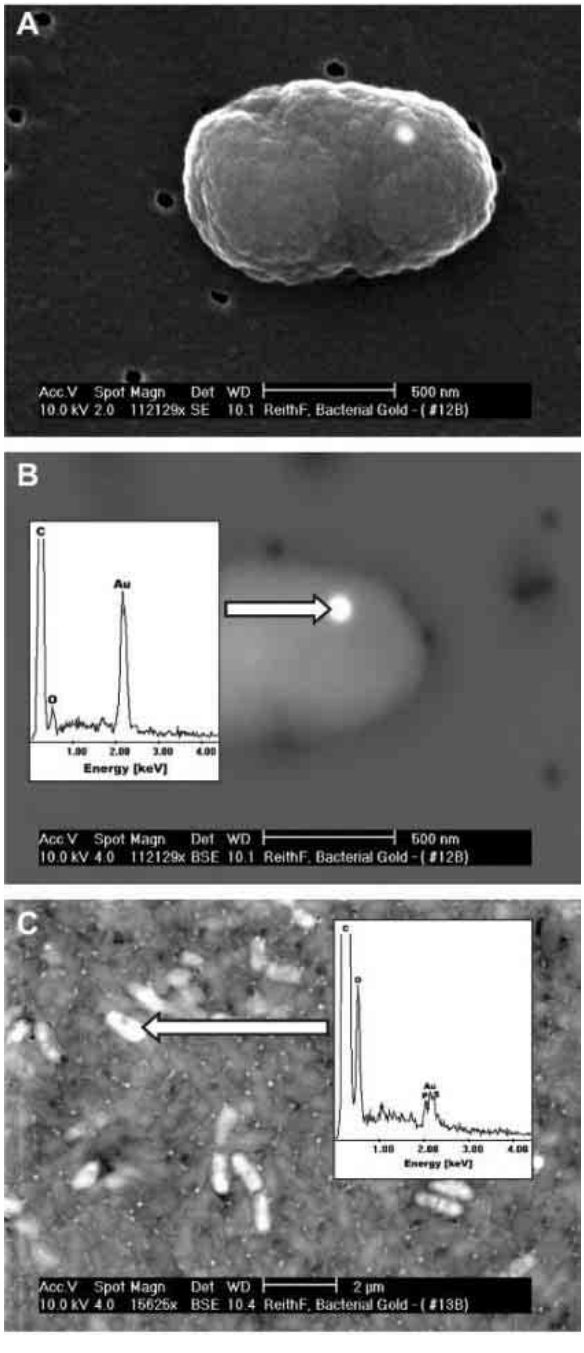

Fig. 3. Secondary (**A**) and backscatter electron micrographs with spot EDX analysis (**B** and **C**) of *Ralstonia metallidurans* cells from experiments amended with 50 μM $AuCl_4^-$ after 5 days of incubation at 30°C on a shaking incubator (100 rpm). Secondary (A) and backscatter (B) electron micrographs show a single *R. metallidurans* cell with colloidal metallic gold precipitate. Scale bar, 500 nm. (C) Backscatter electron micrograph of gold-covered *R. metallidurans* cells. Scale bar, 2 μm.

Two types of gold accumulation, associated with viable *R. metallidurans* cells, were observed. *R. metallidurans* accumulated metallic gold in distinct areas on or just below the cell surface (Fig. 3A); three-dimensional SEM imaging and SEM-EDX spot analysis showed that cells precipitated metallic gold in distinct areas within the cells close to cell walls (Fig. 3B). Other *R. metallidurans* cells displayed no discrete areas of gold accumulation and appeared to be entirely covered by gold, which appeared to be associated with sulfur- and phosphorus-containing substances in the cell membrane or the cell wall (Fig. 3C).

The biochemical mechanisms of gold precipitation in *R. metallidurans* are not yet understood. However, several mechanisms for heavy metal resistance have been observed in the organism, including cation efflux, cation reduction, cytoplasmic accumulation, and organic compound formation (*24*, *25*). Energetic considerations, based on the mechanism for reductive precipitation of monovalent silver complexes, suggest that *R. metallidurans* prefers to reductively precipitate gold nanoparticles from $AuCl_4^-$ in order to detoxify its immediate environment (*25*). Energy-dependent reductive precipitation of gold has been shown for other bacteria and archaea (*10*, *12*, *13*), and Lengke and Southam (*11*) have shown the intracellular precipitation of gold from $Au(S_2O_3)^{3-}$ by *Acidothiobacillus thiooxidans*. Passive gold accumulation via sulfur- and phosphorus-containing molecules (such as the carboxylates and phosphates) present in the lipopolysaccharides in the cell walls of Gram-negative dead or live bacterial cells cannot be ruled out, and such a mechanism may explain the presence of cells that were entirely covered by gold.

This study provides evidence that bacterially mediated processes contribute to the formation of secondary gold grains. The dominant group of organisms identified, *Ralstonia* sp., may gain a metabolic advantage by living in areas of high gold toxicity in that it uses precipitation of toxic gold complexes as a biological detoxification mechanism. It can therefore be concluded that the structures described as bacterioform gold by previous authors may indeed be of bacterial origin.

References and Notes

1. R. W. Boyle, *Geol. Surv. Can. Bull.* **280** (1979).
2. E. D. Korobushkina, G. I. Karavaiko, I. M. Korobushkin, in *Environmental Biogeochemistry*, R. Hallberg, Ed. (Publishing House of the Swedish Research Councils, Stockholm, 1983), vol. 35, pp. 325–333.
3. D. J. Mossman, T. Reimer, H. Durstling, *Geosci. Can.* **26**, 131 (1999).

4. N. N. Lyalikova, L. Y. Mockeicheva, *Microbiology* **38**, 682 (1969).
5. F. Reith, D. C. McPhail, *Geochim. Cosmochim. Acta* **70**, 1421 (2006).
6. V. I. Karamushka *et al.*, *Prikl. Biokhim. Microbiol.* **23**, 697 (1987).
7. A. Nakjima, *World J. Microbiol. Biotechnol.* **19**, 369 (2003).
8. S. Karthikeyan, T. J. Beveridge, *Environ. Microbiol.* **4**, 667 (2002).
9. G. Southam, T. J. Beveridge, *Geochim. Cosmochim. Acta* **58**, 4227 (1994).
10. K. Kashefi, J. M. Tor, K. P. Nevin, D. Lovley, *Appl. Environ. Microbiol.* **67**, 3275 (2001).
11. M. Lengke, G. Southam, *Geochim. Cosmochim. Acta* **69**, 3759 (2005).
12. V. I. Karamushka, Z. R. Ulberg, T. G. Gruzina, *Ukr. Biokhim. Zh.* **62**, 76 (1990).
13. V. I. Karamushka, T. G. Gruzina, Z. R. Ulberg, *Ukr. Biokhim. Zh.* **62**, 103 (1990).
14. S. Mann, *Nature* **357**, 358 (1992).
15. J. R. Watterson, *Geology* **20**, 1147 (1992).
16. G. C. O. Bischoff, *N. Jb. Geol. Palaeont. Abh.* **194**, 187 (1994).
17. G. C. O. Bischoff, *N. Jb. Geol. Palaeont. Abh.* **H6**, 329 (1997).
18. J. L. Keeling, *South Australia Geol. Surv. Q. Geol. N.* **126**, 12 (1993).
19. J. R. Watterson, *Geology* **22**, 1144 (1994).
20. J. Erlebacher, M. J. Aziz, A. Karma, N. Dimitrov, K. Sieradzki, *Nature* **410**, 450 (2001).
21. H. N. Bowman, *A Brief Inspection of the Tomakin Park Gold Mine* (Geol. Surv. Rep. GS. 1979/256, Department of Mineral Resources and Development, Sydney, Australia, 1979).
22. R. J. Bultitude, P. J. T. Donchak, *Pre-Mesozoic Stratigraphy and Structure of the Maytown Region* (Queensland Resource Industries Record 1992/5, Department of Resource Industries, Brisbane, Australia, 1992).
23. See supporting material on *Science* Online.
24. Mergeay *et al.*, *FEMS Microbiol. Rev.* **27**, 385 (2003).
25. M. L. Ledrich, S. Stemmler, P. Laval-Gilly, L. Foucaud, J. Falla, *Biometals* **18**, 643 (2005).
26. P. L. Witkiewicz, C. F. Shaw, *J. Chem. Soc. Chem. Commun.* **21**, 1111 (1981).
27. We thank P. Wyatt, and K. Wyatt, and the Queensland Park and Wildlife Services for access to the sites; S. McClure and S. Welch for help with SEM and EDX analysis; and M. McLaughlin, E. Lombi, S. A. Wakelin, and G. Lawrence for reviewing the manuscript. Supported by grants from the Cooperative Research Centre for Landscape Environments and Mineral Exploration and by the Australasian Institute of Mining and Metallurgy (AusIMM).

Supporting Online Material

www.sciencemag.org/cgi/content/full/313/5784/233/DC1
Materials and Methods
Tables S1 and S2
Figs. S1 to S5
References

6 February 2006; accepted 30 May 2006
10.1126/science.1125878

Selective Silencing of Foreign DNA with Low GC Content by the H-NS Protein in *Salmonella*

William Wiley Navarre,[1] Steffen Porwollik,[4] Yipeng Wang,[4] Michael McClelland,[4] Henry Rosen,[2] Stephen J. Libby,[1]* Ferric C. Fang[1,2,3]*†

Horizontal gene transfer plays a major role in microbial evolution. However, newly acquired sequences can decrease fitness unless integrated into preexisting regulatory networks. We found that the histone-like nucleoid structuring protein (H-NS) selectively silences horizontally acquired genes by targeting sequences with GC content lower than the resident genome. Mutations in *hns* are lethal in *Salmonella* unless accompanied by compensatory mutations in other regulatory loci. Thus, H-NS provides a previously unrecognized mechanism of bacterial defense against foreign DNA, enabling the acquisition of DNA from exogenous sources while avoiding detrimental consequences from unregulated expression of newly acquired genes. Characteristic GC/AT ratios of bacterial genomes may facilitate discrimination between a cell's own DNA and foreign DNA.

H-NS (encoded by *hns*) belongs to a family of small abundant nucleoid-associated proteins of Gram-negative bacteria that have the ability to bind DNA with relatively low sequence specificity (*1*). H-NS has been shown to act as a transcriptional repressor and can multimerize into higher order bridging complexes after DNA binding (*1*, *2*). H-NS also affects local supercoiling, leading to the suggestion that H-NS and other nucleoid binding proteins represent the bacterial functional equivalent of histones or mediate the global modulation of gene expression in response to changes in temperature or osmolarity (*1*, *3*, *4*). H-NS has higher affinity for curved DNA, and no consensus sequence has been identified, although the few H-NS binding sites mapped to date are rich in AT.

To determine the *Salmonella* genes controlled by H-NS, construction of an *hns* null mutation was attempted in *Salmonella enterica* sv. Typhimurium (*S.* Typhimurium). However, *hns* mutant strains were found to be nonviable unless additional mutations were present in either *rpoS* encoding the alternative sigma factor σ^S (σ^{32}) or *phoP* encoding the virulence gene regulator PhoP. These mutants could tolerate an *hns* mutation but exhibited a reduced growth rate, whereas an *hns* mutation in an *rpoS phoP* double-mutant background displayed growth similar to that of the wild type (fig. S1). This suggests that the detrimental effect of an *hns* mutation is due to derepression of one or more σ^S- and PhoP-activated loci and might explain why *hns* mutations are not lethal in some laboratory strains, given that *rpoS* mutant alleles are commonly acquired after laboratory passage (*5*). To enable studies of H-NS function in *Salmonella*, we constructed an *hns* mutation in *S.* Typhimurium carrying a spontaneous *rpoS* mutation that confers diminished σ^S activity (*6*).

Salmonella genes regulated by H-NS were identified by comparing transcript levels in *hns*$^+$ and *hns*$^-$ strains by cDNA microarray analysis (Fig. 1 and table S1). Of 4529 open reading frames (ORFs) represented on the array (4422 from the chromosome and 107 from the virulence plasmid), transcript levels of 178 ORFs exhibited a reduction in abundance in the *hns* mutant to a level less than one-third that of the wild type, whereas 409 transcripts were more abundant in the *hns* mutant. As previously reported for *Escherichia coli*, many H-NS–activated genes are involved in chemotaxis and motility (*7*). Among genes repressed by H-NS are many known virulence loci of *Salmonella*, including the *Salmonella* pathogenicity island (SPI) 2, SPI-3, and SPI-5, most characterized virulence islets, and the plasmid *spv* genes.

A large number of H-NS–repressed genes bear the hallmarks of acquisition from a foreign source—i.e., they are not universally present in the genomes of closely related enteric bacteria and possess substantially reduced GC content compared with that of the resident genome (*8*). Of 409 ORFs exhibiting repression by H-NS, only 40 (9.8%) are common to all reference genomes, whereas 265 (64.7%) are found exclusively in *Salmonella* (table S1). Most H-NS–repressed genes have GC content that is lower than the overall genome: For ORFs in which H-NS was found to repress expression to one-third or less of the original level, the average GC content is 46.8%, whereas the average GC content of the entire *Salmonella* LT2 genome is 52.2% (Fig. 2A).

Microarray analysis of cDNA provides only indirect evidence that a transcription factor interacts directly with a given sequence, because many regulatory interactions are dependent on a cascade of transcription events. For example, the apparent activation of flagellar genes by H-NS most likely occurs by means of H-NS–mediated repression of *hdfR*, a repressor of the

[1]Department of Laboratory Medicine, [2]Department of Medicine, [3]Department of Microbiology, University of Washington, Seattle, WA 98195, USA. [4]Sidney Kimmel Cancer Center, San Diego, CA 92121, USA.

*These authors contributed equally to this work.
†To whom correspondence should be addressed. E-mail: fcfang@u.washington.edu

flagellar regulators *flhDC* (*1*). *Salmonella* genes that interact directly with H-NS were therefore determined by chromatin immunoprecipitation (ChIP) of in vivo cross-linked H-NS–DNA complexes followed by microarray (ChIP-on-chip) analysis on either a custom ORF array or a tiled oligonucleotide array with 385,000 features [NimbleGen, Madison, WI (*6*)].

Of the 4438 chromosomal genes covered in the ORF array, 745 (16%) coimmunoprecipitated with H-NS. A notable correlation was observed between H-NS binding predicted in silico by low GC content and binding measured experimentally by ChIP (Fig. 2). Only 5 of 745 precipitated sequences (0.7%) were not situated within 1000 nucleotides of a chromosomal region displaying an average GC content of ≤49% (averaged over a 1000-nucleotide span) (Fig. 2 and table S2). Of 615 ORFs in the annotated *Salmonella* genome with a GC content of <47%, 433 (70.4%) coprecipitated with H-NS (table S2). The oligonucleotide array provided detailed resolution of H-NS binding sites and revealed a strong correlation between H-NS binding and regional AT content, whether or not the site was in a promoter (fig. S2). Some horizontally transferred sequences (notably SPI-1 and SPI-4) in which cDNA microarray analysis demonstrated only slight transcriptional repression were found to interact directly with H-NS, suggesting either that H-NS binding is not an effective silencer at all binding sites or that conditions used during the cDNA analysis did not favor expression or silencing of these genes.

To prospectively test whether H-NS is capable of targeting AT-rich DNA from a foreign source, a gene from *Helicobacter pylori* [*hp0226*, GC content = 39.7%] was recombined along with its promoter into a nonessential region of the *Salmonella* chromosome with a uniform average GC content of >50% and no demonstrable interaction with H-NS (Fig. 3A and fig. S3). ChIP with quantitative polymerase chain reaction (ChIP/Q-PCR) revealed significant association of H-NS with *hp0226* but not with the adjacent gene *stm1033* (GC content = 52.5%) (Fig. 3B). Reverse transcriptase/Q-PCR measurement of transcript levels revealed significantly higher (>15-fold) *hp0226* expression in the *hns* mutant compared with that of the wild type (Fig. 3C). We concluded that AT-rich content per se is sufficient for H-NS–mediated silencing and that H-NS can target AT-rich sequences irrespective of chromosomal location, a finding that could be exploited to optimize the expression of foreign genes in enteric bacteria for applications in biotechnology.

Our observations suggest a previously unrecognized role for H-NS in recognizing AT-rich sequences as foreign and preventing their expression. Such "xenogeneic silencing" would protect the cell from detrimental consequences of invading DNA. An association has been noted between H-NS and some horizontally transferred genes in pathogenic *E. coli* (*9*–*12*),

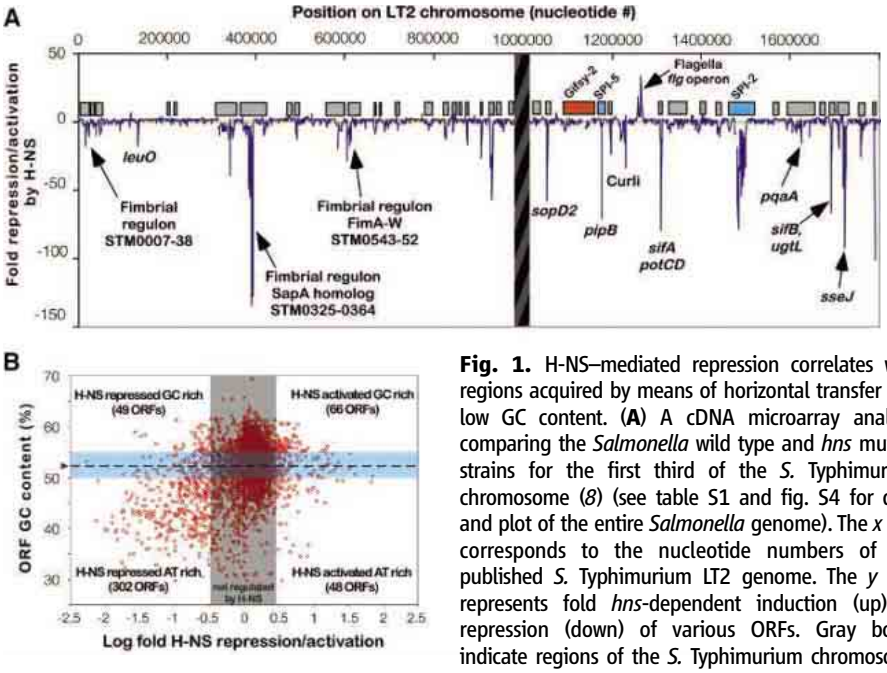

Fig. 1. H-NS–mediated repression correlates with regions acquired by means of horizontal transfer and low GC content. (**A**) A cDNA microarray analysis comparing the *Salmonella* wild type and *hns* mutant strains for the first third of the *S.* Typhimurium chromosome (*8*) (see table S1 and fig. S4 for data and plot of the entire *Salmonella* genome). The *x* axis corresponds to the nucleotide numbers of the published *S.* Typhimurium LT2 genome. The *y* axis represents fold *hns*-dependent induction (up) or repression (down) of various ORFs. Gray boxes indicate regions of the *S.* Typhimurium chromosome that appear to have been acquired by means of horizontal transfer, as determined by comparison with related enteric genomes (*8*). *S.* Typhimurium pathogenicity islands SPI-2 and SPI-5 are indicated by blue boxes; Gifsy-2 prophage region is indicated by an orange box; a region of the LT2 genome absent from the strain used in these studies is marked by a dark vertical stripe. (**B**) Scatter plot of H-NS–dependent expression (*x* axis) of 4696 *S.* Typhimurium ORFs plotted against their corresponding GC content (*y* axis). Genes whose expression varied by less than threefold in the absence of H-NS are shaded in gray. The average GC content of *S.* Typhimurium is indicated (dashed line), and the region ± 2.5% from the average is shaded in blue.

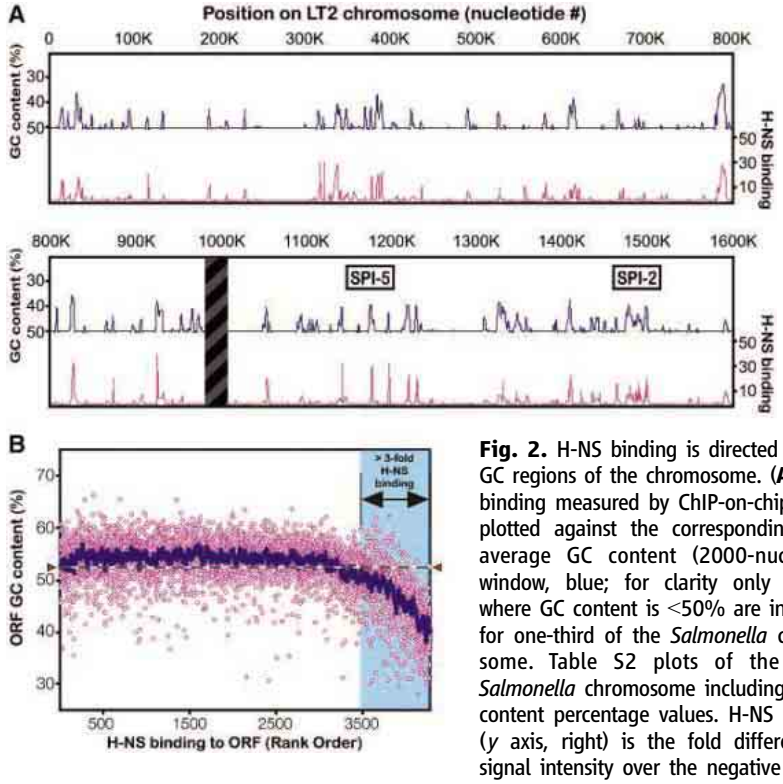

Fig. 2. H-NS binding is directed to low-GC regions of the chromosome. (**A**) H-NS binding measured by ChIP-on-chip (pink) plotted against the corresponding local average GC content (2000-nucleotide window, blue; for clarity only regions where GC content is <50% are included) for one-third of the *Salmonella* chromosome. Table S2 plots of the entire *Salmonella* chromosome including all GC content percentage values. H-NS binding (*y* axis, right) is the fold difference in signal intensity over the negative control (*6*). The LT2 genome region absent from the strain used in these studies is indicated (dark stripe). (**B**) Results of ChIP-on-chip analysis plotted against the GC content of respective *Salmonella* ORFs. ORFs are arranged in rank order according to H-NS binding (*6*) (table S2). The dark blue curve shows the moving average of ORF GC content (window = 20 ORFs). ORFs displaying greater than threefold binding to H-NS are shaded in light blue. The average GC content of *S.* Typhimurium is indicated (dashed line).

Shigella spp. (*13*, *14*), *Vibrio cholerae* (*15*), *Proteus mirabilis* (*16*), *Yersinia* spp. (*17*), and *Erwinia chrysanthemi* (*18*), but it has not been satisfactorily explained (*1*). A number of virulence regulators [e.g., SlyA (*19*), RovA (*17*), Ler (*20*), CRP-PapB (*21*), and ToxT (*22*)] act as antisilencers by displacing H-NS at specific promoters. A model in which H-NS exploits low GC content to silence horizontally acquired sequences provides a unifying explanation for these disparate observations across several bacterial species. The evolutionary development of selective countersilencing mechanisms provides a means by which an organism is protected from adverse consequences of foreign DNA but can nevertheless selectively activate individual loci that confer a fitness advantage.

Our model provides a bacterial analog to the silencing of transposons and mobile genetic elements by heterochromatin/RNA interference in eukaryotes (*23*). Similar to heterochromatin, H-NS appears to function as a silencer of potentially harmful sequences and to exert control over local nucleoid structure. However, whereas histones are highly conserved among eukaryotes, the primary sequence of H-NS is poorly conserved among bacteria outside of the *Enterobacteriaceae* (*24*). Furthermore, the almost exclusive restriction of H-NS binding to AT-rich regions and the maintenance of nucleoid domain structure despite the absence of H-NS (*25*, *26*) suggest that the primary role of H-NS is to silence foreign DNA. A degenerate recognition sequence and the ability to polymerize along and bridge adjacent stretches of DNA ideally suit H-NS for this role and likely account for many of its reported functions, including alteration of recombination events and local supercoiling (*1*, *27*, *28*).

The genome-wide average GC content of various bacterial genera can vary from 25 to 75%, and attempts have been made to explain why bacterial genomes maintain their distinctive GC bias (*29*). The reason for the relative AT richness of horizontally transferred DNA in enteric bacteria has also been enigmatic. We posit that the cell's ability to discriminate between its own DNA and foreign DNA on the basis of differences in GC content can provide a fitness advantage and that xenogeneic silencing has likely shaped bacterial genomes by facilitating the acquisition and preservation of AT-rich DNA. Interestingly, some AT-rich bacteriophages, pathogenicity islands, and mobile genetic elements encode H-NS antagonists (*1*, *30*), indicating that "selfish" genetic elements have evolved countermechanisms to escape H-NS–mediated silencing. Further work will be required to determine whether additional mechanisms of xenogeneic silencing exist in other bacterial species.

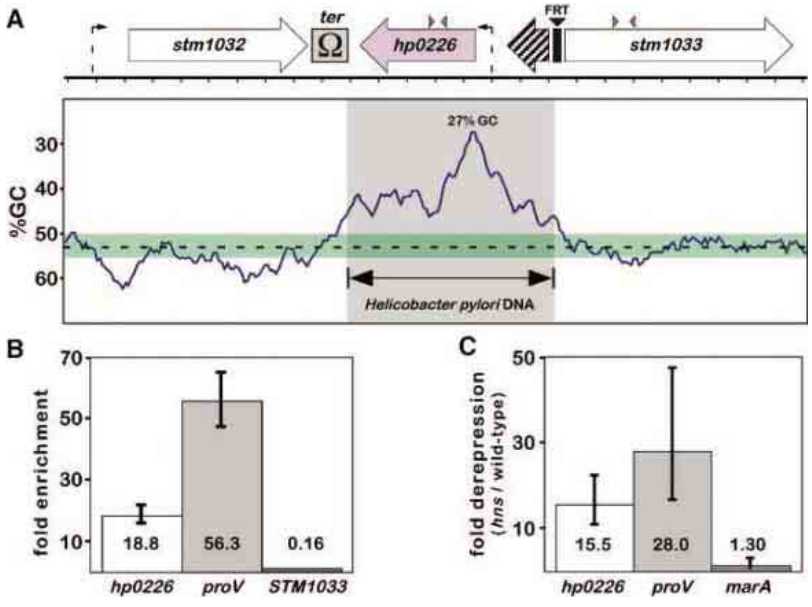

Fig. 3. H-NS binds and silences an experimentally introduced AT-rich foreign gene. (**A**) Region of the *Salmonella* chromosome into which *hp0226*, from *Helicobacter pylori*, was recombined (*6*). Q-PCR primers for *hp0226* and *stm1033* are designated with orange triangles. The 3′ fragment of *hp0227* (hatched arrow) and Flp recombinase target site (FRT) are indicated. Putative *hp0226* and *stm1032* promoters are indicated (thin dashed arrows). Lower panel is the moving average (300-nucleotide window) of the regional GC content. Area corresponding to the *Helicobacter* sequence is shaded in gray. A transcriptional terminator (*ter*) was included to prevent read-through from the promoter upstream of the *stm1032* gene into the *Helicobacter* sequence. The average GC content of *S*. Typhimurium is indicated (dashed line), and the region ± 2.5% from the average is shaded in blue. (**B**) ChIP analysis of H-NS–DNA complexes. Data are shown as fold enrichment normalized to the *marA* gene, which does not interact with H-NS (*6*). H-NS coprecipitates with *proV* (positive control) and *hp0226* but not *stm1033*. Error bars encompass a 95% CI. (**C**) H-NS–mediated silencing of *hp0226* and *proV* but not *marA* (negative control). Reverse transcriptase/Q-PCR analysis of transcript levels in *hns* and isogenic wild-type *Salmonella* normalized to mRNA of the *gyrB* housekeeping gene (*6*). Fold derepression is the amount of transcript in the *hns* mutant divided by wild-type transcript levels. Error bars encompass a 95% CI.

References and Notes

1. C. J. Dorman, *Nat. Rev. Microbiol.* **2**, 391 (2004).
2. R. T. Dame *et al.*, *J. Bacteriol.* **187**, 1845 (2005).
3. R. Amit, A. B. Oppenheim, J. Stavans, *Biophys. J.* **84**, 2467 (2003).
4. M. Goransson *et al.*, *Nature* **344**, 682 (1990).
5. T. Ferenci, *Trends Microbiol.* **11**, 457 (2003).
6. Materials and methods are available as supporting material on *Science* Online.
7. A. E. Hromockyj, S. C. Tucker, A. T. Maurelli, *Mol. Microbiol.* **6**, 2113 (1992).
8. M. McClelland *et al.*, *Nature* **413**, 852 (2001).
9. J. Yang, M. Tauschek, R. Strugnell, R. M. Robins-Browne, *Microbiology* **151**, 1199 (2005).
10. F. Beltrametti, A. U. Kresse, C. A. Guzman, *J. Bacteriol.* **181**, 3409 (1999).
11. M. Westermark, J. Oscarsson, Y. Mizunoe, J. Urbonaviciene, B. E. Uhlin, *J. Bacteriol.* **182**, 6347 (2000).
12. V. H. Bustamante, F. J. Santana, E. Calva, J. L. Puente, *Mol. Microbiol.* **39**, 664 (2001).
13. C. J. Dorman, S. McKenna, C. Beloin, *Int. J. Med. Microbiol.* **291**, 89 (2001).
14. C. Beloin, C. J. Dorman, *Mol. Microbiol.* **47**, 825 (2003).
15. H. H. Krishnan, A. Ghosh, K. Paul, R. Chowdhury, *Infect. Immun.* **72**, 3961 (2004).
16. C. Coker, O. O. Bakare, H. L. Mobley, *J. Bacteriol.* **182**, 2649 (2000).
17. A. K. Heroven, G. Nagel, H. J. Tran, S. Parr, P. Dersch, *Mol. Microbiol.* **53**, 871 (2004).
18. W. Nasser, S. Reverchon, *Mol. Microbiol.* **43**, 733 (2002).
19. N. R. Wyborn *et al.*, *J. Bacteriol.* **186**, 1620 (2004).
20. K. R. Haack, C. L. Robinson, K. J. Miller, J. W. Fowlkes, J. L. Mellies, *Infect. Immun.* **71**, 384 (2003).
21. K. Forsman, B. Sonden, M. Goransson, B. E. Uhlin, *Proc. Natl. Acad. Sci. U.S.A.* **89**, 9880 (1992).
22. R. R. Yu, V. J. DiRita, *Mol. Microbiol.* **43**, 119 (2002).
23. D. Zilberman, S. Henikoff, *Genome Biol.* **5**, 249 (2004).
24. P. Bertin *et al.*, *Mol. Microbiol.* **31**, 319 (1999).
25. R. Brunetti, G. Prosseda, E. Beghetto, B. Colonna, G. Micheli, *Biochimie* **83**, 873 (2001).
26. S. B. Zimmerman, *J. Struct. Biol.* **153**, 160 (2006).
27. C. D. Hardy, N. R. Cozzarelli, *Mol. Microbiol.* **57**, 1636 (2005).
28. A. E. Tupper *et al.*, *EMBO J.* **13**, 258 (1994).
29. S. J. Lee, J. R. Mortimer, D. R. Forsdyke, *Appl. Bioinformatics* **3**, 219 (2004).
30. H. S. Williamson, A. Free, *Mol. Microbiol.* **55**, 808 (2005).

31. We thank B. Marzolf and K. Dimitrov for assistance with microarray analysis, P. Lewis for technical assistance, N. Salama for *H. pylori* constructs, C. Santiviago for assistance with Webarray, and A. Richardson for useful discussions. Research was supported by the NIH (AI034829, AI052237, and AI057733 to M.M.; AI049417 to H.R.; AI48622 to S.J.L.; and AI39557 to F.C.F.). W.W.N. was supported in part by a fellowship from the Damon Runyon Cancer Research Foundation (DRG1588). Microarray data were deposited into the Gene Expression Omnibus (accession numbers GSE4879, GSE4881, and GSE4931).

Supporting Online Material

www.sciencemag.org/cgi/content/full/1128794/DC1
Materials and Methods
Figs. S1 to S5
Table S1 and S2

17 April 2006; accepted 30 May 2006
Published online 8 June 2006;
10.1126/science.1128794
Include this information when citing this paper.

Programmable Syringe Pumps

With new high-precision, fully programmable syringe pumps, up to 100 pumps can be programmed to work together for dual infusion/withdrawal, push/pull pumping, and much more. The pumps can be automated with or without a separate computer. The pumps can be programmed with up to 41 pumping phases to allow researchers to set dispensing volumes, insert pauses, and coordinate with external signals.

Stoelting For information 630-860-9700 www.stoeltingco.com

siRNA Transfection Reagent

A new-generation small-interfering RNA (siRNA) transfection reagent achieves more than 90 percent silencing efficiency at 1nM siRNA or less in a wide variety of adherent and primary cells. Compatible with serum and antibiotics, INTERFERin siRNA Transfection Reagent enables researchers to avoid the unwanted toxic and off-target effects that often occur when transfecting siRNA at higher concentrations. The reagent has even been shown effective at subnanomolar siRNA concentrations.

Polyplus transfection For information 760-481-4918 www.polyplus-transfection.com

Brain Tissue Blots

These unique blots can be used to confirm specific protein localization in brain without the need for time-consuming dissections and sample preparation with brain tissue protein immunoblots. The blots are prepared by carefully dissecting anatomically and functionally distinct regions of adult human, primate, rat, and mouse brain. Each blot has samples of frontal cortex, posterior cortex, cerebellum, hippocampus, olfactory bulb, striatum, thalamus, midbrain, entorhinal cortex (except human), pons, medulla, spinal cord, and total brain.

G Biosciences/Genotech For information 314-991-6034 www.GBiosciences.com

Polymer-HRP Detection System

The Super Sensitive Polymer-HRP Detection System represents state-of-the-art technology in the visualization of antigen–antibody binding reactions. It facilitates the production of high-quality staining results with minimum background, especially in tissue sections that have a lot of endogenous biotin. This method is used in lieu of streptavidin–biotin, thus eliminating background staining that can be caused by endogenous biotin. The system features a proprietary non-biotin polymeric technology made up of two major components: a post-antibody enhancing reagent (Super Enhancer Reagent) and polymerized horseradish peroxidase (HRP) conjugated to anti-mouse and anti-rabbit antibodies (Poly-HRP Reagent). In brief, tissue sections are incubated with rabbit or mouse primary antibody, which are subsequently treated with Super Enhancer Reagent, followed by a Poly-HRP Reagent, before the addition of a chromogen.

Biogenex For information 800-421-4149 www.biogenex.com

Engineering Software

WinA&D 5.0 is an engineering tool for system analysis, requirements management, software models, code generation, re-engineering, and scriptable project reports. The new release adds system models, simulation, and dynamic charts to its suite of software engineering capabilities. Other enhancements include a project scrapbook. The software presents an integrated solution to model dynamic systems as causal loop diagrams, parameterize a model with data and equations, run time simulations, and present system behavior with live charts, graphs, and tables. Data files can provide input data to models or capture output results. It runs on Windows 95 through XP.

Excel Software For information 505-771-3719 www.excelsoftware.com

Monoclonal Antibodies

A series of monoclonal antibodies are available that stain paraffin tissue sections. The Anti-Bcl-2 (Clone bcl-2/100) reacts with Bcl-2 alpha oncoprotein, which is one of the two proteins coded for by the bcl-2 oncogene. Bcl-2 is an integral inner mitochondrial membrane protein, which is frequently overexpressed in lymphoid malignancies. The Anti-Inhibin alpha (Clone R1) stains the cytoplasm of Sertoli cells in testes and granulosa cells in ovaries. Inhibins are dimeric gonadal peptide hormones that negatively regulate pituitary follicle-stimulating hormone synthesis and secretion and belong to the transforming growth factor beta family. The Anti-CDX-2 (Clone CDX2-88) is an antibody to human CDX-2, a member of the caudal-related homeobox family that is an intestine-specific transcription factor that regulates both proliferation and differentiation in intestinal epithelial cells. The Anti-Cytokeratin 7 (Clone OV-TL 12/30) recognizes specific subtypes of adenocarcinomas and can be used to differentiate between cytokeratin 7-positive tissues such as ovarian and transitional cell carcinomas and cytokeratin 7-negative tissues such as carcinomas of the gastrointestinal tract and prostate. The Anti-Cytokeratin Cocktail (Clones AE1 and AE3) stains cytokeratins in epithelial cells.

Biogenex For information 800-421-4149 www.biogenex.com

Newly offered instrumentation, apparatus, and laboratory materials of interest to researchers in all disciplines in academic, industrial, and government organizations are featured in this space. Emphasis is given to purpose, chief characteristics, and availability of products and materials. Endorsement by *Science* or AAAS of any products or materials mentioned is not implied. Additional information may be obtained from the manufacturer or supplier by visiting www.science.labvelocity.com on the Web, where you can request that the information be sent to you by e-mail, fax, mail, or telephone.

ScienceCareers.org

Classified Advertising

For full advertising details, go to **www.sciencecareers.org** and click on **For Advertisers,** or call one of our representatives.

United States & Canada

E-mail: advertise@sciencecareers.org
Fax: 202-289-6742

JILL DOWNING
(CT, DE, DC, FL, GA, MD, ME, MA, NH, NJ, NY, NC, PA, RI, SC, VT, VA)
Phone: 631-580-2445

KRISTINE VON ZEDLITZ
(AK, AZ, CA, CO, HI, ID, IA, KS, MT, NE, NV, NM, ND, OR, SD, TX, UT, WA, WY)
Phone: 415-956-2531

KATHLEEN CLARK
Employment: AR, IL, LA, MN, MO, OK, WI
Canada; Graduate Programs; Meetings & Announcements (U.S., Canada, Caribbean, Central and South America)
Phone: 510-271-8349

DARYL ANDERSON
(AL, IN, KY, MI, MS, OH, TN, WV)
Phone: 202-326-6543

GABRIELLE BOGUSLAWSKI
(U.S. Recruitment Advertising Sales Director)
Phone: 718-491-1607

Europe & International

E-mail: ads@science-int.co.uk
Fax: +44 (0) 1223-326-532

TRACY HOLMES
Phone: +44 (0) 1223-326-525

HELEN MORONEY
Phone: +44 (0) 1223-326-528

CHRISTINA HARRISON
Phone: +44 (0) 1223-326-510

SVITLANA BARNES
Phone: +44 (0) 1223-326-527

JASON HANNAFORD
Phone: +81 (0) 52-789-1860

To subscribe to *Science*:
In U.S./Canada call 202-326-6417 or 1-800-731-4939
In the rest of the world call +44 (0) 1223-326-515

Science makes every effort to screen its ads for offensive and/or discriminatory language in accordance with U.S. and non-U.S. law. Since we are an international journal, you may see ads from non-U.S. countries that request applications from specific demographic groups. Since U.S. law does not apply to other countries we try to accommodate recruiting practices of other countries. However, we encourage our readers to alert us to any ads that they feel are discriminatory or offensive.

ScienceCareers.org
We know science AAAS

POSITIONS OPEN

CHAIR
Department of Physiology and Pharmacology

The Northeastern Ohio Universities College of Medicine is seeking outstanding candidates and nominees for the position of Chair of the Department of Physiology and Pharmacology. We seek an accomplished researcher, an innovative educator, and an experienced administrator who will provide visionary leadership to oversee the growth of the Department. Desirable qualifications include documented leadership, previous administrative experience, experience in graduate and medical education, a successful history of external funding, experience with program development in research and education, evidence of strong communication and organizational skills, and evidence of commitment to working with and supporting a diverse student and faculty population.

The Chair will be responsible for the continued growth of the Department by filling several faculty slots. The Chair should be familiar with an integrated medical curriculum and be prepared to support the educational programs of the recently approved College of Pharmacy with a charter class beginning in the fall of 2007. The Department is housed in excellent facilities with access to numerous core laboratories and affords the opportunity for collaborative clinical and public health research throughout our consortium of 18 affiliated hospitals and two public health departments. The Department's current research area is cardiovascular and pulmonary physiology and pharmacology with a focus on G-protein coupled receptor signaling processes. Additional information about the Department is available at **website: http://www.neoucom.edu/audience/about/departments/PhysioPharma.**

The position will be available beginning January 1, 2007. Salary and startup resources will be competitive and commensurate with experience and qualifications. Candidates must possess a Ph.D., M.D., or equivalent and must be qualified for appointment at the rank of full professor. This is a fully funded position within the College of Medicine that reports directly to the Dean. Interested candidates should submit (1) curriculum vitae; (2) statement of research accomplishments, current interests and future direction; (3) statement of teaching experience and philosophy; (4) summary of administrative experience and philosophy; and (5) names and addresses of five references to: **Physiology and Pharmacology Chair Search Committee, Northeastern Ohio Universities College of Medicine, Office of Human Resources, 4209 State Route 44, P.O. Box 95, Rootstown, Ohio 44272;** or e-mail to **e-mail: jobs@neoucom.edu.** Review of applications will begin immediately, and continue until the position is filled.

The College's dedication to excellence is complemented by its strong commitment to building and sustaining a culturally diverse academic community. Individuals from historically underrepresented groups are encouraged to apply. Northeastern Ohio Universities College of Medicine is an Equal Opportunity Employer and Educator.

POSTDOCTORAL POSITIONS
in Cancer Research
University of Nebraska Medical Center
Eppley Cancer Center
Biochemistry, Cellular, Molecular and Structural Biology, Genetics, Genomics, Immunology

Postdoctoral positions in all aspects of cancer biology, funded by an NCI training grant, are available for *U.S. citizens or permanent residents.* Postdoctoral Fellows in our program receive broad-based training in cancer biology using state-of-the-art facilities. Details regarding faculty research interests can be found at our website **(website: http://www.unmc.edu/Eppley/crgpfaculty.htm).** Applications can be submitted online to position 0587 at **website: https://jobs.unmc.edu.** Additional information can be obtained by contacting **Matt Winfrey (e-mail: winfreym@unmc.edu).**

The University of Nebraska Medical Center is an Equal Opportunity Employer. Minorities are particularly encouraged to apply.

POSITIONS OPEN

CELL BIOLOGIST

Slippery Rock University of Pennsylvania invites applications for a Tenure-Track position in the Department of Biology beginning August 2007.

Teaching responsibilities: Introductory biology courses designed for the liberal studies program, advanced course in cell biology, and contribution to other courses taken by biology majors.

Other duties/expectations: Commitment to excellence in teaching in a liberal arts setting, establishment of a productive research program in the candidate's area of expertise that may involve undergraduates, recognition of Department goals and stated standards of performance, timely execution of work assignments, and contribution to Department, College and University committees.

Requirements: Earned Ph.D. in a biological science and undergraduate teaching experience; evidence of teaching effectiveness, professional competence and ability to work productively with students and colleagues; successful performance in an on-campus interview, including teaching and research presentations.

Send letters of interest, resume, statement of academic philosophy and research goals, teaching evaluations, graduate and undergraduate transcripts (official transcripts will be needed before hiring), and three letters from professional references to: **Dr. Carolyn Steglich, Cell Biologist Search Chair, Department of Biology, Slippery Rock University, Slippery Rock, PA 16057. Telephone: 724-738-2023, fax: 724-738-4782, e-mail: carolyn.steglich@sru.edu**.

No electronic submissions will be accepted. Review of applications will begin September 15, 2006, and will continue until the position is filled. Visit us on our web page at **website: http://www.sru.edu.**

Slippery Rock University of Pennsylvania is a member of the state system of higher education and is an Affirmative Action/Equal Opportunity Employer.

FACULTY POSITION
Marine Ecology

A tenure-track position in the Department of Biological Sciences at California State University, Long Beach (CSULB), starting fall 2007; **ASSISTANT PROFESSOR** preferred; **ASSOCIATE PROFESSOR** considered for exceptional candidates. Required: Ph.D. in biology, marine biology, or marine science with research experience in coastal marine community ecology; record of published research; ability to develop an externally funded research program involving students; commitment to teach an undergraduate course in marine ecology, general ecology or biostatistics, and a graduate seminar; ability to communicate effectively with an ethnically and culturally diverse campus community. Submit hardcopy of application that includes a statement of research and teaching interests, curriculum vitae (with e-mail address), reprints of two relevant publications, and three letters of recommendation sent to: **Marine Ecology Search, Department of Biological Sciences, California State University, 1250 Bellflower Boulevard, Long Beach, CA 90840-3702** by September 1, 2006. *CSULB is an Equal Opportunity Employer committed to excellence through diversity, and takes pride in its multicultural environment.*

RESEARCH SCIENTISTS/ POSTDOCTORAL ASSOCIATES
United States and China

HumanZyme is a biotech company that develops, manufactures, and markets bioactive recombinant human kinases from human cells. We are seeking highly motivated, creative Research Scientists or Postdoctoral Associates to complement the company's existing research and development team in Chicago or China. A Ph.D. and a minimum of two years of experience in mammalian cell culture or kinase biochemistry are required, demonstrated through a proven track record in peer-reviewed publications. Excellent communication and team skills are highly desirable. Proficiency in Chinese is preferred for positions in China. Send curriculum vitae and three names of references to **e-mail: info@humanzyme.com.**

Positions @ NIH
THE NATIONAL INSTITUTES OF HEALTH

Staff Scientist, Clinical Pharmacology Research Core, Medical Oncology Branch

With nation-wide responsibility for improving the health and well being of all Americans, The Department of Health and Human Services oversees the biomedical research programs of the National Institutes of Health and those of NIH's research Institutes.

A Staff Scientist position is now available in the Clinical Pharmacology Research Core (CPRC), Medical Oncology Branch (MOB) of the Center for Cancer Research (CCR), National Cancer Institute (NCI), National Institute of Health (NIH), Department of Health and Human Services (DHHS). This position will focus on pharmacological aspects of clinical trials, including pharmacokinetic and pharmacogenetic studies. Leadership in clinical pharmacology is required. Expertise in pharmacokinetics, including bioanalytical techniques, modeling of pharmacokinetic data, data analysis and study design, and pharmacogenetics is required.

The CCR provides an environment in which interdisciplinary and multidisciplinary translational research is encouraged and supported and uses a disease-based translational research matrix to identify the intersection of research areas and particular cancers to identify programmatic efforts. These specific program areas will enhance and enable collaborations, interdisciplinary and multidisciplinary research and a dynamic translational research process in which discovery, development and delivery flow seamlessly.

The successful candidate must have a Ph.D., Pharm.D., or MD degree (or equivalent).

The NCI offers competitive salaries along with an excellent work environment.

Interested applicants should mail a CV, brief description of research interests and experience, and contact information for three references by **August 31, 2006** to: **Dr. William Douglas Figg, Medical Oncology Branch, Center for Cancer Research, National Cancer Institute, Building 10, Room 5A01, 9000 Rockville Pike, Building 10, Room 5A01, Bethesda, MD, 20892** or e-mail to: **wdfigg@helix.nih.gov**

Laboratory of Molecular Genetics
Research Triangle Park, North Carolina

POSTDOCTORAL FELLOWSHIP IN MECHANISMS OF MUTAGENESIS

Our laboratory investigates the various mechanisms by which organisms produce mutations. We pursue these mechanisms by a combination of genetical and biochemical approaches using the bacterium E. coli as a model system. Specifically, we are aiming to understand the factors that determine the high-fidelity of chromosomal replication by Pol III holoenzyme complex (HE). In this project we are studying: (i) mutator mutants of E. coli whose defect is associated with the polymerase accessory factors, such as newly isolated mutator mutants of the dnaX gene; (ii) The role(s) of accessory DNA polymerases in determining DNA replication fidelity; (iii) the relative contributions of leading and lagging strand DNA replication; and (iv) the role of deoxynucleoside triphosphate (dNTP) pools in mutagenesis. A second main area of research is the mechanism of mutagenesis induced by mutagenic base analogs, including the activation to dNTP form, incorporation into DNA, and analog-specific repair and detoxification mechanisms. Of particular interest is our discovery of a novel detoxification mechanism for N-hydroxylated base analogs, which has been found to be dependent on the molybdenum cofactor.

Applicants must have a Ph.D., M.D. or equivalent and less than five years of postdoctoral experience.

APPLY TO: **Dr. Roel Schaaper, Laboratory of Molecular Genetics, DIR, National Institute of Environmental Health Sciences, Maildrop E3-01, PO. Box 12233, Research Triangle Park, NC 27709-2233, Email: schaaper@niehs.nih.gov**

National Institute of General Medical Sciences
Office of Scientific Review
SCIENTIFIC REVIEW ADMINISTRATOR

The National Institute of General Medical Sciences (NIGMS), a major research component of the National Institutes of Health (NIH) and the Department of Health and Human Services (DHHS), is seeking applications from exceptional scientists to serve as **Scientific Review Administrator in the Office of Scientific Review**. The individual selected will organize and manage the comprehensive scientific and technical merit review of applications for research programs and/or research training and career development grants through interaction with established scientists in a variety of fields. Scientific Review Administrators are responsible for assuring the fairness and consistency of the scientific peer review process, and for providing technical guidance on peer review policies and procedures and review criteria to applicants, reviewers, and Institute staff.

Qualifications: The successful individual will possess a Ph.D., M.D. or equivalent degree in a field relevant to the position, have research experience in biochemistry, cell and molecular biology, pharmacology, or biophysics (or a closely related area), an in-depth knowledge of biological processes, leadership and managerial skills, and strong oral and written communication skills. Applicants must be U.S. citizens.

Salary: The current salary range is $65,048 - $118,828, depending on experience and accomplishments; a full Civil Service package of benefits (including retirement, health, life and long term care insurance, Thrift Savings Plan participation, etc.) is available.

How to Apply: Position requirements and detailed application procedures are provided in vacancy announcement **NIGMS-06-129154**, which can be obtained by accessing the NIGMS website at **http://www.nigms.nih.gov**. All applications and supplemental information must be received no later than **August 18, 2006**. For additional information, contact **Ms. Eric Bandak at (301) 594-2035**.

WWW.NIH.GOV

Director, Office of Human Genetics and Genomic Resources
NATIONAL INSTITUTE OF MENTAL HEALTH
NATIONAL INSTITUTES OF HEALTH

The National Institute of Mental Health (NIMH) seeks candidates for the position of Director, Office of Human Genetics and Genomic Resources. The Director will provide vision and leadership for NIMH extramural funding programs in this research area. With the completion of the Human Genome Project and accompanying advances in the development of new genetic tools and technologies, there are unprecedented opportunities to discover genes that produce vulnerability to mental disorders. The mission of the Office is to accelerate the discovery of such genes and characterize the genetic bases of disorders directly relevant to NIMH's mission, through the application of cutting edge genomic-based approaches and methods. The research supported by this Office will accelerate the development of pharmacogenomics, diagnostics, therapeutics and effective prevention strategies for mental disorders. The Director will develop new research initiatives, oversee the Office's portfolio of extramural research awards, and interact with researchers and related programs at NIMH, NIH, and other funding agencies (both public and private, in the U.S. and abroad). More information on the Office can be viewed at **http://www.nimh.nih.gov/dnbbs/7g-gr.cfm**. Candidates must be a U.S. citizen and have an M.D., Ph.D., or equivalent-level degree and considerable research experience in human genetics. Preference will be given to candidates with experience in research management. Experience in genomics-based genotyping and molecular or statistical genetic analytic methods is highly desirable. The ability to work both independently and collaboratively is required. Strong communication, writing and organizational skills are also required. The position will be filled on a permanent basis. Salary will be commensurate with experience. Send CV, bibliography and the names of 4 references by email to **Dr. Kevin Quinn at kquinn@mail.nih.gov (Tel: 301-443-3563)**. Applications will be accepted on a continuous basis until the position is filled. With nationwide responsibility for improving the health and well being of all Americans, the Department of Health & Human Services oversees the biomedical research programs of the National Institutes of Health **(http://www.os.dhhs.gov)**

Department of Health and Human Services
National Institutes of Health
Director, National Center for Research Resources

The Office of the Director, National Institutes of Health (NIH) in Bethesda, Maryland, is seeking applications from exceptional candidates for the position of Director, National Center for Research Resources (NCRR). The Director, NCRR, will also serve as the NIH Associate Director for Clinical Research (Extramural). NCRR, with a staff of approximately 100 employees and a $1 billion budget, is the focal point at NIH for biomedical, clinical and translational research resources. The incumbent serves as a principal advisor to the Director, NIH; participates in discussions relative to the development of major policy decisions affecting biomedical, clinical and translational research resources; provides advice and consultation to NIH components, advisory councils and grantee organizations and institutions; and assures that effective administrative procedures are established so that program operations and obligations of government funds and other resources are rendered consistent with statutory and regulatory requirements and within limitations imposed by the Department of Health and Human Services (DHHS) and Executive Branch policies. Applicants must possess a Ph.D., M.D., or a comparable doctorate degree in the health sciences field plus senior level scientific experience and knowledge of biomedical, clinical and/or translational research programs in one or more health science areas. Salary is commensurate with experience and a full package of benefits (including retirement, health, life, long term care insurance, Thrift Savings Plan participation, etc.) is available. A detailed vacancy announcement, along with mandatory qualifications and application procedures, can be obtained via the NIH Home Page at: http://www.jobs.nih.gov under the Senior Job Openings section. Dr. Stephen Katz, Director, National Institute of Arthritis and Musculoskeletal and Skin Diseases, and Dr. David Schwartz, Director, National Institute of Environmental Health Sciences, will be serving as co-chairs of the search committee. Questions on application procedures may be addressed to **Ms. Regina Reiter at ReiterR@od.nih.gov** or discussed with **Ms. Reiter by calling 301-402-1130**. **Applications must be received by close of business July 31, 2006.**

UNIVERSITY OF OXFORD

Department of Chemistry,
Inorganic Chemistry Laboratory

Technical Manager at the Multidisciplinary Research Centre for Advanced EPR

Academic-Related Research Staff Grade RSII
Salary in the range of £27,929 - £36,959 p.a.

(subject to review from 1st August 2006 as part of the implementation of the National Framework Agreement for staff in higher education)

Reference DH06017/CRT

You are invited to apply for the position of an EPR Technical Manager at the newly established Multidisciplinary Research Centre for Advanced EPR at the University of Oxford. You will organise and overlook the smooth technical day-to-day running of this facility. You will support the centre's technical, computational and experimental developments and research programme through strong interactions with all research groups (with interest ranging from quantum computing to biomedical applications). The post is available from 1st October 2006 for 1 year initially with the possibility of an additional 4 years. The starting salary is dependent on experience.

Applications Manager at the Multidisciplinary Research Centre for Advanced EPR

Academic-Related Research Staff Grade RSIA
Salary in the range of £20, 044 - £26,470 p.a.

(subject to review from 1 August 2006 as part of the implementation of the National Framework Agreement for staff in higher education)

Reference DH06018/CRT

You are invited to apply for the position of an Applications Manager at the newly established Multidisciplinary Research Centre for Advanced EPR at the University of Oxford. You will be involved in the organisation and day-to-day running of the EPR facility whilst maintaining a lively interest in your own research as well collaborative activities with groups interested in EPR applications ranging from quantum computing to biology. The post is available from 1 October 2006 for 1 year initially with the possibility of an additional 4 years. The starting salary is dependent on experience.

Further particulars for both posts are available from the Administrator, Inorganic Chemistry Laboratory, South Parks Road, Oxford OX1 3QR, or by e-mail from rita.higgs@chem.ox.ac.uk Informal enquiries may be made to Dr C R Timmel, e-mail: christiane.timmel@chem.ox.ac.uk

Four copies of applications in the form of a letter, showing how you fulfil the selection criteria, CV and the names and addresses of two academic referees, should be sent (hard copy only) to The Administrator, (quoting reference), University of Oxford, Inorganic Chemistry Laboratory, South Parks Road, Oxford OX1 3QR, by the closing date of 6th August 2006. At least one of these referees should be your current line manager or supervisor, who may be contacted prior to interview.

The University is an Equal Opportunities Employer.

www.ox.ac.uk/jobs

DEPARTMENT OF THE NAVY
ONR
Science & Technology

The Office of Naval Research is seeking qualified individuals to manage sponsored basic/applied research, and advanced technology development programs and projects. The sponsored efforts are conducted principally at U.S. universities and industry or Federal laboratories. These are Federal Civil Service positions at the GS-13/14/15 level ($77,353 - $139,774) depending on individual qualifications.

Program Officer, Chemical/Synthetic Biologist (Chemical Biologist)

Requires knowledge and experience in the broad areas of Bioprocessing, Molecular Biology, Molecular Biomimetics, Biosynthesis and Biotechnology including, but not limited to, genetic and pathway engineering in bacteria, plants or other organisms to yield cost-effective, renewable synthesis of high-value Naval materials (e.g., energetic materials, blood clotting factors, or biopolymers); or to enhance sustainable bioenergy harvesting.

Program Officer, Cognitive Science (Psychologist)

Requires knowledge and experience in the broad area of cognitive science including, but not limited to, the computational modeling of complex human cognition, psychology of human learning and performance, interdisciplinary cognitive science, training technology, and cognitive engineering of human-system interaction.

For information on qualifications and how to apply, see the Job Announcements at our website http://www.onr.navy.mil/hr. Applications must be submitted by close of business or postmarked as of the closing date noted in the job announcement. For technical information contact us at hrdeptjobs@onr.navy.mil".

U.S. CITIZENSHIP REQUIRED • AN EQUAL OPPORTUNITY EMPLOYER

Developmental Medicine Center Lab of Cognitive Neuroscience

Developmental Medicine Center (DMC) Children's Hospital, Boston

Harvard Medical School

Assistant Professor

The Developmental Medicine Center Lab of Cognitive Neuroscience at Children's Hospital, Boston is recruiting an Assistant Professor. The DMC is one of the largest clinical centers for the diagnosis and treatment of developmental disorders in the US, and is involved in clinical care and research as well as the training of pediatricians and psychologists. The Developmental Medicine Center Lab of Cognitive Neuroscience is the newly formed research center for the DMC and is headed by Charles A. Nelson III, Ph.D. The candidate must have expertise in cognitive neuroscience, with a particular interest in neurodevelopmental disorders. Individuals with expertise in functional or structural MRI would be particularly welcome, although other imaging modalities would also be seriously considered. The candidate must be an MD or Ph.D. who will conduct his/her own research in this field. The successful candidate will have an academic appointment as Assistant Professor. Applications should describe the candidate's research interests.

Please enclose a CV and representative reprints, and arrange to have three letters of recommendation sent to the search committee. Send applications to:

Search Committee
DMC, Fegan 10
Children's Hospital, Boston
300 Longwood Ave.
Boston, MA 02115

Qualified women and minority candidates are especially encouraged to apply. Children's Hospital, Boston is an Affirmative Action/ Equal Opportunity Employer.

MICROBIOLOGIST: ASSISTANT PROFESSOR

Tenure Track; Begin 1/07

University of the Sciences' Dept. of Biological Sciences announces a new, 10-month faculty position. Located in Philadelphia, the dept. offers interdisciplinary bioinformatics BS & MS programs, and is housed in a newly opened Science & Technology Center providing significant opportunity for research. Selected candidate will teach courses in clinical microbiology & microbial physiology, as well as develop an extramurally funded research program. Qualifications include: a Ph.D. or equivalent; postdoctoral training in microbiology investigations; hands-on knowledge of methodologies exploring genomic, proteomic, &/or biophysical research; & a commitment to education, research, & service.

Please submit CV, letter of application, position statements that address teaching philosophy & research interests, and at least 3 references to: **Dr. James Johnson, Chair, Microbiology Search Committee, Dept of Biological Sciences, University of the Sciences in Philadelphia, 600 S. 43rd St., Philadelphia, PA 19104. Email: j.johnson@usip.edu; Tel (215) 596-8919.** Applicant materials received by August 15, 2006 will receive highest consideration. Applicants may also be considered concurrently for the adjunct faculty position (Microbial Physiology) for fall semester 2006, but should abide by the submission requirements for that position separately.
AA/EOE

Celebrating 185 YEARS USP 1821–2006

The Hong Kong University of Science and Technology

Tenure-Track Faculty Position in Analytical Chemistry

The Department of Chemistry invites applications for a tenure-track Assistant Professorship position in the general area of analytical chemistry.

The candidate is expected to develop a vigorous research program in analytical chemistry with teaching responsibilities at both undergraduate and postgraduate levels.

Applicants should have a PhD degree and postdoctoral experience. Starting salary will be commensurate with qualifications and experience. Fringe benefits including medical/dental benefits and annual leave will be provided. Housing will also be provided where applicable.

Applications should be sent with curriculum vitae, statement on research interests and teaching philosophy, and names and addresses (including e-mail addresses) of three referees to: Search Committee, Department of Chemistry, The Hong Kong University of Science and Technology, Clear Water Bay, Hong Kong. (Fax: (852) 35211486 or e-mail : chdoris@ust.hk). Review of applications will start on 1 November 2006, and will continue until the position is filled. Additional information can be found at **http://www.ust.hk.**

(Information provided by applicants will be used for recruitment and other employment-related purposes.)

University of Heidelberg

The **Faculty of Clinical Medicine Mannheim, University of Heidelberg** offers the position of a

Full Professor (W3) of Biochemistry

The Full Professorship will be a tenured position. Given a distinguished record of qualifications in all areas of biochemistry and physiological chemistry, the successful candidate will be appointed as a Director (chairperson) at the newly founded Center for Biomedicine and Medical Technology Mannheim (CBTM). Regarding the implementation of the preclinical medical studies at the faculty (MaReCuM), the successful candidate will be responsible for developing the biochemical parts of the restructured organ- and topic-centered teaching modules. As an independent principle investigator, the candidate will have special responsibility for enforcing the research mission of the Faculty with a focus on the biochemistry of cell-cell interactions or signal transduction in vascular biology, inflammation or cancer. He/she is expected to actively take part in established and developing research programs of the Faculty in the field of molecular oncology or vascular biology such as the European Graduate School "Vascular Medicine" (EU-GRK880), the Graduate School "Molecular Imaging" (GRK 886) and the Cooperative Transregio Research Grant "Vascular Differentiation and Remodeling" (TRR 23). He/she is furthermore expected to obtain extramural funding by grant applications to non-university funding institutions.

and a

Full Professor (W3) of Cellular and Molecular Biology

The Full Professorship will be a tenured position. Given a distinguished record of qualifications in all areas of Cellular and Molecular Biology, the successful candidate will be appointed as a Director (chairperson) at the newly founded Center for Biomedicine and Medical Technology Mannheim (CBTM). Regarding the implementation of the preclinical medical studies at the faculty (MaReCuM), the successful candidate will be responsible for organizing and developing the anatomical parts of the restructured organ-centered teaching modules. In this respect, he/she will be supported by a novel professorship for Anatomy and Developmental Biology at the CBTM and by a novel professorship for Microscopic Anatomy and Histopathology at the Institute of Pathology. As an independent principle investigator, the candidate will have special responsibility for enforcing the research mission of the Faculty with a focus on the cellular and molecular biology of cancer, esp. initiation and metastasis. He/she is expected to closely collaborate with the joint Aventis Endowed Chair of Vascular Biology and Tumor Angiogenesis of the Faculty and the German Cancer Research Center (DKFZ) Heidelberg. He/she should actively take part in established and developing research programs of the Faculty in the field of molecular oncology or vascular biology such as the European Graduate School "Vascular Medicine" (EU-GRK880), the Graduate School "Molecular Imaging" (GRK 886) and the Cooperative Transregio Research Grant "Vascular Differentiation and Remodeling" (TRR 23). He/she is furthermore expected to obtain extramural funding by grant applications to non-university funding institutions.

The successful candidate should have high ranking, internationally acknowledged academic qualifications commensurate with the rank of a full professor with life-time tenure including a PhD or MD/PhD, a distinguished record of original research, mentoring and teaching skills, administrative experience and an understanding of departmental financing in universities. The candidate should be a cooperative personality who will actively master the integrative task of participating in developing and implementing MaReCuM.

The positions are available unlimited. In case that the successful candidate has not been appointed to a professorship position before, State law regulation demands under chapter 50 of the University law to fill the position as a tenure track position for 3 years. Exceptions are possible for candidates from abroad or from non-university institutions if candidates cannot be attracted otherwise. When the position is tenured after the tenure track period, the formal application process need not be repeated.

The University of Heidelberg is an Equal Opportunity/Affirmative Action Employer.
The University of Heidelberg seeks to increase the number of qualified women in teaching and research positions and strongly encourages applications of women. Handicapped persons with equivalent qualifications will be given preference.

Interested candidates should submit a full CV with copies of certificates, publication list and selected reprints within 4 weeks of publication of this advertisement to **Prof. Dr. Dr. h.c. K. van Ackern, Dean of the Faculty of Clinical Medicine Mannheim, University of Heidelberg, University Medical Center Mannheim, 68135 Mannheim, Germany.**

MASSACHUSETTS GENERAL HOSPITAL
HARVARD STEM CELL INSTITUTE

is recruiting faculty in **Mesenchymal Stem Cell Biology** for a newly created, multi-disciplinary **Center for Regenerative Medicine (CRM)** in conjunction with the Orthopedic Department. The successful candidate will also be a member of the new **Harvard Stem Cell Institute (HSCI)** and faculty member of Harvard Medical School. One Assistant Professor level position is available specifically focused on the basic understanding and manipulation of mammalian mesenchymal stem cells.

The goal of the CRM is to provide detailed analyses of tissue development for the purpose of modeling disease states and creating practical methods of tissue regeneration, replacement or repair. It incorporates developmental biology, ES and adult stem cell biology, bioengineering, imaging and computational expertise to understand the complex relationships of primitive cells with their microenvironment. The Orthopedic Department research program emphasizes the biology of skeletal tissues with a focus on osteolysis, osteoarthritis, bone defects and healing, and bone tumors.

This combined recruitment prioritizes basic cell biologic investigation as a base for translation into practical applications in human disease. The centers participate fully in the larger Harvard University-wide stem cell musculoskeletal research efforts and graduate programs; the prospective laboratory is in new space on the MGH main campus. The **HSCI** is a major new university-wide, interdisciplinary endeavor with resources to speed progress in the field. We are seeking Ph.D., M.D., or M.D./Ph.D. scientists with a history of innovative, interactive research.

Candidates should send a letter of interest including research plans, c.v. and 3 letters of support to **Dr. David Scadden, c/o Chris Shambaugh: cpasker@partners.org** and **Dr. Harry Rubash: hrubash@partners.org**.

MERRIAM-MONTGOMERY PROFESSOR, OTOLOGY & LARYNGOLOGY, HARVARD MEDICAL SCHOOL
DIRECTOR, MOSHER LABORATORY FOR LARYNGOLOGY RESEARCH
MASSACHUSETTS EYE AND EAR INFIRMARY

The Harvard Medical School (HMS) and the Massachusetts Eye and Ear Infirmary (MEEI) seek applications from outstanding scientists (Ph.D. or M.D.) interested in the study of laryngeal function, speech production, voice, swallowing or related areas, for appointment to the Department of Otology and Laryngology at the level of Full Professor or Associate Professor. This research-track position is funded by the Merriam-Montgomery Chair at the HMS.

We seek a Director for a laboratory to be located at the MEEI. The MEEI provides an interdisciplinary and collaborative intellectual environment within an active clinical setting, with a large laryngology division and voice laboratory. The wider research base at the MEEI includes 28 NIH-funded investigators studying hearing and deafness, as well as balance and voice disorders, and 15 NIH-funded investigators studying vision and blindness. MEEI researchers have academic ties to numerous Centers, Programs and Departments at HMS and MIT.

Candidates should have an outstanding record of research accomplishment and leadership, and will be expected to contribute to teaching programs for medical students, graduate students, and postdoctoral fellows, at both Harvard and MIT, including the Program in Speech and Hearing Bioscience and Technology.

Interested applicants should send a current CV and a Statement of Research Interests to:

M. Charles Liberman, PhD.
Professor, Otology and Laryngology, Harvard Medical School.
Director, Eaton Peabody Laboratory Massachusetts Eye and Ear Infirmary
243 Charles St. Boston, MA 02114
E-mail: charles_liberman@meei.harvard.edu

The Massachusetts Eye and Ear Infirmary and Harvard Medical School are Equal Opportunity/Affirmative Action Employers. Women and Minorities Encouraged to Apply.

HARVARD MEDICAL SCHOOL

Massachusetts Eye and Ear Infirmary

International Max Planck Research School
PhD Program in Structure and Function of Biological Membranes

Max Planck Institute of Biophysics
Max Planck Institute of Brain Research
Goethe University
Frankfurt am Main, Germany

Several PhD fellowships are available in the International Max Planck Research School in Frankfurt. The two Max Planck Institutes and research groups at Frankfurt University offer a unique environment for the study of biological membranes and membrane proteins. PhD opportunities exist in internationally leading laboratories in the areas of membrane protein structure determination, membrane biochemistry, molecular biology and functional studies by electrophysiological and spectroscopic methods as well as studies of whole membranes, cells and organelles.

Highly qualified candidates with degrees in biochemistry, chemistry, physics, biology, medicine or related subjects are invited to apply for the next round of admission in November 2006. Application forms can be downloaded from the website of the Research School at *www.mpibp-frankfurt.mpg.de/research-school.* Completed application forms and two letters of reference should arrive not later than 31 August 2006.

For further details please contact:
Dr. Janet Vonck , MPI of Biophysics, Max-von-Laue-Str. 3, 60438 Frankfurt am Main, Germany
Tel: +49+69-6303-3004/3001
Fax: +49+69-6303-3002
E-mail: Research.School@mpibp-frankfurt.mpg.de

CHAIR, DEPARTMENT OF CELLULAR AND STRUCTURAL BIOLOGY

The University of Texas Health Science Center at San Antonio

The Search Committee for the position of Chair of the Department of Cellular and Structural Biology at The University of Texas Health Science Center at San Antonio (UTHSCSA) invites applications and nominations for this position. Candidates with an outstanding record of achievement in scientific publication, consistent extramural grant support, training/mentoring, interdisciplinary research and training, advocacy and development of core facilities and national professional involvement, consistent with the rank of professor are sought. Strong leadership and communication skills are required for this position. Applicants with research interests in any area of contemporary biomedical science that complements the ongoing research in the Department and interdisciplinary activities at UTHSCSA, such as vascular biology, diabetes, neuroscience, and genetics, will be considered. Areas of ongoing research within the Department include cancer biology, aging, signaling pathways and gene expression, animal models of human disease, bone pathophysiology and DNA damage and repair. The Department has a major commitment to the teaching of the anatomical sciences in the Medical, Dental and Allied Health Schools.

Interested applicants should submit a curriculum vitae, a succinct statement (3 pages or less) of research interests and academic vision, and a list of 4 referees who know the professional attributes of the applicant very well. The Search Committee will begin reviewing applications on **September 1, 2006** and the search will continue until the position is filled. Please send materials electronically to **smithj@uthscsa.edu** or by mail to: **Chair, Search Committee for Chair of Cellular and Structural Biology, Graduate Dean's Office, MC 7819, UTHSCSA, 7703 Floyd Curl Drive, San Antonio, TX 78229-3900**. Information concerning the Department of Cellular and Structural Biology at UTHSCSA can be found at **http://www.uthscsa.edu/csb/**. All faculty appointments are designated as security-sensitive positions.

The University of Texas Health Science Center at San Antonio is an Equal Employment Opportunity/Affirmative Action Employer.

Group Leaders at the Ecole Normale Supérieure, Paris, France

Applications are invited for Group Leader positions in the **Biology Department** of the **Ecole Normale Supérieure**. The persons appointed will lead an independent research group in an excellent and stimulating scientific environment. For further information, please consult our web site (**www.biologie.ens.fr**). Each group will be accommodated in a 50-100 square meter space. If the applicant does not already hold a permanent position in France, the Department will back his/her application for a tenured CNRS/INSERM position equivalent to an Assistant Professor level.

1) Biological Physics. He/She will develop cutting-edge research at the interface of biological and physical sciences. Applicants are therefore expected to have a strong background in physics/biophysics/biology. He/She will apply advanced imaging technologies to important biological questions in the field of Cell Biology and/or Neurosciences. A strong research project complementary to existing topics in the Department (single molecule tracking and/or imaging of protein complexes in living organisms, imaging of neuronal activity) will be preferred. The group will be located next to the imaging facility of the Department. Contact is Antoine Triller (**Antoine.Triller@ens.fr**).

2) Plant Biology. He/She will develop cutting-edge research in Molecular Plant Biology with emphasis on some aspect of *Arabidopsis* development or physiology. Applicants are therefore expected to have a strong background in *Arabidopsis* genetics and cell biology. A strong research project complementary to existing topics in the Department (genetics, genomics, development, cell biology, evolution, imaging) will be preferred. The group will be located within the Plant Biology unit. Contacts are Chris Bowler (**cbowler@biologie.ens.fr**) and Antoine Triller (**Antoine.Triller@ens.fr**).

Applications should include:

- CVs of the principal investigator and group members
- Recent publications (past five years)
- Summary of recent achievements (1-2 pages)
- Four year research programme (10-12 pages)

Deadline September 15th 2006
Department Head:
Antoine Triller, Ecole Normale Supérieure, 46 rue d'Ulm, 75230 Paris cedex 05, France.

Faculty Positions
Gene Expression and Molecular Cell Biology
University of South Carolina

As part of the Faculty Excellence Initiative at the University of South Carolina, applicants are being sought for two Assistant Professor tenure-track positions in the broad area of gene expression and molecular cell biology. Interests include, but are not limited to, cell signaling, transcriptional and post-transcriptional regulation, gene silencing, and epigenetic control mechanisms. Appointments will be made in participating Departments and include Biological Sciences of the College of Arts and Sciences and School of Medicine Departments of Pharmacology, Physiology and Neuroscience, and of Pathology and Microbiology.

The appointed faculty members are expected to establish a successful research program and secure extramural funding. Participation in graduate student education and research, and a teaching commitment commensurate with a high quality research program are expected. Applicants with an earned doctorate, a strong research record, and postdoctoral experience should provide a curriculum vitae with a description of research plans and goals and arrange for three letters of recommendation to be sent by **October 1, 2006** by email to **felder@biol.sc.edu** or mail to: **Dr. Michael R. Felder, Department of Biological Sciences, University of South Carolina, Columbia, SC 29208**.

The University of South Carolina is an Affirmative Action, Equal Opportunity Institution. ***Minorities and women are encouraged to apply.***

INSTITUTE FOR ADVANCED RESEARCH, NAGOYA UNIVERSITY
15 Tenure-Track Positions (Designated Associate/ Assistant Professors) in All Fields of the Natural Sciences

(Duration of Appointment: November 1, 2006 ~ March 31, 2011)

In recognizing the value of creative research in providing intellectual assets for the future, Nagoya University established the Institute for Advanced Research (IAR) in April 2002 as a research base for achieving the highest level of academic research. IAR's founding director is Dr Ryoji Noyori, the 2001 Nobel Prize Laureate in Chemistry. IAR is the first academic institution in Japan that intensively promotes highly creative research in all academic disciplines. IAR's "Special Rearing Plan for Researchers (Tenure-Track Positions)" has been selected as part of the "Supporting Young Researchers with Fixed-term Appointments" program. This program has been commissioned by the Japanese Ministry of Education, Culture, Sports, Science and Technology (MEXT) and is financially supported by the Special Coordination Fund for Promoting Science and Technology for the financial year of 2006. IAR is inviting applications from young researchers from all over the world for 15 tenure-track positions in all fields of the natural sciences at an associate/assistant professor level. Appointees selected by the IAR Tenure-Track Position Selection Committee will be appointed as designated Associate/Assistant Professors of Nagoya University. Appointees will be provided with an outstanding research environment and will be expected to commit to the highest standards of scholarship and professionalism. Upon completion of the appointment, the appointee may be granted a tenured position (tenured positions at Nagoya University have a compulsory retirement age) if the research undertaken during his/her period of appointment proves to have met the standards agreed upon at the start of the term.

Requirements: A PhD degree in any fields of natural sciences granted within the past 10 years (as of November 1, 2006).

Interested candidates should apply online at: **http://www.iar.nagoya-u.ac.jp/SRPR/index.html**. The closing date is **August 17, 2006**. Offers will be made in late September, 2006. Additional information about IAR and the program can be found at **http://www.iar.nagoya-u.ac.jp/**. Inquiries are handled by email only. Email Address: **SRPR_inquiry@iar.nagoya-u.ac.jp**.

Nagoya University is an Equal Opportunity Employer.

NORTHWESTERN UNIVERSITY

POST-DOCTORAL POSITION
Northwestern University

The Biomedical Engineering Department is offering a post-doctoral position in the area of stem cells and tissue engineering. The project will focus on the characterization, design and development of stem cells and biomaterials as applied to the engineering of cell-based vascular grafts. The position is available immediately and applications will be accepted until the position is filled. Salary will be commensurate with experience. Applicants should have a PhD or equivalent degree and significant experience with standard cell and molecular biology techniques and relevant polymer chemistry. Experience with FACS is also desirable.

Send letter of interest, curriculum vitae, and the names of three references to: **Dr. Guillermo A. Ameer, Northwestern University, Biomedical Engineering Department, 2145 Sheridan Rd. E310, Evanston IL 60208-3107; Email: g-ameer@northwestern.edu (subject line: Stem Cell Post doc); Telephone: 847-467-6719; FAX: 847-491-4928.**

Northwestern University is an Affirmative Action/Equal Opportunity Employer.

LOUISIANA STATE UNIVERSITY

J. Bennett Johnston, Sr., Center of Advanced Microstructures and Devices (CAMD)
Baton Rouge, Louisiana 70803

DIRECTOR

LSU invites applicants for Director of the J. Bennett Johnston, Sr., Center of Advanced Microstructures and Devices, a synchrotron radiation center in Baton Rouge, LA.

The successful candidate will have outstanding national and international scientific credentials, will provide scientific and programmatic leadership to sustain CAMD's exceptional research and development activities in materials science, biological studies, microfabrication, and other targeted areas of scientific and technological exploration, and will guide CAMD toward future goals of being a southeast regional center for basic and applied research using synchrotron radiation.

The successful candidate will report to and work closely with the Vice Chancellor for Research and Economic Development to further the scientific mission of CAMD and to foster LSU's advancement toward continued innovation and greater excellence.

The successful candidate will pursue and coordinate interdisciplinary research, student training and outreach between CAMD and the appropriate colleges, departments, centers, and institutes on the LSU campus, as well as at other universities and research entities, both national and international. The successful candidate will have a strong scientific background and research track record in synchrotron radiation and other related basic and applied research areas and an advanced degree in engineering and/or one of the basic sciences, such as physics, chemistry, or biology. The candidate's academic credentials should be acceptable for tenure as a full professor in one of the engineering or science departments at LSU.

Screening will begin on August 31, 2006 and continue until a successful candidate is selected. Further details about CAMD and LSU can be found at **www.camd.lsu.edu** and **www.lsu.edu**, respectively. An offer of employment is contingent on a satisfactory pre-employment background check. Applications should include a letter of application and a current curriculum vitae (including e-mail address). Applications should be sent to:

Director of CAMD Search
Office of Research & Economic Development
130 David F. Boyd Hall
Louisiana State University
Ref: Log #0666
Baton Rouge, LA 70803
or
Fax: (225)578-5983
or
E-mail: research@lsu.edu

LSU is an Equal Opportunity/Equal Access Employer

JAIST
JAPAN ADVANCED INSTITUTE OF SCIENCE AND TECHNOLOGY 1990

Job title: "Lecturer" (U.S. equivalent of Assistant Professor)
Employer: Japan Advanced Institute of Science and Technology (JAIST)
Location: Nomi-shi, Ishikawa-ken, Japan

JAPAN ADVANCED INSTITUTE OF SCIENCE AND TECHNOLOGY (JAIST)

invites applications for eight Lecturers (U. S. Equivalent of Tenure Track Assistant Professors) for research and education in Nanomaterials Science and Technology, and in Interdisciplinary Areas bridging between Information Science and Nanomaterials Science and Technology.
The appointments start after October 2006.

Background Information:
JAIST was founded in 1990 as the first independent national graduate school to develop innovative approaches to graduate education and research in Japan. It is located on the Japan Sea side near the city of Kanazawa, which is known as "Little Kyoto," rich with traditional Japanese art and culture.

This year JAIST was selected as one of the nine universities to carry out a national program to train and encourage young faculty members. Under the support of this Program eight "lecturers" will be appointed in the Schools of Materials Science and Information Science for the period ending on March 31, 2011.

The successful candidates are expected to establish independent research groups and participate in the training of graduate students. They will be provided with startup fund of 10M yen each and additional fund to employ a postdoctoral researcher. Qualified candidates will be promoted to tenured associate professorship after rigorous evaluation of their accomplishments and potential.

Foreign and women candidates are especially encouraged to apply for these positions. JAIST has a semi-bilingual environment with Japanese and English. Thus fluency in English is required but not in Japanese.

Areas of specialty:
1) Five "Lecturers" in Nanomaterials Science and Technology
2) Three "Lecturers" in Interdisciplinary areas bridging between Information Science and Nanomaterials Science

All applicants are requested to submit the following materials:
1) Curriculum Vitae with candidate's photograph, 2) Publication list in reversed chronological order (Separate categories of research papers in refereed professional journals, refereed presentations at international conferences, and other relevant published materials as evidence of accomplishments), 3) List of educational contributions, academic society activities, including editorship of journals, membership in international conference organizing committees, etc., 4) Reprints of the candidate's most significant papers (up to five), 5) Outline of the above papers explaining the significance of the work, 6) Summary of previous experience in education and research (up to 1000 words), 7) Future education and research plan (up to 1000 words), 8) Names of three professional references including their e-mail addresses.

Deadline: The first selection process will take place on applications received by July 31, 2006, and the Selection Committee will remain active until all positions are filled.

Please send your application to:
Prof. Akio Makishima
(Vice President (Academic Affairs))
JAIST 1-1 Asahidai, Nomi, Ishikawa,
923-1292, JAPAN
Tel: +81-761-51-1002,
Fax: +81-761-51-1058
E-mail: **makisima@jaist.ac.jp**
Institute homepage is at:
http://www.jaist.ac.jp/index-e.html